



© Copyright by Kibraeb A Gebreselassie 2016

All Rights Reserved

DETECTION AND QUANTIFICATION OF STEEL AND COMPOSITE  
CORROSION WITH SMART CEMENT AND POLYMER  
COATING MATERIALS

A Dissertation

Presented to

the Faculty of the Department of Civil and Environmental Engineering

University of Houston

In Partial Fulfillment

of the Requirements for the Degree

Doctor of Philosophy

in Civil Engineering

by

Kibraeb A Gebreselassie

December 2016

DETECTION AND QUANTIFICATION OF STEEL AND COMPOSITE  
CORROSION WITH SMART CEMENT AND POLYMER  
COATING MATERIALS

---

Kibraeb A Gebreselassie

Approved:

---

Chair of the Committee  
Cumaraswamy Vipulanandan, Professor,  
Civil and Environmental Engineering

Committee Members:

---

Ramanan Krishnamoorti, Professor,  
Chemical and Biomolecular Engineering

---

Yuhua Chen, Associate Professor,  
Electrical and Computer Engineering

---

Yi-Lung Mo, Professor,  
Civil and Environmental Engineering

---

Kalyana B. Nakshatrala, Assistant Professor,  
Civil and Environmental Engineering

---

Suresh K. Khator, Associate Dean,  
Cullen College of Engineering

---

Roberto Ballarini, Professor and Chair,  
Civil and Environmental Engineering

## **ACKNOWLEDGEMENT**

I would like to take this great opportunity to give honors and praises to God through His Son Jesus Christ for His mercy and grace.

This study would not have been possible without the valuable assistances of several individuals throughout the course of my research. First, I would like to express my sincere gratitude to my advisor, Dr. Cumaraswamy Vipulanandan, for his valuable guidance, encouragement, and kindness throughout my study.

I would like to extend my great appreciation to Dr. Ramanan Krishnamoorti, Dr. Yuhua Chen, Dr. Yi-Lung Mo, and Dr. Kalyana B. Nakshatrala for serving in my dissertation committee and taking time for exchanging valuable suggestions.

I also wish to acknowledge the past and present friends in the GEM group for their help and companionship throughout my research work.

Special thanks go to my family for their understanding, unconditional help, endless patience, and encouragement without which it would have been a difficult task to accomplish.

The financial supports provided by the CIGMAT, THC-IT, and department of Civil and Environment Engineering at the University of Houston are gratefully acknowledged.

DETECTION AND QUANTIFICATION OF STEEL AND COMPOSITE  
CORROSION WITH SMART CEMENT AND POLYMER  
COATING MATERIALS

An Abstract

of a

Dissertation

Presented to

the Faculty of the Department of Civil and Environmental Engineering

University of Houston

In Partial Fulfillment

of the Requirements for the Degree

Doctor of Philosophy

in Civil Engineering

by

Kibraeb A Gebreselassie

December 2016

## ABSTRACT

Corrosion is the primary factor affecting the longevity and reliability of all the infrastructures supporting the oil and gas industries that transport crucial energy, highway, buildings and water sources throughout the world. The average annual corrosion-related cost in the United States only is estimated to be \$7 billion to monitor, replace, and maintain these assets. Corrosion can be occurred in any material because of reaction with its environment. Various types of coatings are applied to protect steel structures from corrosion.

In this study, a new non-destructive testing method that can be used to detect and quantify the presence bulk and interface was developed. The new method uses the changes in electrical properties of the bulk material and the interfaces to quantify the corrosion. Using this method, the changes in the bulk electrical resistivity of steel specimens were quantified in three principal directions. Corrosion study on steel specimens in dry-air condition, salt and acid solutions were quantified using the new electrical method and the bulk resistivity changes were determined in the three principal directions and were of the order of 1000% compared to the weight change of about 2%. Also, a new material parameter, combining two electrical properties, has been developed to quantify the surface and interface corrosion. Using the new surface corrosion parameter, the corrosion in the steel specimens exposed to various chemical solutions has been quantified and the changes were in the range of 10% to 1800%.

Smart cement and smart polymer composite highly sensing piezoresistive coating materials were developed and used in the evaluating the corrosion in steel-smart coating composites. The composites were exposed to various chemical environments and the

changes in the electrical properties at the steel-coating interface and bulk coating materials were quantified using the new electrical parameters. Over period of one year, the change in the interface corrosion for the non-corroded steel-coating composite exposed in various environmental conditions varied from 0% to 19,600% and for the corroded steel-coating composite exposed in various environmental conditions varied from 27% to 145,000%. The property changes in the smart coatings used to protect the corroded steel was in the range of 2,900% to 11,400%, in smart cement, 57% to 310% in smart polyester, and 24% to 62% in smart polymer concrete.

The interface corrosion concept was also verified in the large model and field model tests simulating the cemented oil wells. The interface corrosion parameter in the field model was comparable to the surface corrosion in steel composite specimens exposed to similar conditions in the laboratory.

# TABLE OF CONTENTS

ACKNOWLEDGEMENT .....	v
ABSTRACT.....	vii
TABLE OF CONTENTS.....	ix
LIST OF FIGURES .....	xii
LIST OF TABLES .....	xxi
CHAPTER 1 INTRODUCTION.....	1
1.1 Background .....	1
1.2 Objectives.....	3
1.3 Organization.....	3
CHAPTER 2 LITERATURE REVIEW .....	4
2.1 Steel Corrosion.....	4
2.2 Interface Corrosion.....	11
2.3 Coatings.....	13
2.3.1 Organic Coatings .....	13
2.3.2 Inorganic Coatings .....	16
2.4 Summary .....	18
CHAPTER 3 MATERIALS AND TEST METHODS.....	19
3.1 Testing Materials.....	19
3.1.1 Steel Bars .....	19
3.1.2 Cement .....	20
3.1.3 Polyester.....	21
3.1.4 Polymer Concrete.....	23
3.2 Testing Method .....	24
3.3 Summary .....	25

CHAPTER 4 DEVELOPING AND CHARACTERIZING SMART COATING MATERIALS .....	26
4.1    Cement .....	26
4.2    Polyester .....	27
4.3    Polymer Concrete .....	28
4.4    Summary .....	30
CHAPTER 5 CORROSION STUDY .....	31
5.1    Modeling .....	31
5.1.1    Impedance Modeling .....	31
5.1.2    Corrosion-Time Modeling .....	34
5.2    Steel Bar .....	35
5.3    Bulk Materials .....	40
5.4    Composite Interface .....	40
5.4.1    Steel-Cement Characterization .....	40
5.4.2    Steel-Polyester Characterization .....	60
5.4.3    Steel-Polymer Concrete Characterization .....	81
5.5    Summary .....	102
CHAPTER 6 LARGE MODEL TESTS AND FIELD MODEL TESTS .....	104
6.1    Large Model Tests .....	104
6.1.1    Cement Characterization .....	107
6.1.2    Steel-Cement Characterization .....	109
6.2    Field Model Tests .....	121
6.2.1    Cement Characterization .....	124
6.2.2    Steel-Cement Characterization .....	127
6.3    Summary .....	142

CHAPTER 7 CONCLUSION AND RECOMMENDATION .....	144
7.1 Conclusion.....	144
7.2 Recommendation.....	147
REFERENCES .....	148

## LIST OF FIGURES

Figure 2.1 Workers monitor the site of an underground oil pipe break up.....	6
Figure 2.2 Pipeline failure due to severe corrosion .....	7
Figure 2.3 Casing failure due to severe corrosion .....	7
Figure 2.4 Collapsed pedestrian bridge .....	8
Figure 2.5 A schematic test setup for EIS measurement .....	12
Figure 3.1 AISI steel 1018 bars .....	19
Figure 3.2 Non-corroded and corroded steel bars.....	20
Figure 3.3 Cement composite specimens.....	21
Figure 3.4 Materials used for polyester specimens.....	22
Figure 3.5 Polyester composite specimens .....	22
Figure 3.6 Sand used for polymer concrete specimens.....	23
Figure 3.7 Polymer concrete composites .....	24
Figure 3.8 LCR meter device.....	24
Figure 3.9 Schematic test setup for measuring using LCR meter device .....	25
Figure 4.1 Typical piezoresistive behavior of cement mix.....	27
Figure 4.2: Typical piezoresistive behavior of polyester coating.....	28
Figure 4.3: Typical piezoresistive behavior of polymer concrete.....	29
Figure 5.1 Equivalent circuits adopted .....	32
Figure 5.2 Directional measurements on steel bar.....	35
Figure 5.3 Bode plot for steel bars.....	36
Figure 5.4 Bode plot of for steel bars alone the impedance model.....	37
Figure 5.5 $R_c \cdot C_c$ vs distance for steel bars .....	38

Figure 5.6 Resistivity of the steel bars .....	39
Figure 5.7 Bode plot of cement composite with embedded non-corroded bar .....	41
Figure 5.8 Bode plot of cement composite with embedded corroded bar .....	42
Figure 5.9 Bode plot of cement composites with embedded non-corroded and corroded bar along respective impedance models .....	42
Figure 5.10 Resistances ( $R_i$ & $R_c$ ) of the non-corroded bar embedded in smart cement under air dry condition.....	44
Figure 5.11 Capacitances ( $C_i$ & $C_c$ ) of the non-corroded bar embedded in smart cement in air dry condition.....	44
Figure 5.12 $R \cdot C$ vs. time of the non-corroded bar embedded in smart cement in air dry condition .....	45
Figure 5.13 Corrosion-time model for non-corroded cement composite under dry condition .....	46
Figure 5.14 Resistances ( $R_i$ & $R_c$ ) of the corroded bar embedded in smart cement under dry air condition.....	48
Figure 5.15 Capacitances ( $C_i$ & $C_c$ ) of the corroded bar embedded in smart cement under dry air condition .....	48
Figure 5.16 $R \cdot C$ vs. time of the corroded bar embedded in smart cement under dry air condition .....	49
Figure 5.17 Corrosion-time model for corroded cement composite under dry condition .	50
Figure 5.18 Bode plot of cement composite with embedded non-corroded bar after immersed in salt-water solution for 28 weeks .....	51

Figure 5.19 Bode plot of cement composite with embedded corroded bar after immersed in salt-water solution for 28 weeks .....	52
Figure 5.20 Bode plot cement composite with embedded non-corroded and corroded bar along impedance models after immersed in salt-water for 28 weeks .....	52
Figure 5.21 Resistances ( $R_i$ & $R_c$ ) of the non-corroded bar embedded in smart cement specimen under salt water condition.....	54
Figure 5.22 Capacitances ( $C_i$ & $C_c$ ) of the non-corroded bar embedded in smart cement specimen under salt water condition.....	55
Figure 5.23 $R \cdot C$ vs. time of the non-corroded bar embedded in smart cement specimen under salt water condition.....	55
Figure 5.24 Corrosion-time model for non-corroded cement composite under salt water condition .....	56
Figure 5.25 Resistances ( $R_i$ & $R_c$ ) of the corroded bar embedded in smart cement specimen under salt water condition.....	58
Figure 5.26 Capacitances ( $C_i$ & $C_c$ ) of the corroded bar embedded in smart cement specimen under salt water condition.....	58
Figure 5.27 $R \cdot C$ vs. time of the corroded bar embedded in smart cement specimen under salt water condition.....	59
Figure 5.28 Corrosion-time model for corroded cement composite under salt water condition .....	60
Figure 5.29 Bode plot of polyester composite with embedded non-corroded bar .....	61
Figure 5.30 Bode plot of polyester composite with embedded corroded bar .....	62

Figure 5.31 Bode plot of polyester composites with embedded non-corroded and corroded bar along respective impedance models .....	62
Figure 5.32 Resistances ( $R_i$ & $R_c$ ) of the non-corroded bar embedded in smart polyester under air dry condition.....	64
Figure 5.33 Capacitances ( $C_i$ & $C_c$ ) of the non-corroded bar embedded in smart polyester in air dry condition.....	65
Figure 5.34 $R^*C$ vs. time of the non-corroded bar embedded in smart polyester in air dry condition .....	65
Figure 5.35 Corrosion-time model for non-corroded polyester composite under dry condition .....	66
Figure 5.36 Resistances ( $R_i$ & $R_c$ ) of the corroded bar embedded in smart polyester under air dry condition.....	68
Figure 5.37 Capacitances ( $C_i$ & $C_c$ ) of the corroded bar embedded in smart polyester in air dry condition.....	69
Figure 5.38 $R^*C$ vs. time of the corroded bar embedded in smart polyester in air dry condition .....	69
Figure 5.39 Corrosion-time model for corroded polyester composite under dry condition	70
Figure 5.40 Bode plot of polyester composite with embedded non-corroded bar after immersed in salt- water for 5 weeks .....	72
Figure 5.41 Bode plot of polyester composite with embedded corroded bar after immersed in salt-water for 5 weeks .....	72
Figure 5.42 Bode plot polyester composite with embedded non-corroded and corroded bar along impedance models after immersed in salt-water for 5 weeks.....	73

Figure 5.43 Resistances ( $R_i$ & $R_c$ ) of the non-corroded bar embedded in smart polyester specimen under salt water condition.....	75
Figure 5.44 Capacitances ( $C_i$ & $C_c$ ) of the non-corroded bar embedded in smart polyester specimen under salt water condition.....	75
Figure 5.45 $R \cdot C$ vs. time of the non-corroded bar embedded in smart polyester specimen under salt water condition.....	76
Figure 5.46 Corrosion-time model for non-corroded polyester composite under salt-water condition .....	77
Figure 5.47 Resistances ( $R_i$ & $R_c$ ) of the corroded bar embedded in smart polyester specimen under salt water condition.....	79
Figure 5.48 Capacitances ( $C_i$ & $C_c$ ) of the corroded bar embedded in smart polyester specimen under salt water condition.....	79
Figure 5.49 $R \cdot C$ vs. time of the corroded bar embedded in smart polyester specimen under salt water condition.....	80
Figure 5.50 Corrosion-time model for corroded polyester composite under salt-water condition .....	81
Figure 5.51 Bode plot of polymer concrete composite with embedded non-corroded bar	82
Figure 5.52 Bode plot of polymer concrete composite with embedded corroded bar .....	83
Figure 5.53 Bode plot of polymer concrete composites with embedded non-corroded and corroded bar along respective impedance models .....	83
Figure 5.54 Resistances ( $R_i$ & $R_c$ ) of the non-corroded bar embedded in smart polymer concrete under air dry condition .....	85

Figure 5.55 Capacitances ( $C_i$ & $C_c$ ) of the non-corroded bar embedded in smart polymer concrete in air dry condition .....	86
Figure 5.56 $R^*C$ vs. time of the non-corroded bar embedded in smart polymer concrete in air dry condition .....	86
Figure 5.57 Corrosion-time model for non-corroded polymer concrete composite under dry condition .....	87
Figure 5.58 Resistances ( $R_i$ & $R_c$ ) of the corroded bar embedded in smart polymer concrete under air dry condition .....	89
Figure 5.59 Capacitances ( $C_i$ & $C_c$ ) of the corroded bar embedded in smart polymer concrete in air dry condition .....	90
Figure 5.60 $R^*C$ vs. time of the corroded bar embedded in smart polymer concrete in air dry condition .....	90
Figure 5.61 Corrosion-time model for corroded polymer concrete composite under dry condition .....	91
Figure 5.62 Bode plot of polymer concrete composite with embedded non-corroded bar after immersed in salt-solution water for 5 weeks .....	92
Figure 5.63 Bode plot of polymer concrete composite with embedded corroded bar after immersed in salt-solution water for 5 weeks .....	93
Figure 5.64 Bode plot of polymer concrete composite with embedded non-corroded and corroded bars with models after immersed in salt-water for 5 weeks .....	93
Figure 5.65 Resistances ( $R_i$ & $R_c$ ) of the non-corroded bar embedded in smart polymer concrete specimen under salt water condition .....	95

Figure 5.66 Capacitances ( $C_i$ & $C_c$ ) of the non-corroded bar embedded in smart polymer concrete specimen under salt water condition .....	96
Figure 5.67 $R^*C$ vs. time of the non-corroded bar embedded in smart polymer concrete specimen under salt water condition.....	96
Figure 5.68 Corrosion-time model for non-corroded polymer concrete composite under salt-water condition.....	97
Figure 5.69 Resistances ( $R_i$ & $R_c$ ) of the corroded bar embedded in smart polymer concrete specimen under salt water condition .....	99
Figure 5.70 Capacitances ( $C_i$ & $C_c$ ) of the corroded bar embedded in smart polymer concrete specimen under salt water condition .....	100
Figure 5.71 $R^*C$ vs. time of the corroded bar embedded in smart polymer concrete specimen under salt water condition.....	100
Figure 5.72 Corrosion-time model for corroded polymer concrete composite under salt-water condition.....	101
Figure 6.1 Steel casing pipe embedded in the PVC pipe.....	105
Figure 6.2 Schematic diagrams for the casing and wires instrumentation .....	106
Figure 6.3 Bulk resistance vs. depth of the casing at each measuring level .....	108
Figure 6.4 Bulk resistance ( $R_b$ ) of the casing at level-1, level-7, and level 14 for one year period .....	108
Figure 6.5 Bode plot of casing for level-1 .....	110
Figure 6.6 Bode plot of casing along respective impedance models for level-1 .....	110
Figure 6.7 Bode plot of casing for level-7 .....	111
Figure 6.8 Bode plot of casing along respective impedance models for level-7 .....	111

Figure 6.9 Bode plot of casing for level-14 .....	112
Figure 6.10 Bode plot of casing along respective impedance models for level-14 .....	112
Figure 6.11 Resistance vs. depth of the casing at each measuring level .....	113
Figure 6.12 Resistances ( $R_i$ & $R_c$ ) of the casing at level-1 for one year period .....	114
Figure 6.13 Resistances ( $R_i$ & $R_c$ ) of the casing at level-7 for one year period .....	114
Figure 6.14 Resistances ( $R_i$ & $R_c$ ) of the casing at level-14 for one year period .....	115
Figure 6.15 Capacitance vs. depth of the casing at each measuring level .....	116
Figure 6.16 Capacities ( $C_i$ & $C_c$ ) of the casing at level-1 for one year period .....	116
Figure 6.17 Capacities ( $C_i$ & $C_c$ ) of the casing at level-7 for one year period .....	117
Figure 6.18 Capacities ( $C_i$ & $C_c$ ) of the casing at level-14 for one year period .....	117
Figure 6.19 $R \cdot C$ vs. depth of the casing at each measuring level .....	119
Figure 6.20 $R \cdot C$ vs. depth of the casing at level-1 for one year period .....	119
Figure 6.21 $R \cdot C$ vs. depth of the casing at level-7 for one year period .....	120
Figure 6.22 $R \cdot C$ vs. depth of the casing at level-14 for one year period .....	120
Figure 6.23 A 40 ft. long steel casing pipe with diameter of 8 inches.....	122
Figure 6.24 A steel pipe during casing construction.....	123
Figure 6.25 Schematic diagrams for the casing and wires instrumentation .....	124
Figure 6.26 Bulk resistance vs. depth of the casing at each measuring level .....	125
Figure 6.27 Bulk resistance of the casing at level-1 and level-7 for one year period.....	126
Figure 6.28 Bulk resistance ( $R_b$ ) of the casing at level-1, level-7 and level-13 for one year period .....	126
Figure 6.29 Bode plot of casing for level-1 .....	128
Figure 6.30 Bode plot of casing along respective impedance models for level-1 .....	128

Figure 6.31 Bode plot of casing for level-7 .....	129
Figure 6.32 Bode plot of casing along respective impedance models for level-7 .....	129
Figure 6.33 Bode plot of casing for level-13 .....	130
Figure 6.34 Bode plot of casing along respective impedance models for level-13 .....	130
Figure 6.35 Resistance vs. depth of the casing at each measuring level .....	131
Figure 6.36 Resistances ( $R_i$ & $R_c$ ) of the casing at level-1 for one year period .....	132
Figure 6.37 Resistances ( $R_i$ & $R_c$ ) of the casing at level-7 for one year period .....	132
Figure 6.38 Resistances ( $R_i$ & $R_c$ ) of the casing at level-13 for one year period .....	133
Figure 6.39 Capacitance vs. depth of the casing at each measuring level .....	134
Figure 6.40 Capacities ( $C_i$ & $C_c$ ) of the casing at level-1 for one year period .....	134
Figure 6.41 Capacities ( $C_i$ & $C_c$ ) of the casing at level-7 for one year period .....	135
Figure 6.42 Capacities ( $C_i$ & $C_c$ ) of the casing at level-13 for one year period .....	135
Figure 6.43 $R \cdot C$ vs. depth of the casing at each measuring level .....	136
Figure 6.44 $R \cdot C$ vs. depth of the casing at level-1 for one year period .....	137
Figure 6.45 $R \cdot C$ vs. depth of the casing at level-7 for one year period .....	137
Figure 6.46 $R \cdot C$ vs. depth of the casing at level-13 for one year period .....	138
Figure 6.47 Corrosion-time model for the casing at level-1 .....	139
Figure 6.48 Corrosion-time model for the casing at level-7 .....	140
Figure 6.49 Corrosion-time model for the casing at level-13 .....	140
Figure 6.50 Corrosion-time model for corroded cement composite and field casing .....	141

## LIST OF TABLES

Table 2.1 ASTM corrosion test methods .....	8
Table 2.2 A summary of steel corrosion studies.....	10
Table 2.3 A summary of cementitious composites studies.....	15
Table 2.4 A summary of polymer composites studies.....	17

# CHAPTER 1

## INTRODUCTION

### 1.1 Background

Corrosion is defined as the destruction or deterioration of a material because of the continuous biochemical, physical, and thermal reactions with the environment. Practically all environments are corrosive to some degree. Some examples are air and moisture; fresh, distilled, salt, and mine waters; rural, urban, and industrial atmospheres; steam and other gases such as chlorine, ammonia, hydrogen sulfide, sulfur dioxide, and fuel gases; mineral acids such as hydrochloric, sulfuric, and nitric; organic acids such as naphthenic, acetic, and formic; alkalis; soils; solvents; vegetable and petroleum oils; and a variety of food products. In general, the “inorganic” materials are more corrosive than the “organics.” For example, corrosion in the petroleum industry is mainly due to sodium chloride, hydrochloric and sulfuric acids, and water, than to the oil, naphtha, or gasoline (Fontana, 1987).

Corrosion is the primary factor affecting the longevity and reliability of pipelines that transport crucial energy sources throughout United States. According to the 1999 to 2001 U.S. corrosion study, the direct cost of metallic corrosion is \$276 billion on an annual basis. This represents 3.1% of the U.S. Gross Domestic Product (GDP). The average annual corrosion-related cost is estimated at \$7 billion to monitor, replace, and maintain these assets (NACE International, 2002).

A simple way of measuring corrosion of a metal is to measure the loss of weight of the material after it is exposed to a corrosive medium. The weight loss is estimated as the difference between the weight of the metal before exposed to corrosive environment and the weight of the cleaned metal after corrosion occurred. Although this test method is simple, it cannot be applicable where the metal is buried in concrete or cement mortar or where there's no access to the metal.

Other test methods involve measuring corrosion potential to estimate the corrosion activity in the metal under investigation. ASTM C876 (Standard Test Method for Corrosion Potentials of Uncoated Reinforcing Steel in Concrete) suggests to use the estimation of the electrical corrosion potential of uncoated reinforcing steel in field and laboratory concrete, for the purpose of determining the corrosion activity of the reinforcing steel. The method uses voltmeter to measure the potential difference between steel in concrete and a reference electrode such as Cu/CuSO<sub>4</sub>.

Coatings are applied to protect steel structures from corrosion. Coatings act as a barrier to a corrosive solution. The long-term performance of a coating is influenced significantly by its ability to adhere properly to the material to which it is applied. This is because poor adhesion will allow moisture or corrosion products to undercut the coating film from areas of damage (Saha et al., 2010). Earlier detection of the presence of corrosion is sought for appropriate corrosion mitigation steps before it results in high financial burned, environmental damage, and costs life in some case.

For the past two decades, there has been a tremendous amount of research focused on smart coatings for structural applications; coatings that can sense certain conditions

and then respond (Wheat, 2012). These are coatings that typically contain one or more indicators that can sense condition such as corrosion and respond by means of changes in pH, color, fluorescence or a combination thereof (Wheat, 2012). The applicability of such coatings for the steel casing in oil wellbore is difficult and impractical to monitor the changes that the coatings may exhibit through time due to the inaccessible nature of wellbore.

## **1.2 Objectives**

The overall objective of this research study was to develop bulk materials and sensing coating to detect and quantify the interface corrosion in composite materials.

The specific objectives are as follows:

- i. Developing sensing coating materials for corrosion and damage detection
- ii. Detect and quantify the interface properties related to corrosion in composites (steel-cement and steel-polymer)
- iii. Modeling the progression of the corrosion-time relationships for corroding composite

## **1.3 Organization**

In this dissertation, Chapter 2 summarizes literature review related to steel corrosion in composites. The testing materials and methods are presented in Chapter 3. Development of sensing coating materials for corrosion study is presented in Chapter 4. Corrosion study details are presented in Chapter 5. Large model tests and field model tests are presented in Chapter 6. Finally, summary and recommendations of this research are outlined in Chapter 7.

## CHAPTER 2

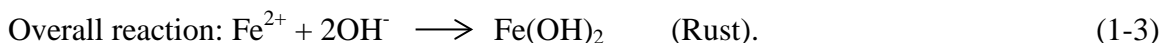
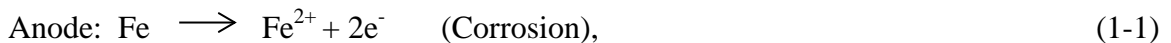
### LITERATURE REVIEW

#### 2.1 Steel Corrosion

Corrosion-resistant coated steel is widely used in the places where the working conditions and requirement for corrosion resistance are ramified. Corrosion is an intrinsic problem for utility metals. In case of steel, stainless steel, galvanized, electro galvanized, and weathering steel of which corrosion can be prevented or moderated have been put to practical use. This has led to an increase in the volume of steel used along with the improvement in performance for corrosion resistance. It is worth mentioning that coatings may delay initiation of corrosion by 10–20 years.

Steel corrosion form can be of one or a combination of the different forms of corrosion. Conveniently corrosion forms are classified in eight forms based of the appearance of the corroded metal. These eight forms are: uniform or general attack, galvanic or two-metal corrosion, crevice corrosion, pitting, intergranular corrosion, selective leaching or parting, erosion corrosion, and stress corrosion. The most common corrosion mechanism for steel under water can be described as follows:

#### General corrosion mechanism



When steel rebar is embedded in cement mortar or concrete, a layer of passive film will form on its bare surface due to the high alkalinity condition (pH 12.5 – 13.5) of the pore solution in concrete, which can protect it against corrosion (Hope et al., 19987). However, as the thickness of the passive film is only tens of angstroms, it can be easily destroyed by aggressive mediums such as chloride, sulfate and carbonate in the environment (Moreno et al., 2004). Furthermore, once the passive film is destroyed locally, the expansion force caused by rust accumulation on the rebar surface will induce the breakage of the thin passive film in the large area. As result, the corrosion will then expand rapidly on the whole rebar surface.

Another serious form of steel corrosion is microbiologically influenced corrosion (MIC) which affects most commonly used metals and alloys. Most types of microbes in water or soils have the potential to participate in corrosion. One important group of bacteria associated with corrosion is the sulfate reducing bacteria (SRB). Sulfate reducing bacteria are ubiquitous and are known to cause severe operational problems, which significantly increase the cost of various operations in the entire petroleum industry. These operational problems include corrosion, hydrocarbon souring, increased formation of emulsions and suspended solids, and reservoir plugging. SRB produces hydrogen sulfide that increases safety and environmental concerns.

Oil and gas industries estimate that 30-90% of their serious corrosion, pitting-type, is related to MIC. The direct cost of MIC in these industries has been estimated to be about \$10 billion per year. Also, in the United States, the industry spends \$1.2 billion annually on biocidal chemical to mitigate MIC (Pope 1992).

Corrosion induced structural failures such as oil and gas pipeline ruptures, bridge deck spalling, bridge piers failure, underground steel support failure, and steel connection (e.g., bolts) failure are among many disasters that could result in human loss and property damages. For instance, a 30-inch natural gas pipeline owned by El Paso Natural Gas (EPNG) exploded in August, 2000 in New Mexico because of a significant reduction in the pipe wall thickness due to severe corrosion on a 50 year old pipeline. The released gas ignited and burned for 55 minutes. The greatest cost of the pipeline explosion was the human loss -- 12 fatalities, including children and infants. The total property damage was nearly \$1 million (NACE, corrosion failure).

Another corrosion failure case was a pipeline rupture that spilled an estimated 101,000 gallons of crude oil near Santa Barbara, CA in May, 2015. Investigations found corrosion at the break site had degraded the pipe wall thickness to 1/16 of an inch, and that there was a 6-inch opening near the bottom of the pipe. Figure 2.1 shows workers monitoring the site of spilled oil. Typical pipeline and casing failure due to severe corrosion are shown in Figure 2.2 and Figure 2.3.



Figure 2.1 Workers monitor the site of an underground oil pipe break up



Figure 2.2 Pipeline failure due to severe corrosion



Figure 2.3 Casing failure due to severe corrosion

In May, 2000, the 320-foot concrete-and-steel pedestrian walkway failure injured 107 people. Investigators identified corrosion as the cause of the span's weakened steel supports. The corrosion was caused by calcium chloride, a highly corrosive chemical compound, which was a component of the grout surrounding the steel prestressing cables in the bridge. It was reported that all 11 cables buried in the concrete were corroded causing the bridge collapse (NACE, corrosion failure). The collapsed bridge is shown in Figure 2.4.



Figure 2.4 Collapsed pedestrian bridge

Available standard test methods related to steel corrosion in water environment can be summarized in Table 2.1.

Table 2.1 ASTM corrosion test methods

<b>Publication</b>	<b>ASTM G62-07<sup>1</sup></b>	<b>ASTM G78-01<sup>2</sup></b>	<b>ASTM D1654-08<sup>3</sup></b>
<b>Year, reapproved</b>	2013	2012	2008
<b>Objective</b>	Exposing & evaluating metals, alloys	Cervic-corrosion	Evaluating corrosion performance of coating system
<b>Material made of</b>	Metals, alloys	Iron & Nickel base alloys	NA
<b>Material form</b>	Panels, tanks, sheet, tubing, bars	Sheet, plate, tubing, bars	Metals, organic and metal coatings
<b>Environment</b>	Seawater	Seawater and other aqueous	Atmosphere

Table 2.1 (continued) ASTM corrosion test methods

<b>Corrosion due to</b>	NA	Chloride	NA
<b>Evaluating factors</b>	Corrosion or marine fouling behavior	Environmental, metallurgical, geometrical	Blistering associated with corrosion, loss of adhesion
<b>Test type</b>	Exposure to water	Exposure to seawater	Scribing & exposing
<b>Test specimen size</b>	100 by 300 mm	300 by 300 mm Length 100 to 300 mm	(Any size of coated specimen/metal)
<b>Weight loss.</b>	Recommended	Recommended	NA
<b>Accuracy</b>	Depends on test procedures strict follow	Depends on test procedures strict follow	Dependent on level of measurement precision
<b>Remark</b>	From 6 mo. to 20 years of test duration, not applicable for testing of cement or other polymer coatings	At least 30 days of test duration, not applicable for testing of cement or other polymer coatings	Applicable to paint related coatings, not cement or other polymer coatings

<sup>1</sup> Standard Test Methods for Holiday Detection in Pipeline Coatings

<sup>2</sup> Standard Guide for Crevice Corrosion Testing of Iron-Base and Nickel-Base Stainless Alloys in Seawater and Other Chloride-Containing Aqueous Environments

<sup>3</sup> Standard Test Method for Evaluation of Painted or Coated Specimens Subjected to Corrosive Environments

A summary of steel corrosion studies are shown in Table 2.2.

Table 2.2 A summary of steel corrosion studies

Reference	Size	Environment	Measurement	Duration	Remarks
Criado et al., 2015	52 x 30 x 1 mm,	Carbonated synthetic solution	EIS, SEM	30 days	Surface or bulk corrosion not quantified, Not applicable for field test
Hou et al., 1997	#3, #6 rebars, 152.4 x 152.4 x 152.4 mm,	NaCl solution	Electrical four-probe	35 days	Surface or bulk corrosion not quantified, Not applicable for field test
Baronio et al., 1996	80 x 80 x 300 mm, and 100 x 100 x 100 mm	Chloride, sulphate solution	Potential	365 days	No impedance properties quantified, Not applicable for field test
Huang et al., 1996	10 x 2 mm	Acidic chloride, H <sub>2</sub> S solution	EIS	1 day	Not applicable for buried steel Not applicable for field test

## 2.2 Interface Corrosion

Almost all corrosions of a metal result in corrosion products between the surface of the metal and its environment, by which we call its presence of corrosion products at the interface level. Many researchers have studied and proposed different test methods to determine presence of corrosion products. Many of the available test methods focus on studying on the changes of the properties of coatings as results of corrosion. And most of them are only applicable in laboratory tests but not for in situ tests.

Mahdavi, et al., 2015 proposed the use of electrochemical impedance spectroscopy (EIS) and X-ray photoelectron spectroscopy (XPS) analysis to measure cathodic disbondment on epoxy coated steel surfaces. The disbondment of protective organic coatings under excessive cathodic protection potentials is a widely reported coating failure mechanism (Mahdavi, et al., 2015). Pipeline steel plates (API X65) of 100mm by 100mm were used for making working electrodes. The coating used was a two components clear epoxy composing of Bisphenol A epoxy resin (Araldite GY 250) and polyamine hardener (Aradur 2965) mixed in 2/1 ratio and the coating was applied on the metal plate surface. An artificial defect with 6 mm diameter ( $0.28 \text{ cm}^2$ ) was created in coated sample using flat-ended drill bit on the metal surface. Sample with the same thickness without any defect was also prepared and used as reference sample. Testing cells were filled with 3 wt.% aqueous solution of NaCl to 8 cm of PVC cylinder height.

For application of cathodic protection to specimens, a three electrodes cell configuration and a potentiostat (VSP Bio-Logic) were used. To accelerate the coating disbondment a constant potential of  $-1.4 \text{ V}_{\text{Ag/AgCl}}$  was applied using an Ag/AgCl

reference electrode and a platinum wire counter electrode. EIS was measured after selected periods of exposure time by applying a  $\pm 10$  mV peak to peak sine wave modulation in frequency range of 100 kHz-100 mHz. The XPS analysis was performed on the samples in order to determine if the formed circle is the disbanded areas. The presence of sodium and chloride elements inside and outside of circular halos that were formed around the defects after various testing periods was determined by XPS. A schematic diagram of a test setup for EIS measurement is shown in Figure 2.5.

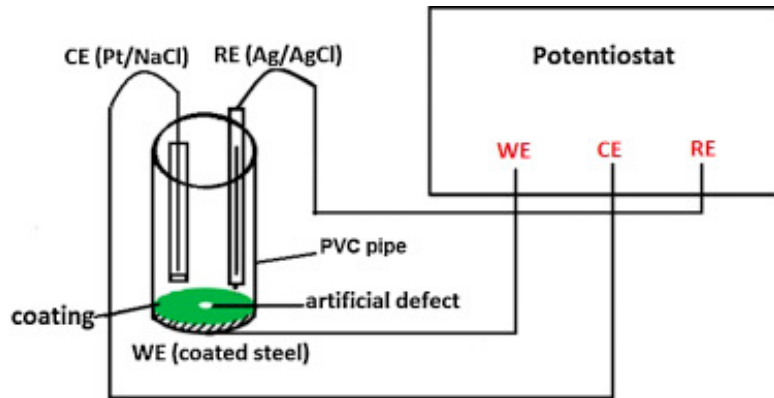


Figure 2.5 A schematic test setup for EIS measurement

## **2.3 Coatings**

The protection of metals from corrosive environment is usually achieved by deposition of coatings on the material surface to establish a physical barrier against aggressive ions. Coatings can broadly be categorized as organic coatings and inorganic coatings (Fontana, 1987).

### **2.3.1 Organic Coatings**

Organic coatings also involve a relatively thin barrier between substrate material and the corrosive environment. Paints, varnishes, lacquers, and similar coatings protect more metal on a tonnage basis than any other method for combating corrosion. Proper application of organic coating requires three main factors to be considered such as surface preparation, selection of primer or priming coat, and selection of top coat or coats. If the metal surface is not properly prepared, the paint may peel off because of poor bonding. If primer does not have good adherence or is not compatible with top coat, early failure occurs. If the two factors are wrong, the system will fail regardless of the top coat used. Poor paint performance is, in most cases, due to poor application and surface preparation. Surface preparation involves surface roughening to obtain mechanical bonding as well as removal of dirt, rust, mill scale, oil grease, welding flux, crayon marks, wax and other impurities (Fontana, 1987). The coating thickness must be such that no bare metal is exposed. Multiple layers of coating are needed so that a pinhole or other defects such as holidays will be covered completely. The thickness is important also because paint deteriorates or weathers with time.

Corrosive environment that can cause a greater or lesser degree of damage on coatings and/or metals includes, but not limited to, sodium chloride (sea water), sulfuric acid, hydrochloric acid, nitric acid, hydrofluoric acid, phosphoric acid and acetic acid. For oil and gas industry, saline water and sulfides are often present in oil and gas wells. The industry consumes a tremendous amount of iron and steel pipe, tubing, casings, pumps, valves, and sucker rods. Leaks cause loss of oil and gas and also permit infiltration of water and silt, thus increasing corrosion damage. Corrosion in wells occurs inside and outside the casing.

In oil and gas industry, the components of intact coating performance that give corrosion protection to a metal substrate are the barrier properties and the adhesion to the substrate under the exposure conditions. Oil-Well Cement (OWC) is mainly used for sealing the annular space between borehole and steel casing. Among its different purposes, the corrosion protection of the casings is to be mentioned (Joshi and Lohita, 1997). OWC is designed to withstand severe temperature and pressure and to comply with weak or permeable formations, corrosive substances, and over-pressured formations. A summary of corrosion studies on cementitious composites are given in Table 2.3

Table 2.3 A summary of cementitious composites studies

Reference	Size	Environment	Measurement	Duration	Remarks
Loto 1992	160 x 100 x 100 mm, 16 mm dia. Steel	Seawater	Potential	54 days	No impedance properties quantified, Not applicable for field test
Michel et al., 2011	40 x 60 x 150 mm	40 x 60 x 150 mm	Application DC	X-ray attenuation	Not applicable for field test
Zafeiropoulou et al., 2011	100 x 40 mm, 12 mm dia. Steel	NaCl solution, Carbonated concrete	Potential, Carbonation depth, Mass loss	730 days	No quantification b/n coating & steel Not applicable for field test
Wei et al., 2012	80 x 80 mm	Chlorinated concrete	EIS	365 days	No quantification b/n cement & steel Not applicable for field test
Baronio et al., 1996	80 x 80 x 300 mm, 100 x 100 x 100 mm	Chloride, sulphate solution	Potential	365 days	No impedance properties quantified, Not applicable for field test

### **2.3.2 Inorganic Coatings**

Inorganic coatings are an alternative to conventional organic coatings due to their excellent abrasion resistance and high density, but they also tend to be brittle and require high processing temperatures (Guglielmi, 1997). The main function of relatively thin coatings of inorganic (metallic) materials is to provide effective barrier. Some metallic coatings such zinc coating provides protection of corrosion by being sacrificial to react with the corrosive environment (Fontana, 1987). Inorganic coatings are applied or formed by spraying with elevated temperatures, electrodeposition, hot dipping or chemical conversion. Generally inorganic coatings are characterized by their excellent abrasion resistance and high density but they also tend to be brittle and require high processing temperatures (Guglielmi, 1997). Porosity or other defects can result in accelerated localized attack on the basic metal because of two-metal effects. A summary of corrosion studies on polymer coated composites are given in Table 2.4.

Table 2.4 A summary of polymer composites studies

Reference	Coating	Size	Environment	Measurement	Duration	Remarks
Wheat et al., 2011	Coumarin paint system, steel	255 x 75 x 1 mm	Salt water solutions, salt spray	Prototype paint scanner, EIS, SEM, EDS	19 days	No electrical properties quantified, Not applicable for field test
Ramezanzadeh et al., 2014	Epoxy/Polyamide, aluminum particles, steel	35 mm x 35 mm x 50 $\mu$ m	Salt spray	EIS, XRD	30 days	No quantification b/n coating & steel Not applicable for field test
El-Shazly 2012	Polyaniline, steel, sand	20 x 30 x 1 mm	NaCl, moisture, H <sub>2</sub> SO <sub>4</sub> solution	Potential, XPS, Ellipsometric analysis	NA	No quantification b/n coating & steel Not applicable for field test
Selvaraj et al., 2009	Acrylic, polyester, polyamide, epoxy	50 x 75 mm, and 100 x 150 mm	Salt spray	Adhesion, flexibility, Abrasion, EIS	30 days	No quantification b/n coating & steel Not applicable for field test
Huang et al., 2009	Cerium-based coatings	30 x 60 x 0.8 mm	NaCl solution	EIS	1 day	No quantification b/n coating & steel Not applicable for field test

## 2.4 Summary

Based on the review of literature related to steel corrosion, coatings and methods of testing corrosion in steel embedded in different kinds of coatings, the following can be summarized:

1. Corrosion induced structural failures such as oil and gas pipeline ruptures, bridge deck spalling, bridge piers failure, underground steel support failure, and steel connection (e.g., bolts) failure are among many disasters that could result in human loss and property damages.
2. Coatings are applied to protect steel structures from corrosion. They act as a barrier to a corrosive environment. Primary types of such coatings are organic and inorganic coating.
3. The long-term performance of a coating is influenced significantly by its ability to adhere properly to the material to which it is applied.
4. Almost all corrosions of a metal result in corrosion products between the surface of the metal and its environment, by which we call its presence of corrosion products at the interface level.
5. Many of the available test methods focus on studying on the changes of the properties of coatings as results of corrosion. And most of them are only applicable in laboratory tests but not for in situ tests

## CHAPTER 3

### MATERIALS AND TEST METHODS

#### 3.1 Testing Materials

##### 3.1.1 Steel Bars

AISI steel 1018 bars with the size of No. 3 and No. 4 were used throughout the testing procedures. Steel bars were cut into a length of 6 inches. The No. 4 steel bars were immersed in acidic solution (HCl solution) to make them corroded. The No. 3 steel bars were left to be non-corroded bars as shown in Figure 3.1.



a. Non-corroded steel bar

b. Corroded steel bar

Figure 3.1 AISI steel 1018 bars

Another set of flat steel bars whose length was 6 inches, width of 1 inch and thickness of  $3/16$  inch were investigated for surface and bulk corrosion properties. Three of the steel bars were immersed in sulfuric acid solution and to get them highly corroded. Another set was immersed in tap water and allowed to be exposed to dry air so that corrosion will develop. Non-corroded steel bars were also used as control specimens as shown in Figure 3.2.



a. Non-corroded bar



b. Corroded bar due to water and moisture at age of 35 days



c. Corroded bar due to sulfuric acid at age of 56 days

Figure 3.2 Non-corroded and corroded steel bars

### 3.1.2 Cement

Cement slurry was used to prepare cement composite specimens. The type of cement used was oil-well Class H cement. Water cement ratio of 0.4 was used. The specimens had cylindrical shape with diameter of 2 inches and height of 4 inches.

Non-corroded and corroded steel bars were steel bars were prepared for laboratory tests to characterize electrical properties of the interface between the steel bar and the cement paste. The specimens were instrumented with 2 silver-paint wires connected to the cement paste and typical non-corroded and corroded cement composites are as shown in Figure 3.3.



a. Corroded bar embedded



b. Non-corroded bar embedded

Figure 3.3 Cement composite specimens

### 3.1.3 Polyester

Polyester specimens were prepared from composition of polyester coating, methyl ethyl ketone peroxide (MEKPO), and naphthenate as shown in Figure 3.4. The specimens had cylindrical shape with diameter of 1.5 inches and height of 4 inches. For a single specimen preparation 97.8 g of polyester, 2% (in weight of polyester) MEKPO and 0.2% (in weight of polyester) naphthenate were used. Methyl ethyl ketone peroxide (MEKPO) was used as hardener and naphthenate was used as catalyst



a. Polyester



b. MEKPO



c. Naphthenate

Figure 3.4 Materials used for polyester specimens

Non-corroded and corroded steel bars were prepared for laboratory tests to characterize electrical properties of the interface between the steel bar and the polyester. The specimens were instrumented with 2 silver-paint wires connected to the polyester coating. The specimens were instrumented with 2 silver-paint wires connected to the polyester coating and typical non-corroded and corroded polyester composites are shown as shown in Figure 3.5



a. Corroded bar embedded



b. Non-corroded bar embedded

Figure 3.5 Polyester composite specimens

### 3.1.4 Polymer Concrete

Polymer concrete specimens were prepared from composition of fine aggregates (sand), polyester, methyl ethyl ketone peroxide (MEKPO), and naphthenate. The specimens had cylindrical shape with diameter of 1.5 inches and height of 4 inches. The polymer concrete was composed of polyester with 20% by total weight and sand with 80% by total weight. Methyl ethyl ketone peroxide and naphthenate were used as hardener and catalyst respectively.



Figure 3.6 Sand used for polymer concrete specimens

Non-corroded and corroded steel bars were steel bars were prepared for laboratory tests to characterize electrical properties of the interface between the steel bar and the polymer concrete. The specimens were instrumented with 2 silver-paint wires connected to the polymer concrete and typical non-corroded and corroded polymer concrete composites are shown as shown in Figure 3.7



a. Corroded bar embedded



b. Non-corroded bar embedded

Figure 3.7 Polymer concrete composites

### 3.2 Testing Method

The testing method used in the experimental procedures was non-destructive electrical test method. A general-purpose LCR meter device was used to measure and evaluate impedance spectroscopy data such as electrical resistance and capacitance of the testing specimens as shown in Figure 3.8. A wide range of frequencies 20 Hz to 300 kHz was used. A schematic test setup for measuring using LCR meter device is shown in Figure 3.9.



Figure 3.8 LCR meter device

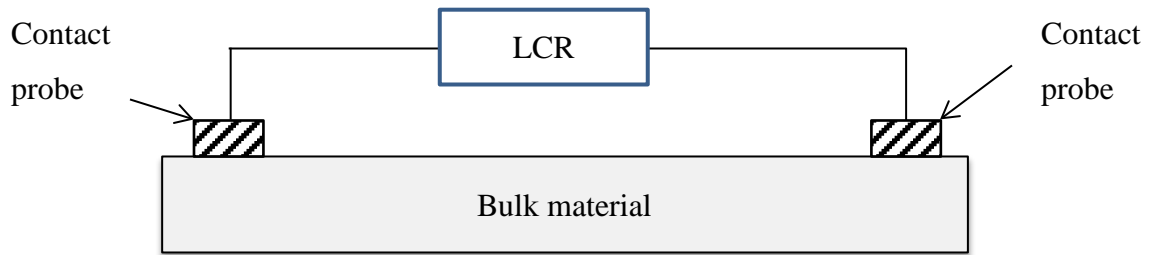


Figure 3.9 Schematic test setup for measuring using LCR meter device

### 3.3 Summary

The summary of laboratory experimental study is as follows:

1. Non-corroded and corroded steel bars were studied for their surface and bulk corrosion impedance properties.
2. Non-destructive electrical test method using general-purpose LCR meter device was used to measure and evaluate impedance spectroscopy properties of the testing specimens.
3. Cement composites embedding non-corroded and corroded steel bars were studied for corrosion impedance properties under air-dry conditions and salt-water conditions.
4. Polyester composites embedding non-corroded and corroded steel bars were studied for corrosion impedance properties under air-dry conditions and salt-water conditions.
5. Polymer concrete composites embedding non-corroded and corroded steel bars were studied for corrosion impedance properties under air-dry conditions and salt-water conditions.

# **CHAPTER 4**

## **DEVELOPING AND CHARACTERIZING SMART COATING MATERIALS**

### **4.1 Cement**

Normal cement mix is poor in its electrical properties under dry conditions. In order to improve the electrical properties of the cement paste, conductive fillers of 0.075% by weight of the cement paste were added and dispersed well in the cement mix. The conductive fillers are small in diameter with high aspect ratio and lightness. They are very stable in chemical and high thermal environment. Their excellent electrical properties improve the overall electrical conductivity of the cement mix. Hence, the resulting cement mix, which is modified with conductive fillers, can be referred to as smart cement. The smart cement is capable of self-sensing of changes in its loading condition or environment condition including the presence of corrosion based on the change in resistivity (or piezoresistivity).

Typical piezoresistive behavior of the smart cement compared to the cement mix without added conductive fillers (neat cement) with respect to compressive stress is shown in Figure 4.1. The smart cement sensing was about 50 times greater than that of neat cement. The rheological properties were not affected by the addition of conductive filler (Praveen, 2014).

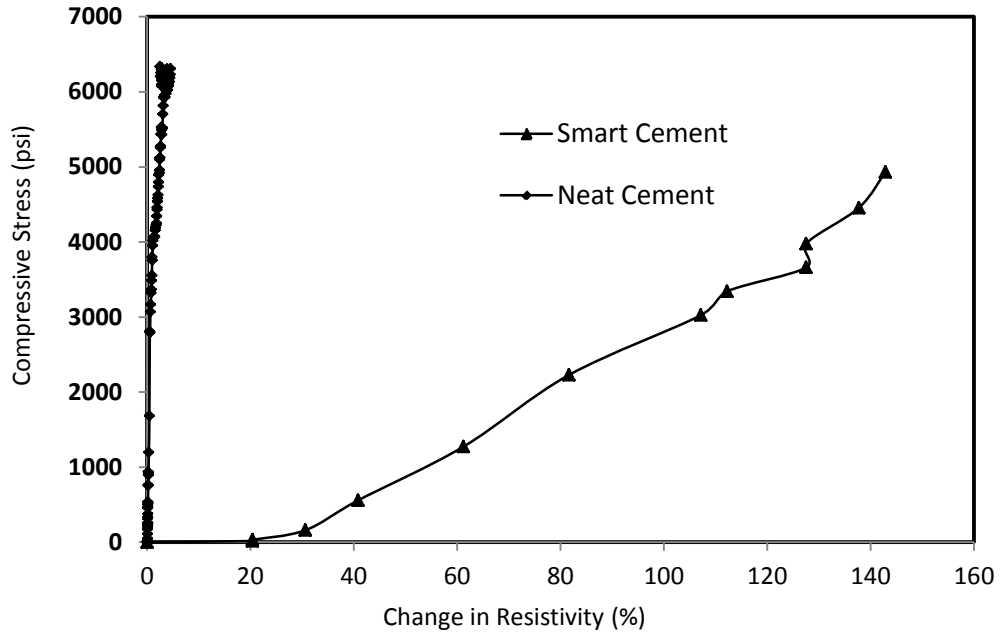


Figure 4.1 Typical piezoresistive behavior of cement mix  
(Data from Praveen, 2014)

## 4.2 Polyester

Polyester coating under its normal dry condition it is very poor electrical conductor. In order to improve the electrical properties of the polyester coating, conductive fillers of 0.1% by weight of the polyester were added and dispersed well in the polyester coating mix. The conductive fillers are small in diameter with high aspect ratio and lightness. They are very stable in chemical and high thermal environment. Their excellent electrical properties improve the electrical conductivity of the polyester coating. Hence, the resulting polyester coating can be referred to as smart polyester coating. The smart polyester coating is capable of self-sensing of changes in its loading condition or environment condition including the presence of corrosion.

Typical electrical property of the smart polyester coating compared to the polyester coating without added conductive fillers (neat polyester coating) is shown in Figure 4.2. From Figure 4.2, it can be seen that the smart polyester sensing was about 3 times greater than that of neat polyester.

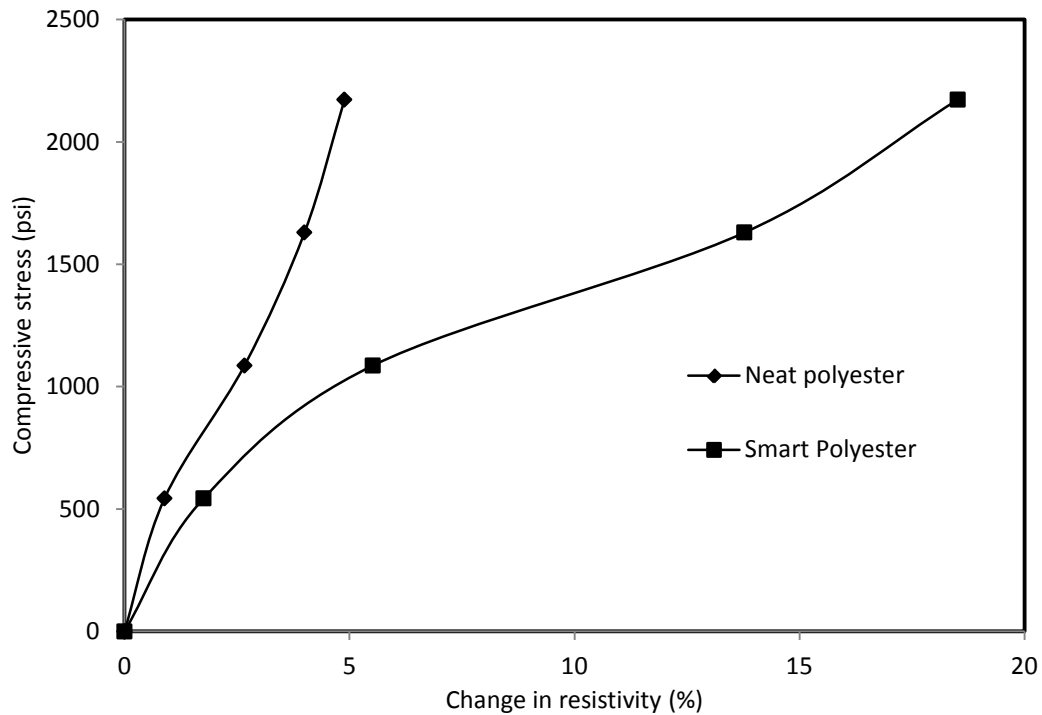


Figure 4.2: Typical piezoresistive behavior of polyester coating

### 4.3 Polymer Concrete

Polymer concrete under its normal dry condition it is very poor electrical conductor. In order to improve the electrical properties of the polyester concrete, conductive fillers of 0.1% by weight of the polyester were added and dispersed well in the polyester concrete mix. The conductive fillers are small in diameter with high aspect

ratio and lightness. They are very stable in chemical and high thermal environment. Their excellent electrical properties improve the electrical conductivity of the polyester concrete. Hence, the resulting polyester concrete can be referred to as smart polyester concrete. The smart polyester concrete is capable of self-sensing of changes in its loading condition or environment condition including the presence of corrosion.

Typical electrical property of the smart polymer concrete compared to the polymer concrete without added conductive fillers (neat polymer concrete) is shown in Figure 4.3. From Figure 4.3, it can be seen that the smart polymer concrete sensing was about 5 times greater than that of neat polymer concrete.

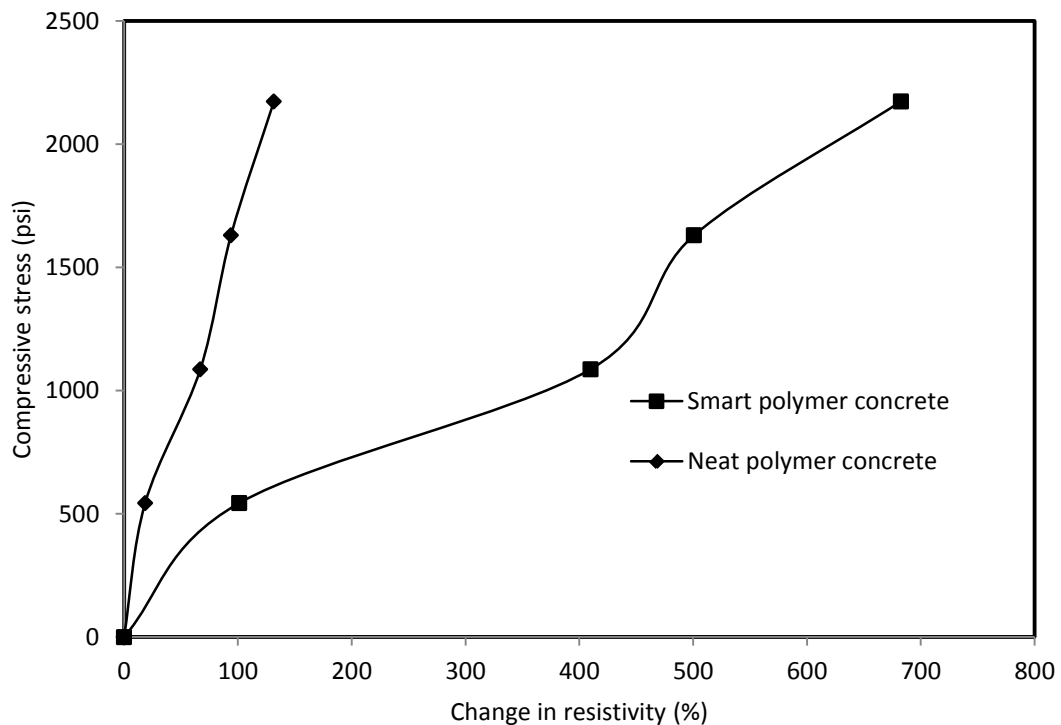


Figure 4.3: Typical piezoresistive behavior of polymer concrete

## 4.4 Summary

The summary of developing and characterizing smart coating materials is as follows:

1. All the testing specimens were modified with conductive fillers in their mix preparation so that they would be capable of self-sensing of changes in their loading or environment condition including the presence of corrosion.
2. The smart cement specimens (modified with conductive fillers) sensing was about 50 times greater than that of neat cement specimens (without conductive fillers).
3. The smart polyester (modified with conductive fillers) sensing was about 3 times greater than that of neat polyester (without conductive fillers).
4. The smart polymer concrete (modified with conductive fillers) sensing was about 5 times greater than that of neat polymer concrete (without conductive fillers).

## **CHAPTER 5**

### **CORROSION STUDY**

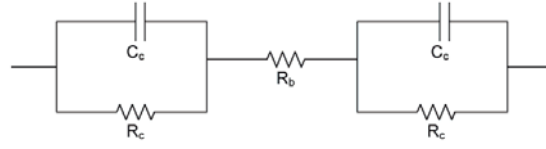
#### **5.1 Modeling**

Identification of the most appropriate equivalent circuit to represent the electrical properties of the composite material is essential in order for the material's properties to be further understood (West et al., 1997). In this study, an equivalent circuit to represent the composite material was required for better characterization through analysis of the impedance spectroscopy data.

There were many difficulties associated with choosing a correct equivalent circuit. It was necessary to somehow make a link between the different elements in the circuit and the different regions in the impedance data of the corresponding sample (West et al., 1997). Given the difficulties and uncertainties, researchers tend to use a pragmatic approach and adopt a circuit that they believe is most appropriate based on their knowledge of the expected behavior of the material under study, and they then demonstrate that the results are consistent with the circuit used (Vipulanandan et al., 2013).

##### **5.1.1 Impedance Modeling**

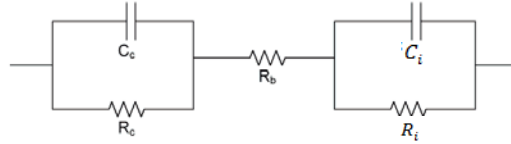
In this research study to model the experimental impedance measurements, the equivalent circuits adopted based on expected behavior of the material are shown in Figure 5.1. The total impedance of the equivalent circuits and corresponding impedance equations are given as follows:



Case 1

$$Z = R_b + \frac{2R_c}{1 + \omega^2 R_c^2 C_c^2} - j \left( \frac{2\omega R_c^2 C_c}{1 + \omega^2 R_c^2 C_c^2} \right) \quad (5-1)$$

and



Case 2

$$Z = R_b + \frac{R_c}{1 + \omega^2 R_c^2 C_c^2} + \frac{R_i}{1 + \omega^2 R_i^2 C_i^2} - j \left( \frac{\omega R_c^2 C_c}{1 + \omega^2 R_c^2 C_c^2} + \frac{\omega R_i^2 C_i}{1 + \omega^2 R_i^2 C_i^2} \right). \quad (5-2)$$

Figure 5.1 Equivalent circuits adopted

In both equations,  $\omega$  is the angular frequency of the applied signal. Applied signal was carried out with frequency range of 20 Hz to 300 kHz.

Case 1 equivalent circuit was used to determine the contact electrical resistance ( $R_c$ ) and capacitance ( $C_c$ ) between the bulk material and wire probes. When the frequency of the applied signal is very high,  $\omega \rightarrow \infty$ ,  $Z = R_b$  from equation (5-1). Then when it is very low,  $\omega \rightarrow 0$ , equation (5-2) can be rearranged as follows after substituting  $Z$  for  $R$  (real impedance),

$$\frac{1}{R - R_b} = \frac{1}{2R_c} + \frac{R_c C_c^2}{2} \omega^2. \quad (5-3)$$

Equation (5-3) can be plotted as a parabola,  $Y = A + B * \omega^2$ , for data points whose frequency are less than 80 Hz. Hence from the parabola equation we can determine  $R_c$  and  $C_c$  as

$$R_c = \frac{1}{2A} \text{ and } C_c = \sqrt{\frac{2B}{R_c}}. \quad (5-4)$$

Case 2 equivalent circuit was used to determine the contact electrical resistance ( $R_i$ ) and capacitance ( $C_i$ ) between the steel bars and the bulk material. When the frequency of the applied signal is very high,  $\omega \rightarrow \infty$ ,  $Z = R_b$  from equation (5-2). Then when it is very low,  $\omega \rightarrow 0$ , equation (5-2) can be rearranged as follows after substituting  $Z$  for  $R$  (real impedance),

$$\frac{1}{R - R_b - \frac{R_c}{1 + \omega^2 R_c^2 C_c^2}} = \frac{1}{R_i} + R_i C_i^2 \omega^2. \quad (5-5)$$

Equation (5-5) can be plotted as a parabola,  $Y = A + B * \omega^2$ , for data points whose frequency are less than 50 Hz. Since  $R_c$  and  $C_c$  are determined from equation (5-4), from the parabola of equation (5-5) we can determine  $R_i$  and  $C_i$  as

$$R_i = \frac{1}{A} \text{ and } C_i = \sqrt{\frac{B}{R_i}}. \quad (5-6)$$

The resistance ( $R$ ) and capacitance ( $C$ ) of a composite material between two points is define as

$$R = \rho \frac{L}{A} \text{ and} \quad (5-7)$$

$$C = \epsilon \frac{A}{L}, \quad (5-8)$$

where:

$A$  = cross-sectional area, and

$L$  = distance between the electrode contacts

$\rho$  = resistivity of the material

$\epsilon$  = absolute permittivity of the material

The product of equations given in (5-7) and (5-8) results

$$R * C = \rho * \epsilon. \quad (5-9)$$

Since  $\rho * \epsilon$  in equation (5-9) is material property,  $R*C$  is also material property (corrosion parameter). The term  $R_iC_i$  can be referred as interface corrosion parameter. The advantage of equation (5-9) is that we now are able to characterize the material property of the corrosion products at the interface level without dependence on the geometry factor such as the length or thickness and area.

### 5.1.2 Corrosion-Time Modeling

The progression of the interface corrosion with respect to time is modeled using p-q model (Vipulanandan and Paul, 1990) which can be used as

$$\frac{R_iC_i - (R_iC_i)_0}{(R_iC_i)_m} = \left[ \frac{\left(\frac{t}{t_m}\right)^p}{q + (1-p-q) * \left(\frac{t}{t_m}\right) + p * \left(\frac{t}{t_m}\right)^{p-q}} \right], \quad (5-10)$$

where  $R_iC_i$  is interface corrosion parameter,  $(R_iC_i)_0$  is initial estimated interface corrosion parameter,  $(R_iC_i)_m$  is measured interface corrosion parameter at time  $t_m$ ,  $t_m$  is time

corresponding to measured interface corrosion parameter,  $t$  is time, and  $p$  and  $q$  are model parameters that will explain changes due to presence of corrosion products.

For  $p < q$  and  $(p + q) < 1$ , when  $t \rightarrow \infty$ , the corresponding interface corrosion parameter can be estimated as

$$R_i C_i = (R_i C_i)_0 + \frac{(R_i C_i)_m}{1-p-q}. \quad (5-11)$$

## 5.2 Steel Bar

The 6-inches flat steel bars were measured for their impedance properties using the LCR meter device. The measurements were taken at a distance of ranging from 1 inch to 5 inches along three directions. The measuring directions were along x-x, y-y, and z-z as shown in Figure 5.2

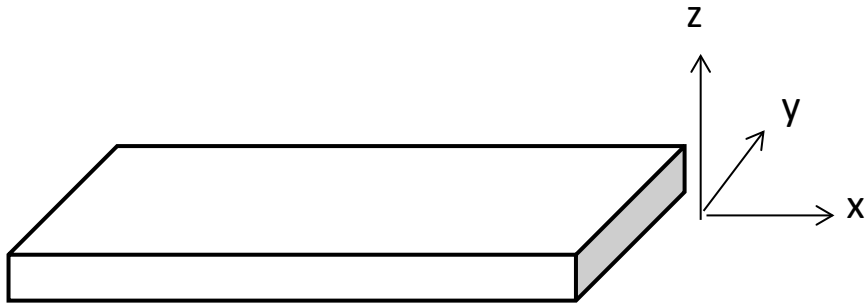


Figure 5.2 Directional measurements on steel bar

The Bode plot of impedance measurements for the non-corroded and corroded steel bars shown are shown in Figure 5.3. From the Figure 5.3, it is shown that the impedance of the corroded steel bars was higher than the impedance of the non-corroded

steel bars. Using Case 1 equivalent circuit and equations (5-3), equation (5-4), and equation (5-9), the contact resistance and contact capacitance and the RC material properties for both the non-corroded and corroded steel bars were determined and shown in Figure 5.7.

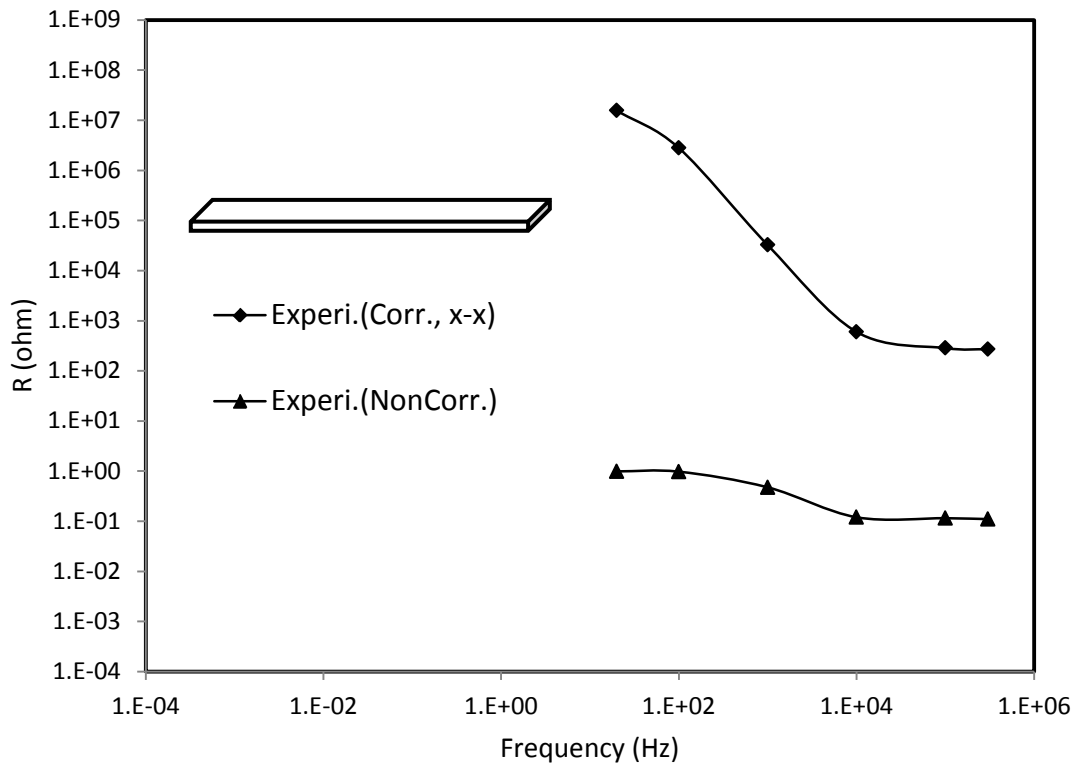


Figure 5.3 Bode plot for steel bars

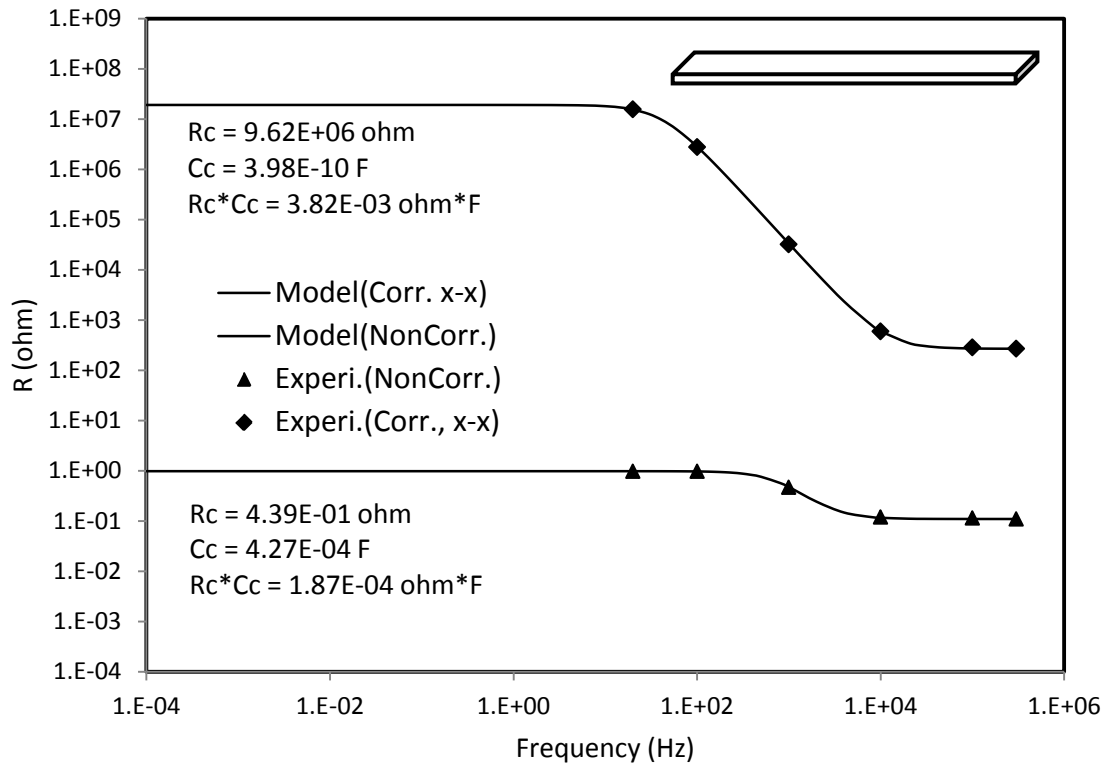


Figure 5.4 Bode plot of for steel bars along the impedance model

For the corroded steel bar, the impedance measurements that were taken in the three X, Y, and Z directions indicated different impedance values. This could indicate that the formation of the corrosion was direction dependent due to the non-uniformity nature of corrosion. After analyzing the impedance measured data to determine the  $R_c$  and  $C_c$  for each directions, the surface material property  $R_c * C_c$ , were determined and plotted as shown in Figure 5.5.

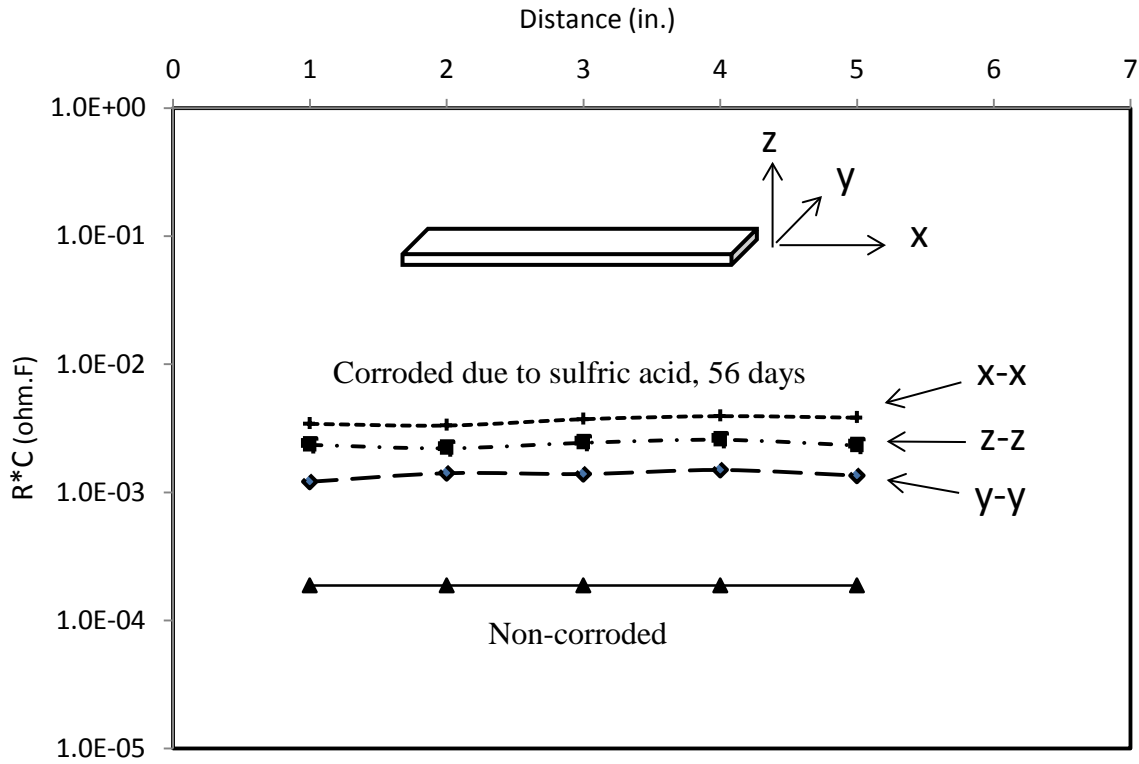


Figure 5.5  $R_c \cdot C_c$  vs distance for steel bars

Further, at the maximum frequency of 300 kHz, the bulk resistance,  $R_b$ , for the corroded bar was determined. From equation (5-7), the normalized change in the bulk resistance with respect to the non-corroded steel bar as

$$\frac{\Delta R}{R_0} = \frac{\Delta \rho}{\rho_0} \quad (5-12)$$

From equation (5-12), the resistivity of the corroded steel bars for each direction could be determined as

$$\rho = \rho_0 + \Delta \rho, \quad (5-13)$$

where  $\rho_0$  is the resistivity of non-corroded steel bar at value of  $1.47 \times 10^{-7}$  ohm-m.

The resistivity for the corroded steel bars were determined in direction of X, Y, and Z and plotted as shown in Figure 5.6. From the Figure 5.6, it can be shown that the corrosion along the y-y direction (along the width of the steel bar) was more corroded than the other directions.

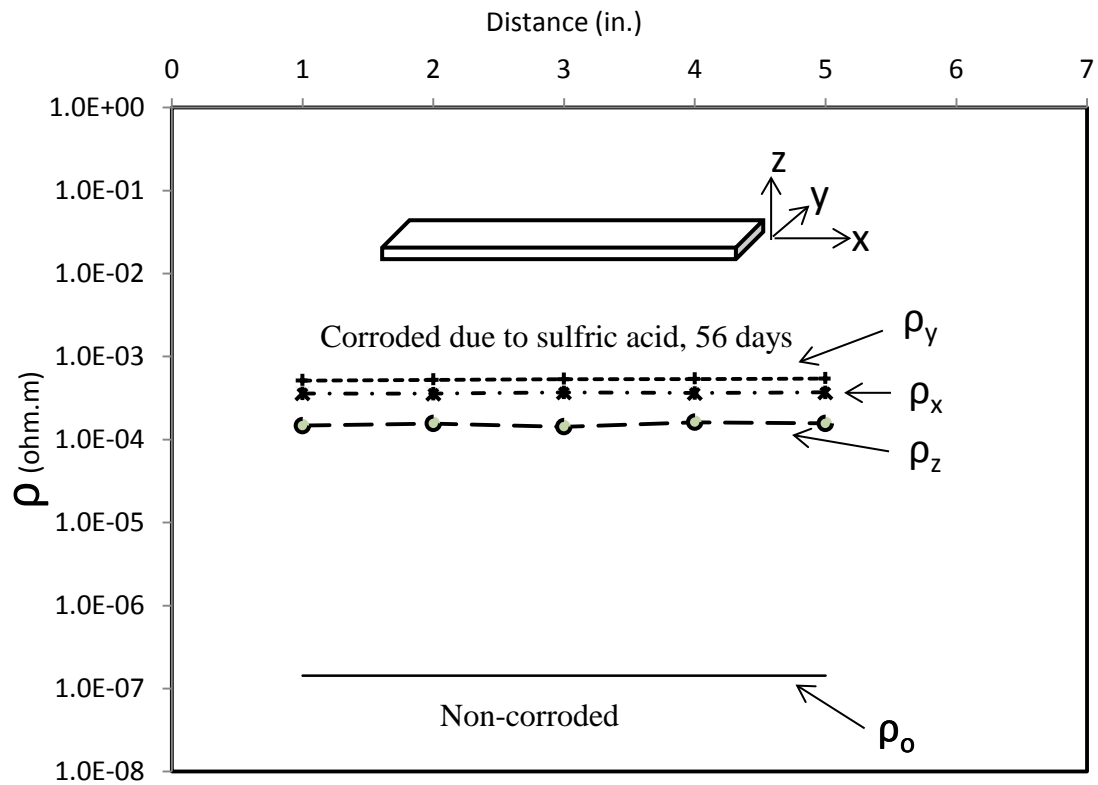


Figure 5.6 Resistivity of the steel bars

### **5.3 Bulk Materials**

The electrical properties of bulk materials such as cement slurry, polyester and polymer concrete having embedded non-corroded and corroded steel bars in dry air laboratory condition and immersed in salt-water solution are characterized by evaluating the impedance at maximum frequency of 300 kHz.

### **5.4 Composite Interface**

Corrosion first occurs primarily on the surface of steel. In this research study we have embedded steel bar in different materials and hence we refer the surface where the corrosion occurs as interface between the steel bar and the bulk material in the study at hand. As the corrosion reaction progresses with the application of moisture, oxygen and/or chloride ions or other corrosive elements or low alkaline environment the steel will be corroded highly and hence the corrosion may occur at the steel bulk level. Thus, it is desirable to be able to detect the presence of corrosion products at interface level between steel and its environment in which it is embedded.

#### **5.4.1 Steel-Cement Characterization**

##### **5.4.1.1 Under Dry-Air Condition**

The electrical resistance and capacitance of the cement paste, steel bar, and transitional contact between the cement paste and the bar were measured with impedance analyzer precision LCR meter device. The impedance measurements were performed on a weekly basis for about a year. The frequency range used was from 20 Hz to 300 kHz. For 28<sup>th</sup> week test, a typical plot of impedance vs frequency for non-corroded bar

embedded in smart cement specimen is shown in Figure 5.7. For 28<sup>th</sup> week test, a typical plot of impedance vs frequency for corroded bar embedded in smart cement specimen is shown in Figure 5.8.

The Bode plot of the adopted equivalent circuit for non-corroded and corroded composite specimens is shown in Figure 5.9. As the Figure 5.9 shown, the impedance of the corroded composite specimen was higher than that of non-corroded composite specimen, and therefore it was possible to detect the presence of the corrosion.

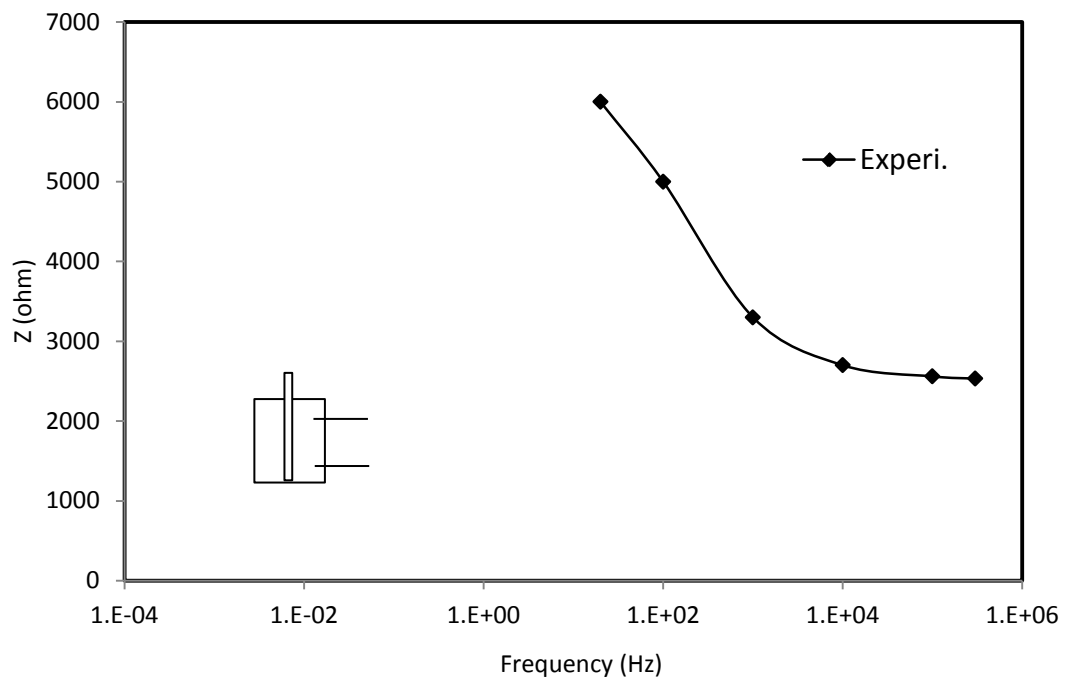


Figure 5.7 Bode plot of cement composite with embedded non-corroded bar

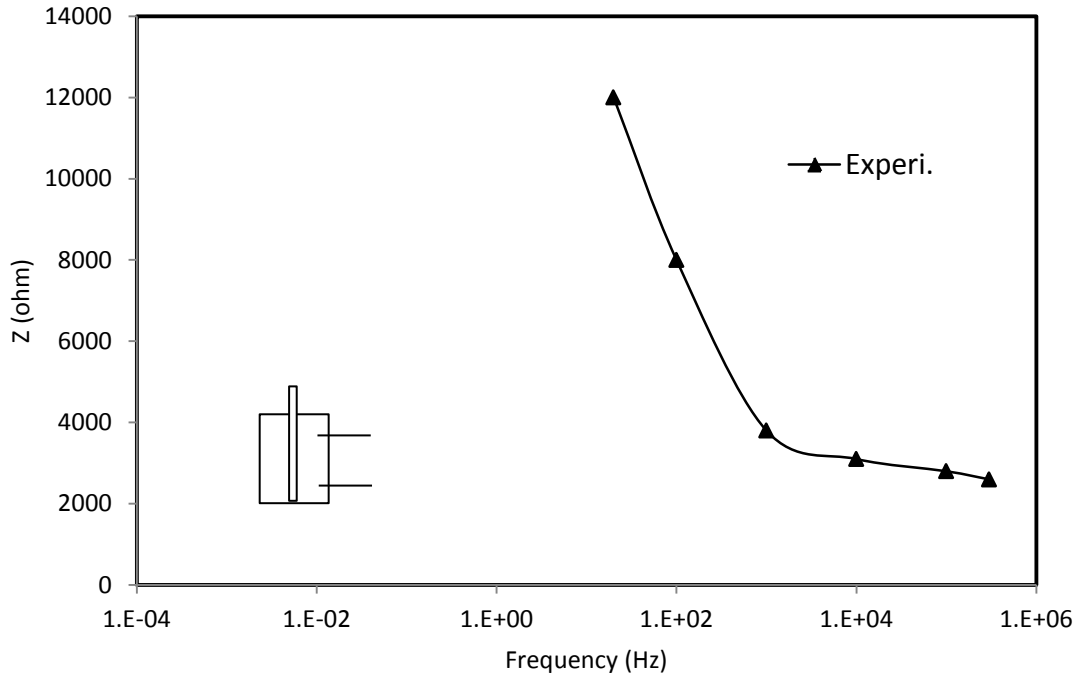


Figure 5.8 Bode plot of cement composite with embedded corroded bar

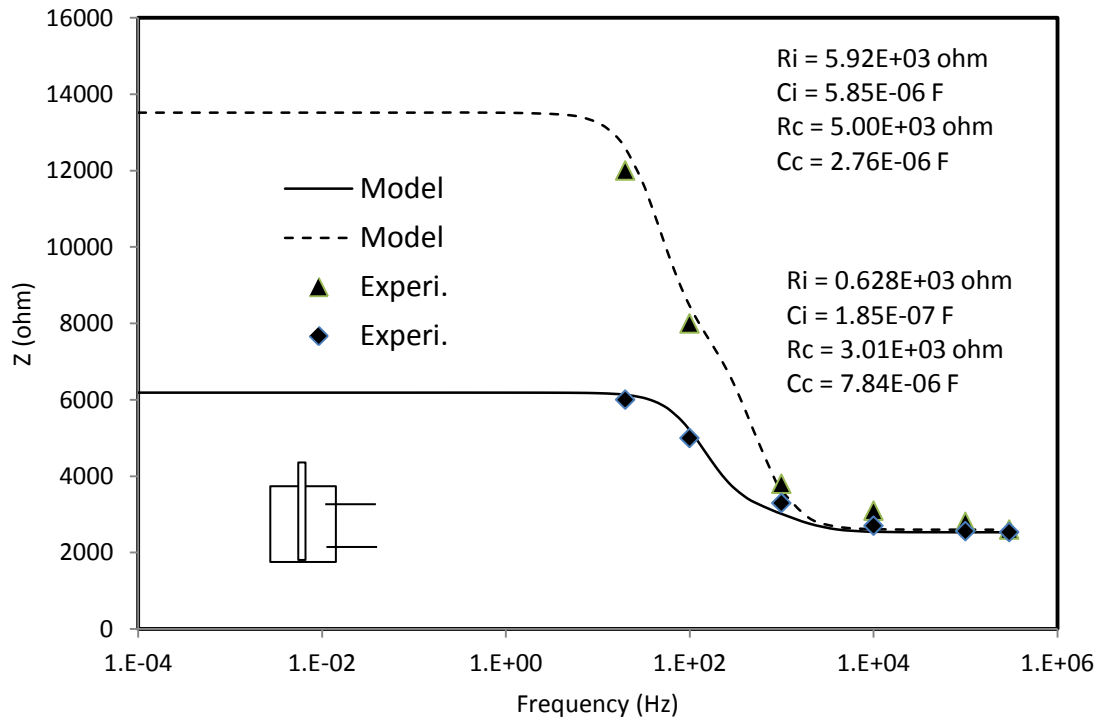


Figure 5.9 Bode plot of cement composites with embedded non-corroded and corroded bar along respective impedance models

#### 5.4.1.1.1 Non-Corroded Cement Composites

The resistance at the interface ( $R_i$ ) between non-corroded bar and the smart cement paste and the resistance at the contact ( $R_c$ ) for the measuring time period are shown in Figure 5.10. From Figure 5.10, it could be observed that the interface resistance ( $R_i$ ) was lower than the contact resistance ( $R_c$ ) during the course of the measuring time period. The lower value of the interface resistance ( $R_i$ ) could be attributed to the fact that the embedded bar was initially non-corroded. Both the interface resistance ( $R_i$ ) and the contact resistance ( $R_c$ ) were increased with respect to time as shown in Figure 5.10.

The capacitance at the interface ( $C_i$ ) between non-corroded bar and the smart cement paste and the capacitance at the contact ( $C_c$ ) for the measuring time period are shown in Figure 5.11. From Figure 5.11, it could be observed that the interface capacitance ( $C_i$ ) was higher than the contact capacitance ( $C_c$ ) during the course of the measuring time period. Both the interface capacitance ( $C_i$ ) and the contact capacitance ( $C_c$ ) were increased with respect to time as shown in Figure 5.11.

The material property parameter defined as product of resistance and capacitance,  $R \cdot C$ , for the non-corroded bar embedded in the smart cement is shown Figure 5.12. From the Figure 5.12, the interface  $R_i \cdot C_i$  between of the non-corroded bar and the smart cement was greater than the  $R_c \cdot C_c$  at the cement contact for the measuring time period. It can also be observed that both the interface  $R_i \cdot C_i$  and the contact  $R_c \cdot C_c$  were increased with respect to time. Therefore, from Figure 5.10 through Figure 5.12, it could be observed that it was possible to detect and quantify the presence of the corrosion in non-corroded bar embedded in the smart cement.

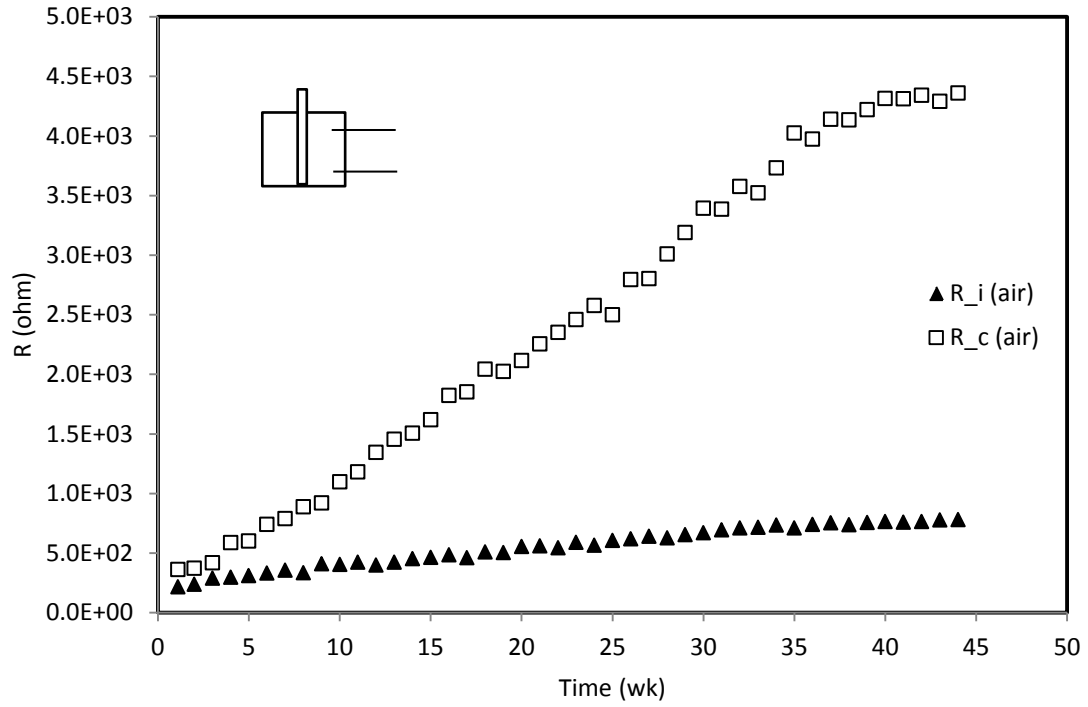


Figure 5.10 Resistances ( $R_i$  &  $R_c$ ) of the non-corroded bar embedded in smart cement under air dry condition

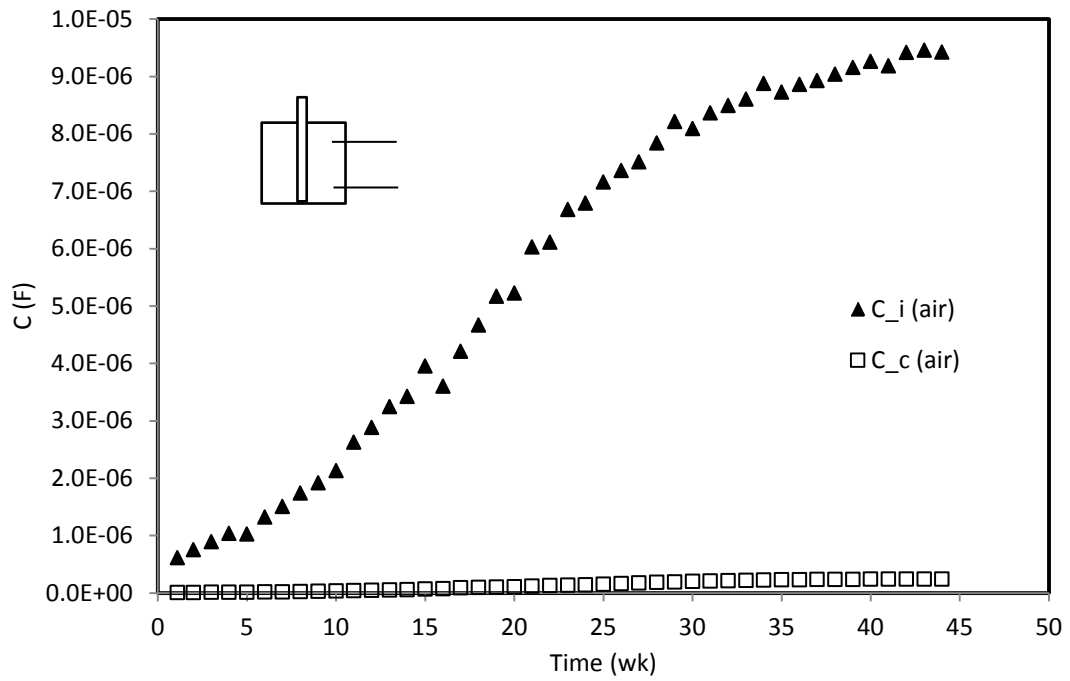


Figure 5.11 Capacitances ( $C_i$  &  $C_c$ ) of the non-corroded bar embedded in smart cement in air dry condition

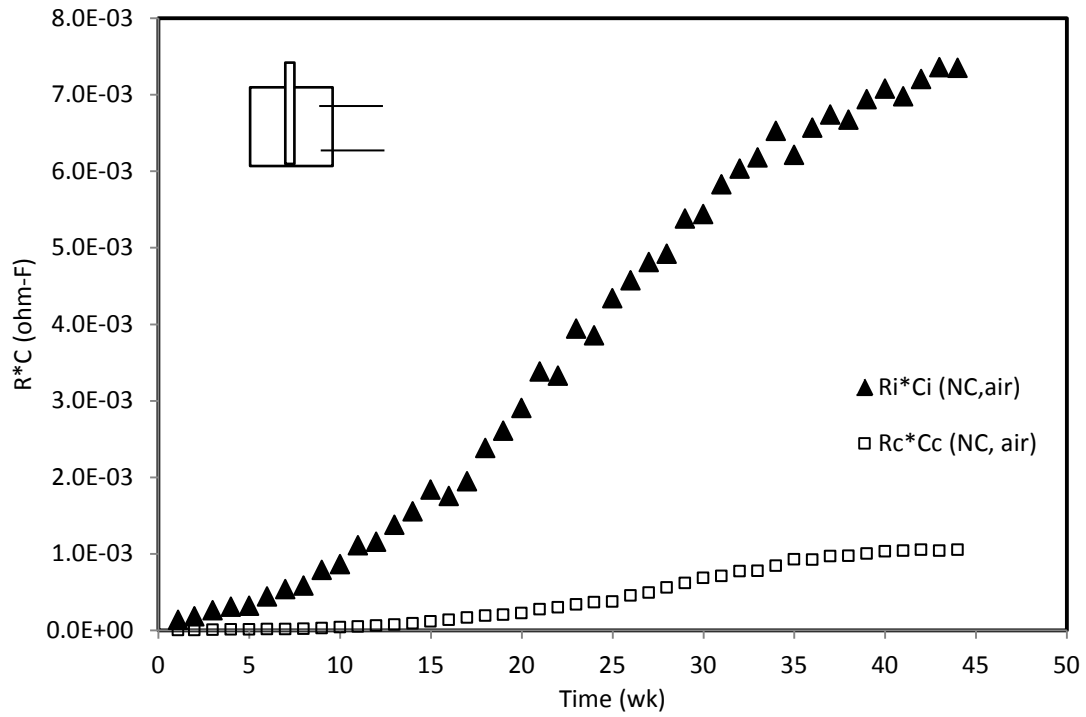


Figure 5.12  $R^*C$  vs. time of the non-corroded bar embedded in smart cement in air dry condition

The progression of the interface corrosion with respect to time is modeled using equation (5-10) of p-q model and the plot is shown in Figure 5.13. The model parameters p and q are estimated to be 0.21 and 0.37 respectively. As  $t \rightarrow \infty$ , the corresponding interface corrosion parameter  $R_iC_i$  is estimated to be  $1.69E-02$  ohm-F using equation (5-11).

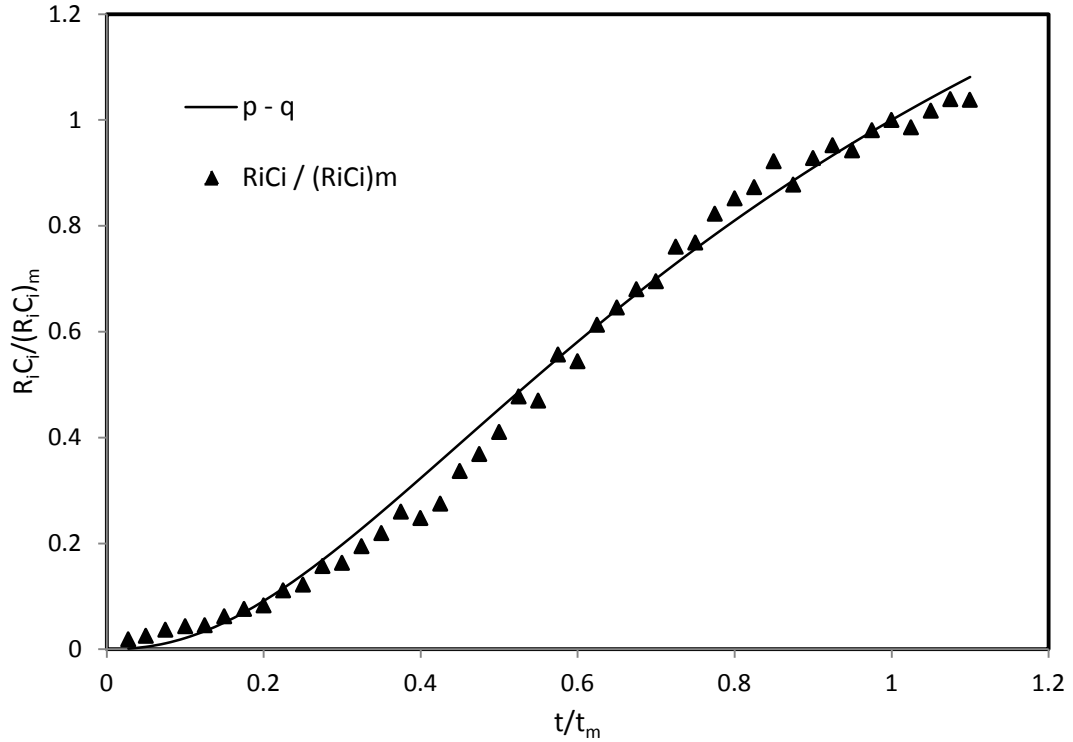


Figure 5.13 Corrosion-time model for non-corroded cement composite under dry condition

#### 5.4.1.1.2 Corroded Cement Composites

The resistance at the interface ( $R_i$ ) between corroded bar and the smart cement specimen under dry air condition and the resistance at the contact ( $R_c$ ) for the measuring time period are shown in Figure 5.14. From the Figure 5.14, it could be observed that the interface resistance ( $R_i$ ) was higher than the contact resistance ( $R_c$ ) during the course of the measuring time period. The higher value of the interface resistance ( $R_i$ ) could be attributed to the fact that the embedded bar was initially corroded. Both the interface resistance ( $R_i$ ) and the contact resistance ( $R_c$ ) were increased with respect to time as shown in Figure 5.14.

The capacitance at the interface ( $C_i$ ) between corroded bar and the smart cement specimen under dry air condition and the capacitance at the contact ( $C_c$ ) for the measuring time period are shown in Figure 5.15. From the Figure 5.15, it could be observed that the interface capacitance ( $C_i$ ) was higher than the contact capacitance ( $C_c$ ) during the course of the measuring time period. Both the interface capacitance ( $C_i$ ) and the contact capacitance ( $C_c$ ) were increased with respect to time as shown in Figure 5.15.

The material property parameter defined as product of resistance and capacitance,  $R \cdot C$ , for the corroded bar embedded in the smart cement specimen under dry air condition is shown Figure 5.16. From the Figure 5.16, the interface  $R_i \cdot C_i$  between of the corroded bar and the smart cement was greater than the  $R_c \cdot C_c$  at the cement contact for the measuring time period. It can also be observed that both the interface  $R_i \cdot C_i$  and the contact  $R_c \cdot C_c$  were increased with respect to time. Therefore, from Figure 5.14 through Figure 5.16, it could be observed that it was possible to detect and quantify the presence of the corrosion in corroded bar embedded in the smart cement specimen under dry air condition.

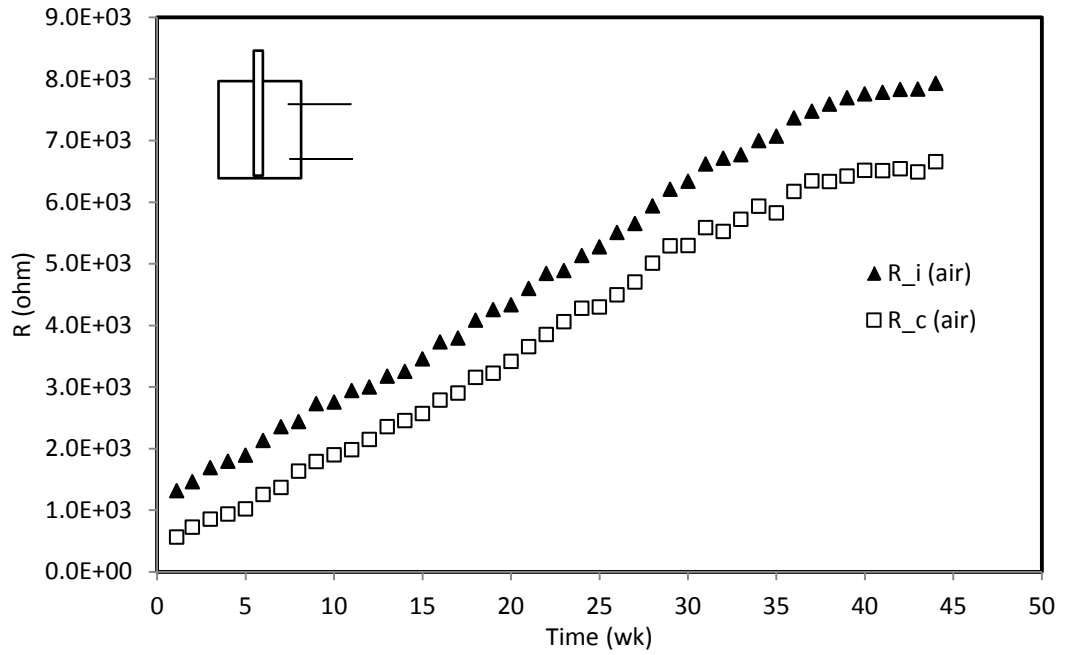


Figure 5.14 Resistances ( $R_i$  &  $R_c$ ) of the corroded bar embedded in smart cement under dry air condition

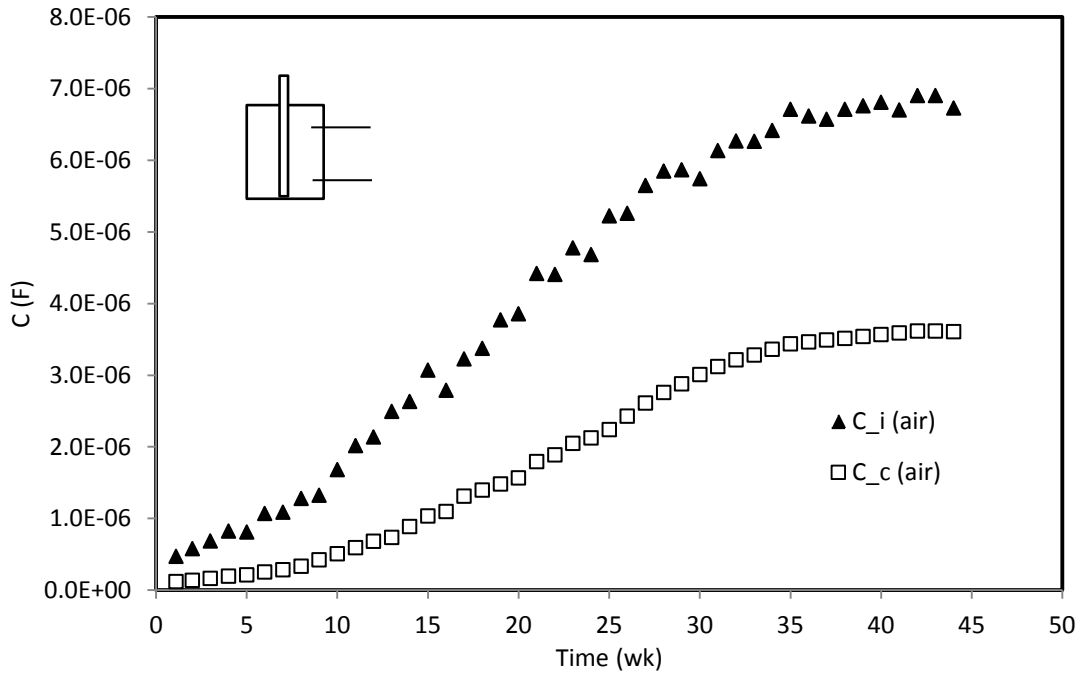


Figure 5.15 Capacitances ( $C_i$  &  $C_c$ ) of the corroded bar embedded in smart cement under dry air condition

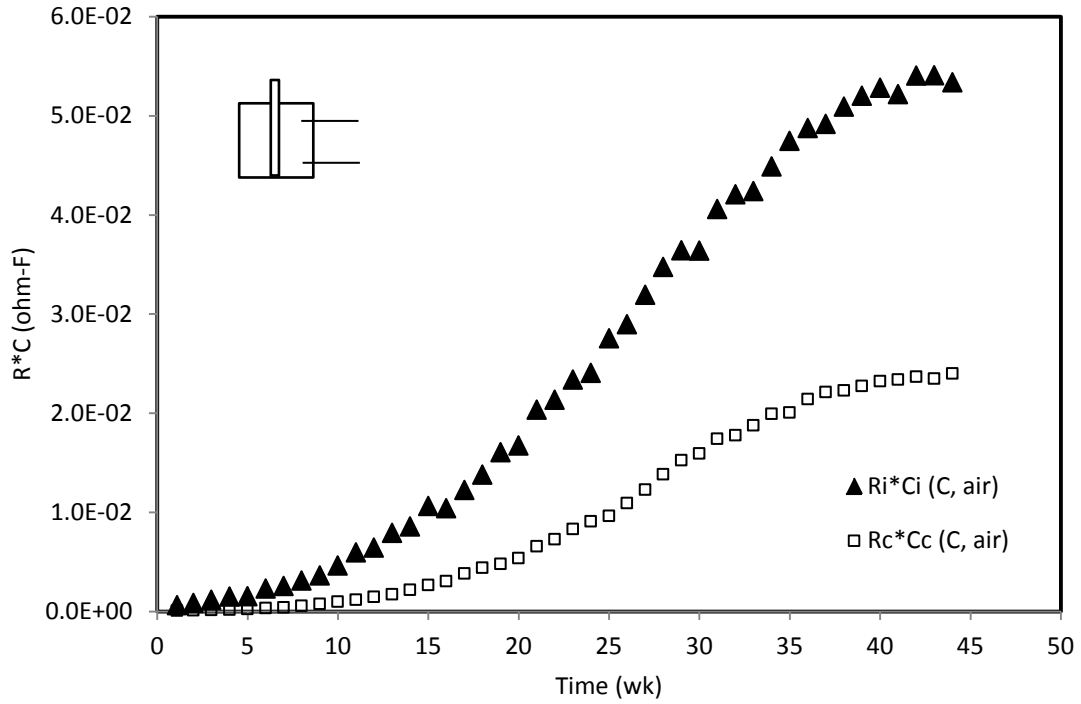


Figure 5.16  $R^*C$  vs. time of the corroded bar embedded in smart cement under dry air condition

The progression of the interface corrosion with respect to time is modeled using equation (5-10) of p-q model and the plot is shown in Figure 5.17. The model parameters p and q are estimated to be 0.24 and 0.37 respectively. As  $t \rightarrow \infty$ , the corresponding interface corrosion parameter  $R_iC_i$  is estimated to be  $1.35E-01$  ohm-F using equation (5-11).

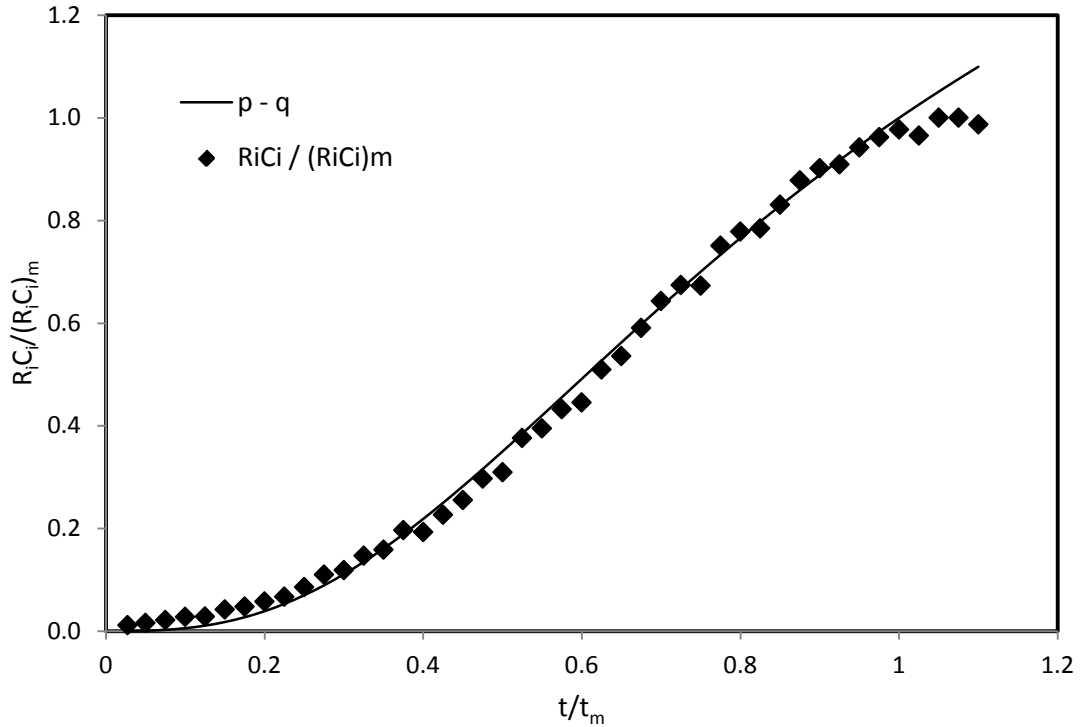


Figure 5.17 Corrosion-time model for corroded cement composite under dry condition

#### 5.4.1.2 Under Salt-Water Solution

Another set of specimens was immersed in a salt water solution (3.5% wt. NaCl) continually for about a year. The electrical resistance and capacitance of the cement paste, steel bar, and transitional contact between the cement paste and the bar were measured with impedance analyzer precision LCR meter device. The impedance measurements were performed on a weekly basis for about a year. The frequency range used was from 20 Hz to 300 kHz. For 28<sup>th</sup> week test, a typical plot of impedance vs frequency for non-corroded bar embedded in smart cement specimen is shown in Figure

5.18. For 28<sup>th</sup> week test, a typical plot of impedance vs frequency for corroded bar embedded in smart cement specimen is shown in Figure 5.19.

The Bode plot of the adopted equivalent circuit for non-corroded and corroded composite specimens is shown in Figure 5.20. As the Figure 5.20. shown, the impedance of the corroded composite specimen was higher than that of non-corroded composite specimen, and therefore it was possible to detect the presence of the corrosion.

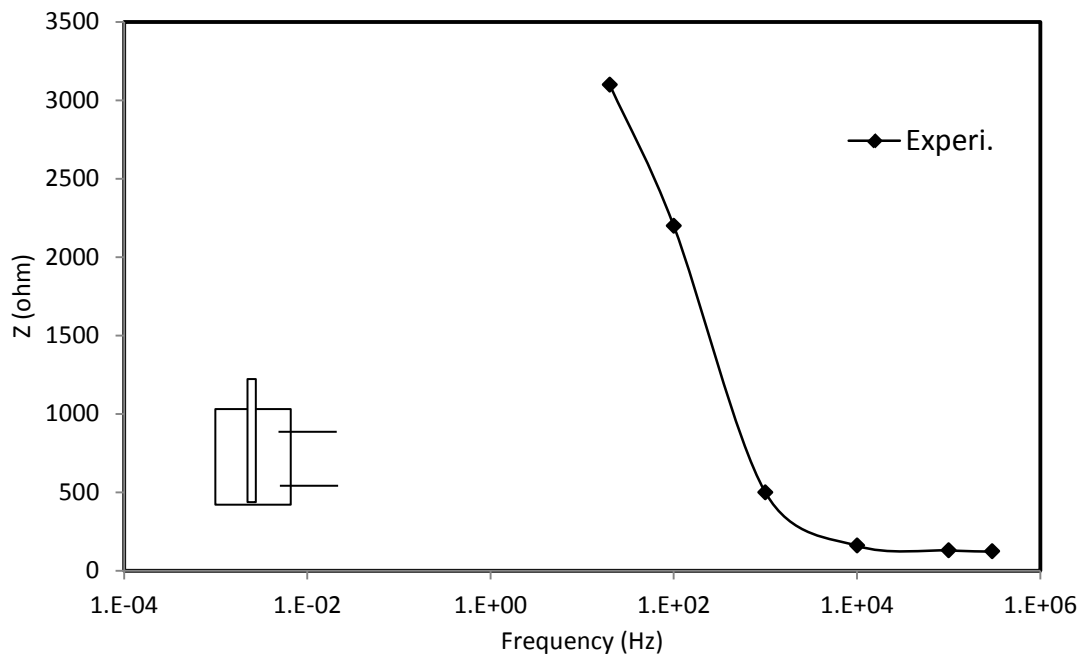


Figure 5.18 Bode plot of cement composite with embedded non-corroded bar after immersed in salt-water solution for 28 weeks

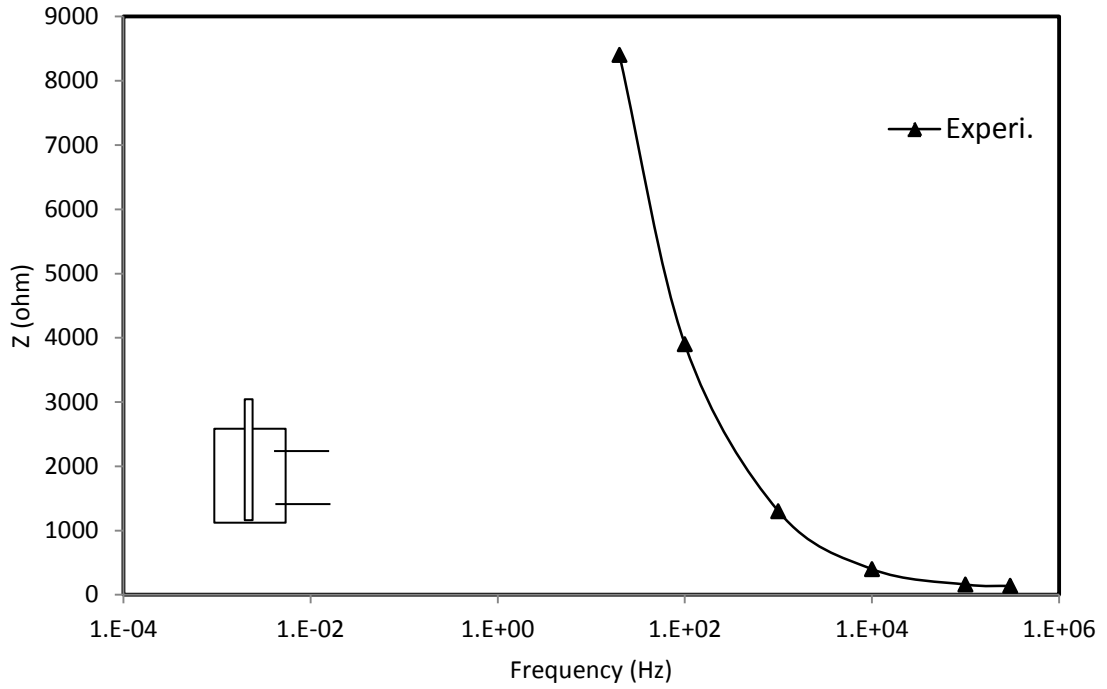


Figure 5.19 Bode plot of cement composite with embedded corroded bar after immersed in salt-water solution for 28 weeks

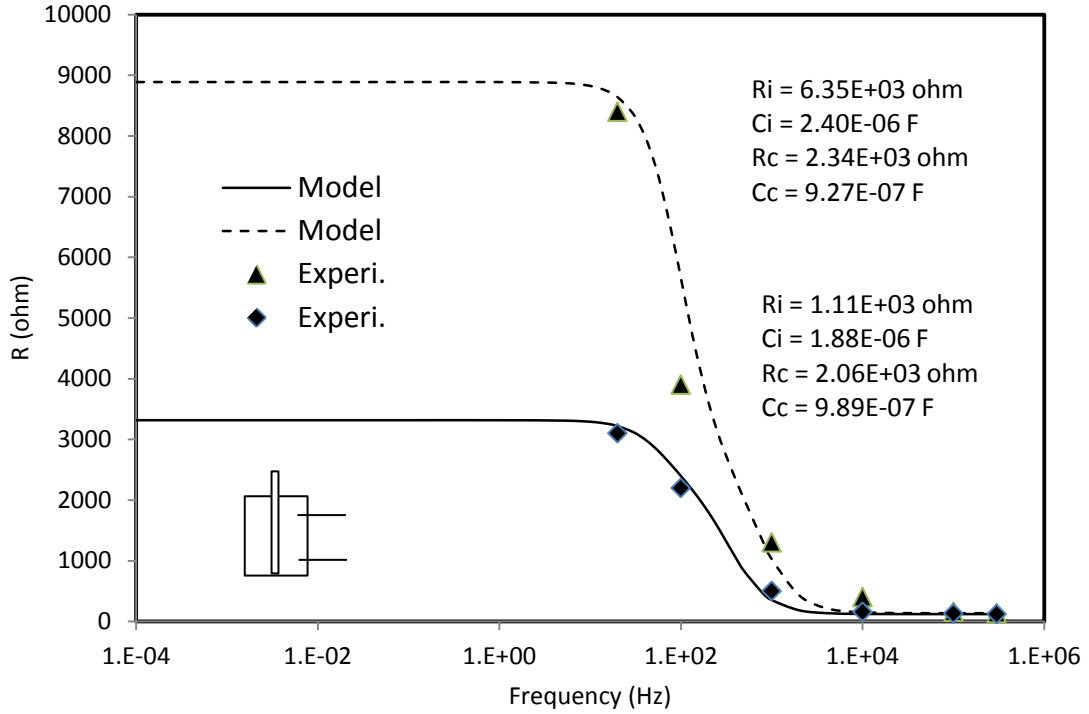


Figure 5.20 Bode plot cement composite with embedded non-corroded and corroded bar along impedance models after immersed in salt-water for 28 weeks

#### 5.4.1.2.1 Non-Corroded Cement Composites

The resistance at the interface ( $R_i$ ) between the non-corroded bar and the smart cement specimen immersed in salt water solution and the resistance at the contact ( $R_c$ ) for the measuring time period are shown in Figure 5.21. From the Figure 5.21, it could be observed that the interface resistance ( $R_i$ ) was lower than the contact resistance ( $R_c$ ) during the course of the measuring time period. The lower value of the interface resistance ( $R_i$ ) could be attributed to the fact that the embedded bar was initially non-corroded. Both the interface resistance ( $R_i$ ) and the contact resistance ( $R_c$ ) were increased with respect to time as shown in Figure 5.21.

The capacitance at the interface ( $C_i$ ) between the non-corroded bar and the smart cement specimen immersed in salt water solution and the capacitance at the contact ( $C_c$ ) for the measuring time period are shown in Figure 5.22. From the Figure 5.22, it could be observed that the interface capacitance ( $C_i$ ) was higher than the contact capacitance ( $C_c$ ) during the course of the measuring time period. Both the interface capacitance ( $C_i$ ) and the contact capacitance ( $C_c$ ) were increased with respect to time as shown in Figure 5.22.

The material property parameter defined as product of resistance and capacitance,  $R \cdot C$ , for the non-corroded bar embedded in the smart cement specimen immersed in salt water solution is shown Figure 5.23. From the Figure 5.23, the interface  $R_i \cdot C_i$  between of the non-corroded bar and the smart cement specimen immersed in salt water solution was greater than the  $R_c \cdot C_c$  at the cement contact for the measuring time period. It can also be observed that both the interface  $R_i \cdot C_i$  and the contact  $R_c \cdot C_c$  were increased with respect to time. Therefore, from Figure 5.21 through Figure 5.23, it could be observed

that it was possible to detect and quantify the presence of the corrosion in non-corroded bar embedded in the smart cement specimen immersed in salt water solution.

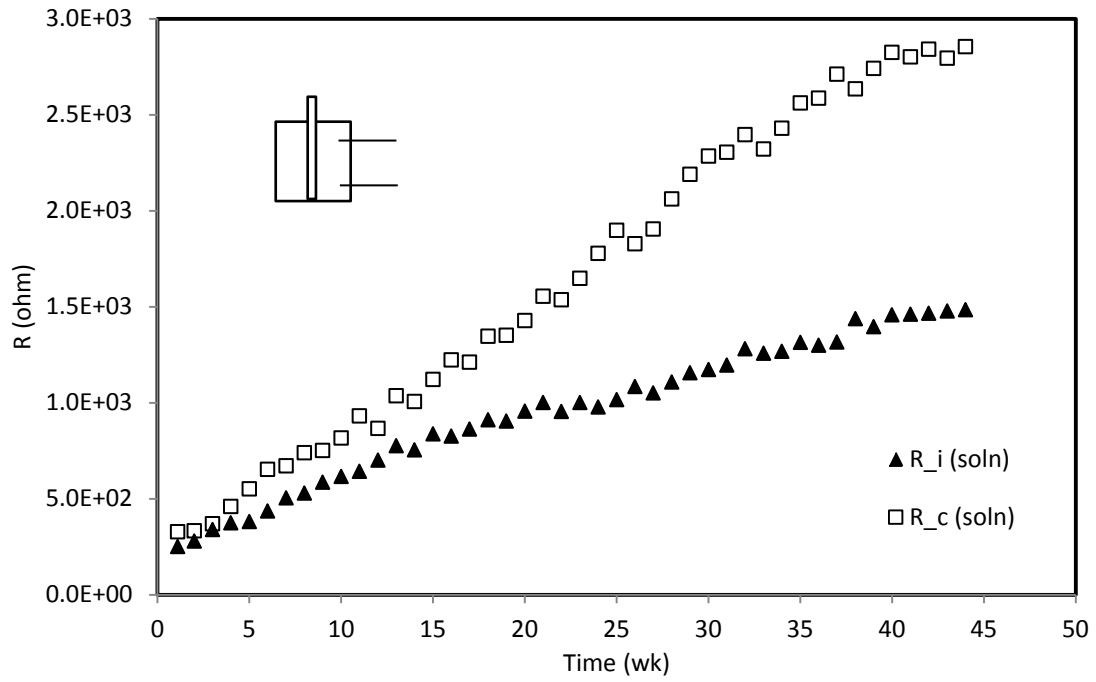


Figure 5.21 Resistances (R<sub>i</sub> & R<sub>c</sub>) of the non-corroded bar embedded in smart cement specimen under salt water condition

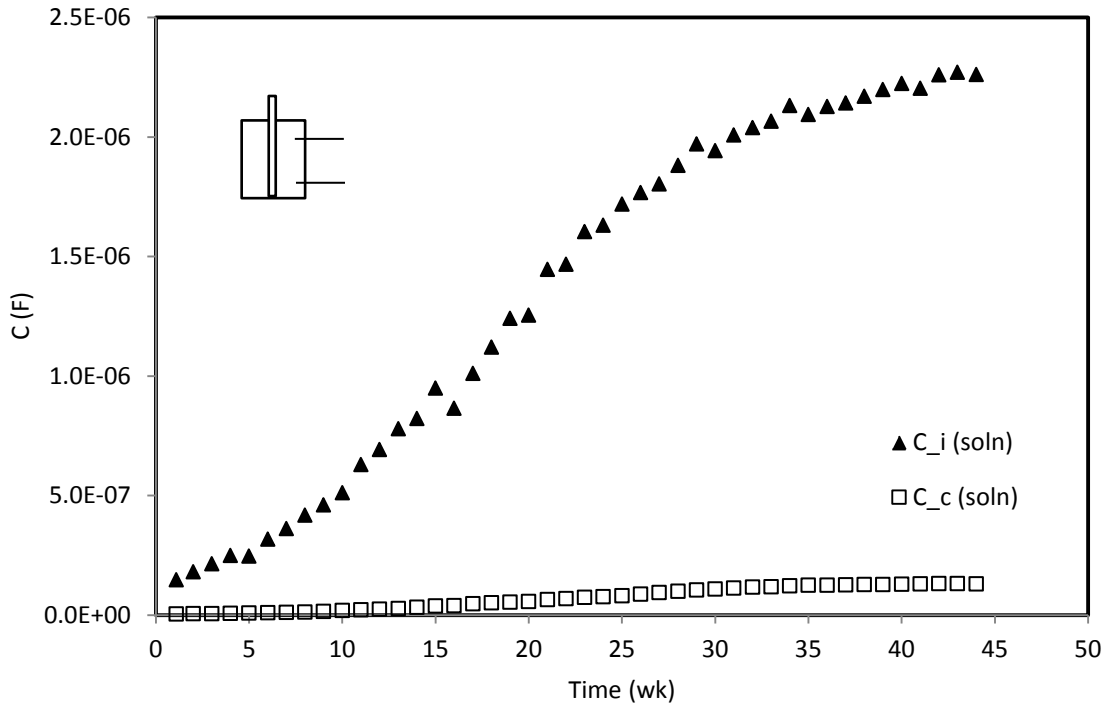


Figure 5.22 Capacitances ( $C_i$  &  $C_c$ ) of the non-corroded bar embedded in smart cement specimen under salt water condition

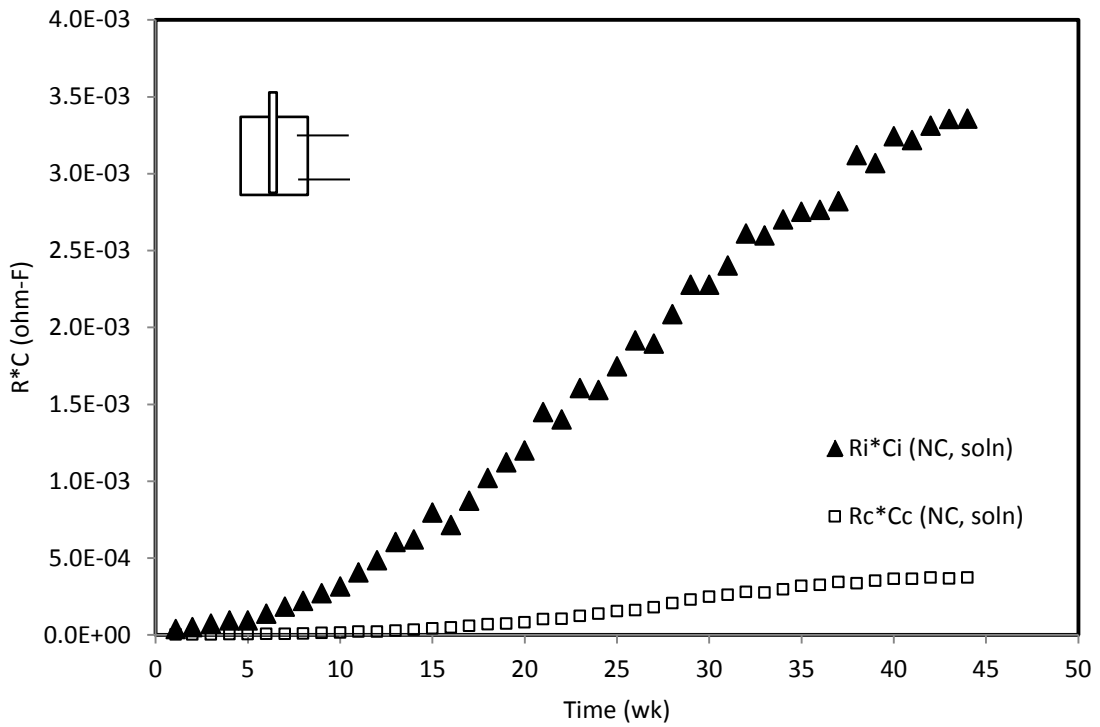


Figure 5.23  $R * C$  vs. time of the non-corroded bar embedded in smart cement specimen under salt water condition

The progression of the interface corrosion with respect to time is modeled using equation (5-10) of p-q model and the plot is shown in Figure 5.24. The model parameters p and q are estimated to be 0.22 and 0.37 respectively. As  $t \rightarrow \infty$ , the corresponding interface corrosion parameter  $R_i C_i$  is estimated to be  $7.91E-03$  ohm-F using equation (5-11).

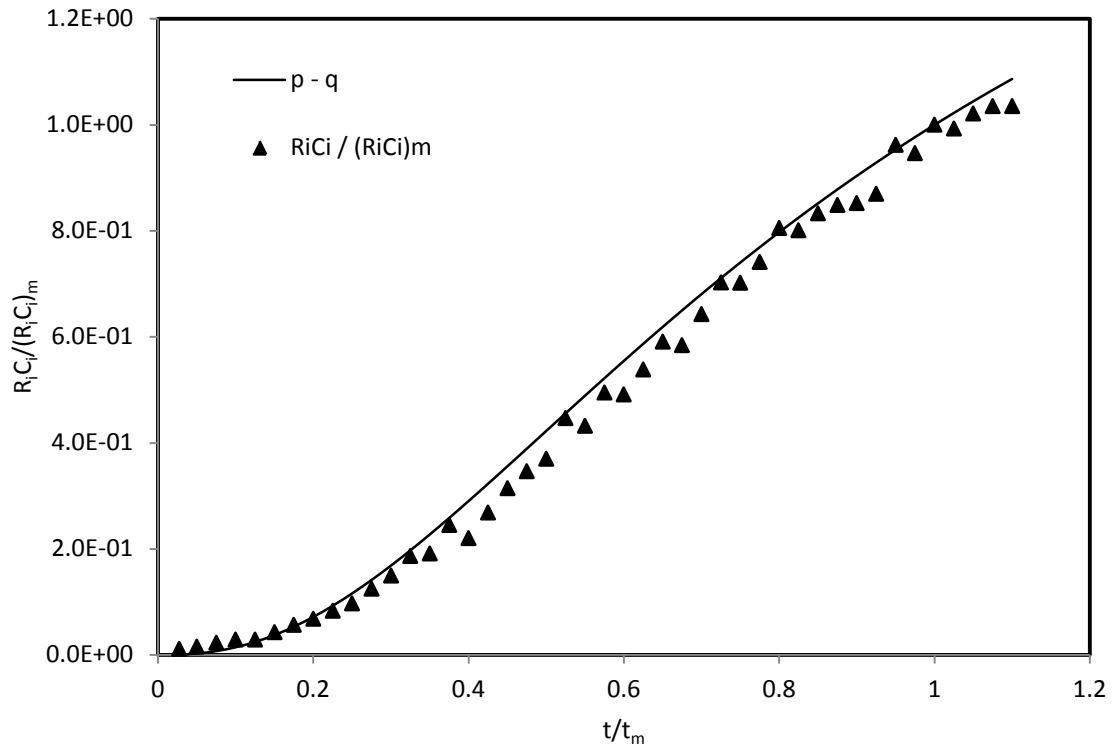


Figure 5.24 Corrosion-time model for non-corroded cement composite under salt water condition

#### 5.4.1.2.2 Corroded Cement Composites

The resistance at the interface ( $R_i$ ) between the corroded bar and the smart cement specimen immersed in salt water solution and the resistance at the contact ( $R_c$ ) for the measuring time period are shown in Figure 5.25. From the Figure 5.25, it could be

observed that the interface resistance ( $R_i$ ) was lower than the contact resistance ( $R_c$ ) during the course of the measuring time period. The lower value of the interface resistance ( $R_i$ ) could be attributed to the fact that the embedded bar was initially corroded. Both the interface resistance ( $R_i$ ) and the contact resistance ( $R_c$ ) were increased with respect to time as shown in Figure 5.25.

The capacitance at the interface ( $C_i$ ) between the corroded bar and the smart cement specimen immersed in salt water solution and the capacitance at the contact ( $C_c$ ) for the measuring time period are shown in Figure 5.26. From the Figure 5.26, it could be observed that the interface capacitance ( $C_i$ ) was higher than the contact capacitance ( $C_c$ ) during the course of the measuring time period. Both the interface capacitance ( $C_i$ ) and the contact capacitance ( $C_c$ ) were increased with respect to time as shown in Figure 5.26.

The material property parameter defined as product of resistance and capacitance,  $R \cdot C$ , for the corroded bar embedded in the smart cement specimen immersed in salt water solution is shown Figure 5.27. From the Figure 5.27, the interface  $R_i \cdot C_i$  between of the corroded bar and the smart cement specimen immersed in salt water solution was greater than the  $R_c \cdot C_c$  at the cement contact for the measuring time period. It can also be observed that both the interface  $R_i \cdot C_i$  and the contact  $R_c \cdot C_c$  were increased with respect to time. Therefore, from Figure 5.25 through Figure 5.27, it could be observed that it was possible to detect and quantify the presence of the corrosion in corroded bar embedded in the smart cement specimen immersed in salt water solution.

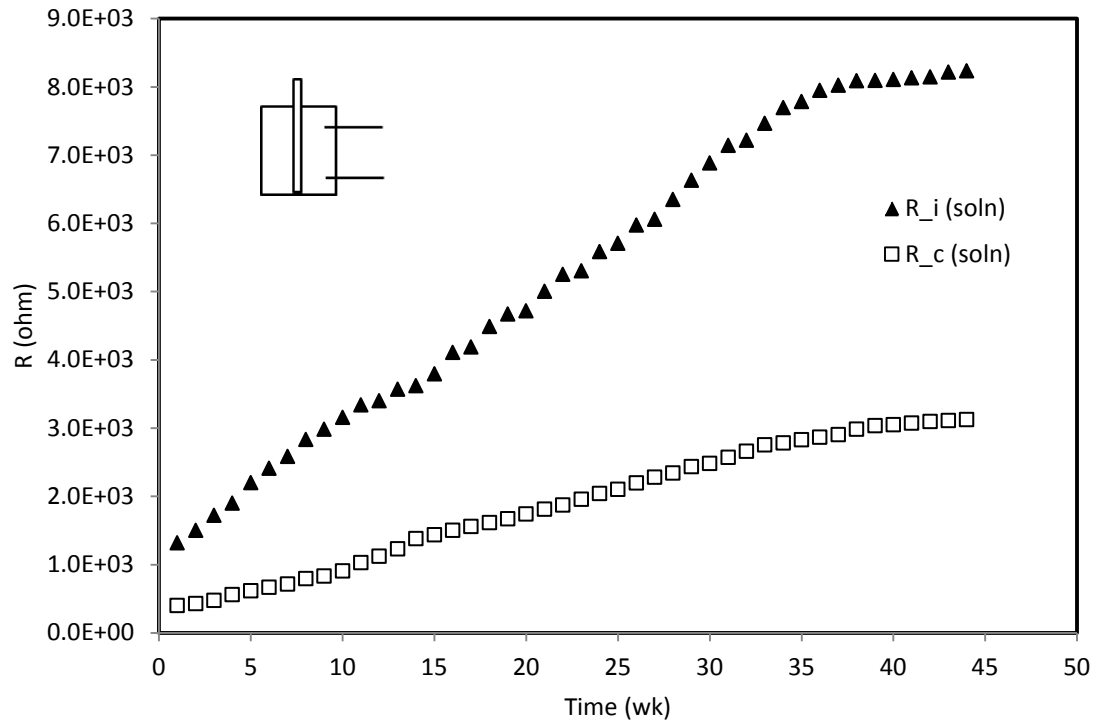


Figure 5.25 Resistances ( $R_i$  &  $R_c$ ) of the corroded bar embedded in smart cement specimen under salt water condition

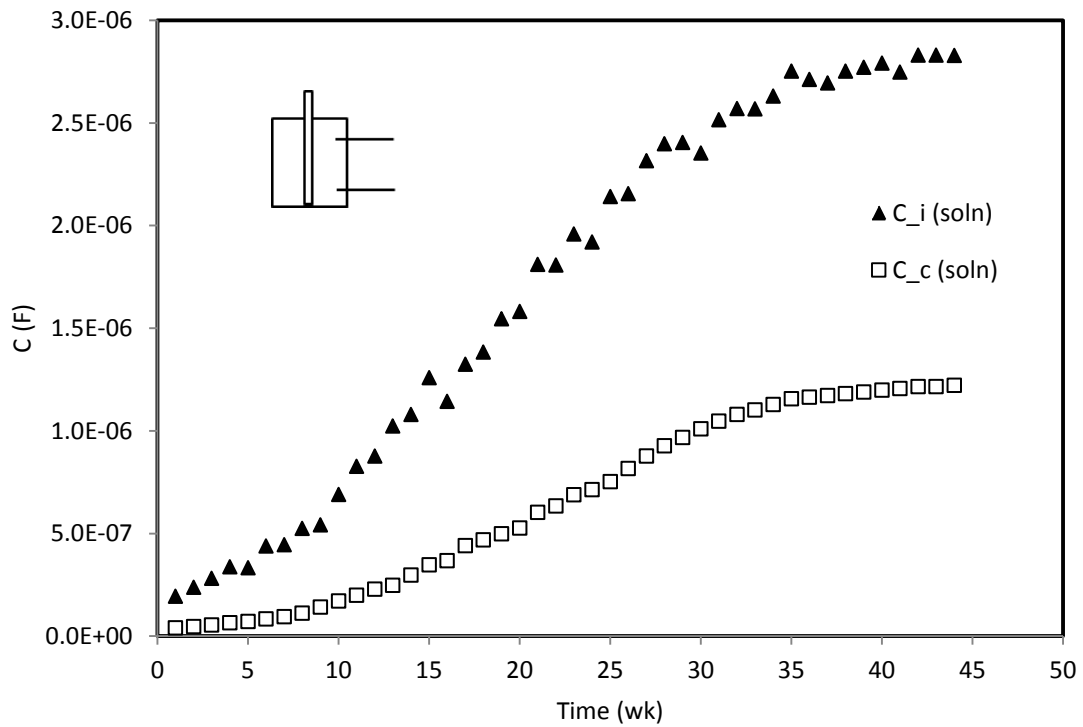


Figure 5.26 Capacitances ( $C_i$  &  $C_c$ ) of the corroded bar embedded in smart cement specimen under salt water condition

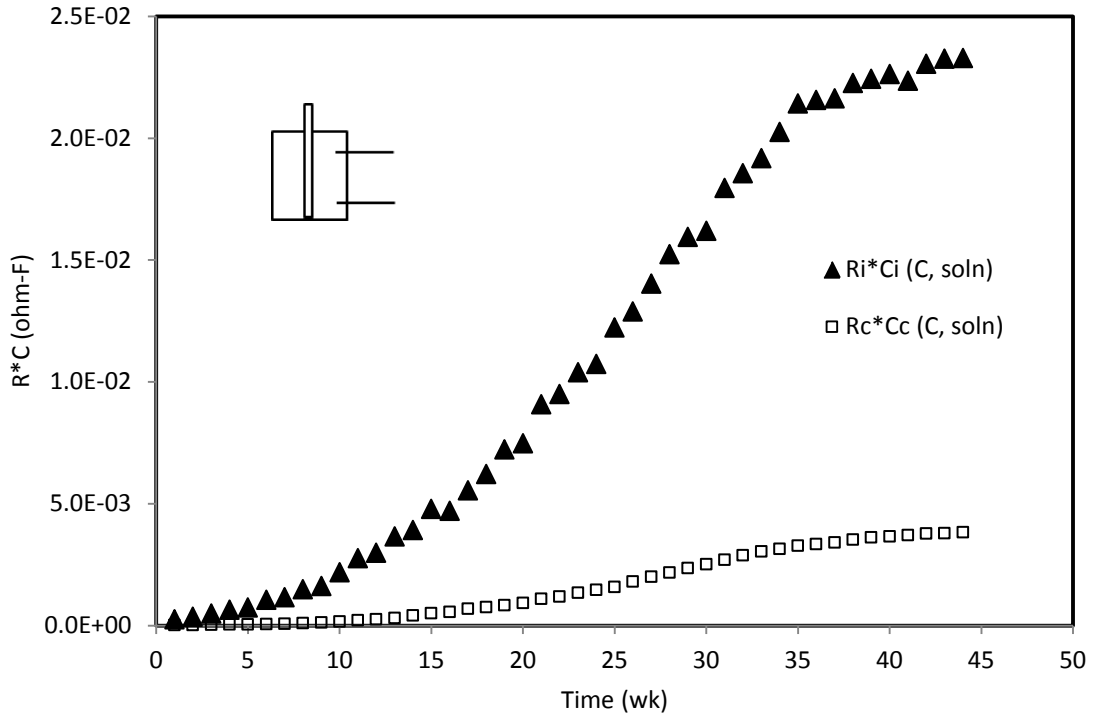


Figure 5.27 R\*C vs. time of the corroded bar embedded in smart cement specimen under salt water condition

The progression of the interface corrosion with respect to time is modeled using equation (5-10) of p-q model and the plot is shown in Figure 5.28. The model parameters p and q are estimated to be 0.24 and 0.39 respectively. As  $t \rightarrow \infty$ , the corresponding interface corrosion parameter  $R_i C_i$  is estimated to be  $6.12E-02$  ohm-F using equation (5-11).

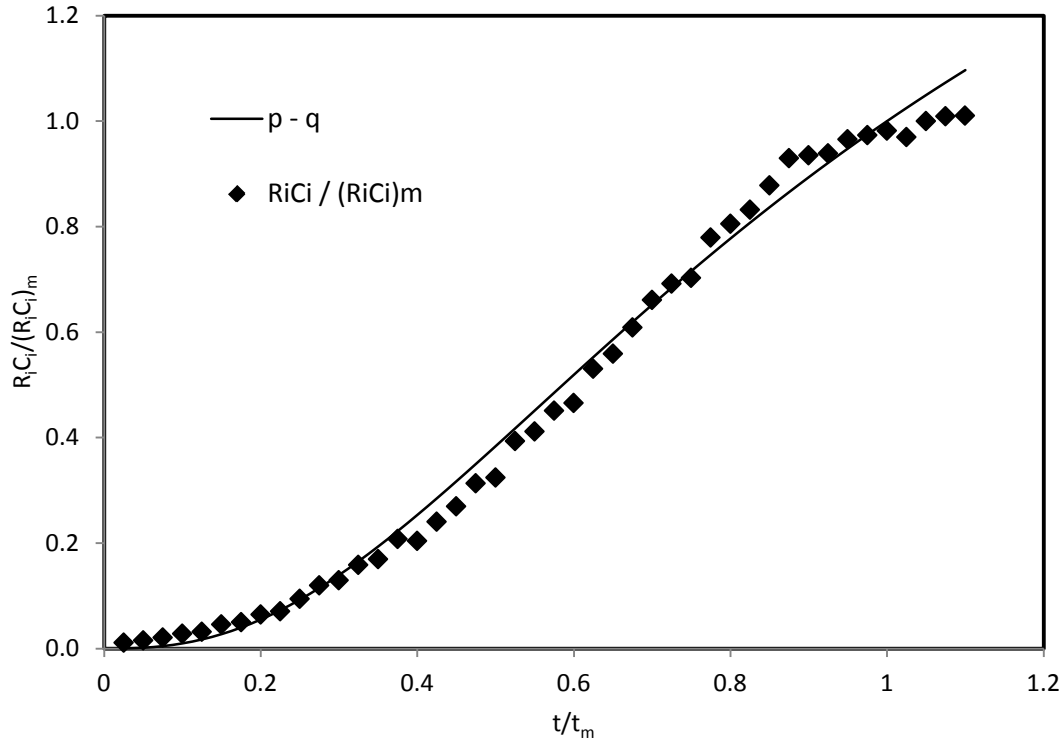


Figure 5.28 Corrosion-time model for corroded cement composite under salt water condition

## 5.4.2 Steel-Polyester Characterization

### 5.4.2.1 Under Dry-Air Condition

The electrical resistances and capacitances of the polyester composite specimen, bar, and transitional contact surface between the polyester and bar were measured with impedance analyzer precision LCR meter. The impedance measurements were performed on a weekly basis for about a year. The frequency range used was from 20 Hz to 300 kHz. For 5<sup>th</sup> week test, a typical Bode plot of impedance vs frequency for non-corroded bar embedded in smart polyester specimen is shown in Figure 5.29. For 5<sup>th</sup> week test, a

typical Bode plot of impedance vs frequency for corroded bar embedded in smart polyester specimen is shown in Figure 5.30.

The Bode plot of the adopted equivalent circuit for non-corroded and corroded composite specimens is shown in Figure 5.31. As the Figure 5.31 shown, the impedance of the corroded composite specimen was higher than that of non-corroded composite specimen, and therefore it was possible to detect the presence of the corrosion.

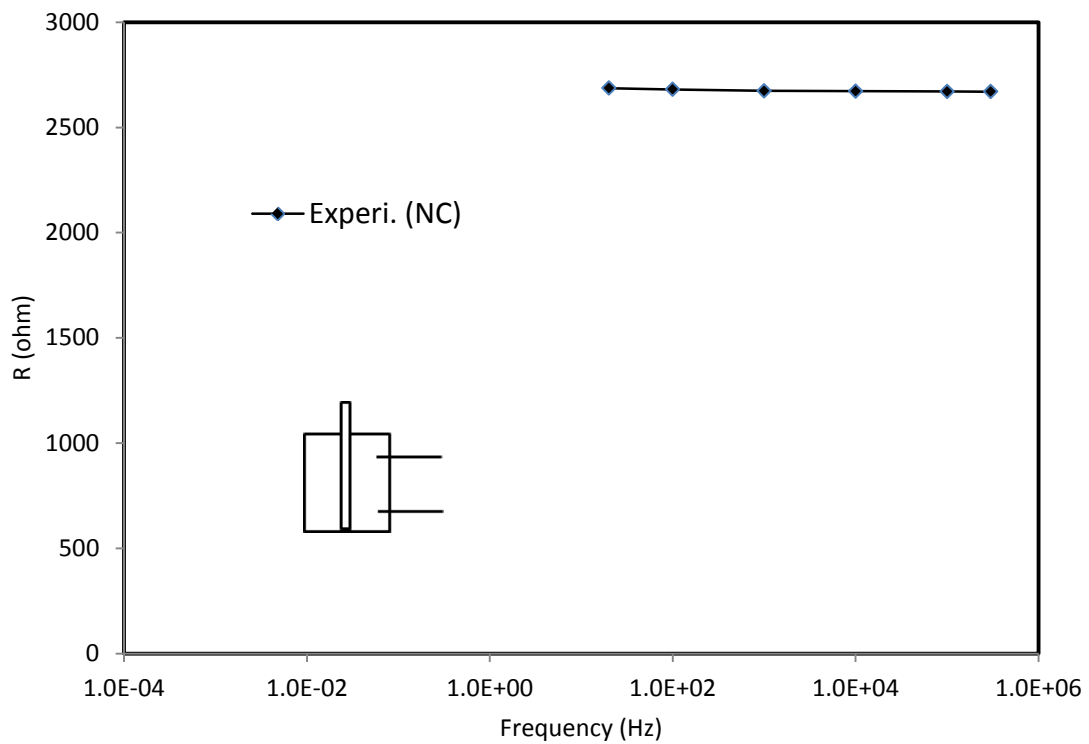


Figure 5.29 Bode plot of polyester composite with embedded non-corroded bar

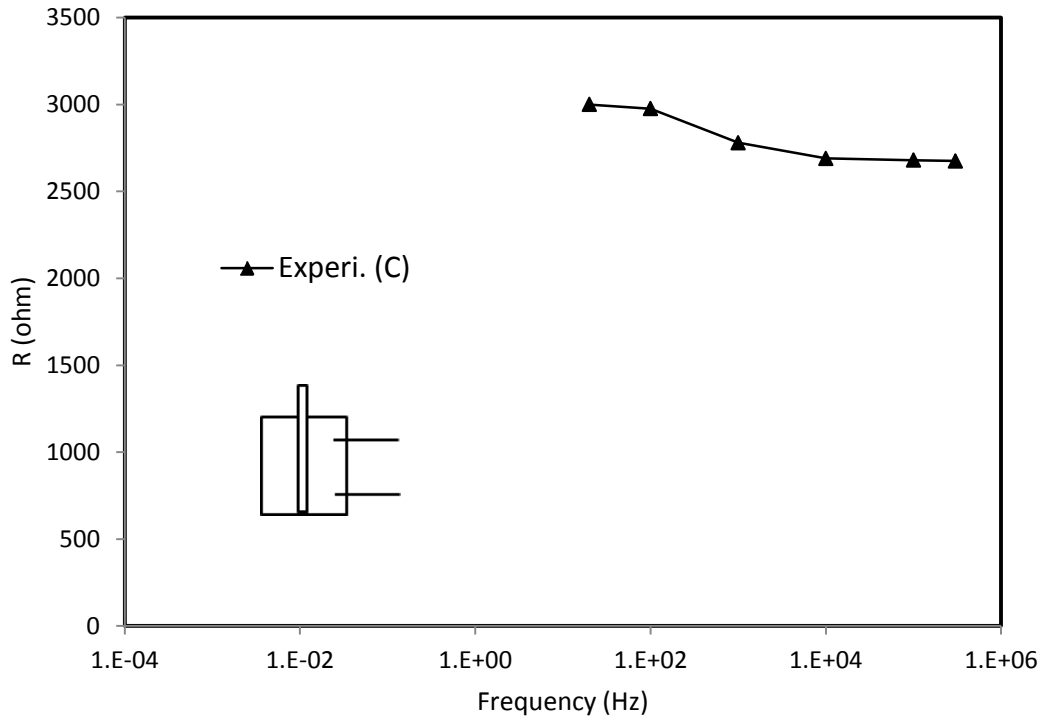


Figure 5.30 Bode plot of polyester composite with embedded corroded bar

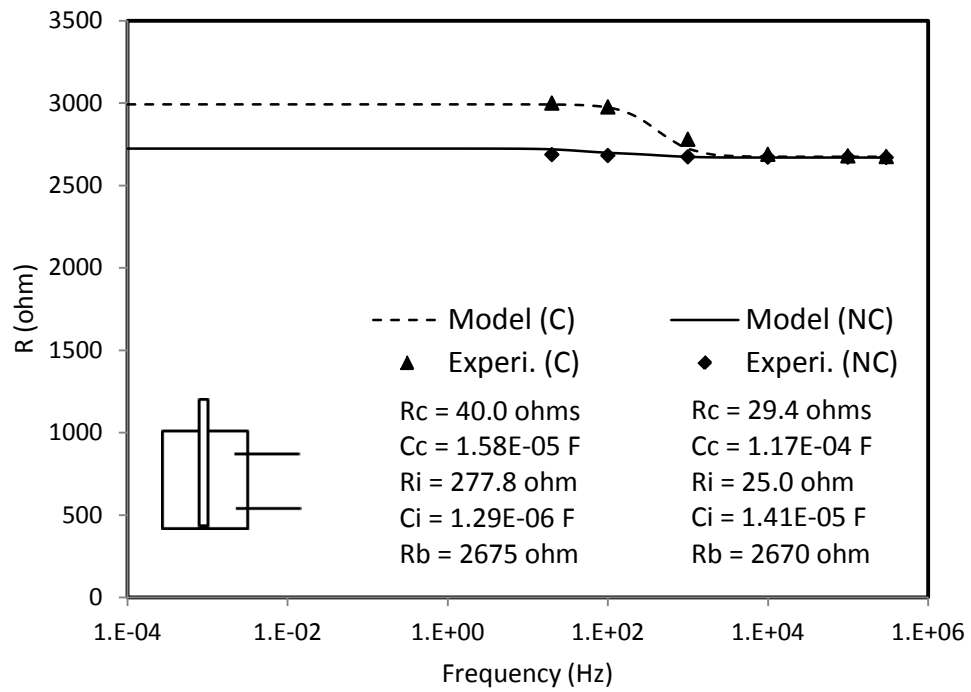


Figure 5.31 Bode plot of polyester composites with embedded non-corroded and corroded bar along respective impedance models

#### 5.4.2.1.1 Non-Corroded Polyester Composites

The resistance at the interface ( $R_i$ ) between non-corroded bar and the smart polyester and the resistance at the contact ( $R_c$ ) for the measuring time period are shown in Figure 5.32. From Figure 5.32, it could be observed that the interface resistance ( $R_i$ ) was lower than the contact resistance ( $R_c$ ) during the course of the measuring time period. The lower value of the interface resistance ( $R_i$ ) could be attributed to the fact that the embedded bar was initially non-corroded. Both the interface resistance ( $R_i$ ) and the contact resistance ( $R_c$ ) generally remained in constant at about 25 ohm with respect to time as shown in Figure 5.32.

The capacitance at the interface ( $C_i$ ) between non-corroded bar and the smart polyester and the capacitance at the contact ( $C_c$ ) for the measuring time period are shown in Figure 5.33. From Figure 5.33, it could be observed that the interface capacitance ( $C_i$ ) was higher than the contact capacitance ( $C_c$ ) during the course of the measuring time period. Both the interface capacitance ( $C_i$ ) and the contact capacitance ( $C_c$ ) generally remained constant with respect to time as shown in Figure 5.33.

The material property parameter defined as product of resistance and capacitance,  $R \cdot C$ , for the non-corroded bar embedded in the smart polyester is shown in Figure 5.34. From Figure 5.34, the interface  $R_i \cdot C_i$  between of the non-corroded bar and the smart polyester was greater than the  $R_c \cdot C_c$  at the polyester contact for the measuring time period. It can also be observed that both the interface  $R_i \cdot C_i$  and the contact  $R_c \cdot C_c$  generally remained constant with respect to time. This could be attributed to the dry air

condition in which the specimens were kept. The value of  $R_i \cdot C_i$  had between  $2.61E-4$  ohm-F and  $2.75E-4$  ohm-F. These values are greater than  $1.87E-4$  ohm-F which corresponds to that of non-corroded steel bar as discussed in section 5.2. Therefore, from Figure 5.32 through Figure 5.34, it could be observed that it was possible to detect and quantify the small presence of interface corrosion in the non-corroded bar embedded in the smart polyester.

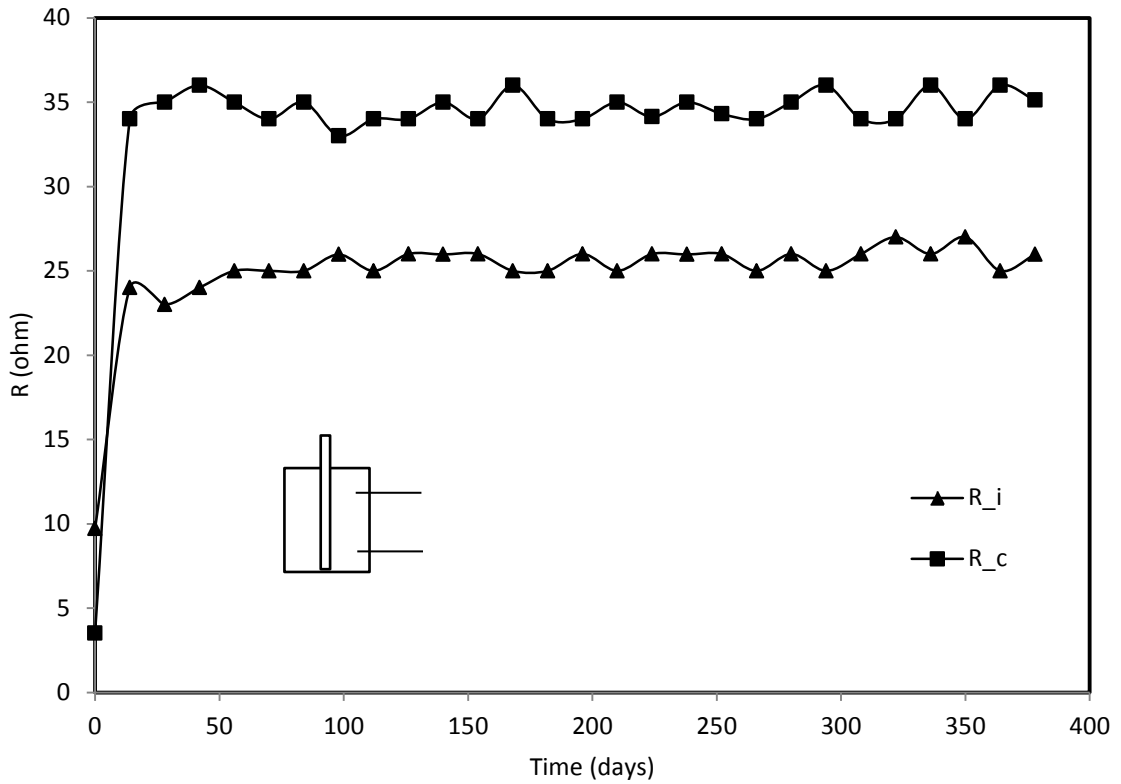


Figure 5.32 Resistances ( $R_i$  &  $R_c$ ) of the non-corroded bar embedded in smart polyester under air dry condition

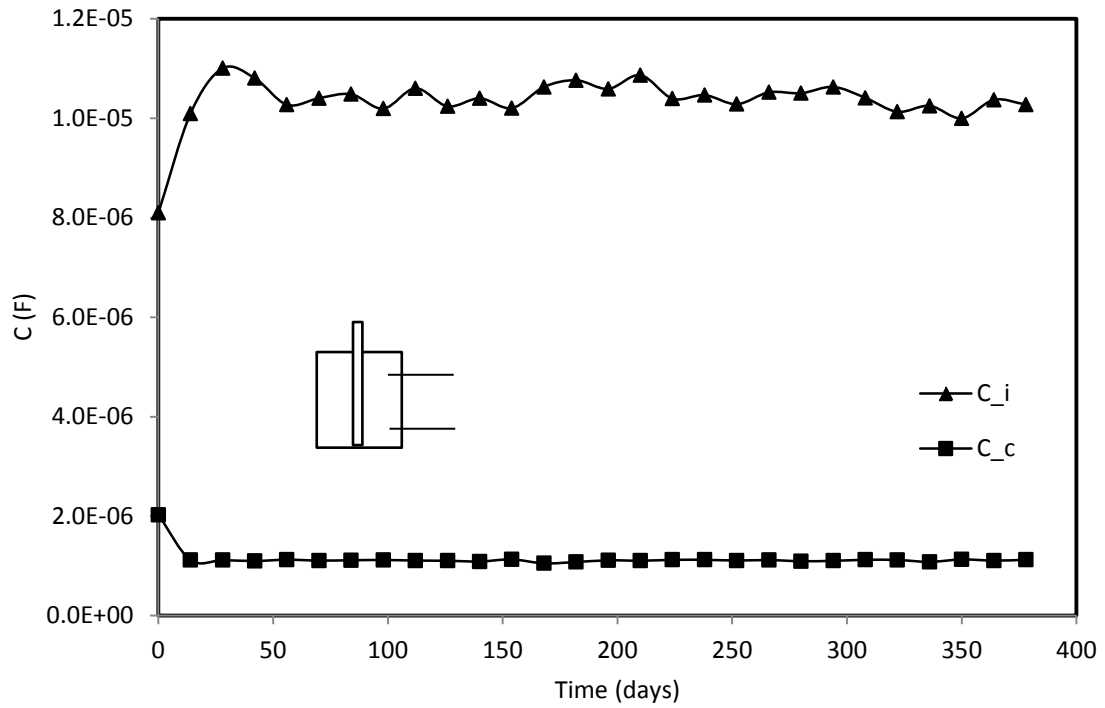


Figure 5.33 Capacitances ( $C_i$  &  $C_c$ ) of the non-corroded bar embedded in smart polyester in air dry condition

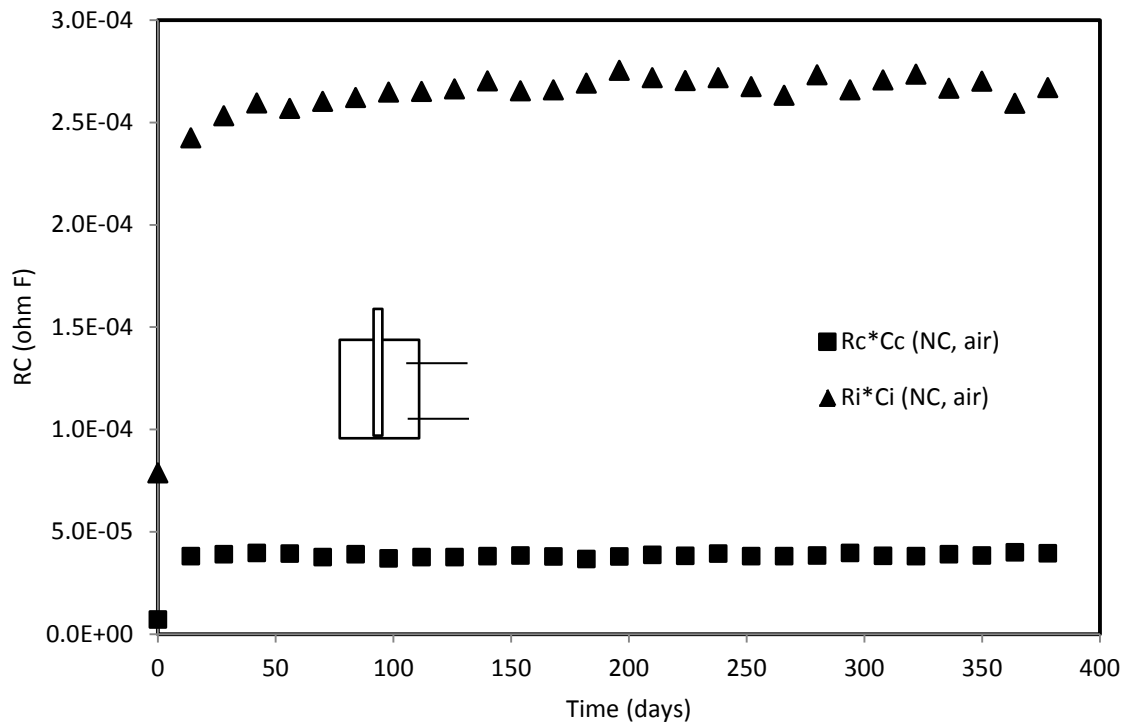


Figure 5.34  $R * C$  vs. time of the non-corroded bar embedded in smart polyester in air dry condition

The progression of the interface corrosion with respect to time is modeled using equation (5-10) of p-q model and the plot is shown in Figure 5.35. The model parameters p and q are estimated to be 0.0 and 0.004 respectively. As  $t \rightarrow \infty$ , the corresponding interface corrosion parameter  $R_i C_i$  is estimated to be  $3.54E-04$  ohm-F using equation (5-11). The initial corrosion parameter was  $(R_i C_i)_o$  is  $7.87E-05$  ohm-F.

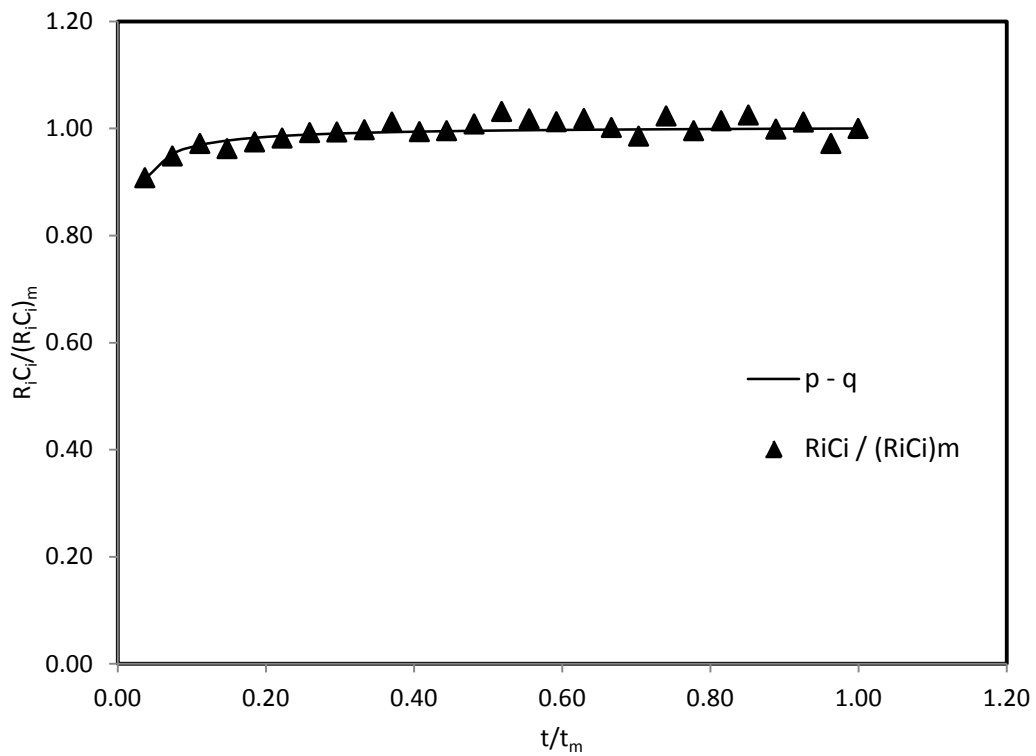


Figure 5.35 Corrosion-time model for non-corroded polyester composite under dry condition

#### 5.4.2.1.2 Corroded Polyester Composites

The resistance at the interface ( $R_i$ ) between corroded bar and the smart polyester specimen under dry air condition and the resistance at the contact ( $R_c$ ) for the measuring

time period are shown in Figure 5.36. From the Figure 5.36, it could be observed that the interface resistance ( $R_i$ ) was higher than the contact resistance ( $R_c$ ) during the course of the measuring time period. The higher value of the interface resistance ( $R_i$ ) could be attributed to the fact that the embedded bar was initially corroded. Both the interface resistance ( $R_i$ ) and the contact resistance ( $R_c$ ) were increased with respect to time as shown in Figure 5.36.

The capacitance at the interface ( $C_i$ ) between corroded bar and the smart polyester specimen under dry air condition and the capacitance at the contact ( $C_c$ ) for the measuring time period are shown in Figure 5.37. From the Figure 5.37, it could be observed that the interface capacitance ( $C_i$ ) was higher than the contact capacitance ( $C_c$ ) during the course of the measuring time period. Both the interface capacitance ( $C_i$ ) and the contact capacitance ( $C_c$ ) were increased with respect to time as shown in Figure 5.37.

The material property parameter defined as product of resistance and capacitance,  $R*C$ , for the corroded bar embedded in the smart polyester specimen under dry air condition is shown Figure 5.38. From the Figure 5.38, the interface  $R_i*C_i$  between of the corroded bar and the smart polyester was greater than the  $R_c*C_c$  at the polyester contact for the measuring time period. It can also be observed that both the interface  $R_i*C_i$  and the contact  $R_c*C_c$  generally remained constant with respect to time. This could be attributed to the dry air condition in which the specimens where kept. The value of  $R_i*C_i$  had between  $3.47E-4$  ohm-F and  $3.66E-4$  ohm-F. These values are greater than  $1.87E-4$  ohm-F which corresponds to that of non-corroded steel bar as discussed in section 5.2. Therefore, from Figure 5.36 through Figure 5.38, it could be observed that it was possible

to detect and quantify the presence of interface corrosion in the corroded bar embedded in the smart polyester under dry air condition.

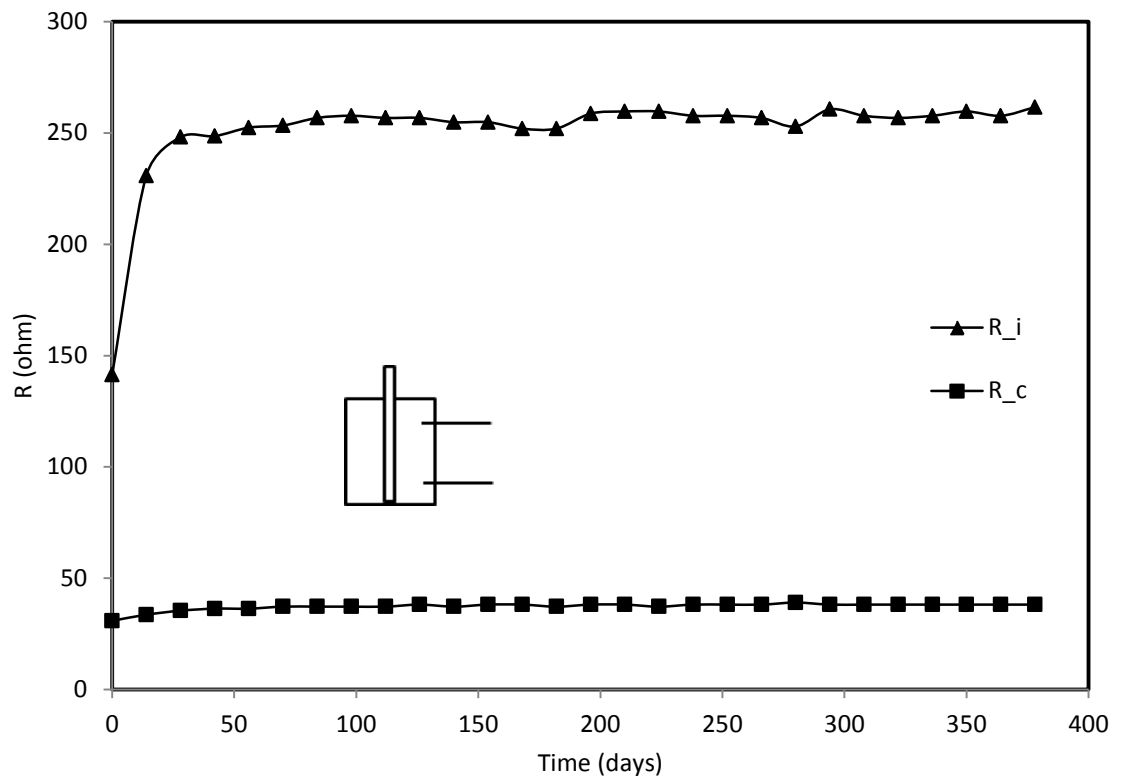


Figure 5.36 Resistances ( $R_i$  &  $R_c$ ) of the corroded bar embedded in smart polyester under air dry condition

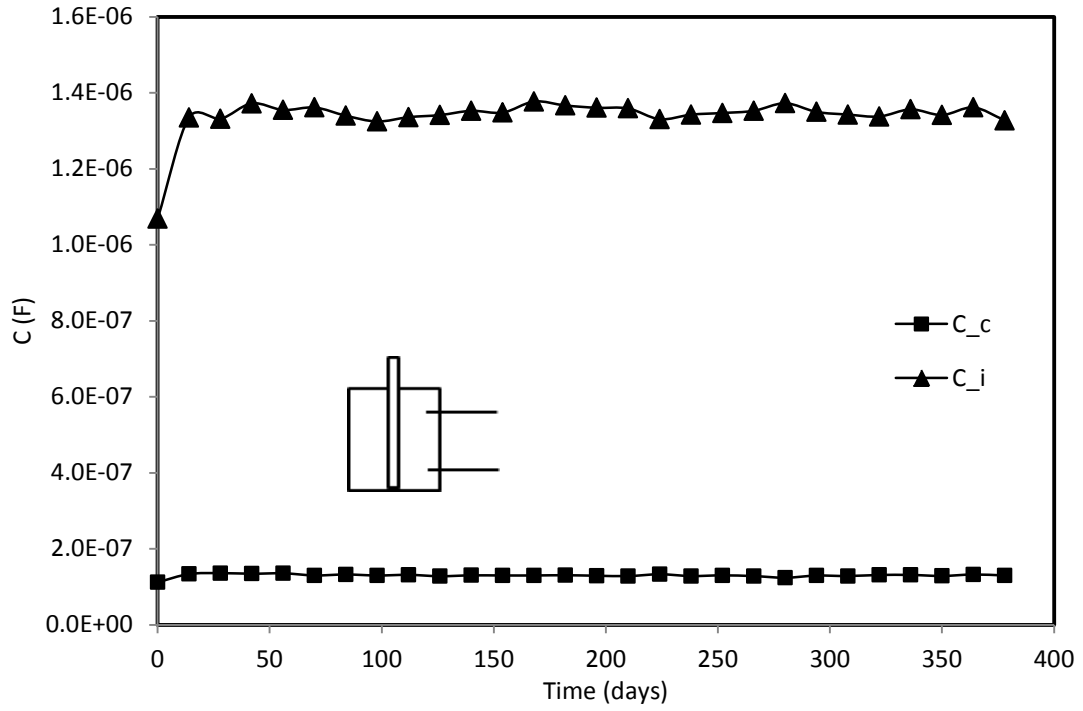


Figure 5.37 Capacitances ( $C_i$  &  $C_c$ ) of the corroded bar embedded in smart polyester in air dry condition

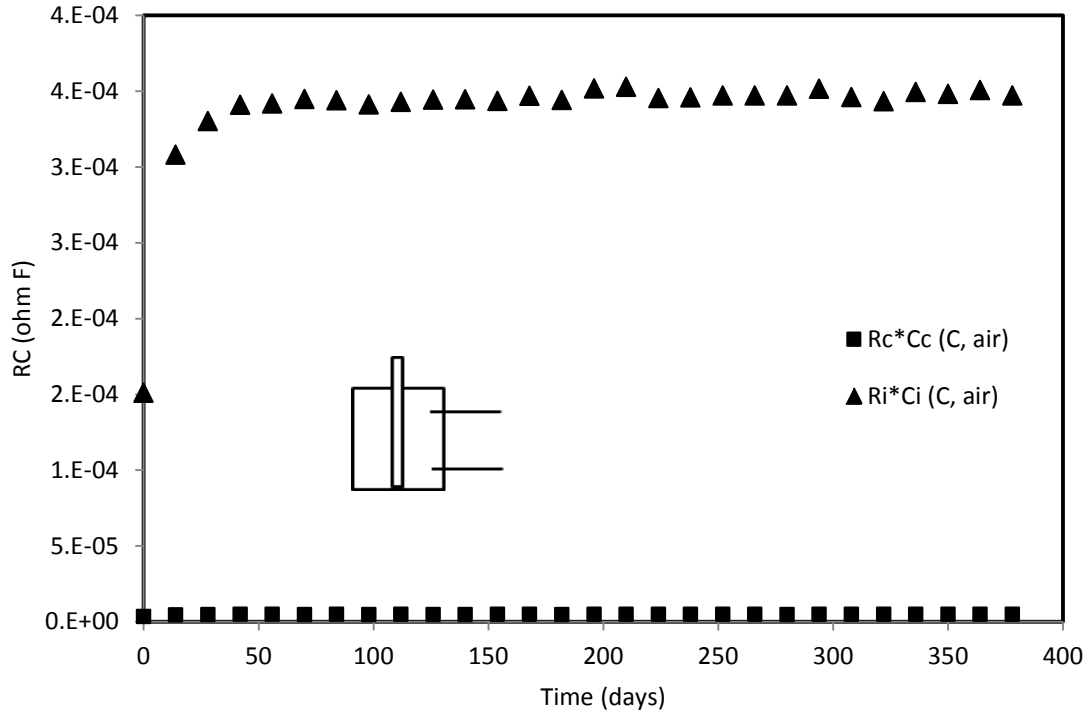


Figure 5.38  $R^*C$  vs. time of the corroded bar embedded in smart polyester in air dry condition

The progression of the interface corrosion with respect to time is modeled using equation (5-10) of p-q model and the plot is shown in Figure 5.39. The model parameters p and q are estimated to be 0.0 and 0.004 respectively. As  $t \rightarrow \infty$ , the corresponding interface corrosion parameter RiCi is estimated to be 5.00E-04 ohm-F using equation (5-11). The initial corrosion parameter was  $(RiCi)_o$  is 1.51E-04 ohm-F.

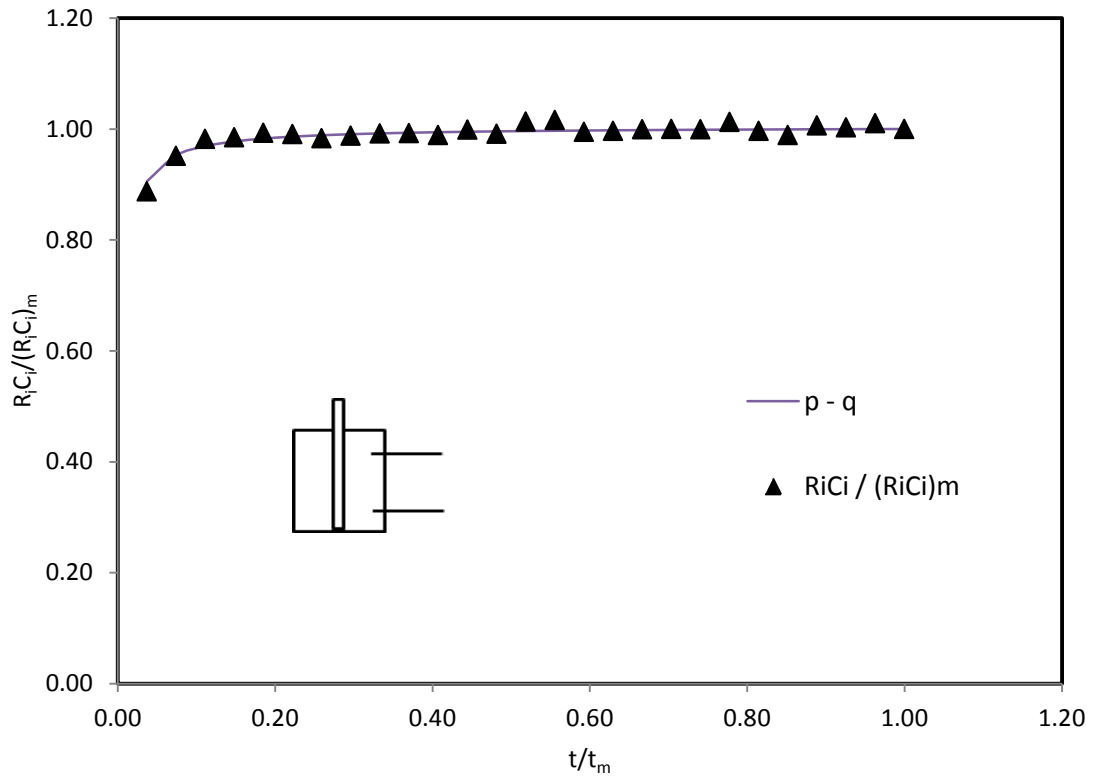


Figure 5.39 Corrosion-time model for corroded polyester composite under dry condition

#### 5.4.2.2 Under Salt-Water Solution

Another set of specimens was immersed in a salt water solution (3.5% wt. NaCl) continually for about a year. The impedance measurements were performed on a weekly

basis for about a year. The frequency range used was from 20 Hz to 300 kHz. For 5<sup>th</sup> week test, a typical Bode plot of impedance vs frequency for non-corroded bar embedded in smart polyester specimen is shown in Figure 5.40. For 5<sup>th</sup> week test, a typical Bode plot of impedance vs frequency for corroded bar embedded in smart polyester specimen is shown in Figure 5.41.

The Bode plot of the adopted equivalent circuit for non-corroded and corroded composite specimens is shown in Figure 5.42. As the Figure 5.42 shown, the impedance of the corroded composite specimen was only slightly higher than that of non-corroded composite specimen, and therefore it was possible to detect the presence of the corrosion. The small increase (between 0.74% and 1%) in the impedance of polyester composite specimens immersed in salt water solution could be attributed its low water absorption property.

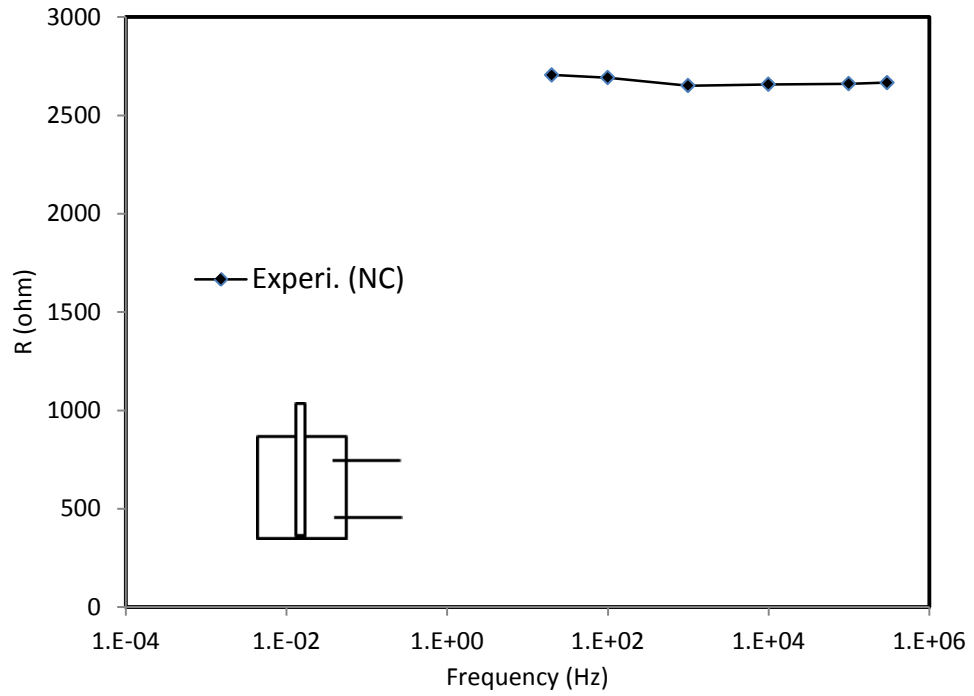


Figure 5.40 Bode plot of polyester composite with embedded non-corroded bar after immersed in salt- water for 5 weeks

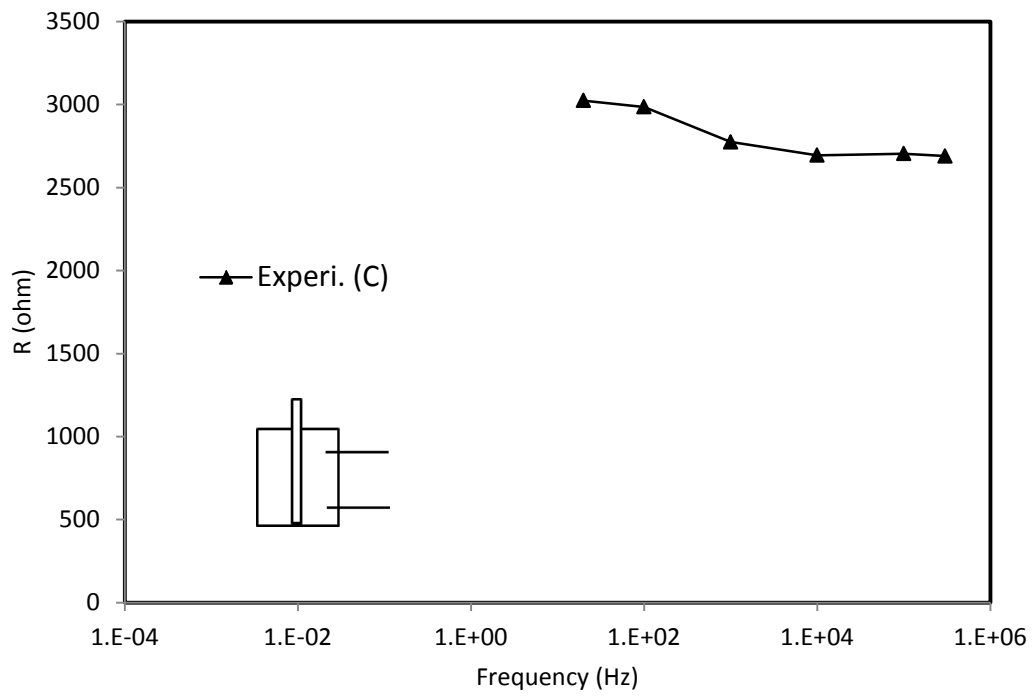


Figure 5.41 Bode plot of polyester composite with embedded corroded bar after immersed in salt-water for 5 weeks

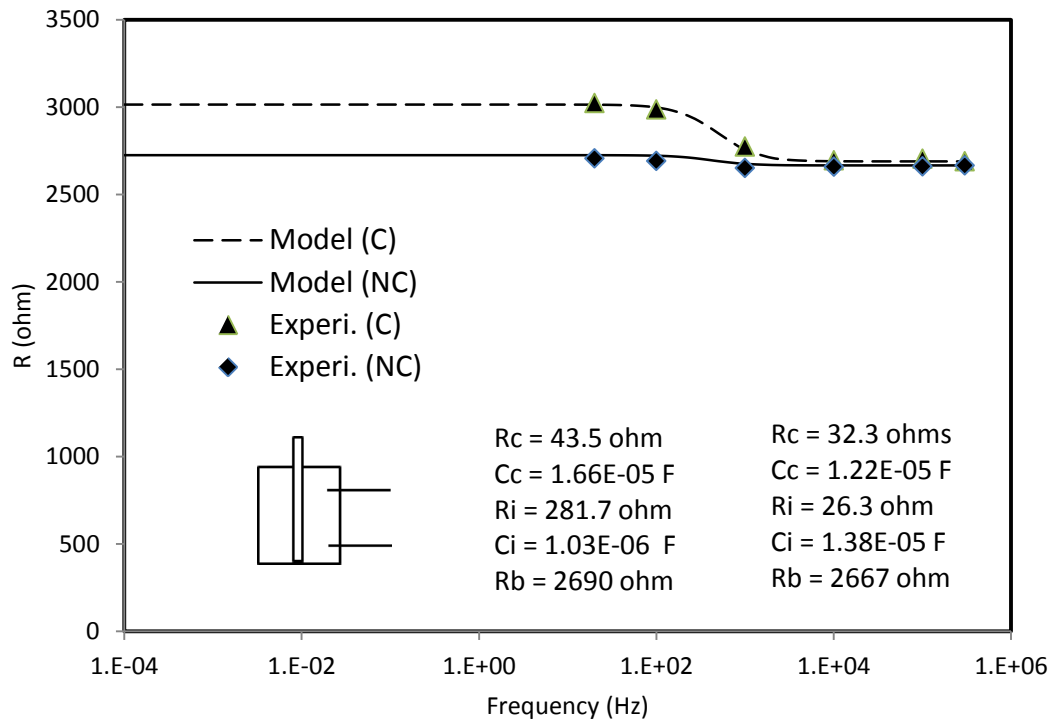


Figure 5.42 Bode plot polyester composite with embedded non-corroded and corroded bar along impedance models after immersed in salt-water for 5 weeks

#### 5.4.2.2.1 Non-Corroded Polyester Composites

The resistance at the interface ( $R_i$ ) between the non-corroded bar and the smart polyester specimen immersed in salt water solution and the resistance at the contact ( $R_c$ ) for the measuring time period are shown in Figure 5.43. From the Figure 5.43, it could be observed that the interface resistance ( $R_i$ ) was lower than the contact resistance ( $R_c$ ) during the course of the measuring time period. The lower value of the interface resistance ( $R_i$ ) could be attributed to the fact that the embedded bar was initially non-corroded. Both the interface resistance ( $R_i$ ) and the contact resistance ( $R_c$ ) were increased with respect to time as shown in Figure 5.43.

The capacitance at the interface ( $C_i$ ) between the non-corroded bar and the smart polyester specimen immersed in salt water solution and the capacitance at the contact ( $C_c$ ) for the measuring time period are shown in Figure 5.44. From the Figure 5.44, it could be observed that the interface capacitance ( $C_i$ ) was higher than the contact capacitance ( $C_c$ ) during the course of the measuring time period. Both the interface capacitance ( $C_i$ ) and the contact capacitance ( $C_c$ ) were increased with respect to time as shown in Figure 5.44.

The material property parameter defined as product of resistance and capacitance,  $R \cdot C$ , for the non-corroded bar embedded in the smart polyester specimen immersed in salt water solution is shown Figure 5.45. From the Figure 5.45, the interface  $R_i \cdot C_i$  between of the non-corroded bar and the smart polyester specimen immersed in salt water solution was greater than the  $R_c \cdot C_c$  at the polyester contact for the measuring time period. It can also be observed that both the interface  $R_i \cdot C_i$  and the contact  $R_c \cdot C_c$  generally remained constant with respect to time. The value of  $R_i \cdot C_i$  had between  $2.47 \text{E-}4 \text{ ohm-F}$  and  $2.63 \text{E-}4 \text{ ohm-F}$ . These values are greater than  $1.87 \text{E-}4 \text{ ohm-F}$  which corresponds to that of non-corroded steel bar as discussed in section 5.2. Therefore, from Figure 5.43 through Figure 5.45, it could be observed that it was possible to detect and quantify the small presence of interface corrosion in the non-corroded bar embedded in the smart polyester.

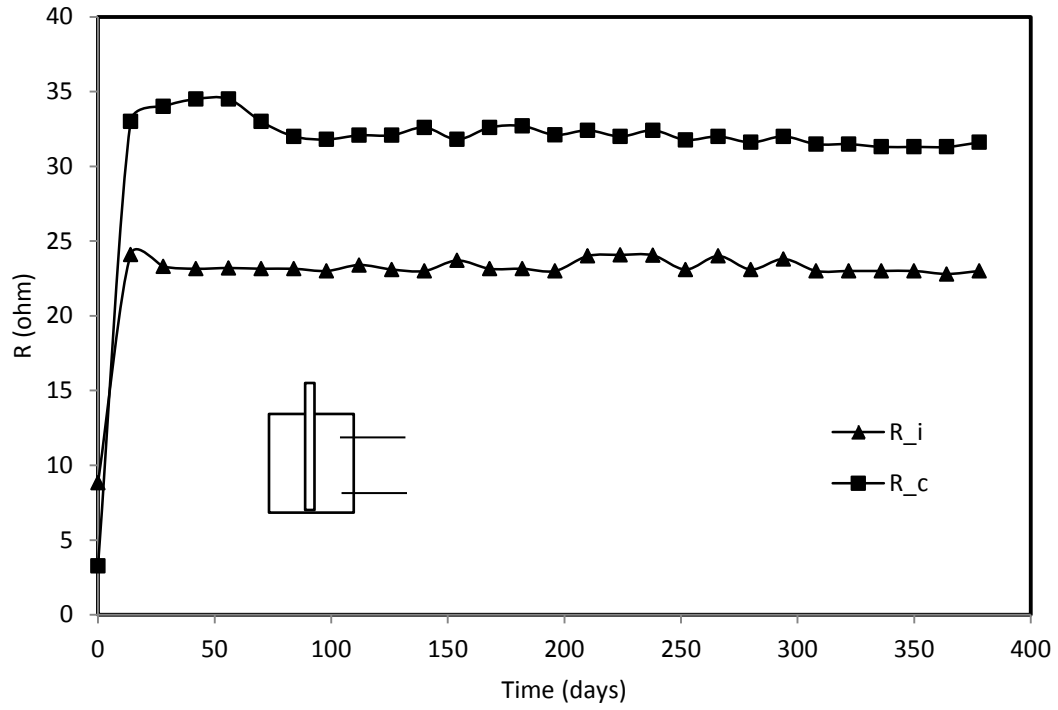


Figure 5.43 Resistances (R<sub>i</sub> & R<sub>c</sub>) of the non-corroded bar embedded in smart polyester specimen under salt water condition

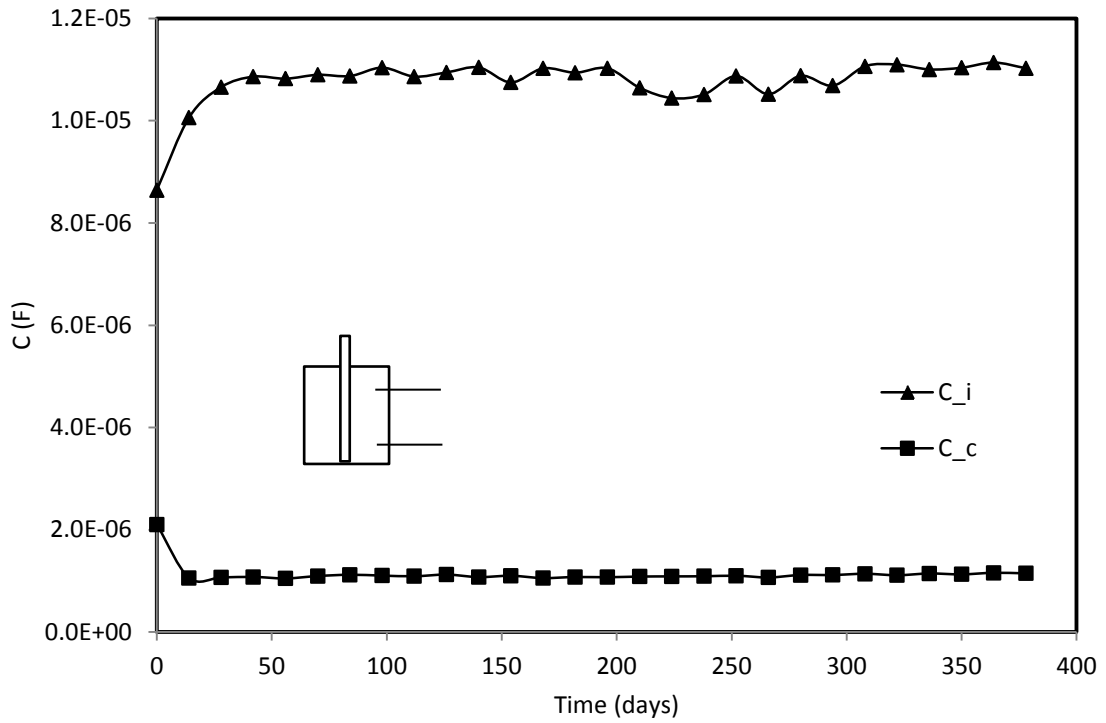


Figure 5.44 Capacitances (C<sub>i</sub> & C<sub>c</sub>) of the non-corroded bar embedded in smart polyester specimen under salt water condition

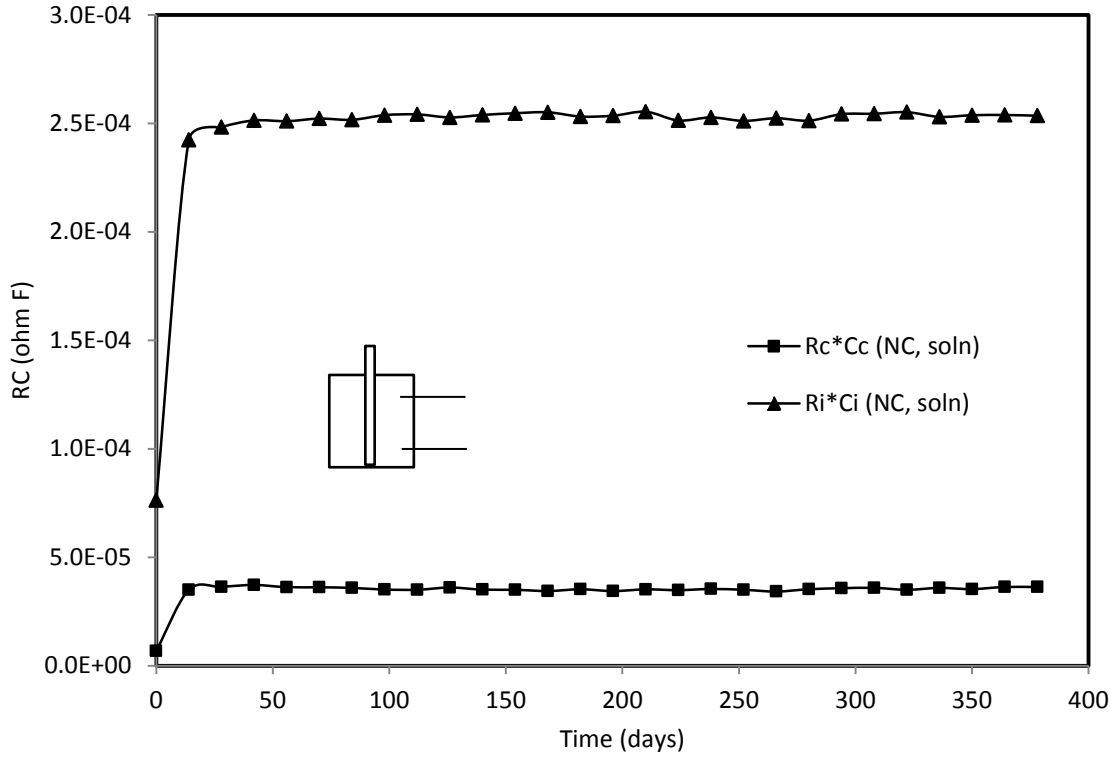


Figure 5.45  $R^*C$  vs. time of the non-corroded bar embedded in smart polyester specimen under salt water condition

The progression of the interface corrosion with respect to time is modeled using equation (5-10) of p-q model and the plot is shown in Figure 5.46. The model parameters p and q are estimated to be 0.0 and 0.0016 respectively. As  $t \rightarrow \infty$ , the corresponding interface corrosion parameter  $RiCi$  is estimated to be  $3.28E-04$  ohm-F using equation (5-11). The initial corrosion parameter was  $(RiCi)_o$  is  $7.63E-05$  ohm-F.

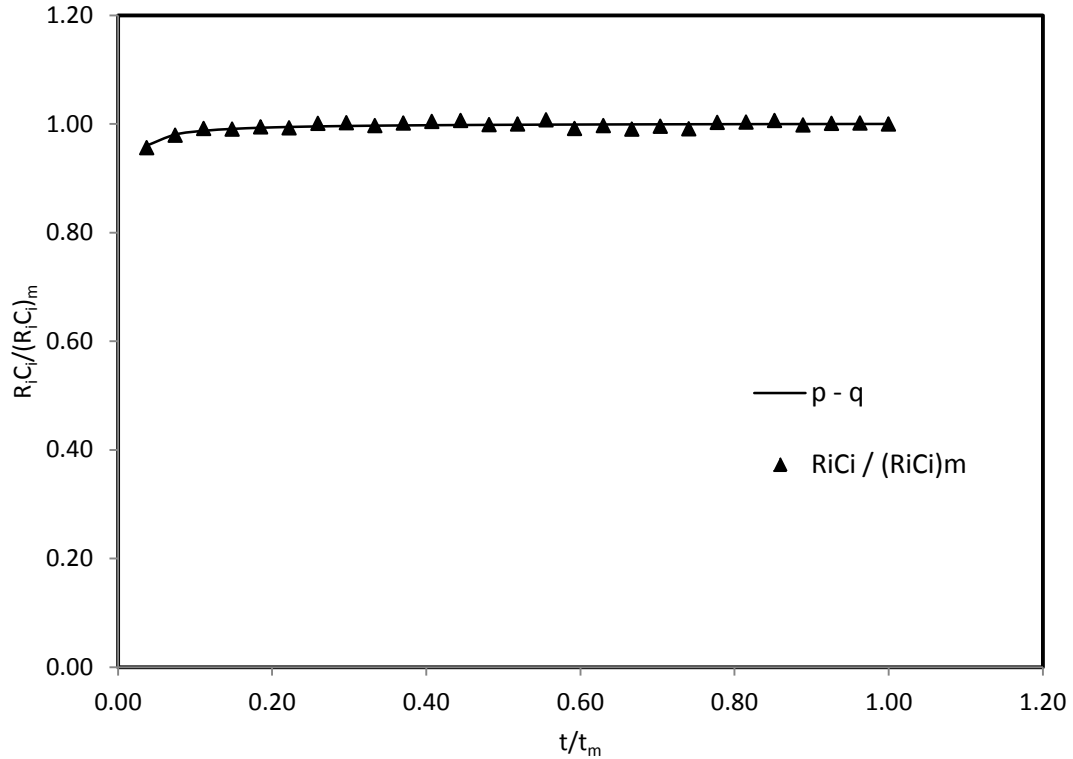


Figure 5.46 Corrosion-time model for non-corroded polyester composite under salt-water condition

#### 5.4.2.2.2 Corroded Polyester Composites

The resistance at the interface ( $R_i$ ) between the corroded bar and the smart polyester specimen immersed in salt water solution and the resistance at the contact ( $R_c$ ) for the measuring time period are shown in Figure 5.47. From the Figure 5.47, it could be observed that the interface resistance ( $R_i$ ) was higher than the contact resistance ( $R_c$ ) during the course of the measuring time period. The higher value of the interface resistance ( $R_i$ ) could be attributed to the fact that the embedded bar was initially corroded and being further corroded because of salt-water solution. Both the interface resistance ( $R_i$ ) and the contact resistance ( $R_c$ ) were increased with respect to time as shown in Figure 5.47.

The capacitance at the interface ( $C_i$ ) between the corroded bar and the smart polyester specimen immersed in salt water solution and the capacitance at the contact ( $C_c$ ) for the measuring time period are shown in Figure 5.48. From the Figure 5.48, it could be observed that the interface capacitance ( $C_i$ ) was higher than the contact capacitance ( $C_c$ ) during the course of the measuring time period. Both the interface capacitance ( $C_i$ ) and the contact capacitance ( $C_c$ ) were increased with respect to time as shown in Figure 5.48.

The material property parameter defined as product of resistance and capacitance,  $R \cdot C$ , for the corroded bar embedded in the smart polyester specimen immersed in salt water solution is shown Figure 5.49. From the Figure 5.49, the interface  $R_i \cdot C_i$  between of the corroded bar and the smart polyester specimen immersed in salt water solution was greater than the  $R_c \cdot C_c$  at the polyester contact for the measuring time period. It can also be observed that both the interface  $R_i \cdot C_i$  and the contact  $R_c \cdot C_c$  were increased with respect to time. Therefore, from Figure 5.47 through Figure 5.49, it could be observed that it was possible to detect and quantify the presence of the corrosion in corroded bar embedded in the smart polyester specimen immersed in salt water solution.

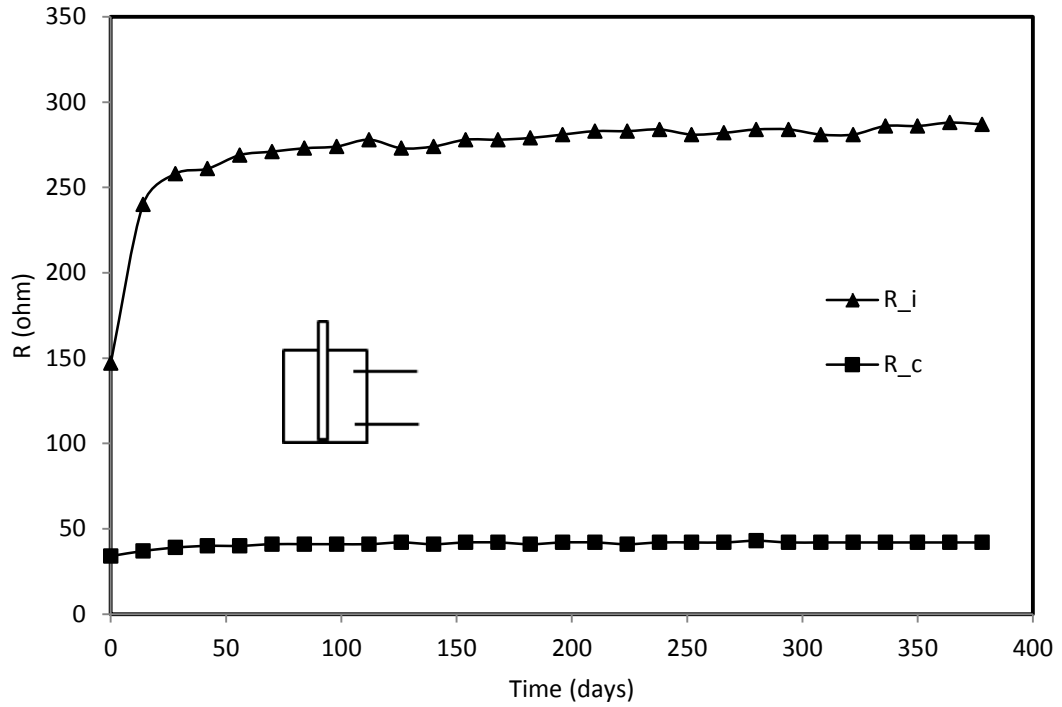


Figure 5.47 Resistances ( $R_i$  &  $R_c$ ) of the corroded bar embedded in smart polyester specimen under salt water condition

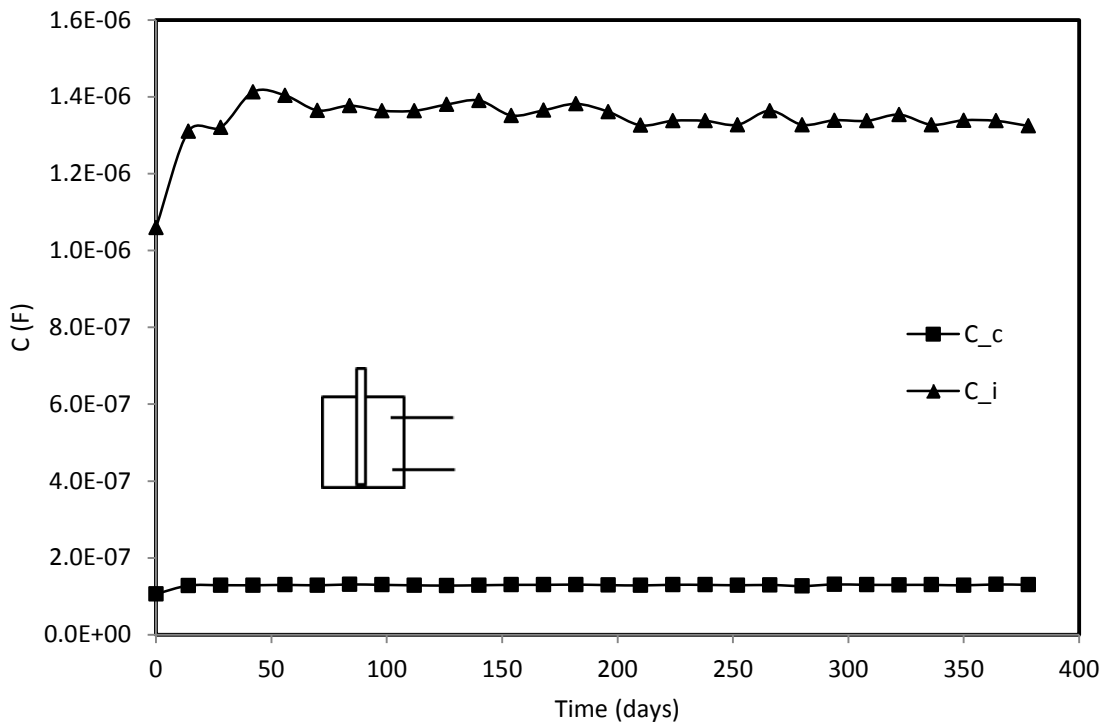


Figure 5.48 Capacitances ( $C_i$  &  $C_c$ ) of the corroded bar embedded in smart polyester specimen under salt water condition

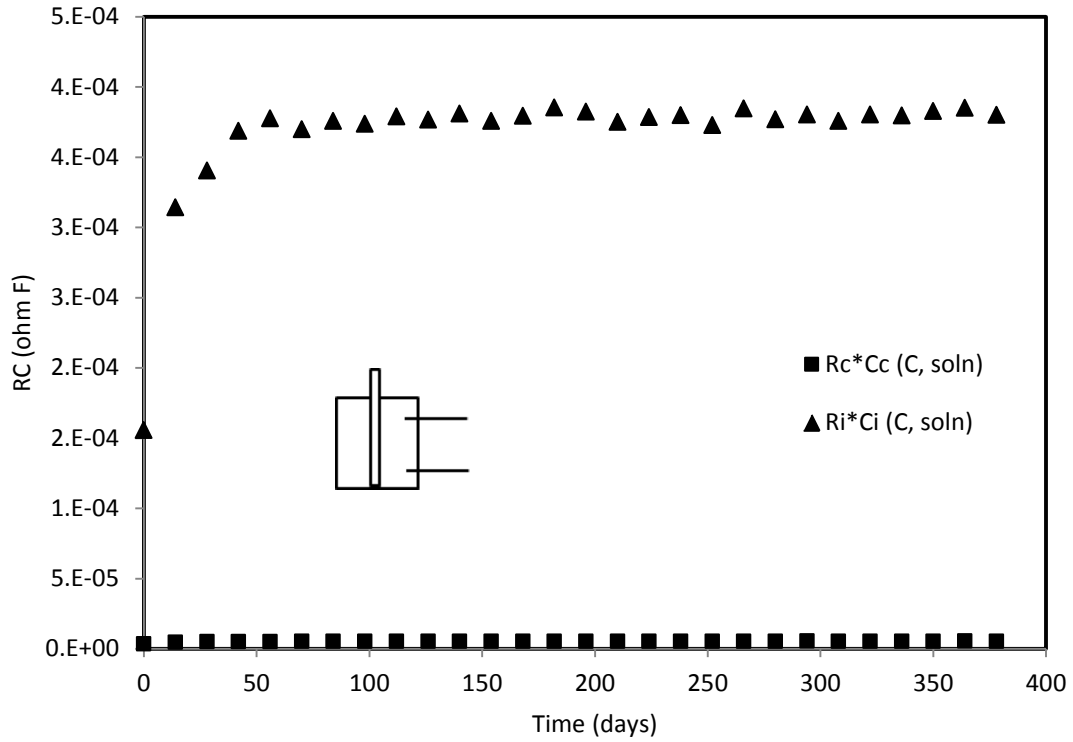


Figure 5.49  $R^*C$  vs. time of the corroded bar embedded in smart polyester specimen under salt water condition

The progression of the interface corrosion with respect to time is modeled using equation (5-10) of p-q model and the plot is shown in Figure 5.50. The model parameters p and q are estimated to be 0.00054 and 0.0012 respectively. As  $t \rightarrow \infty$ , the corresponding interface corrosion parameter  $RiCi$  is estimated to be  $5.28E-04$  ohm-F using equation (5-11). The initial corrosion parameter was  $(RiCi)_0$  is  $1.54E-04$  ohm-F.

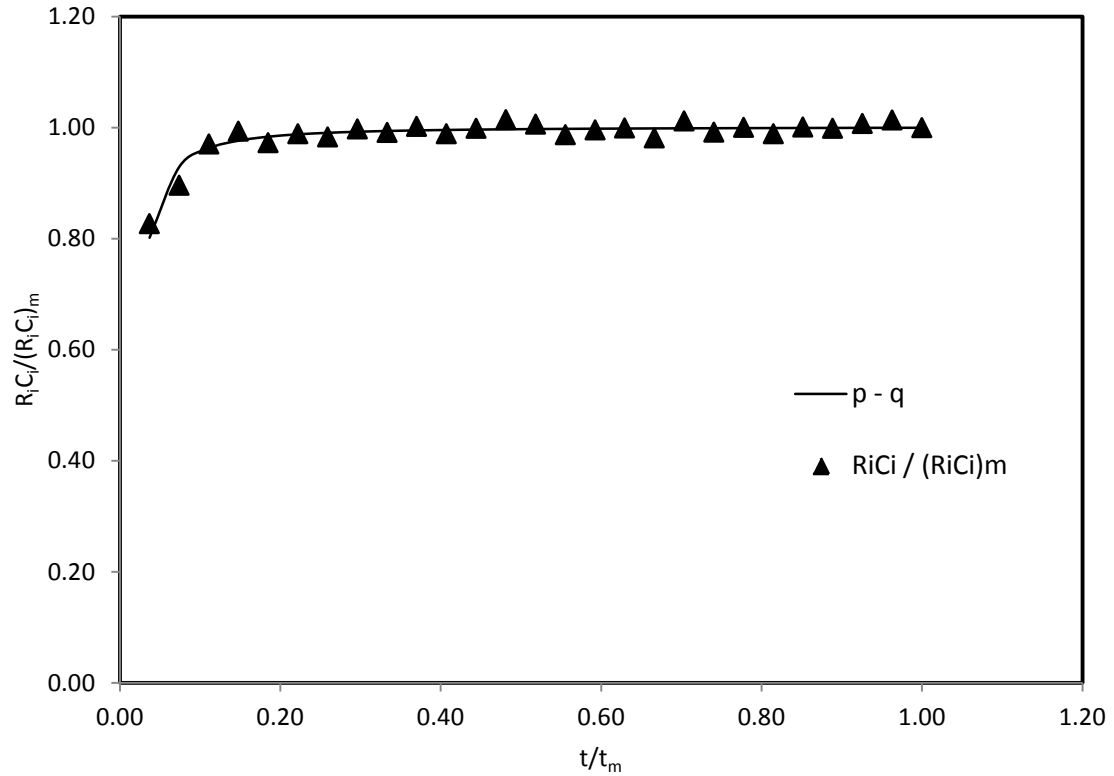


Figure 5.50 Corrosion-time model for corroded polyester composite under salt-water condition

### 5.4.3 Steel-Polymer Concrete Characterization

#### 5.4.3.1 Under Dry-Air Condition

The electrical resistances and capacitance of the polymer concrete, bar, and transitional contact surface between the polymer concrete and bar were measured with impedance analyzer precision LCR meter. The impedance measurements were performed on a weekly basis for about a year. The frequency range used in the measurements was from 20 Hz to 300 kHz. For 5<sup>th</sup> week test, a typical Bode plot of impedance vs frequency for non-corroded bar embedded in smart polymer concrete specimen is shown in Figure

5.51. For 5th week test, a typical Bode plot of impedance vs frequency for corroded bar embedded in smart polymer concrete specimen is shown in Figure 5.52.

The Bode plot of the adopted equivalent circuit for non-corroded and corroded composite specimens is shown in Figure 5.53. As the Figure 5.53 shown, the impedance of the corroded composite specimen was higher than that of non-corroded composite specimen, and therefore it was possible to detect the presence of the corrosion.

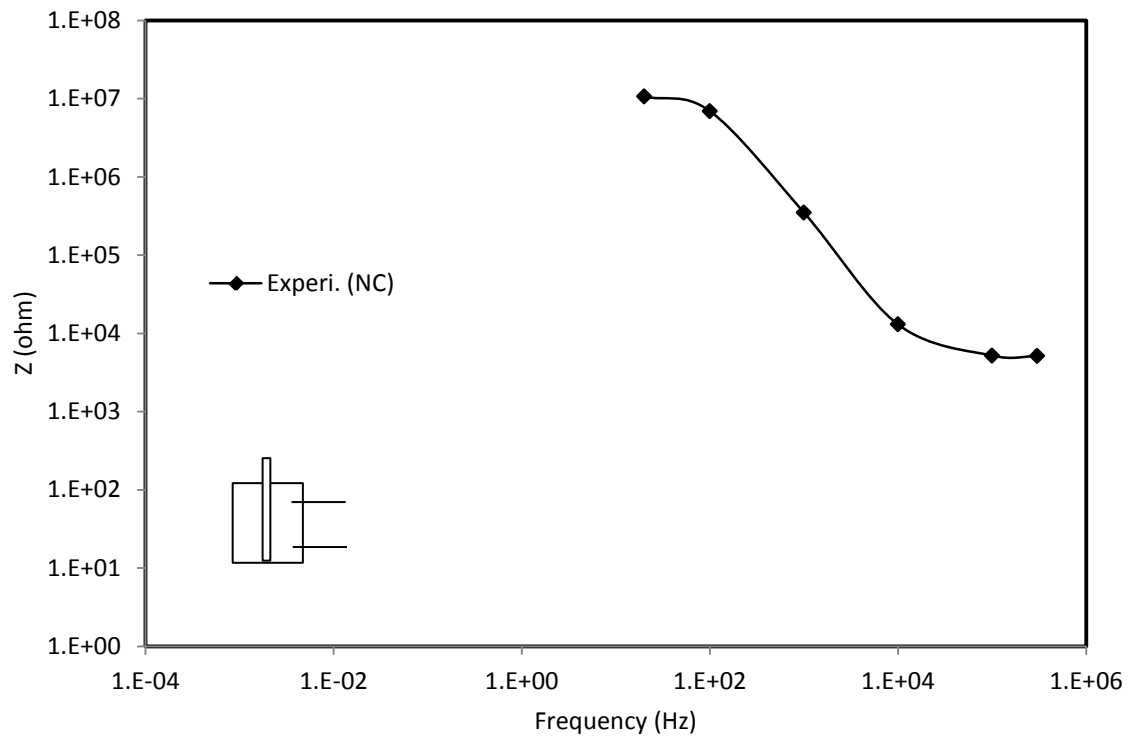


Figure 5.51 Bode plot of polymer concrete composite with embedded non-corroded bar

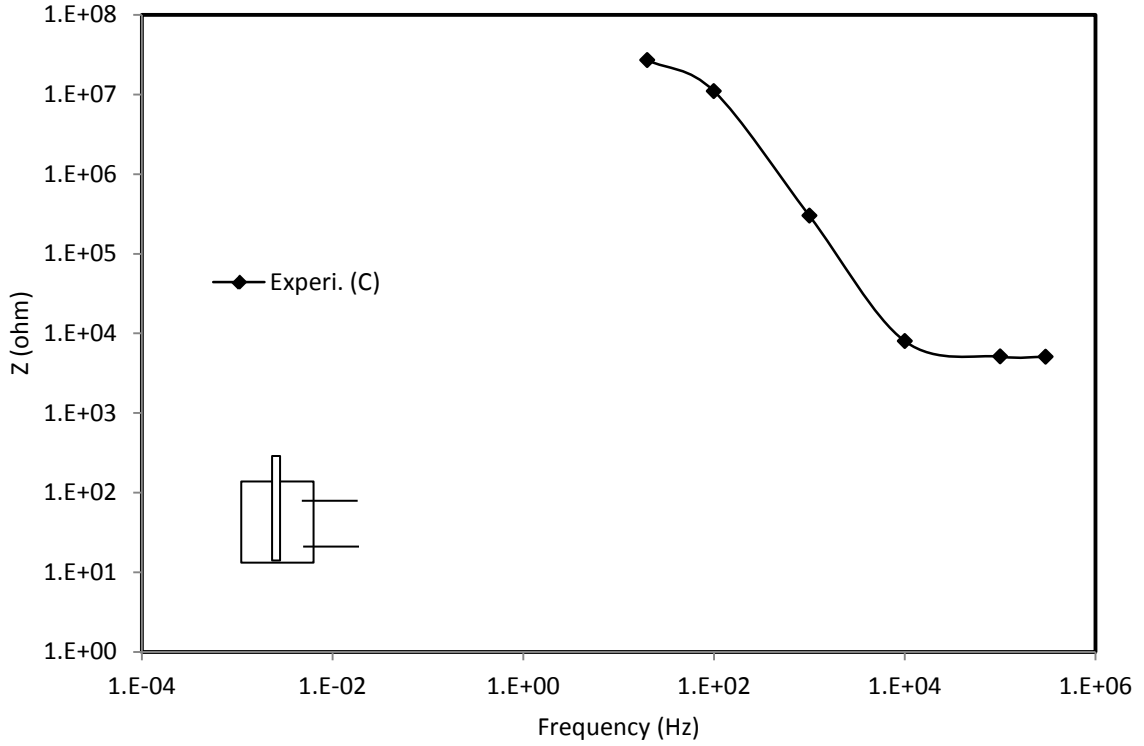


Figure 5.52 Bode plot of polymer concrete composite with embedded corroded bar

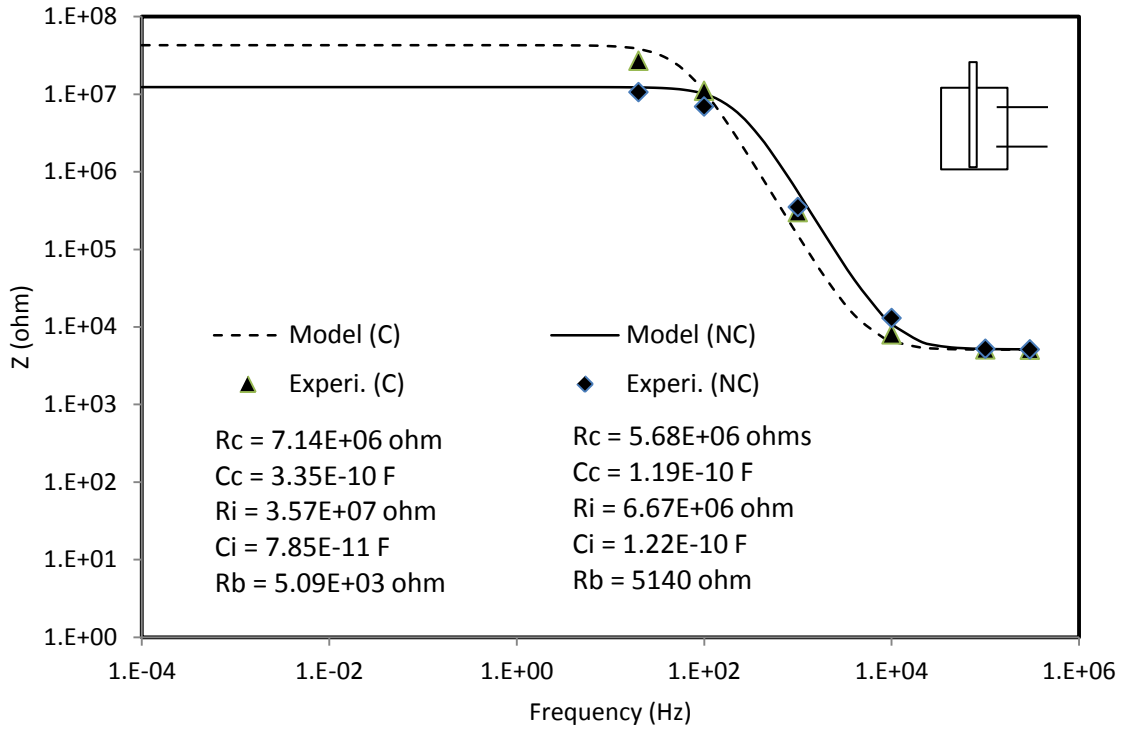


Figure 5.53 Bode plot of polymer concrete composites with embedded non-corroded and corroded bar along respective impedance models

#### 5.4.3.1.1 Non-Corroded Polymer Concrete Composites

The resistance at the interface ( $R_i$ ) between non-corroded bar and the smart polymer concrete and the resistance at the contact ( $R_c$ ) for the measuring time period are shown in Figure 5.54. From Figure 5.54, it could be observed that the interface resistance ( $R_i$ ) was higher than the contact resistance ( $R_c$ ) during the course of the measuring time period. Both the interface resistance ( $R_i$ ) and the contact resistance ( $R_c$ ) generally remained in constant at about 25 ohm with respect to time as shown in Figure 5.54.

The capacitance at the interface ( $C_i$ ) between non-corroded bar and the smart polymer concrete and the capacitance at the contact ( $C_c$ ) for the measuring time period are shown in Figure 5.55. From Figure 5.55 it could be observed that the interface capacitance ( $C_i$ ) was lower than the contact capacitance ( $C_c$ ) during the course of the measuring time period. Both the interface capacitance ( $C_i$ ) and the contact capacitance ( $C_c$ ) generally remained constant with respect to time as shown in Figure 5.55.

The material property parameter defined as product of resistance and capacitance,  $R*C$ , for the non-corroded bar embedded in the smart polymer concrete is shown in Figure 5.56. From Figure 5.56, the interface  $R_i*C_i$  between of the non-corroded bar and the smart polymer concrete was lower than the  $R_c*C_c$  at the polymer concrete contact for the measuring time period. It can also be observed that both the interface  $R_i*C_i$  and the contact  $R_c*C_c$  generally remained constant with respect to time. This could be attributed to the dry air condition in which the specimens where kept. The value of  $R_i*C_i$  was between  $6.16E-5$  ohm-F and  $6.49E-5$  ohm-F. These values are less than  $1.87E-4$  ohm-F which corresponds to that of non-corroded steel bar as discussed in section 5.2. Therefore, from Figure 5.54 through Figure 5.56, it could be observed that it was possible

to detect and quantify the small presence of interface corrosion in the non-corroded bar embedded in the smart polymer concrete.

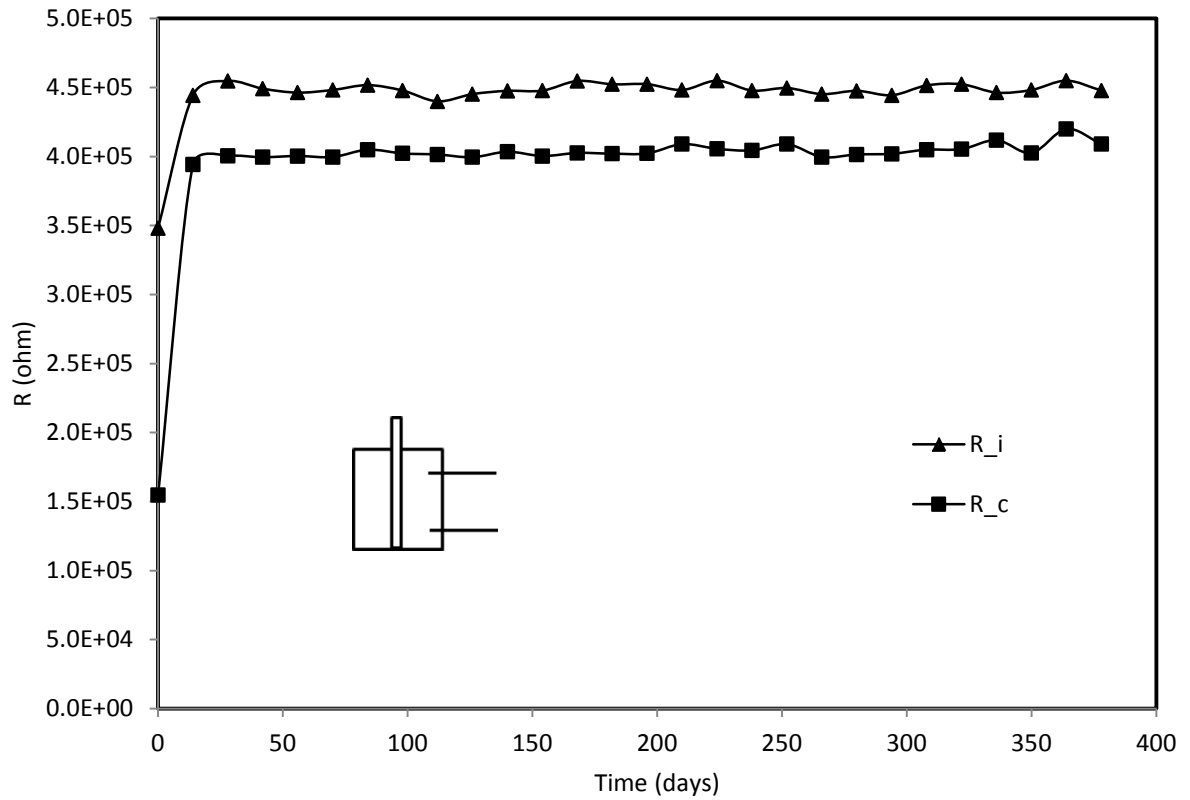


Figure 5.54 Resistances ( $R_i$  &  $R_c$ ) of the non-corroded bar embedded in smart polymer concrete under air dry condition

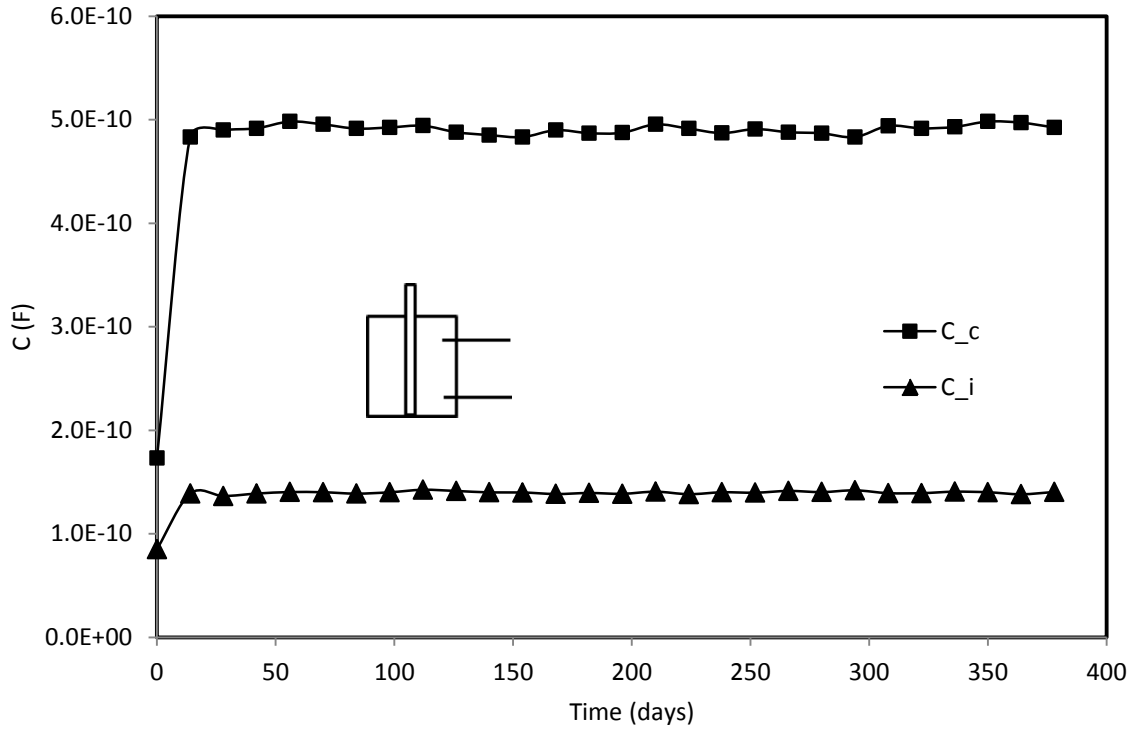


Figure 5.55 Capacitances ( $C_i$  &  $C_c$ ) of the non-corroded bar embedded in smart polymer concrete in air dry condition

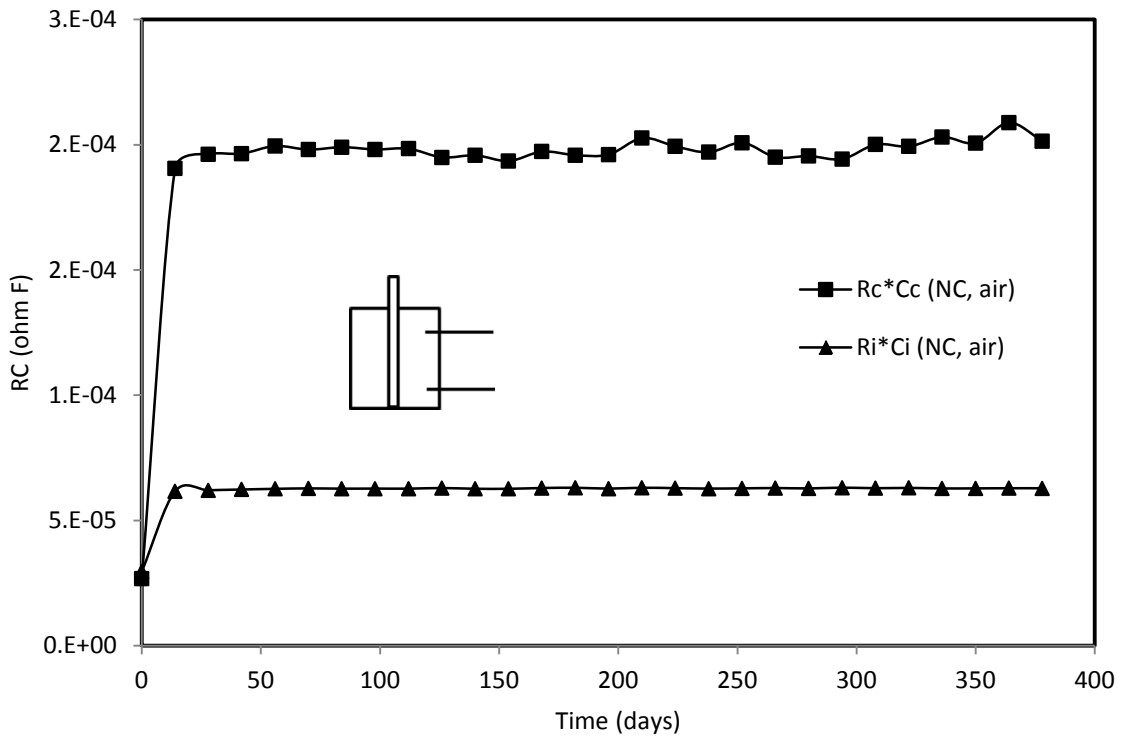


Figure 5.56  $R \cdot C$  vs. time of the non-corroded bar embedded in smart polymer concrete in air dry condition

The progression of the interface corrosion with respect to time is modeled using equation (5-10) of p-q model and the plot is shown in Figure 5.57 The model parameters p and q are estimated to be 0.0 and 0.001 respectively. As  $t \rightarrow \infty$ , the corresponding interface corrosion parameter  $R_i C_i$  is estimated to be  $9.25E-05$  ohm-F using equation (5-11). The initial corrosion parameter was  $(R_i C_i)_o$  is  $2.96E-05$  ohm-F.

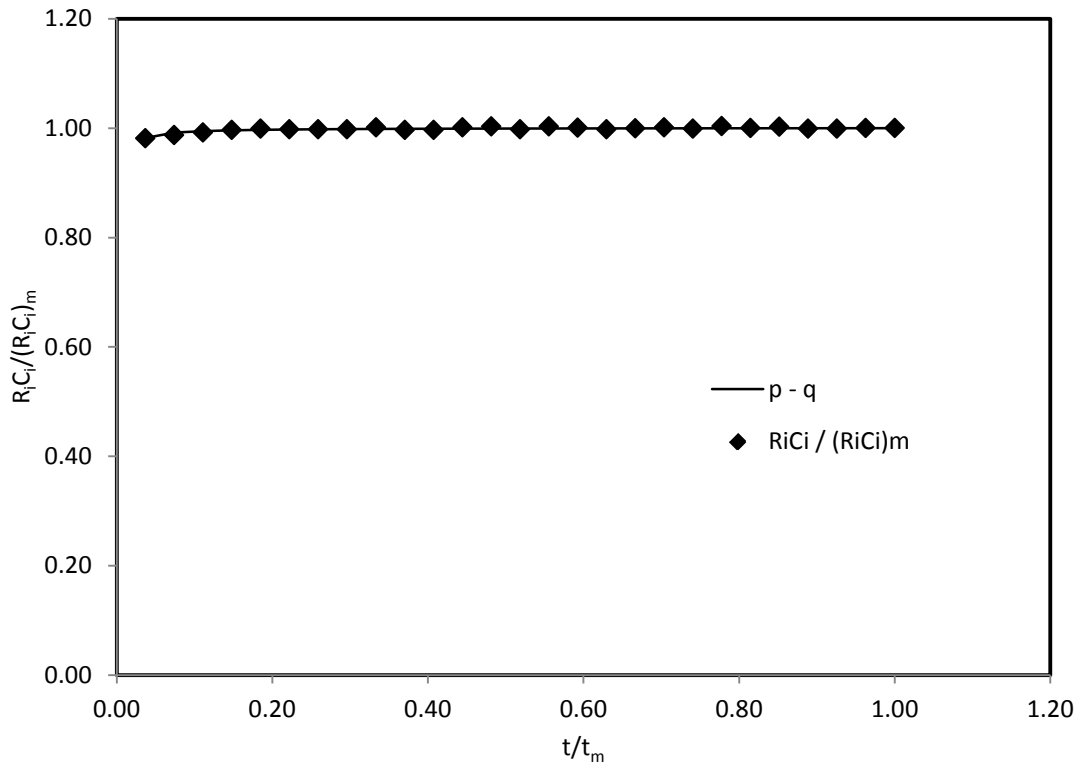


Figure 5.57 Corrosion-time model for non-corroded polymer concrete composite under dry condition

#### 5.4.3.1.2 Corroded Polymer Concrete Composites

The resistance at the interface ( $R_i$ ) between corroded bar and the smart polymer concrete specimen under dry air condition and the resistance at the contact ( $R_c$ ) for the

measuring time period are shown in Figure 5.58. From the Figure 5.58, it could be observed that the interface resistance ( $R_i$ ) was higher than the contact resistance ( $R_c$ ) during the course of the measuring time period. The higher value of the interface resistance ( $R_i$ ) could be attributed to the fact that the embedded bar was initially corroded. Both the interface resistance ( $R_i$ ) and the contact resistance ( $R_c$ ) were increased with respect to time as shown in Figure 5.58.

The capacitance at the interface ( $C_i$ ) between corroded bar and the smart polymer concrete specimen under dry air condition and the capacitance at the contact ( $C_c$ ) for the measuring time period are shown in Figure 5.59. From the Figure 5.59, it could be observed that the interface capacitance ( $C_i$ ) was lower than the contact capacitance ( $C_c$ ) during the course of the measuring time period. Both the interface capacitance ( $C_i$ ) and the contact capacitance ( $C_c$ ) were increased with respect to time as shown in Figure 5.59.

The material property parameter defined as product of resistance and capacitance,  $R*C$ , for the corroded bar embedded in the smart polymer concrete specimen under dry air condition is shown Figure 5.60. From the Figure 5.60, the interface  $R_i*C_i$  between of the corroded bar and the smart polymer concrete was greater than the  $R_c*C_c$  at the polymer concrete contact for the measuring time period. It can also be observed that both the interface  $R_i*C_i$  and the contact  $R_c*C_c$  generally remained constant with respect to time. This could be attributed to the dry air condition in which the specimens were kept. The value of  $R_i*C_i$  had between  $4.95E-4$  ohm-F and  $5.14E-4$  ohm-F. These values are greater than  $1.87E-4$  ohm-F which corresponds to that of non-corroded steel bar as discussed in section 5.2. Therefore, from Figure 5.58 through Figure 5.60, it could be

observed that it was possible to detect and quantify the presence of interface corrosion in the corroded bar embedded in the smart polymer concrete under dry air condition.

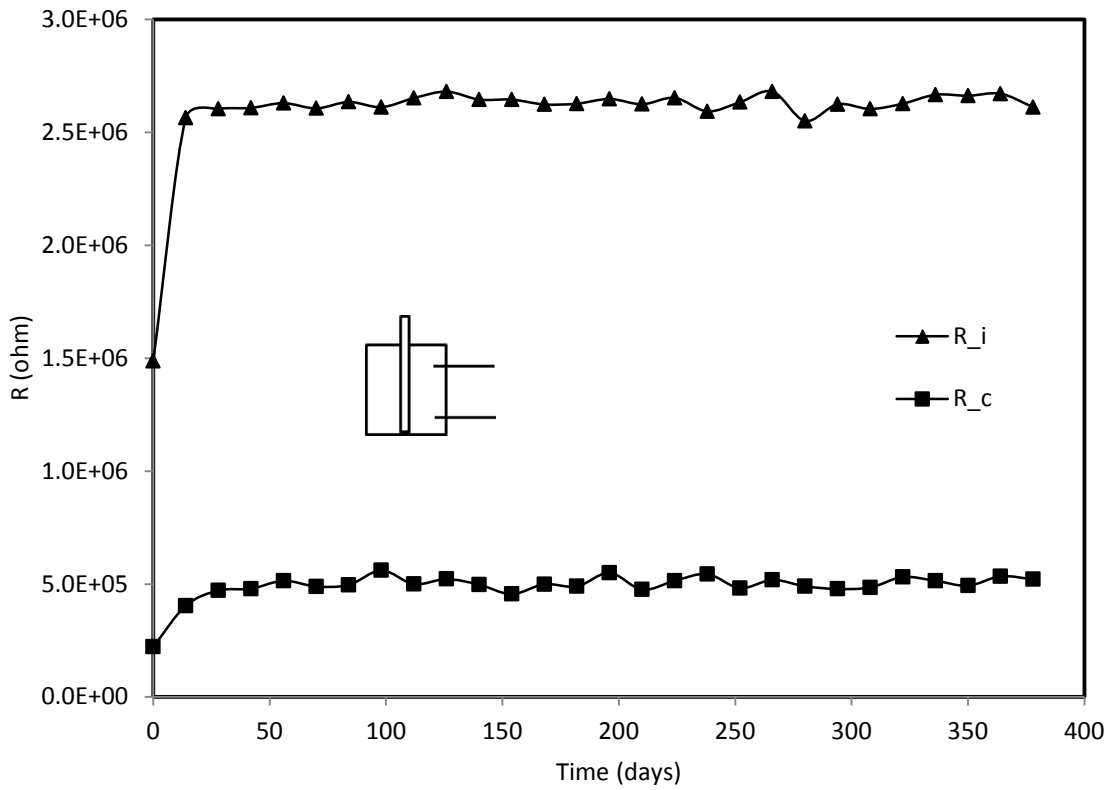


Figure 5.58 Resistances ( $R_i$  &  $R_c$ ) of the corroded bar embedded in smart polymer concrete under air dry condition

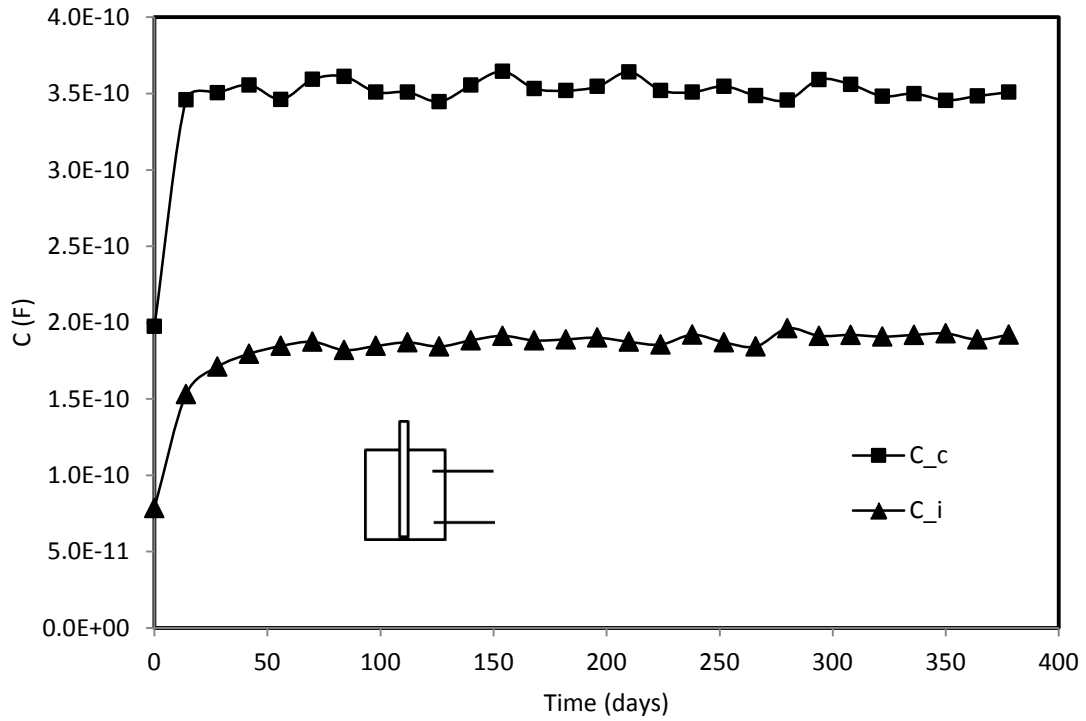


Figure 5.59 Capacitances ( $C_i$  &  $C_c$ ) of the corroded bar embedded in smart polymer concrete in air dry condition

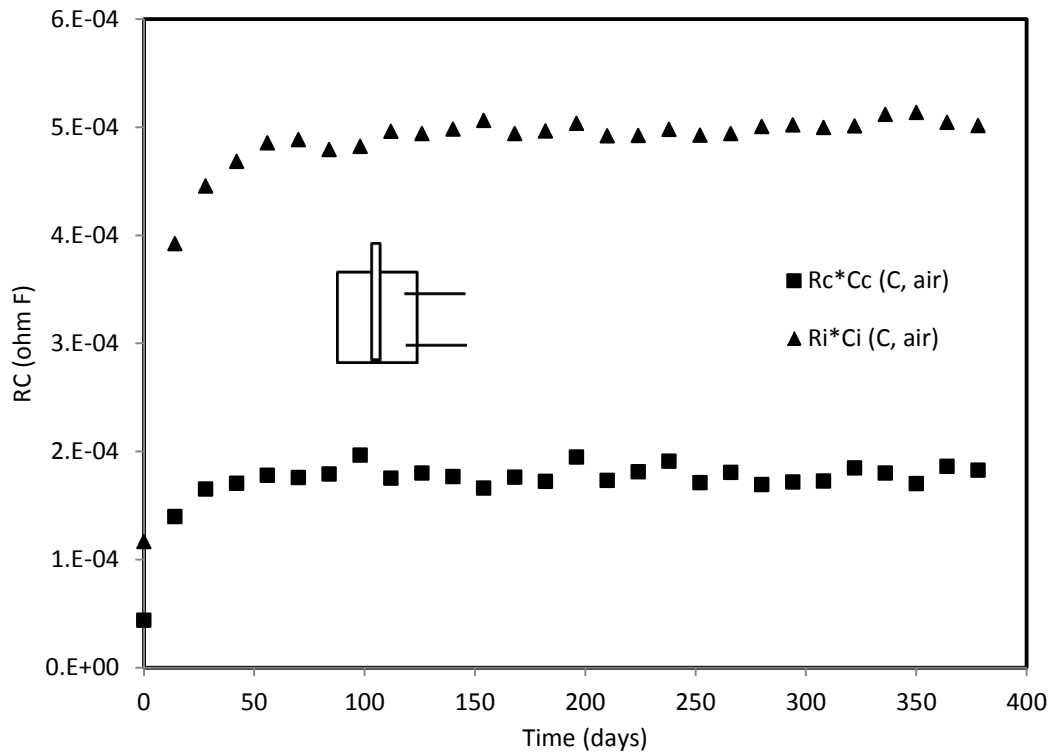


Figure 5.60  $R \cdot C$  vs. time of the corroded bar embedded in smart polymer concrete in air dry condition

The progression of the interface corrosion with respect to time is modeled using equation (5-10) of p-q model and the plot is shown in Figure 5.61 The model parameters p and q are estimated to be 0.0 and 0.0012 respectively. As  $t \rightarrow \infty$ , the corresponding interface corrosion parameter  $R_i C_i$  is estimated to be  $6.23E-04$  ohm-F using equation (5-11). The initial corrosion parameter was  $(R_i C_i)_o$  is  $1.17E-04$  ohm-F.

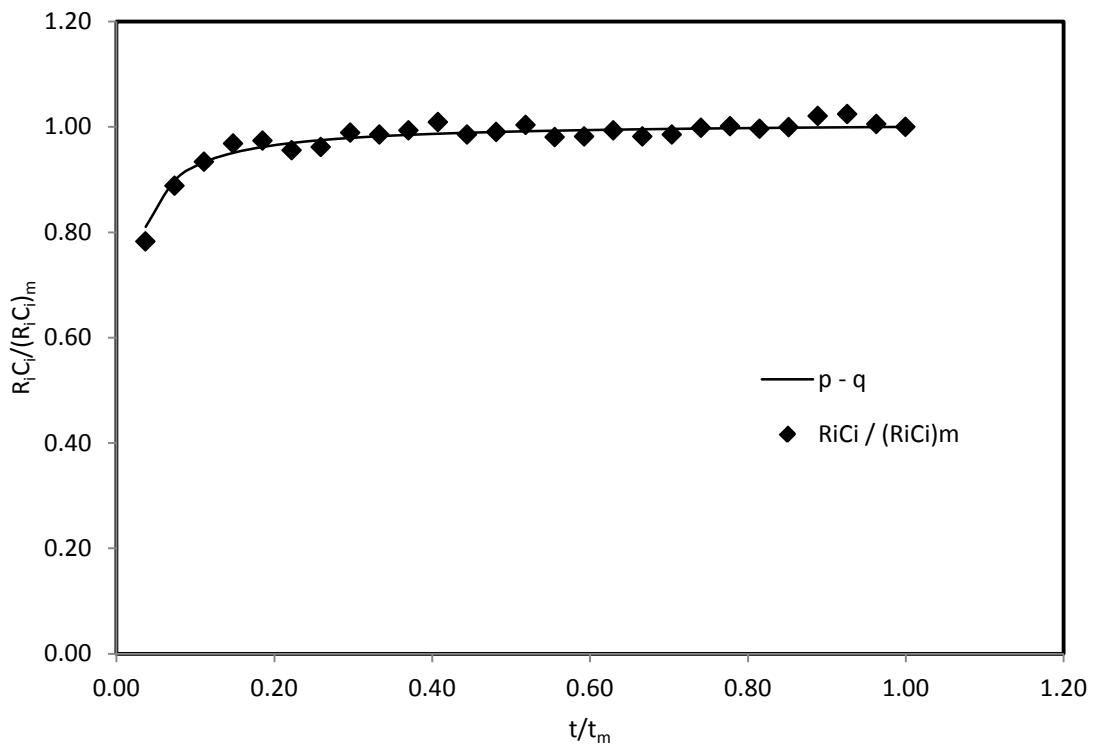


Figure 5.61 Corrosion-time model for corroded polymer concrete composite under dry condition

#### 5.4.3.2 Under Salt-Water Solution

Another set of specimens was immersed in a salt (3.5% wt.) water solution continually for about a year. The impedance measurements were performed on a weekly

basis for about a year. The frequency range used was from 20 Hz to 300 kHz. For 5<sup>th</sup> week test, a typical Bode plot of impedance vs frequency for non-corroded bar embedded in smart polymer concrete specimen is shown in Figure 5.62. For 5<sup>th</sup> week test, a typical Bode plot of impedance vs frequency for corroded bar embedded in smart polymer concrete specimen is shown in Figure 5.63.

The Bode plot of the adopted equivalent circuit for non-corroded and corroded composite specimens is shown in Figure 5.64. As the Figure 5.64 shown, the impedance of the corroded composite specimen was higher than that of non-corroded composite specimen, and therefore it was possible to detect the presence of the corrosion.

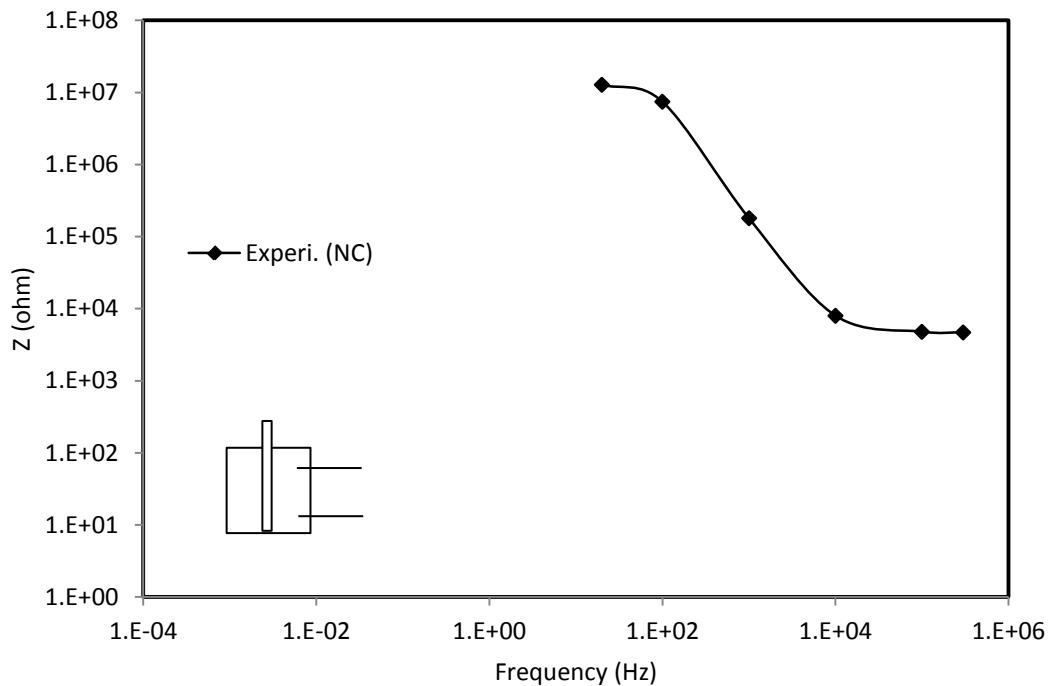


Figure 5.62 Bode plot of polymer concrete composite with embedded non-corroded bar after immersed in salt-solution water for 5 weeks

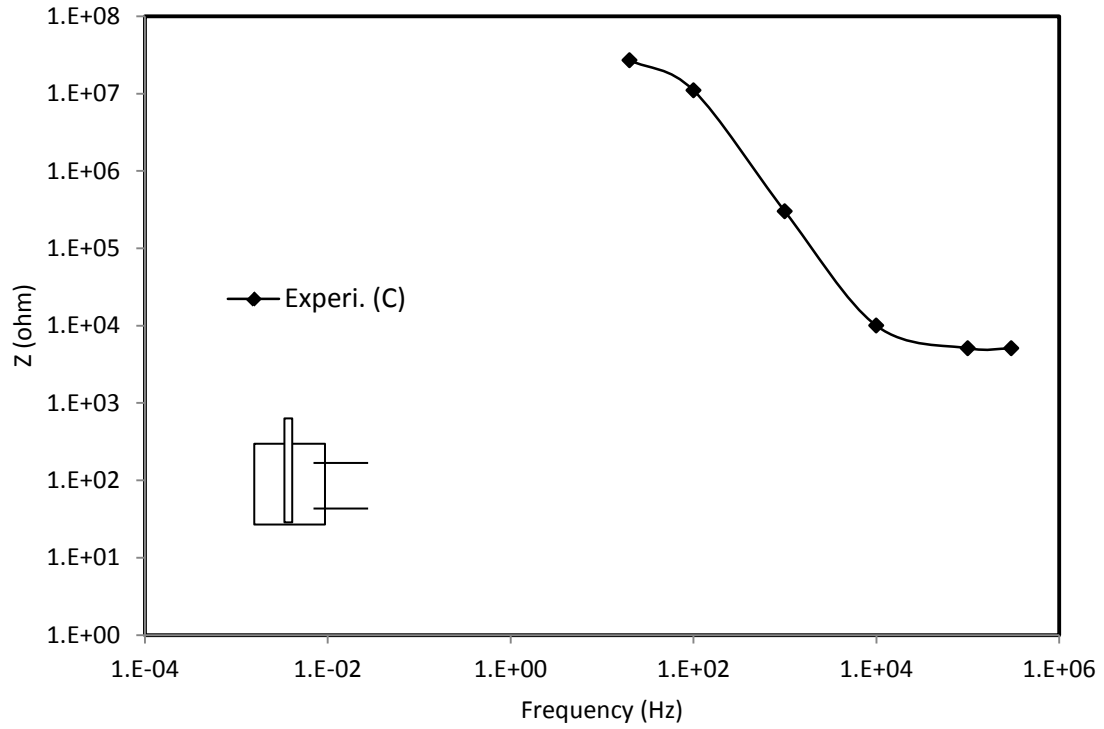


Figure 5.63 Bode plot of polymer concrete composite with embedded corroded bar after immersed in salt-solution water for 5 weeks

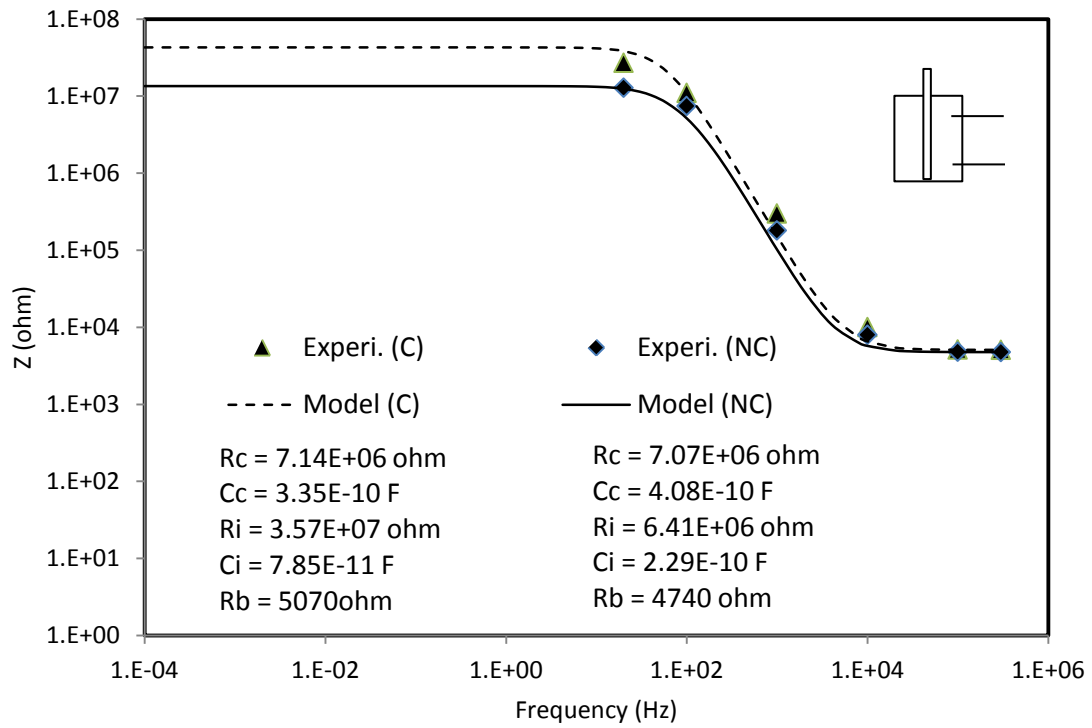


Figure 5.64 Bode plot of polymer concrete composite with embedded non-corroded and corroded bars with models after immersed in salt-water for 5 weeks

#### 5.4.3.2.1 Non-Corroded Polymer Concrete Composites

The resistance at the interface ( $R_i$ ) between the non-corroded bar and the smart polymer concrete specimen immersed in salt water solution and the resistance at the contact ( $R_c$ ) for the measuring time period are shown in Figure 5.65. From the Figure 5.65, it could be observed that the interface resistance ( $R_i$ ) was higher than the contact resistance ( $R_c$ ) and was gradually increasing in its value during the course of the measuring time period. Both the interface resistance ( $R_i$ ) and the contact resistance ( $R_c$ ) were increased with respect to time as shown in Figure 5.65.

The capacitance at the interface ( $C_i$ ) between the non-corroded bar and the smart polymer concrete specimen immersed in salt water solution and the capacitance at the contact ( $C_c$ ) for the measuring time period are shown in Figure 5.66. From the Figure 5.66, it could be observed that the interface capacitance ( $C_i$ ) was lower than the contact capacitance ( $C_c$ ) during the course of the measuring time period. Both the interface capacitance ( $C_i$ ) and the contact capacitance ( $C_c$ ) were increased with respect to time as shown in Figure 5.66.

The material property parameter defined as product of resistance and capacitance,  $R \cdot C$ , for the non-corroded bar embedded in the smart polymer concrete specimen immersed in salt water solution is shown Figure 5.67. From the Figure 5.67, the interface  $R_i \cdot C_i$  between of the non-corroded bar and the smart polymer concrete specimen immersed in salt water solution was greater than the  $R_c \cdot C_c$  at the polymer concrete contact for the measuring time period. It can also be observed that both the interface  $R_i \cdot C_i$  gradually increased while the contact  $R_c \cdot C_c$  generally remained constant with respect to time. The value of  $R_i \cdot C_i$  was increasing from  $6.28E-5$  ohm-F to  $7.34E-5$  ohm-

F. These values are greater than  $1.87E-4$  ohm-F which corresponds to that of non-corroded steel bar as discussed in section 5.2. Therefore, from Figure 5.65 through Figure 5.67, it could be observed that it was possible to detect and quantify the small initiation of interface corrosion in the non-corroded bar embedded in the smart polymer concrete.

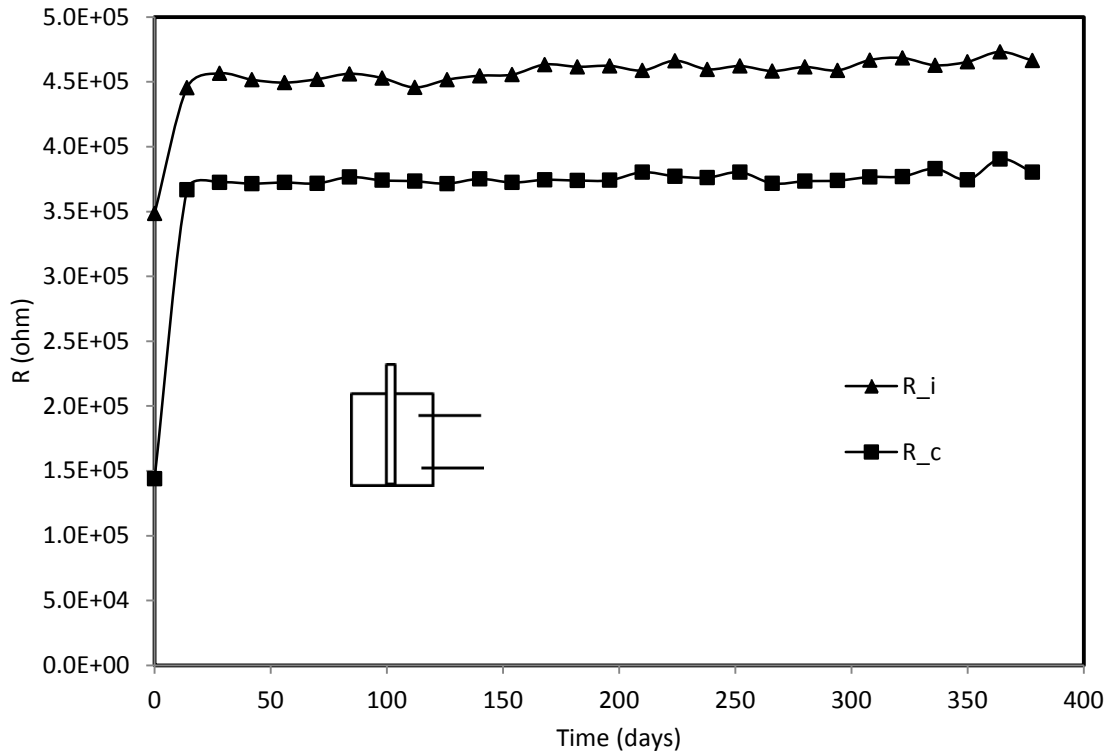


Figure 5.65 Resistances ( $R_i$  &  $R_c$ ) of the non-corroded bar embedded in smart polymer concrete specimen under salt water condition

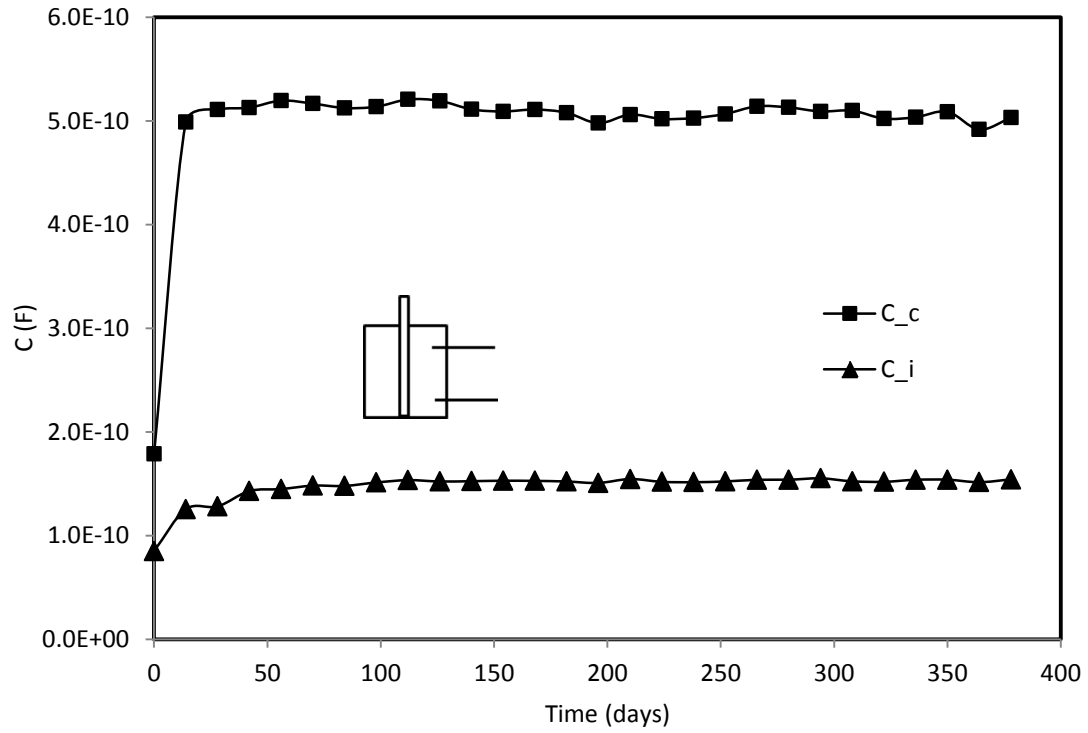


Figure 5.66 Capacitances ( $C_i$  &  $C_c$ ) of the non-corroded bar embedded in smart polymer concrete specimen under salt water condition

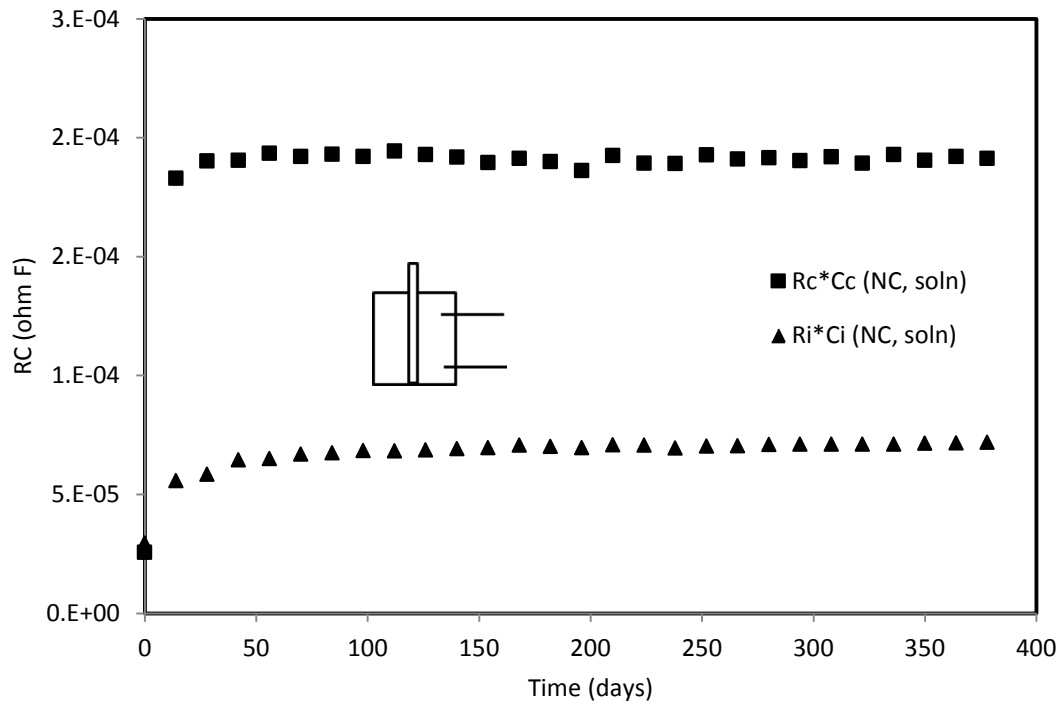


Figure 5.67  $R \cdot C$  vs. time of the non-corroded bar embedded in smart polymer concrete specimen under salt water condition

The progression of the interface corrosion with respect to time is modeled using equation (5-10) of p-q model and the plot is shown in Figure 5.68 The model parameters p and q are estimated to be 0.0 and 0.014 respectively. As  $t \rightarrow \infty$ , the corresponding interface corrosion parameter  $R_i C_i$  is estimated to be  $1.02E-04$  ohm-F using equation (5-11). The initial corrosion parameter was  $(R_i C_i)_o$  is  $2.96E-05$  ohm-F.

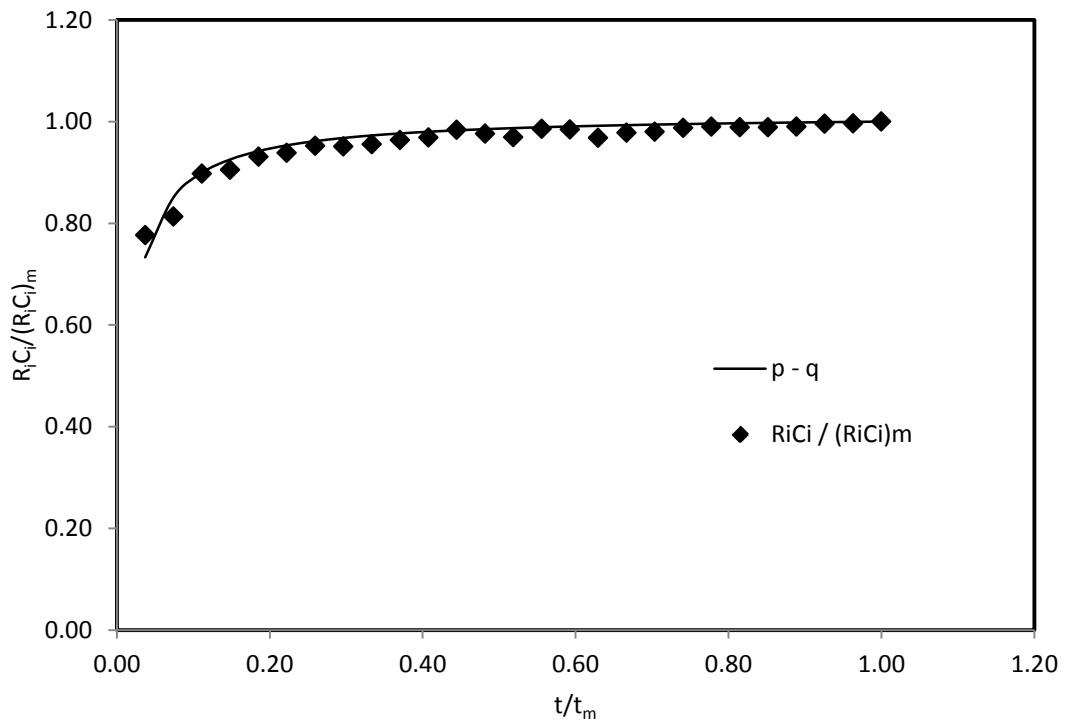


Figure 5.68 Corrosion-time model for non-corroded polymer concrete composite under salt-water condition

#### 5.4.3.2.2 Corroded Polymer Concrete Composites

The resistance at the interface ( $R_i$ ) between the corroded bar and the smart polymer concrete specimen immersed in salt water solution and the resistance at the contact ( $R_c$ ) for the measuring time period are shown in Figure 5.69. From the Figure

5.69, it could be observed that the interface resistance ( $R_i$ ) was higher than the contact resistance ( $R_c$ ) and was increasing in its value during the course of the measuring time period. The higher value of the interface resistance ( $R_i$ ) could be attributed to the fact that the embedded bar was initially corroded and being further corroded because of salt-water solution. Both the interface resistance ( $R_i$ ) and the contact resistance ( $R_c$ ) were increased with respect to time as shown in Figure 5.69.

The capacitance at the interface ( $C_i$ ) between the corroded bar and the smart polymer concrete specimen immersed in salt water solution and the capacitance at the contact ( $C_c$ ) for the measuring time period are shown in Figure 5.70. From the Figure 5.70, it could be observed that the interface capacitance ( $C_i$ ) was lower than the contact capacitance ( $C_c$ ) during the course of the measuring time period. Both the interface capacitance ( $C_i$ ) and the contact capacitance ( $C_c$ ) were increased with respect to time as shown in Figure 5.70.

The material property parameter defined as product of resistance and capacitance,  $R \cdot C$ , for the corroded bar embedded in the smart polymer concrete specimen immersed in salt water solution is shown Figure 5.71. From the Figure 5.71, the interface  $R_i \cdot C_i$  between of the corroded bar and the smart polymer concrete specimen immersed in salt water solution was greater than the  $R_c \cdot C_c$  at the polymer concrete contact for the measuring time period. It can also be observed that both the interface  $R_i \cdot C_i$  was increasing while the contact  $R_c \cdot C_c$  generally remained constant with respect to time. The value of  $R_i \cdot C_i$  was increasing from  $5.05E-4$  ohm-F to  $5.86E-5$  ohm-F. These values are greater than  $1.87E-4$  ohm-F which corresponds to that of non-corroded steel bar as discussed in section 5.2. Therefore, from Figure 5.69 through Figure 5.71, it could be

observed that it was possible to detect and quantify the presence and progression of the corrosion in corroded bar embedded in the smart polymer concrete specimen immersed in salt water solution.

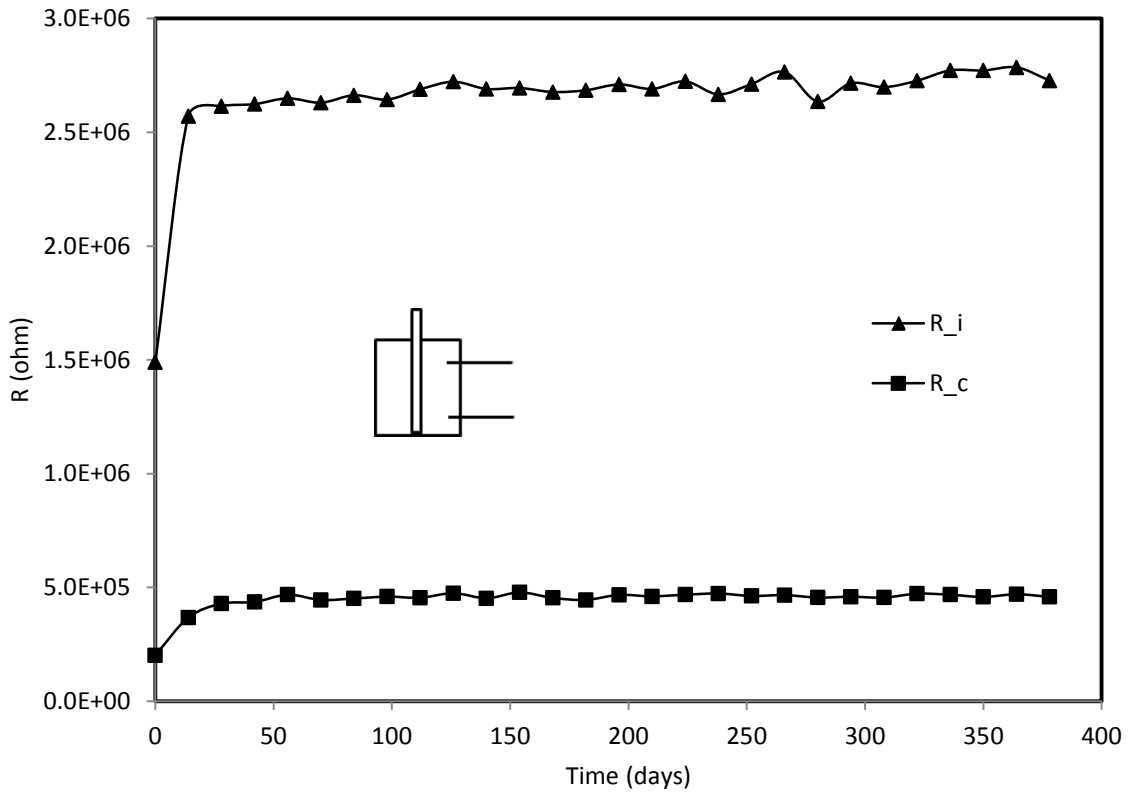


Figure 5.69 Resistances ( $R_i$  &  $R_c$ ) of the corroded bar embedded in smart polymer concrete specimen under salt water condition

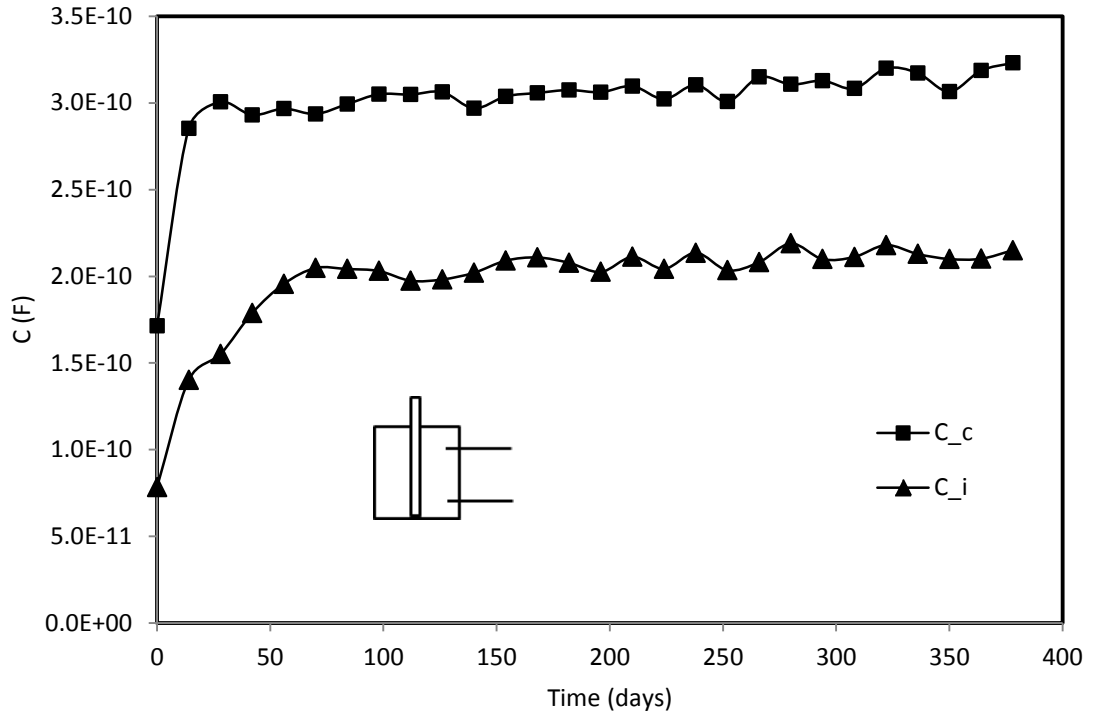


Figure 5.70 Capacitances ( $C_i$  &  $C_c$ ) of the corroded bar embedded in smart polymer concrete specimen under salt water condition

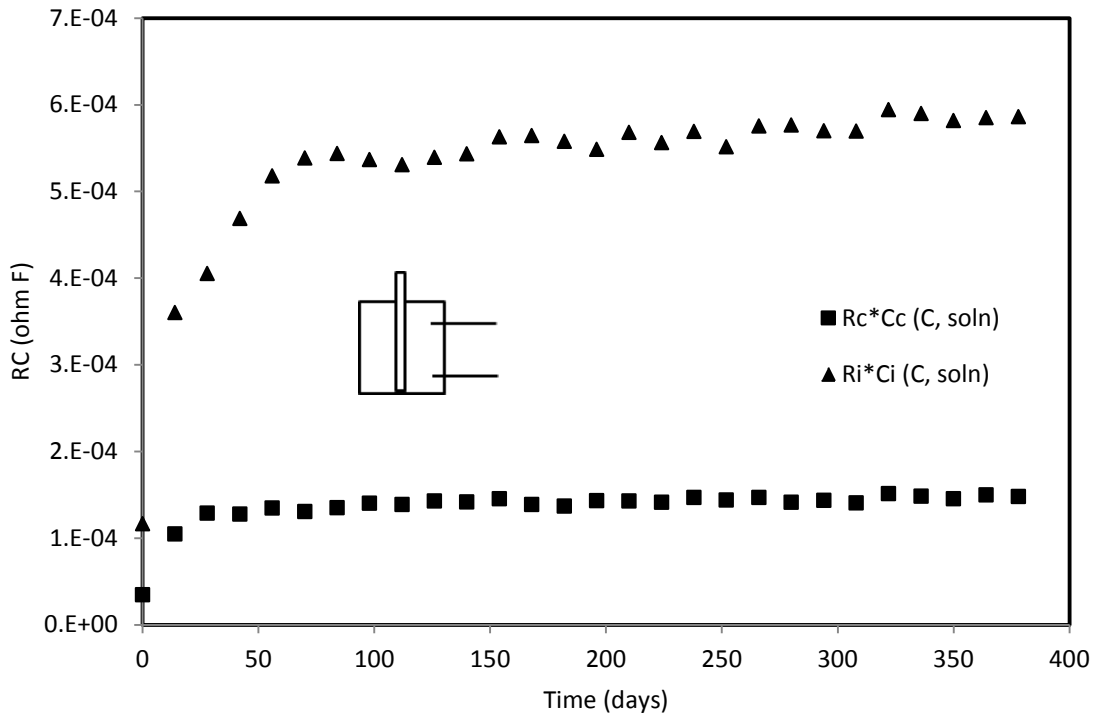


Figure 5.71  $R \cdot C$  vs. time of the corroded bar embedded in smart polymer concrete specimen under salt water condition

The progression of the interface corrosion with respect to time is modeled using equation (5-10) of p-q model and the plot is shown in Figure 5.72. The model parameters p and q are estimated to be 0.0 and 0.025 respectively. As  $t \rightarrow \infty$ , the corresponding interface corrosion parameter  $R_i C_i$  is estimated to be  $7.12E-04$  ohm-F using equation (5-11). The initial corrosion parameter was  $(R_i C_i)_o$  is  $1.17E-04$  ohm-F.

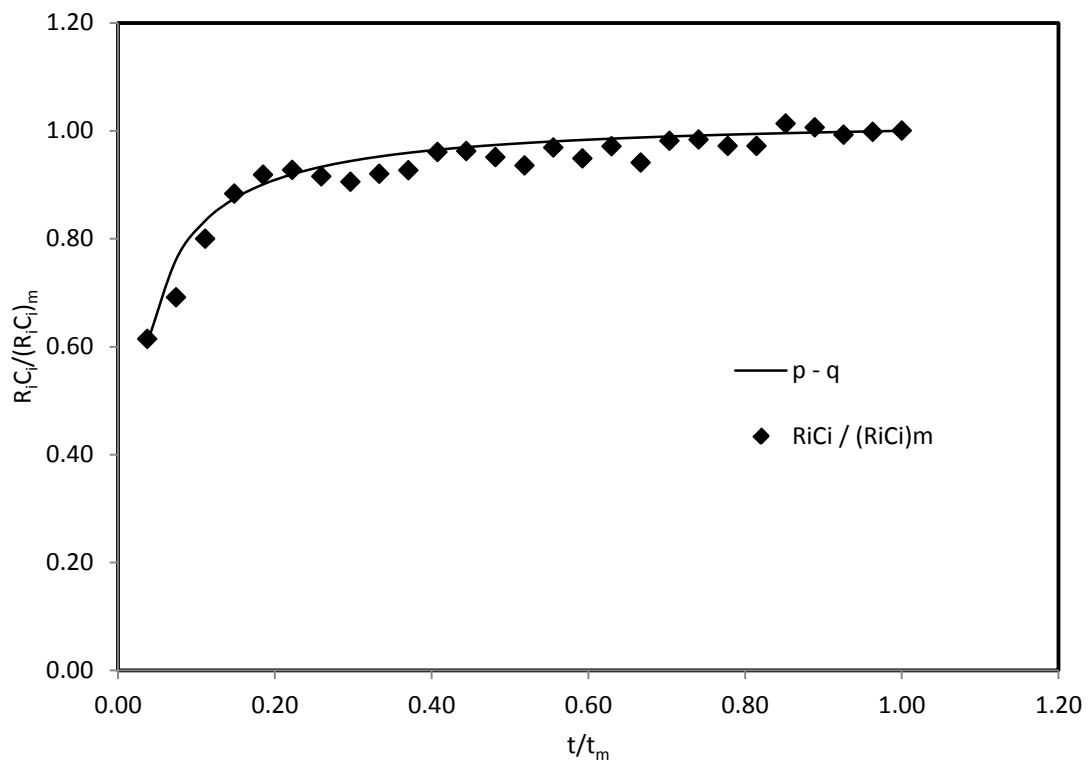


Figure 5.72 Corrosion-time model for corroded polymer concrete composite under salt-water condition

## 5.5 Summary

In this study, the interface corrosion between steel and smart cement, smart polyester coating, and smart polymer concrete coatings were investigated for its impedances spectroscopy properties. A material property which characterizes the interface corrosion was determined to be as product of interface resistance and interface capacitance,  $R_i \cdot C_i$ . And the following summaries and conclusions could be made:

1. Cement composite specimens under dry-air condition, the  $R_i \cdot C_i$  of interface corrosion for corroded composites increased from  $6.24E-4$  ohm-F to  $5.41E-2$  ohm-F while the non-corroded composites increased from  $1.34E-4$  ohm-F to  $7.34E-3$  ohm-F.
2. Cement composite specimens under salt-water condition, the  $R_i \cdot C_i$  of interface corrosion for corroded composites increased from  $2.56E-4$  ohm-F to  $2.33E-2$  ohm-F while the non-corroded composites increased from  $3.72E-5$  ohm-F to  $3.36E-3$  ohm-F.
3. Polyester composite specimens under dry-air condition, the  $R_i \cdot C_i$  of interface corrosion for corroded composites generally remained in the range of  $3.30E-4$  ohm-F to  $3.58E-4$  ohm-F while the non-corroded composites generally remained in the range of  $2.57E-4$  ohm-F to  $2.67E-4$  ohm-F.
4. Polyester composite specimens under salt-water condition, the  $R_i \cdot C_i$  of interface corrosion for corroded composites increased from  $3.14E-4$  ohm-F to  $3.80E-4$  ohm-F while the non-corroded composites increased from  $2.47E-4$  ohm-F to  $2.63E-4$  ohm-F.
5. Polymer concrete composite specimens under dry-air condition, the  $R_i \cdot C_i$  of interface corrosion for corroded composites generally remained in the range of  $4.95E-4$  ohm-F to  $5.14E-4$  ohm-F while the non-corroded composites generally remained in the range of  $6.16E-5$  ohm-F to  $6.28E-5$  ohm-F.

6. Polymer concrete composite specimens under salt-water condition, the  $R_i \cdot C_i$  of interface corrosion for corroded composites increased from  $5.05E-4$  ohm-F to  $5.81E-4$  ohm-F while the non-corroded composites increased from  $6.28E-5$  ohm-F to  $7.31E-5$  ohm-F.

## CHAPTER 6

### LARGE MODEL TESTS AND FIELD MODEL TESTS

#### 6.1 Large Model Tests

A large scale cement well (composite specimen) was prepared in the material laboratory of Civil and Environmental Engineering department and was under continuous tests and monitoring procedures for its electrical properties. The model composed of steel casing pipe of 8 feet in length and 4 inches in diameter. The steel case was placed in the PVC pipe, simulating the borehole, whose length was 8 feet and inside diameter was 8 inches as shown in Figure 6.1. The gap between the steel casing and the PVC pipe was filled with smart cement slurry. The water-to-cement ratio used was 0.4. The cemented sheath was instrumented with probes spaced at distance of 6 inches and placed at four different directions along the entire length to monitor and test the bulk material (cement slurry).

Schematic diagrams for the casing and wires instrumentation is shown in Figure 6.2. A wire probe was attached to the top of the steel casing pipe to monitor and test the steel casing pipe. Conductive fillers were added in the cement slurry to improve the electrical property of the composite.

Steel casing



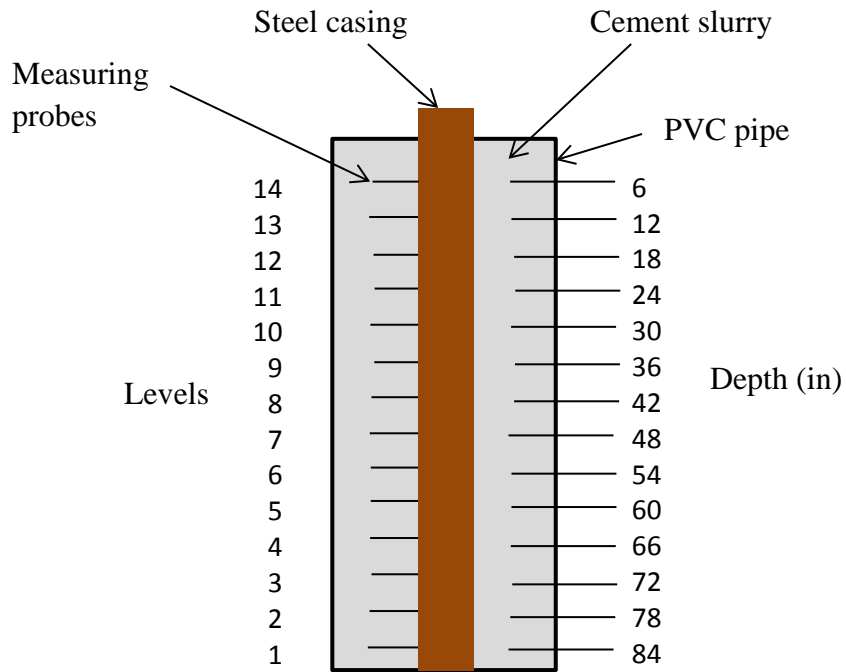
a. Steel casing pipe with instrumentation

PVC pipe with casing inside

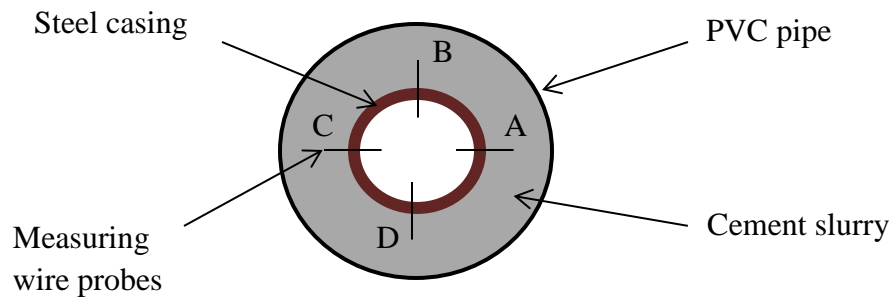


b. Casing embedded in PVC pipe

Figure 6.1 Steel casing pipe embedded in the PVC pipe



a. Profile view of the casing



b. Plan view of the casing

Figure 6.2 Schematic diagrams for the casing and wires instrumentation

### **6.1.1 Cement Characterization**

The impedance of the cement slurry closer to the steel casing was measured with impedance analyzer precision LCR meter. The impedance measurements were performed on a monthly basis for about a year. The frequency range used was from 20 Hz to 300 kHz. The evaluation of impedance measured at the maximum frequency of 300 kHz gave the bulk resistance of the cement slurry.

The bulk resistance of the smart cement slurry ( $R_b$ ) along the depth for the measuring time of 2<sup>nd</sup> week, 6<sup>th</sup> month and 1<sup>st</sup> year were shown in Figure 6.3. From the Figure 6.3, it could be observed that the bulk resistance ( $R_b$ ) was generally remained in constant range along the depth of the casing. The bulk resistance ( $R_b$ ) for typical measuring levels such as level-1, level-7 and level-14 with respect to time was given in Figure 6.4. From the Figure 6.4, it could be observed that the bulk resistance ( $R_b$ ) at each measuring level remained in stable range during the course of the test time period.

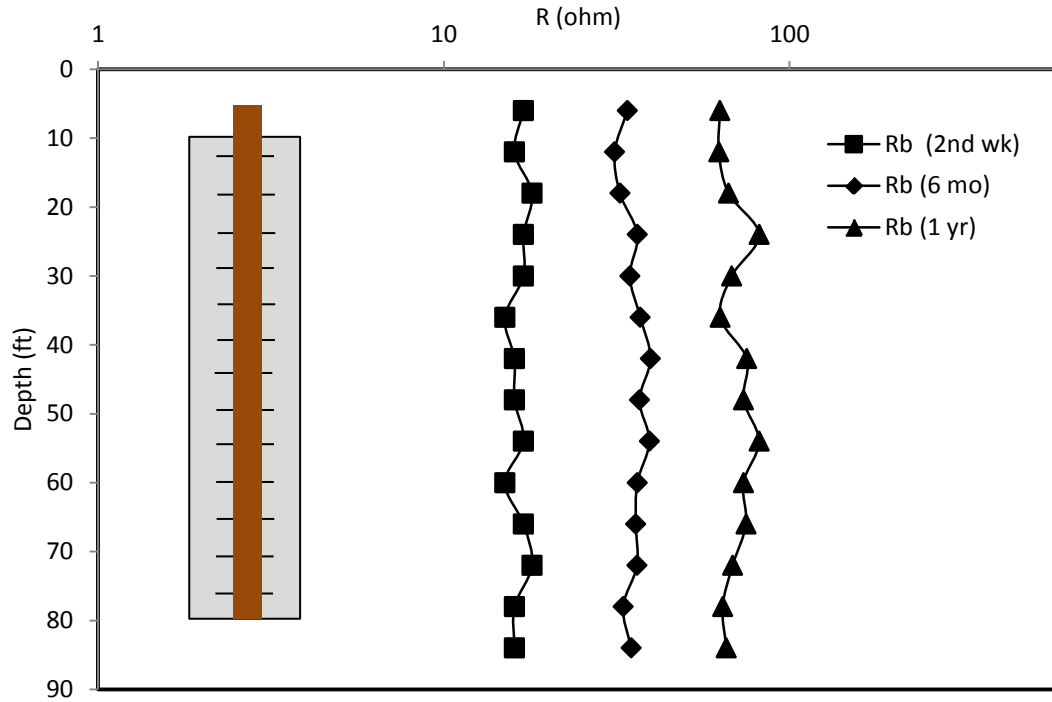


Figure 6.3 Bulk resistance vs. depth of the casing at each measuring level

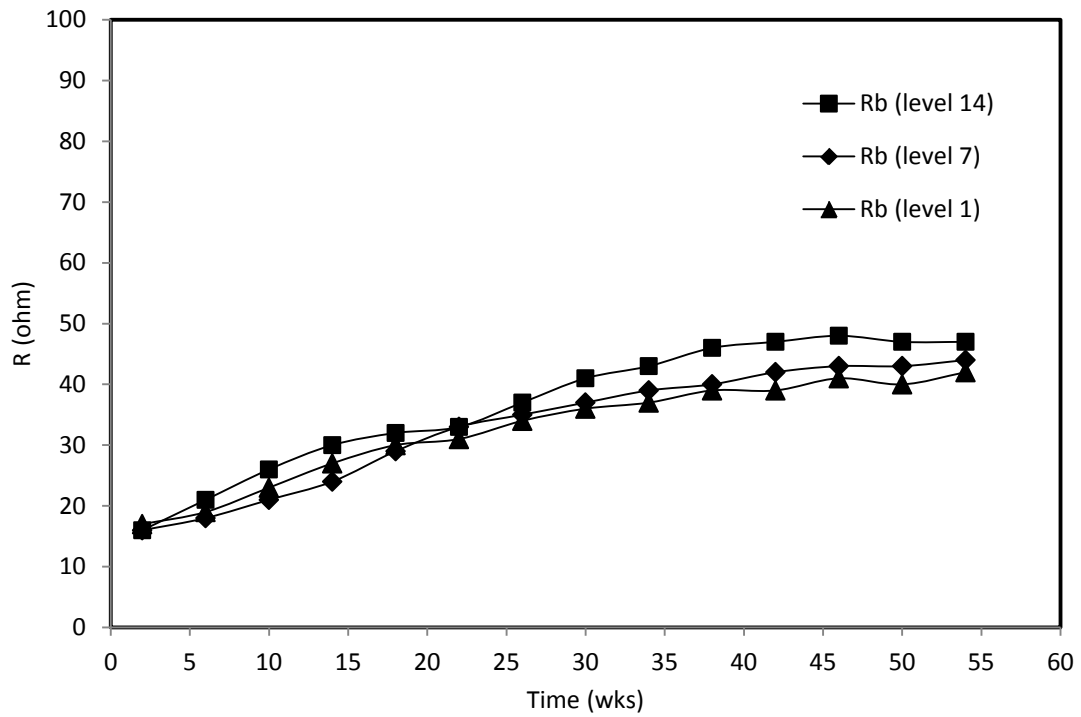


Figure 6.4 Bulk resistance (Rb) of the casing at level-1, level-7, and level 14 for one year period

### 6.1.2 Steel-Cement Characterization

The electrical resistance and capacitance of the cement paste, steel casing, and transitional contact between the cement slurry and the casing were measured with impedance analyzer precision LCR meter. The impedance measurements were performed on a monthly basis for about a year. The frequency range used was from 20 Hz to 300 kHz. For 2<sup>nd</sup> week test, 6<sup>th</sup> month test and 12<sup>th</sup> month test, typical plots of impedance vs frequency for the steel casing buried in smart cement slurry is shown in Figure 6.5, Figure 6.7 and Figure 6.9 for level-1, level-7, and level-14 respectively.

The Bode plot of the adopted equivalent circuit for the steel casing buried in smart cement slurry is shown in Figure 6.6, Figure 6.8, and Figure 6.10 for level-1, level-7, and level-13 respectively. From Figure 6.5 through Figure 6.10, the impedance of steel casing buried in the smart cement slurry had generally increased with time at a given depth of measuring level.

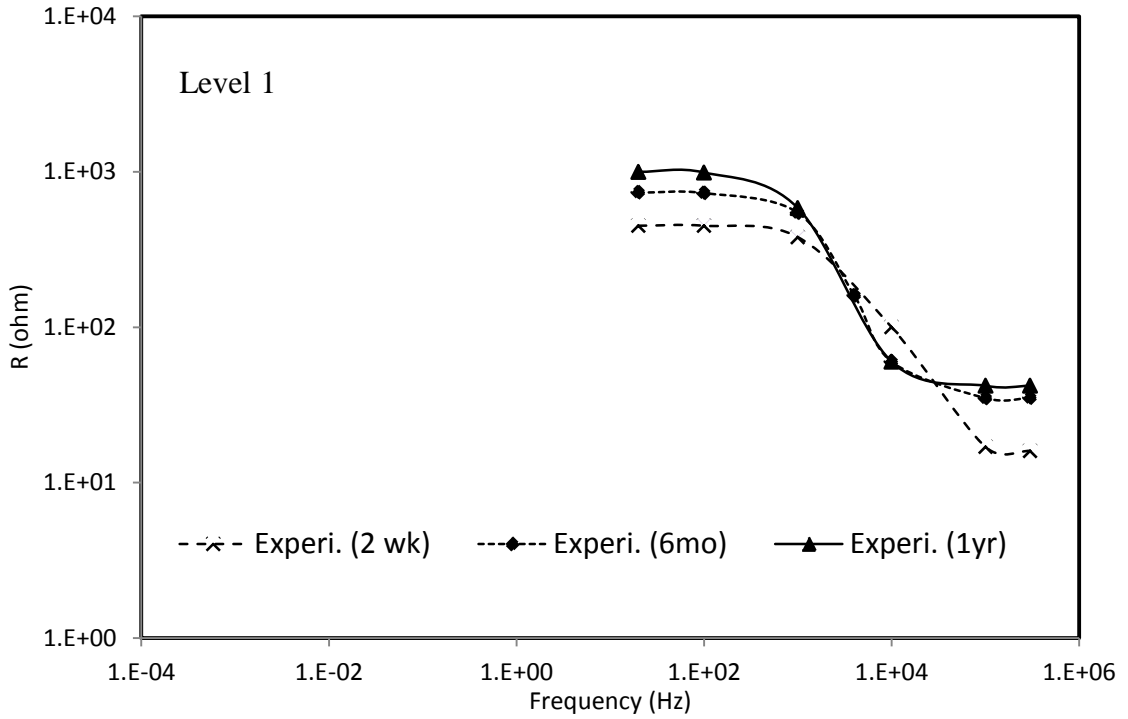


Figure 6.5 Bode plot of casing for level-1

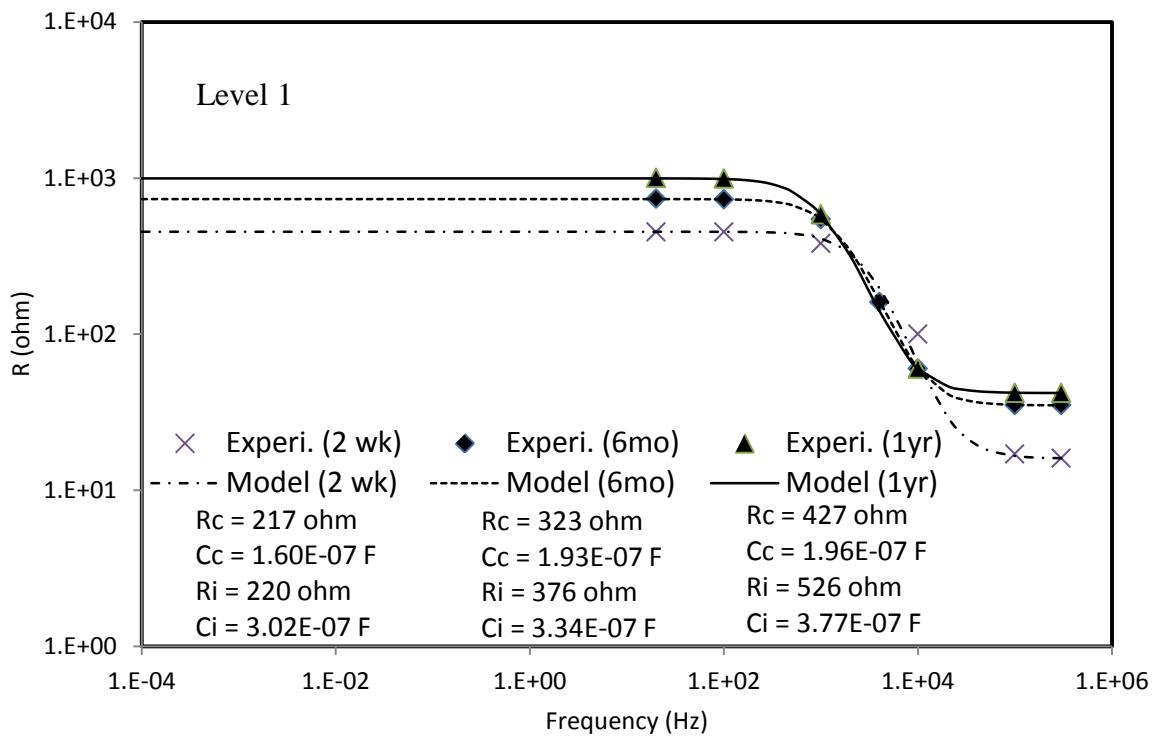


Figure 6.6 Bode plot of casing along respective impedance models for level-1

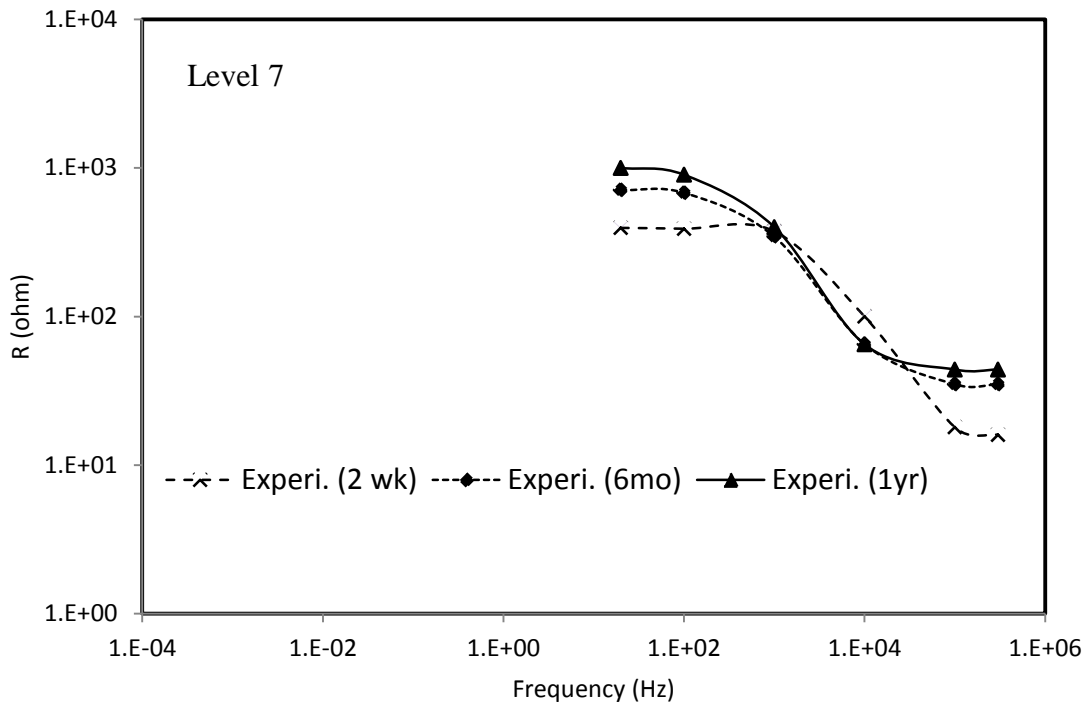


Figure 6.7 Bode plot of casing for level-7

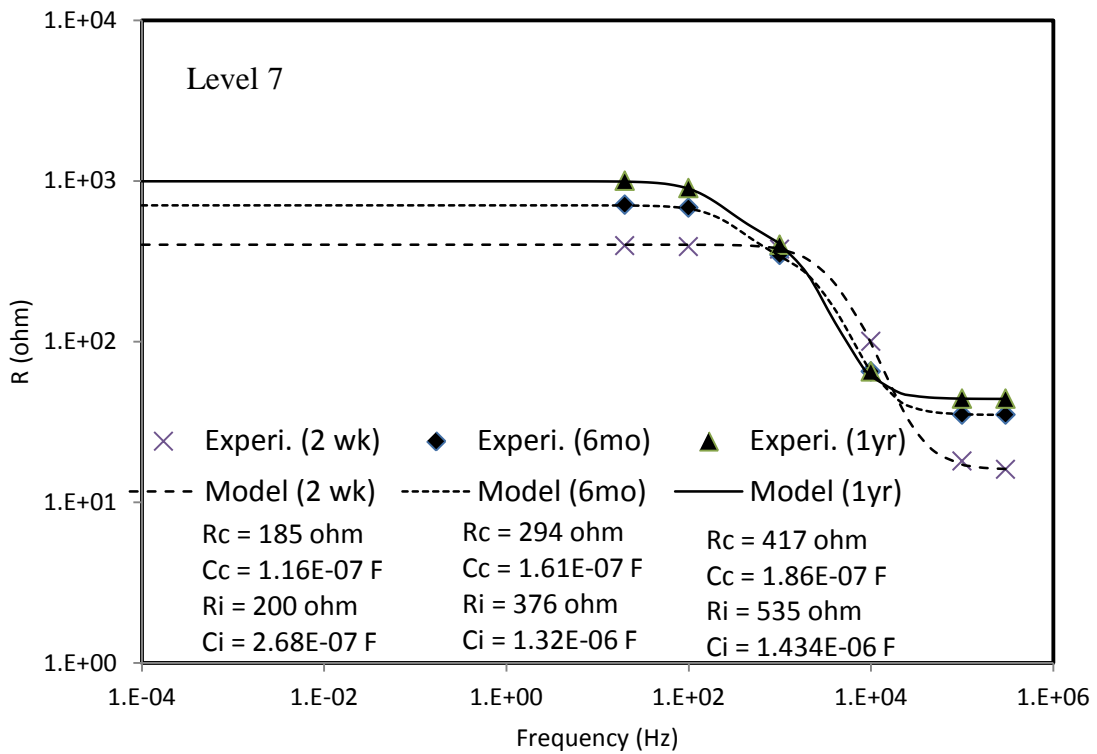


Figure 6.8 Bode plot of casing along respective impedance models for level-7

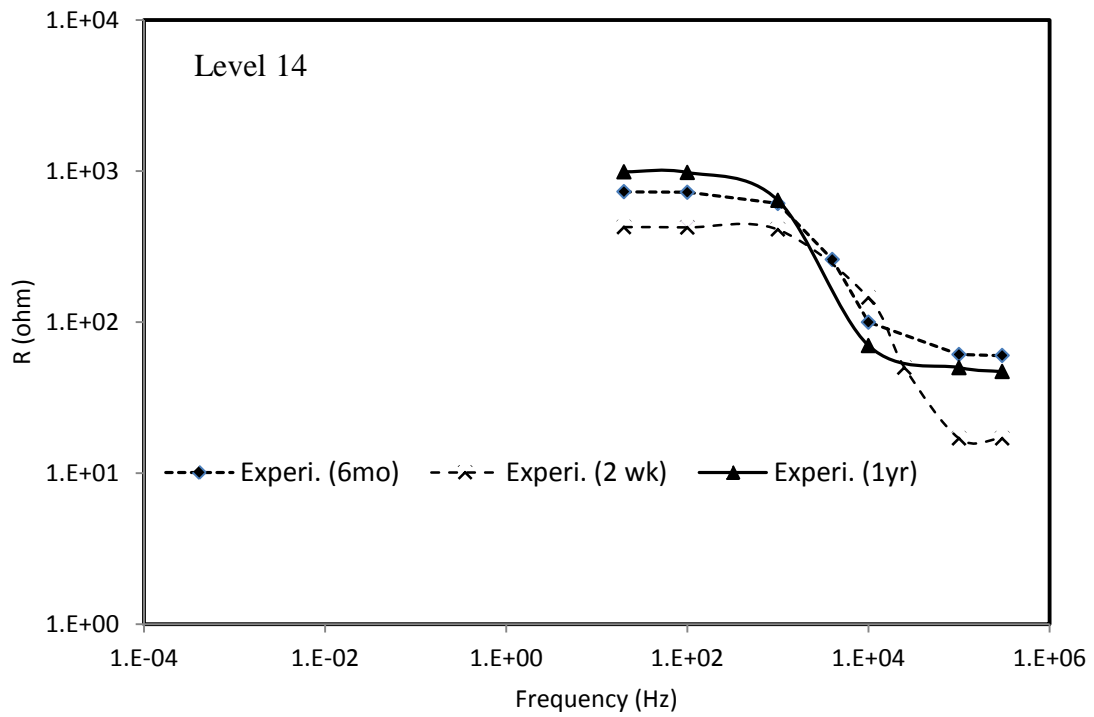


Figure 6.9 Bode plot of casing for level-14

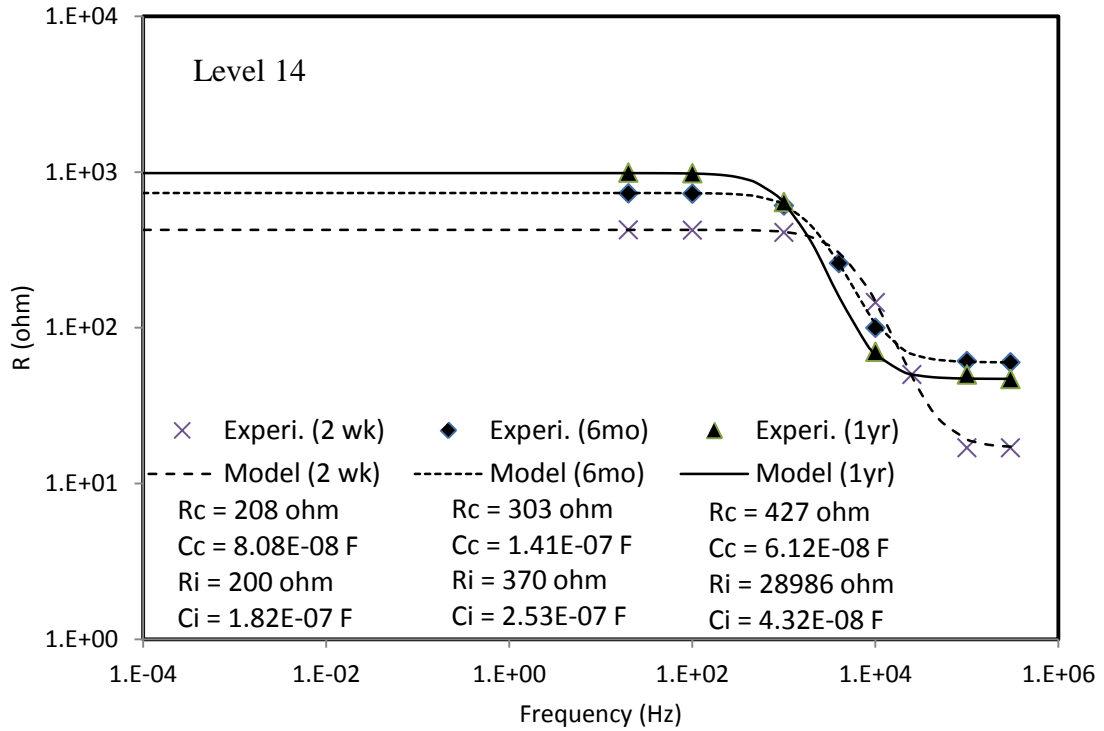


Figure 6.10 Bode plot of casing along respective impedance models for level-14

The resistance at the interface between of steel casing and the smart cement slurry ( $R_i$ ) and the resistance at the contact ( $R_c$ ) along the depth for the measuring time period of a year were shown in Figure 6.11. From Figure 6.11, it could be observed that the interface resistance ( $R_i$ ) was higher than the contact resistance ( $R_c$ ) along the depth during the course of the measuring time period. Both the interface resistance ( $R_i$ ) and the contact resistance ( $R_c$ ) were increased with respect to time. Typical plots  $R_i$  vs time and  $R_c$  vs time for level-1, level-7 and level-14 were shown in Figure 6.12 through Figure 6.14.

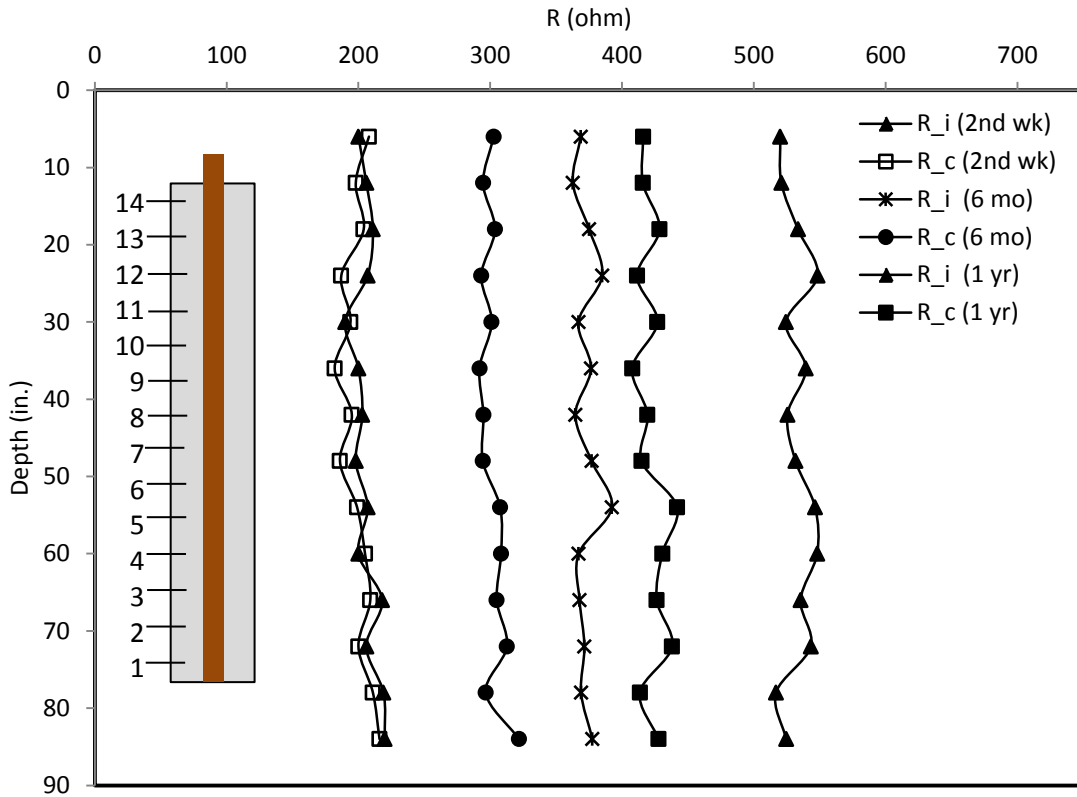


Figure 6.11 Resistance vs. depth of the casing at each measuring level

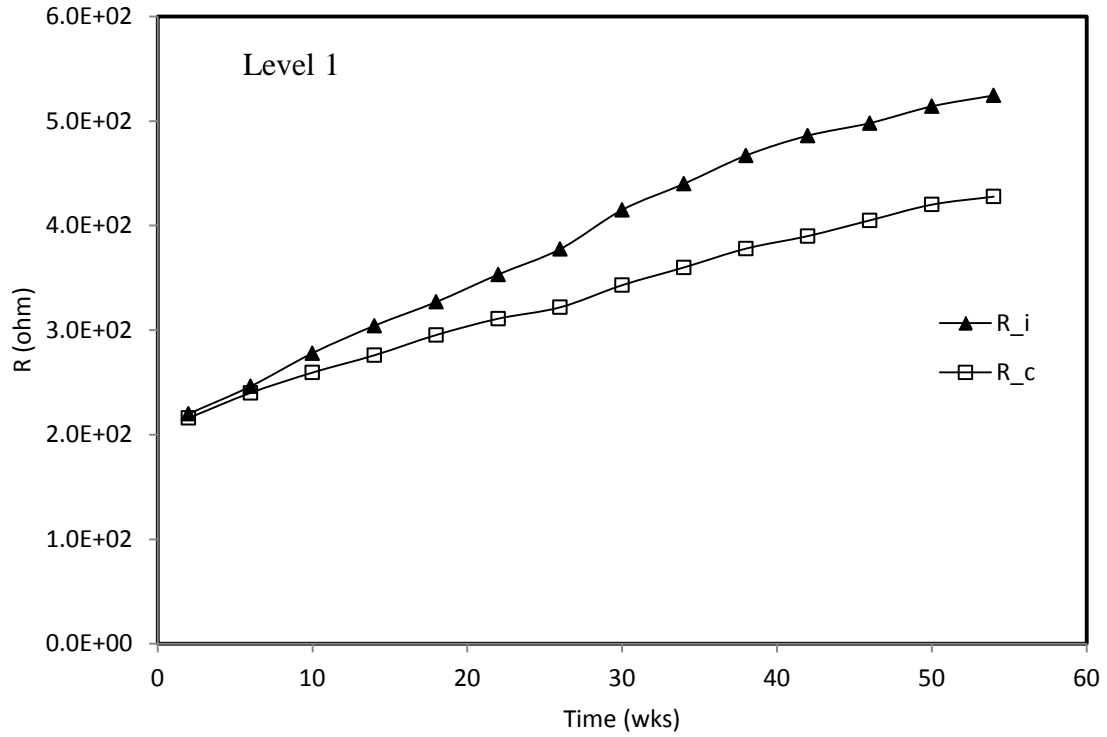


Figure 6.12 Resistances (Ri & Rc) of the casing at level-1 for one year period

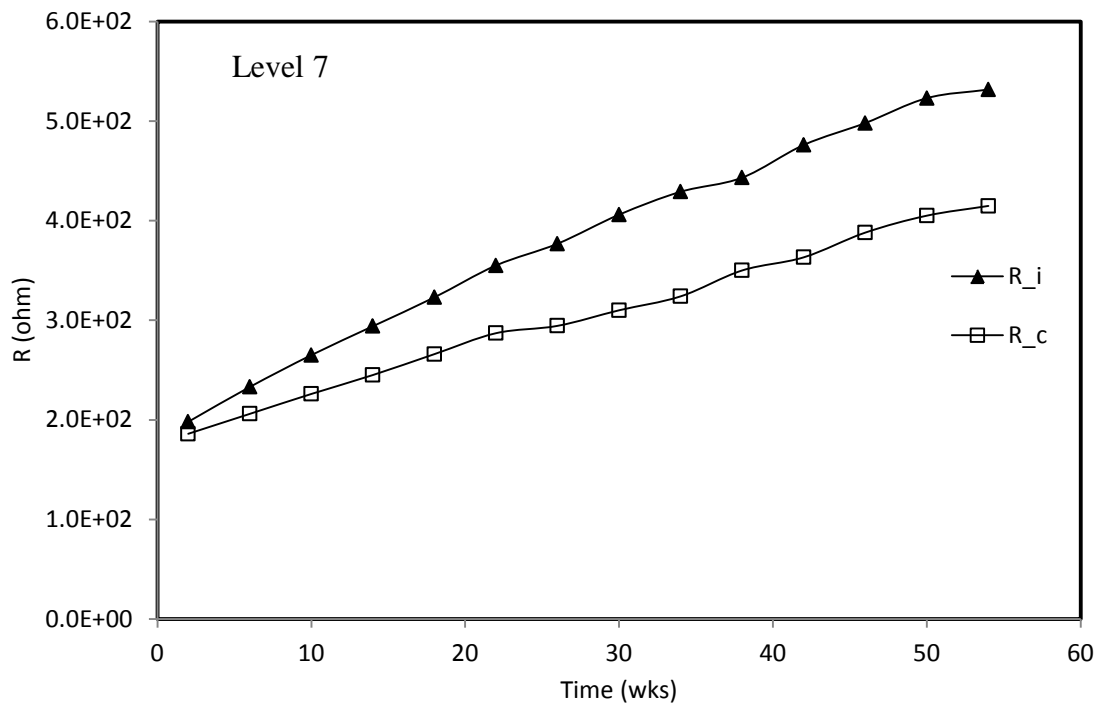


Figure 6.13 Resistances (Ri & Rc) of the casing at level-7 for one year period

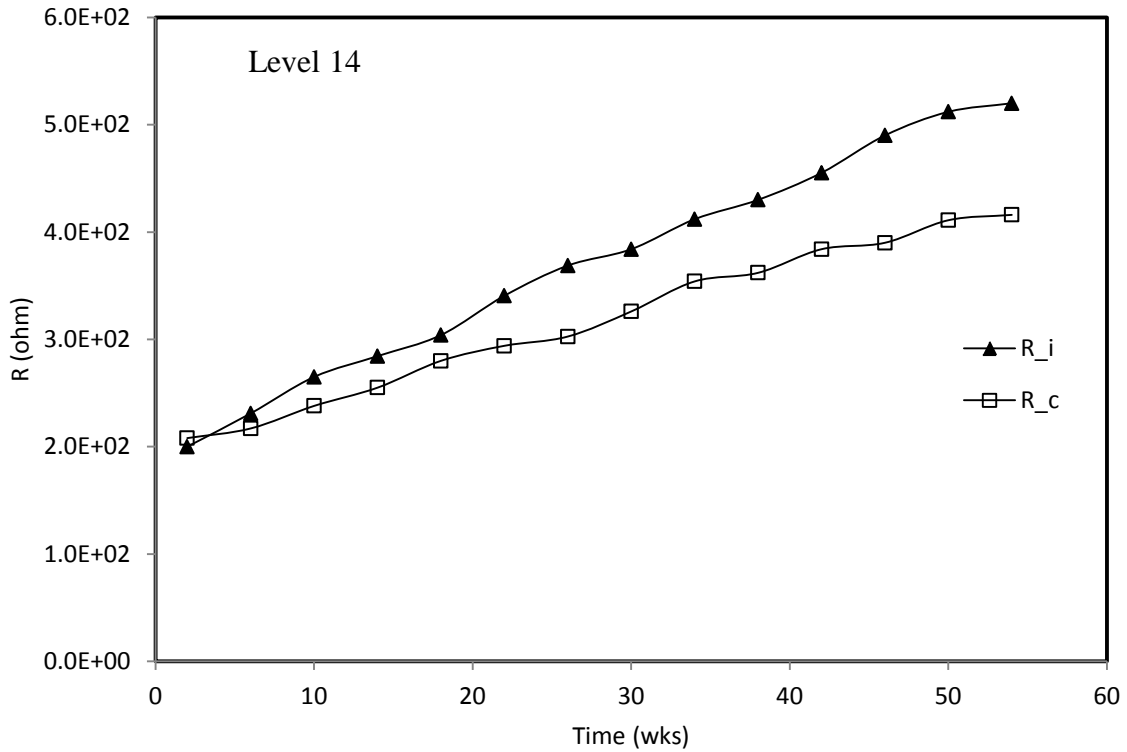


Figure 6.14 Resistances (Ri & Rc) of the casing at level-14 for one year period

The capacitance at the interface between of steel casing and the smart cement slurry (Ci) and the capacitance at the contact (Cc) along the depth for the measuring time period of a year were shown in Figure 6.15. From Figure 6.15, it could be observed that the interface capacitance (Ci) was higher than the contact capacitance (Cc) along the depth during the course of the measuring time period. Both the interface capacitance (Ci) and the contact capacitance (Cc) were increased with respect to time and typical plots for levels 1, 7 and 13 were shown in Figure 6.16 through Figure 6.18.

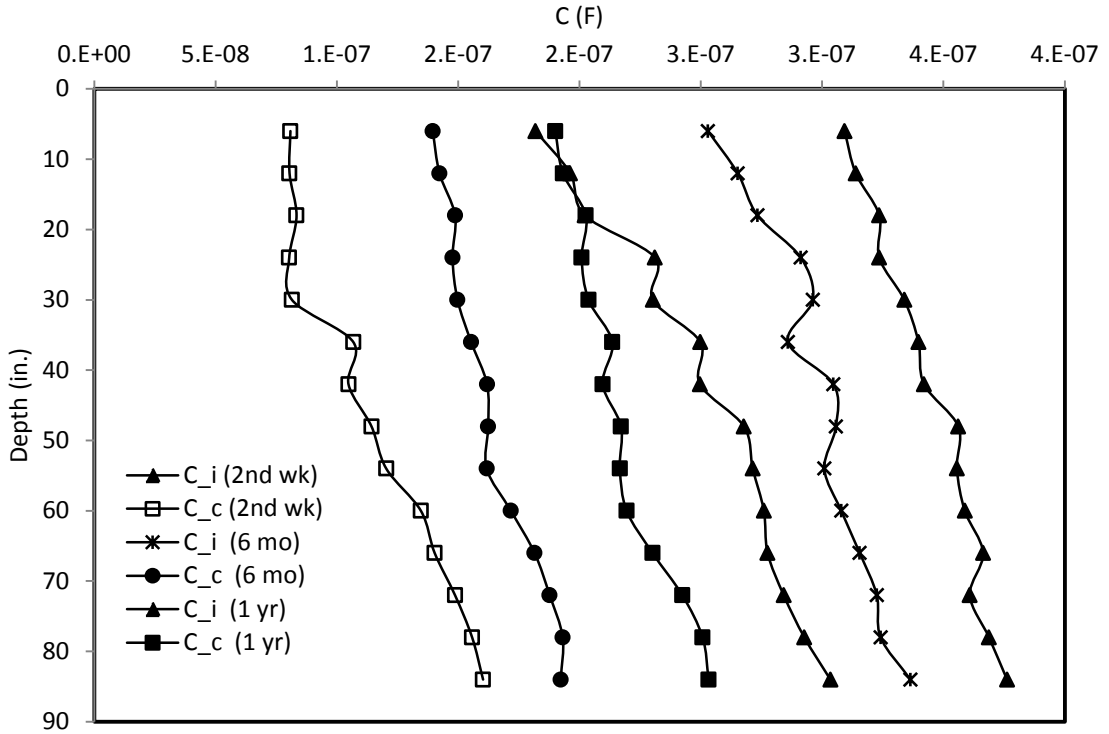


Figure 6.15 Capacitance vs. depth of the casing at each measuring level

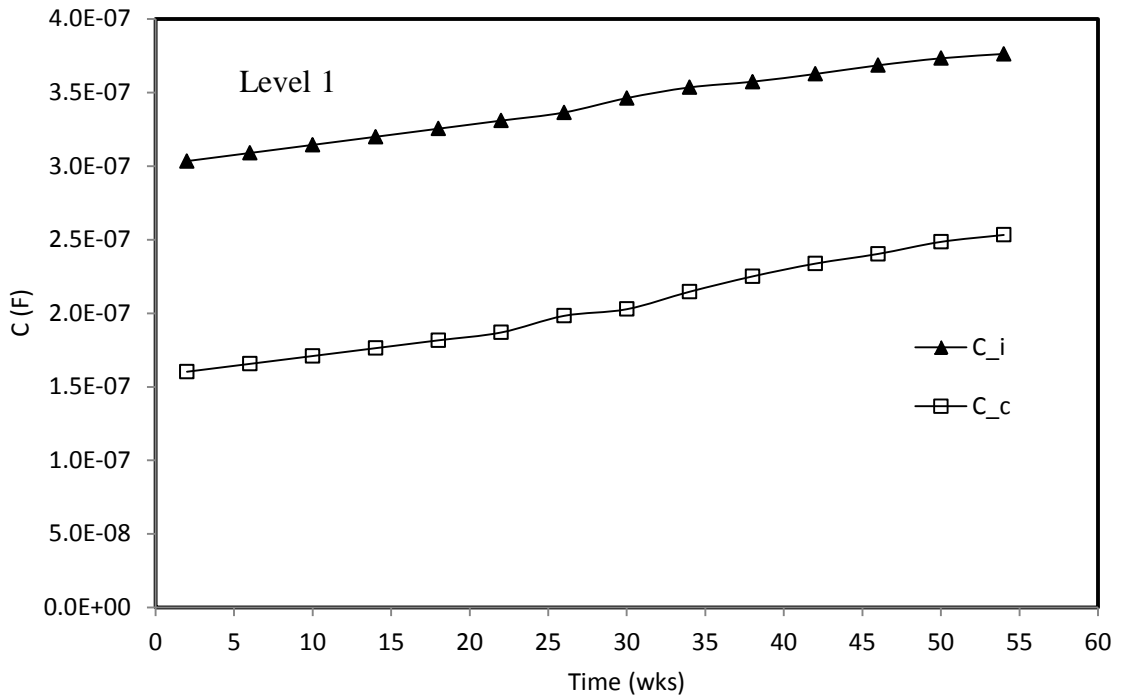


Figure 6.16 Capacities (Ci & Cc) of the casing at level-1 for one year period

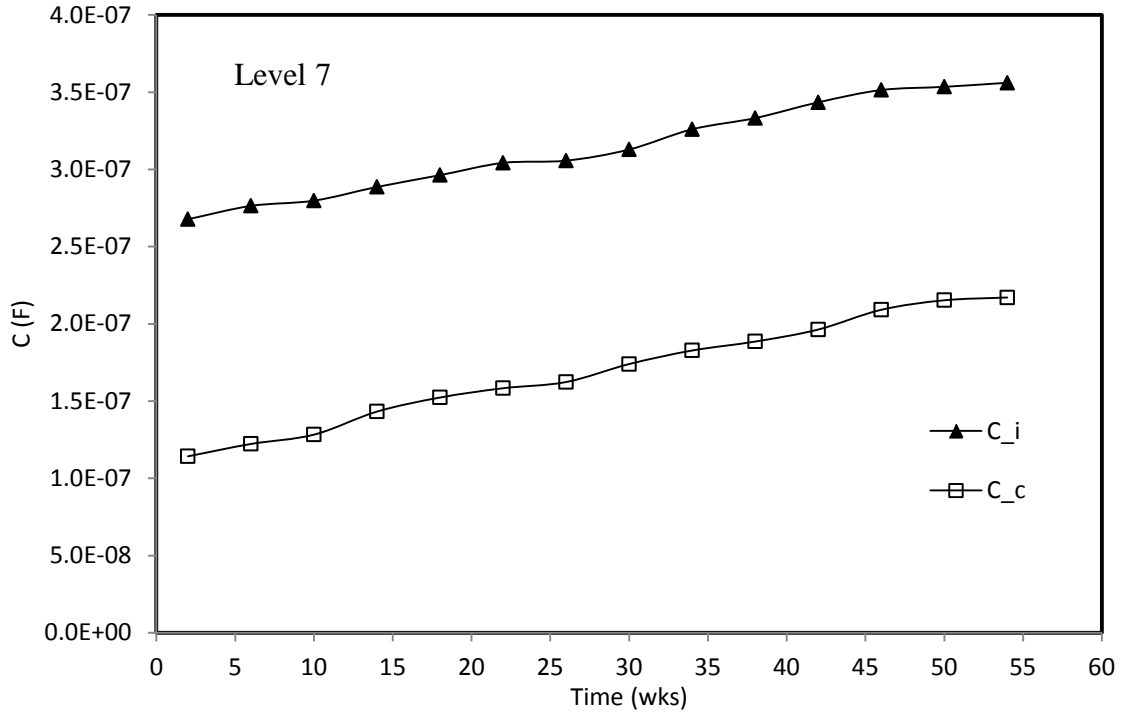


Figure 6.17 Capacities (Ci & Cc) of the casing at level-7 for one year period

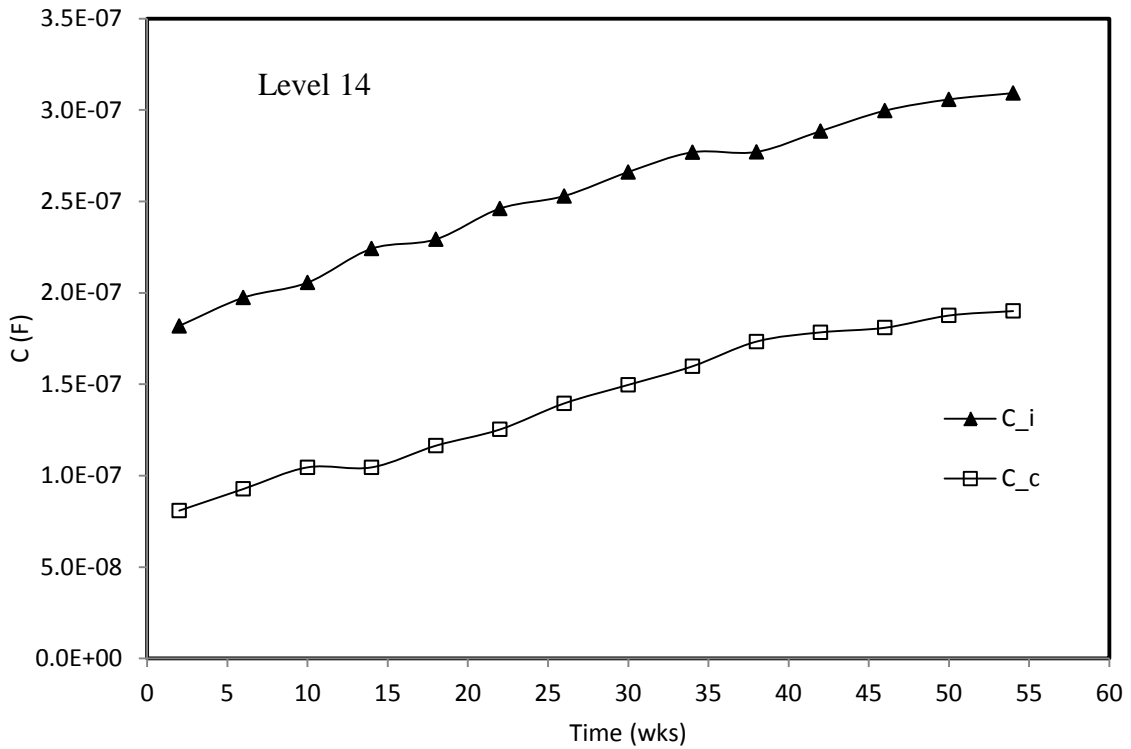


Figure 6.18 Capacities (Ci & Cc) of the casing at level-14 for one year period

The material property parameter defined as product of resistance and capacitance,  $R^*C$ , for the steel casing buried in the smart cement is shown Figure 6.19. From the Figure 6.19, the interface  $R_i^*C_i$  between of the steel casing and the smart cement slurry was greater than the  $R_c^*C_c$  at the cement contact along the depth for the measuring time period of a year. Both the interface  $R_i^*C_i$  and the contact  $R_c^*C_c$  were increased with respect to time and typical plots for levels 1, 7 and 13 were shown in Figure 6.20 through Figure 6.22.

The general trend of rates of increase in both  $R_i^*C_i$  and  $R_c^*C_c$  were changed below the depth of about 20 ft. from the ground. This could be attributed to the presence of ground water in the vicinity at about 20 ft. below the ground. Therefore, from Figure 6.11.through Figure 6.19, it could be observed that it was possible to detect and quantify the presence of the corrosion in the steel casing buried in the cement slurry.

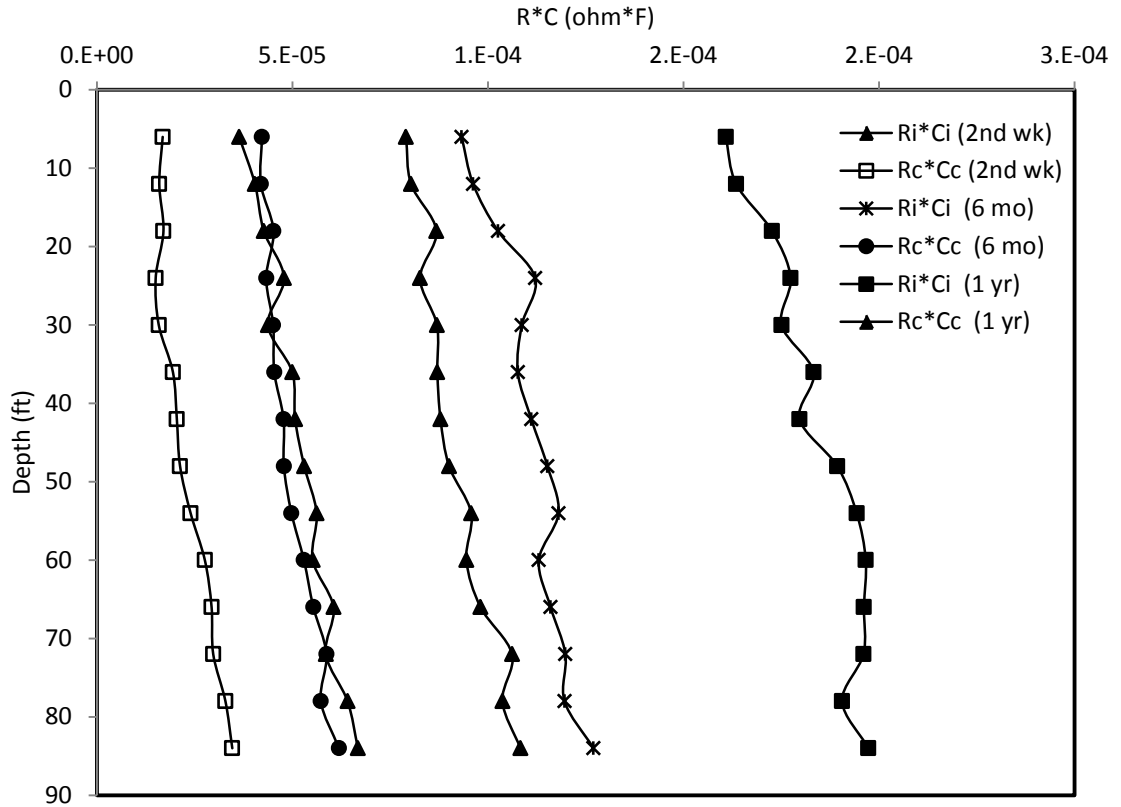


Figure 6.19 R\*C vs. depth of the casing at each measuring level

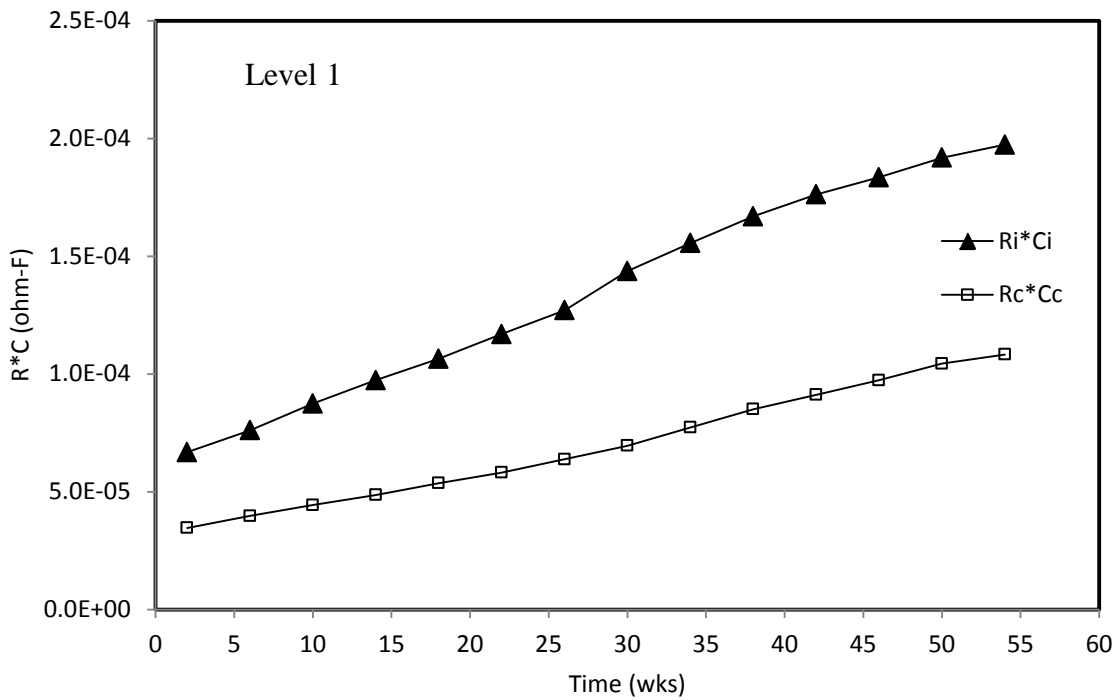


Figure 6.20 R\*C vs. depth of the casing at level-1 for one year period

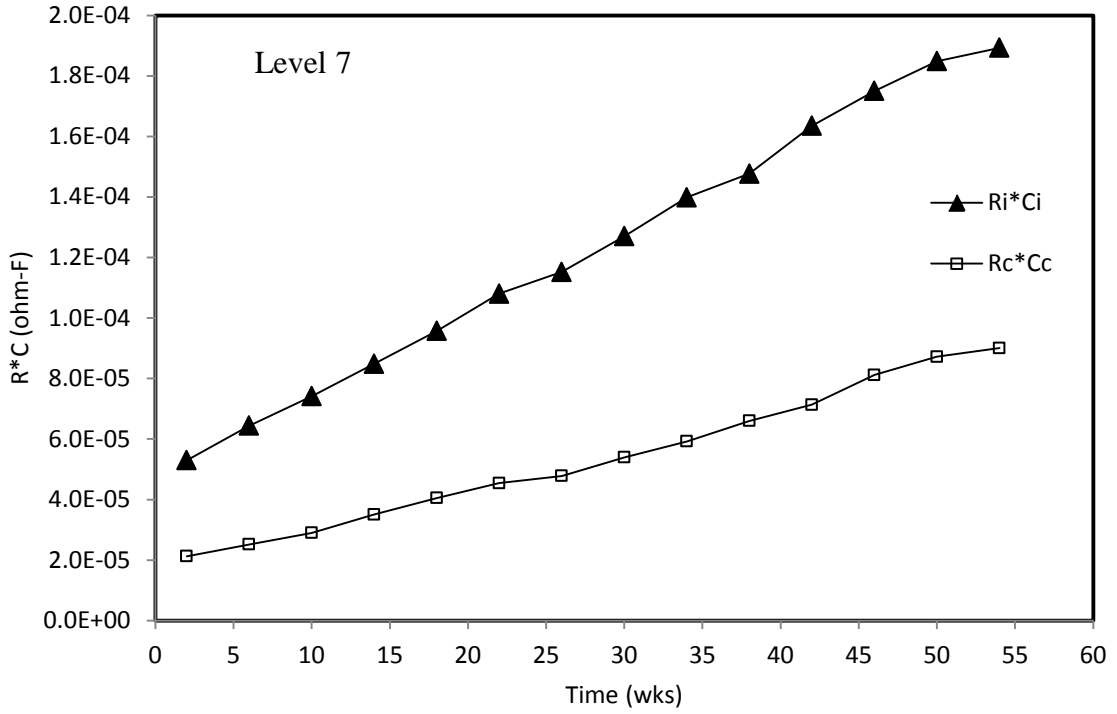


Figure 6.21 R\*C vs. depth of the casing at level-7 for one year period

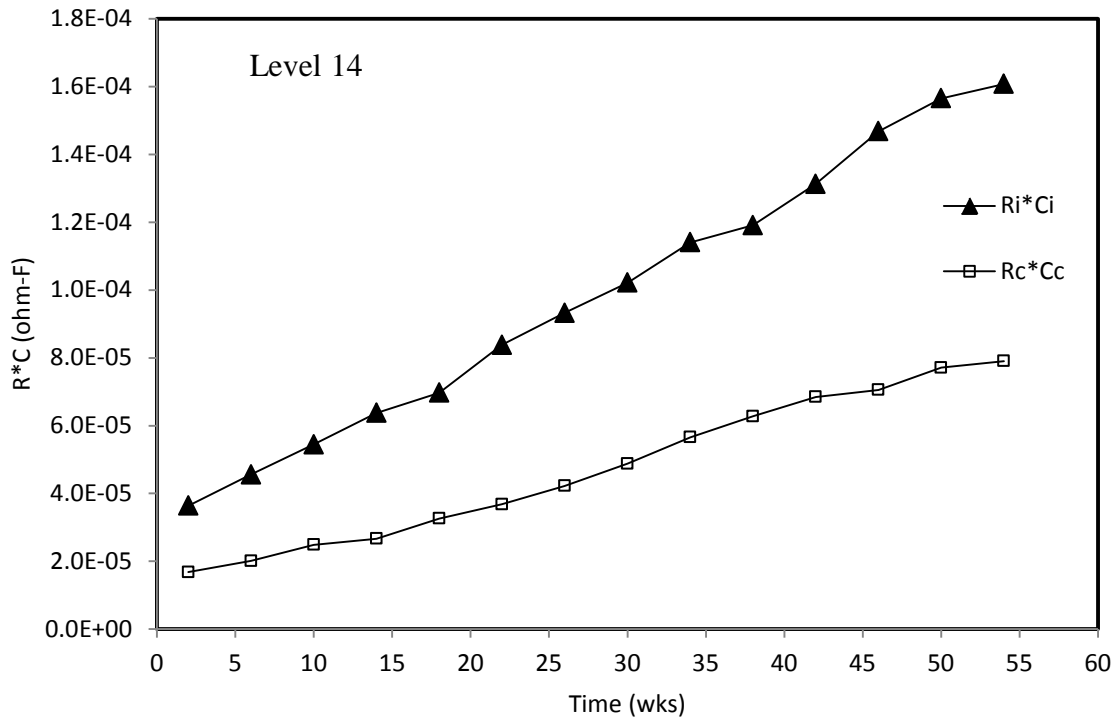
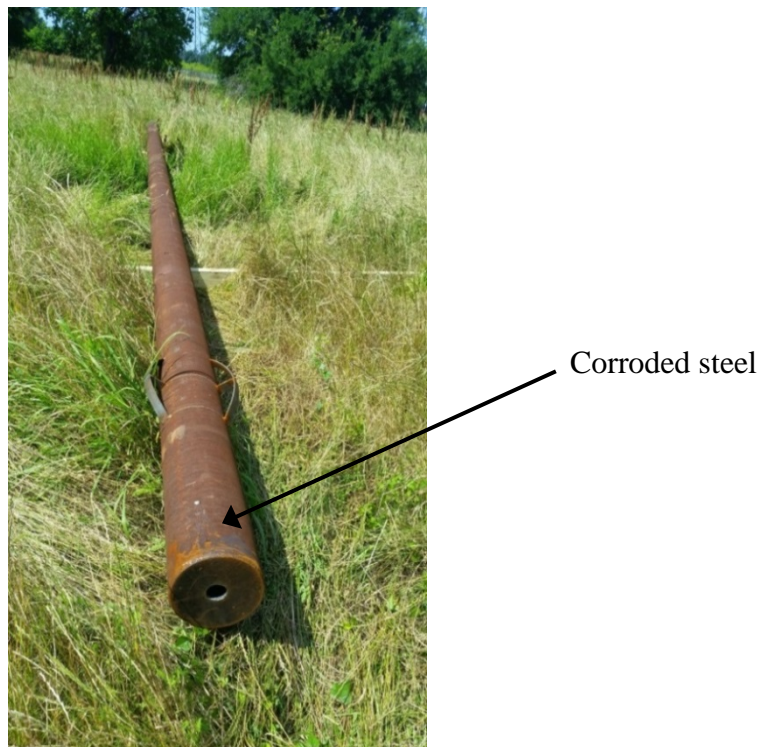


Figure 6.22 R\*C vs. depth of the casing at level-14 for one year period

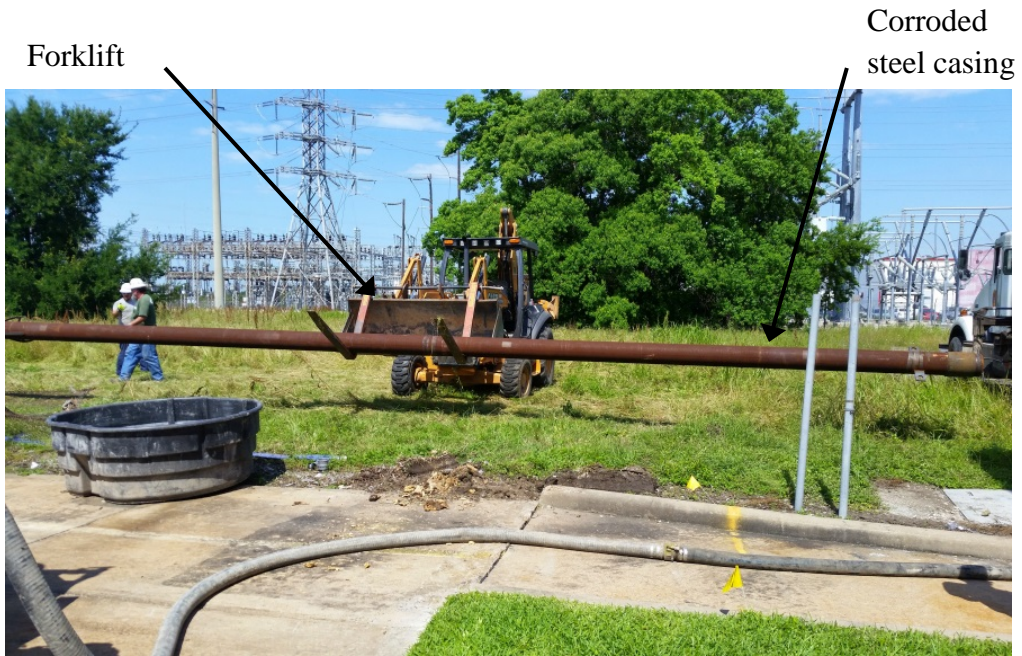
## 6.2 Field Model Tests

A 40 feet long steel casing pipe with diameter of 8 inches was buried in a borehole of 16 inches in diameter and 38 feet depth as shown in Figure 6.23. The borehole place is located in the vicinity of Energy Research Park (ERP) of University of Houston. Prior to burying the casing, visual inspection of the casing pipe indicated that the surface of the pipe was highly corroded as shown in Figure 6.23. Four pairs of fourteen wires were instrumented around the casing for long its entire length before cement slurry was casted as shown in Figure 6.24.

Schematic diagram for the casing and wires instrumentation are indicated in Figure 6.25. The water cement ratio used was 0.8. Conductive fillers were added in the cement slurry to improve the electrical property of the composite.

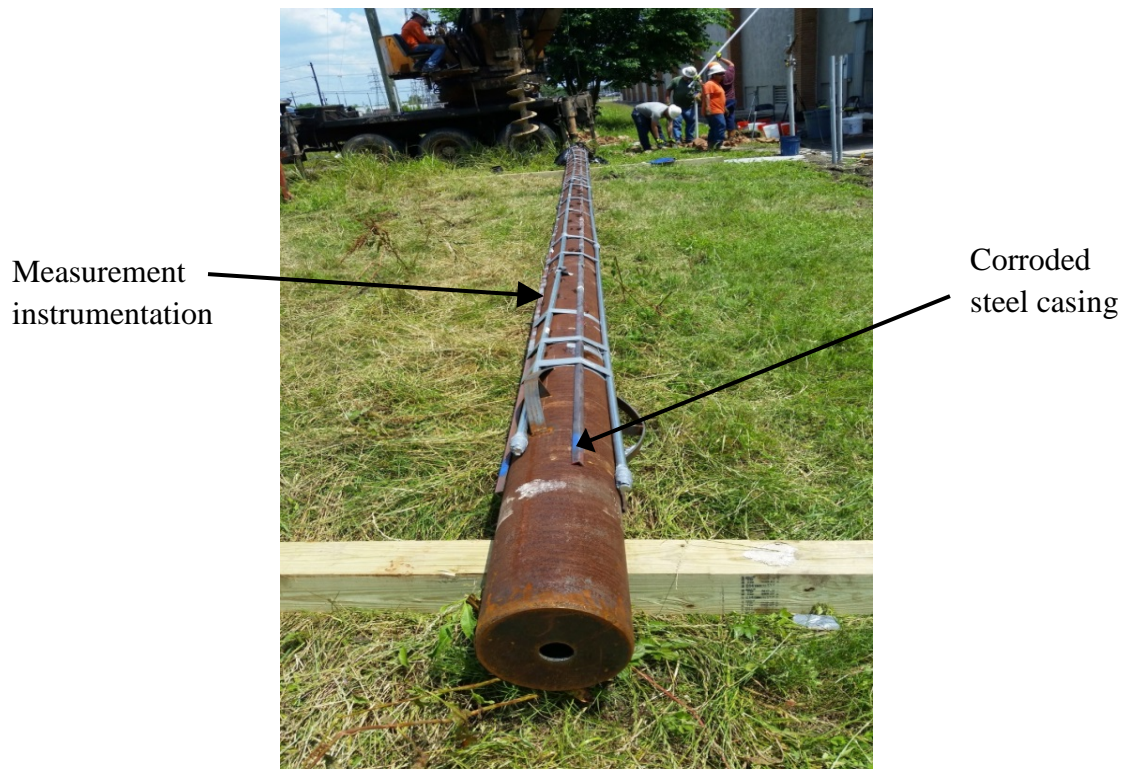


a. Corroded steel casing pipe

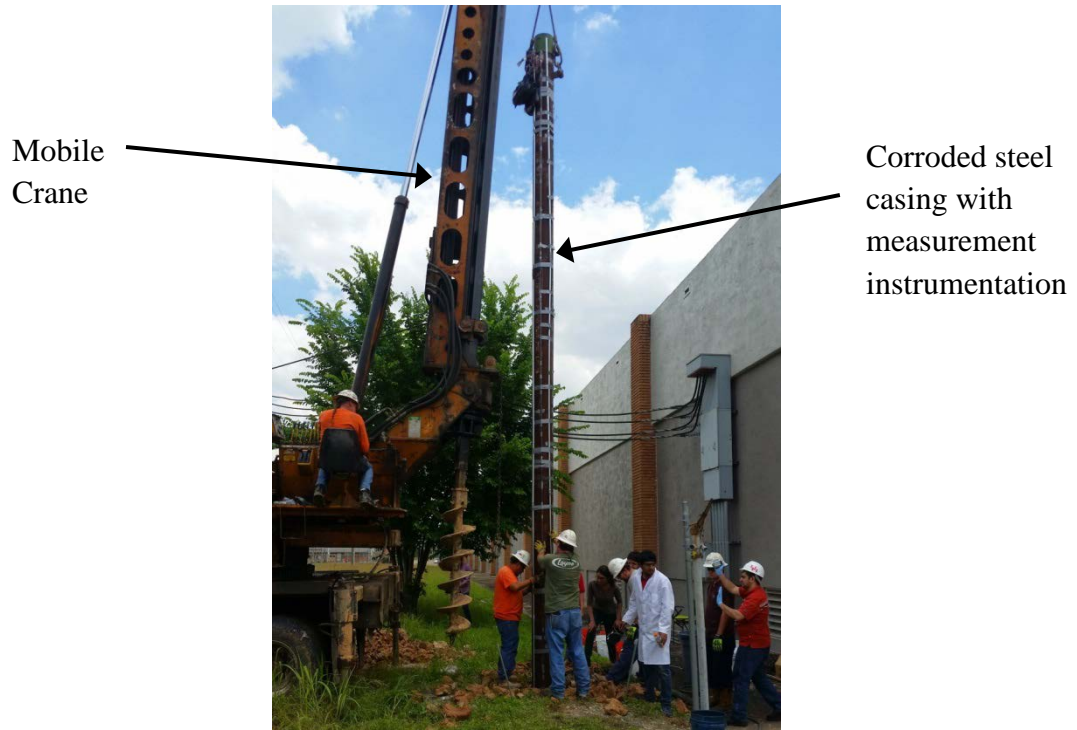


b. Steel casing pipe being transported to a borehole

Figure 6.23 A 40 ft. long steel casing pipe with diameter of 8 inches

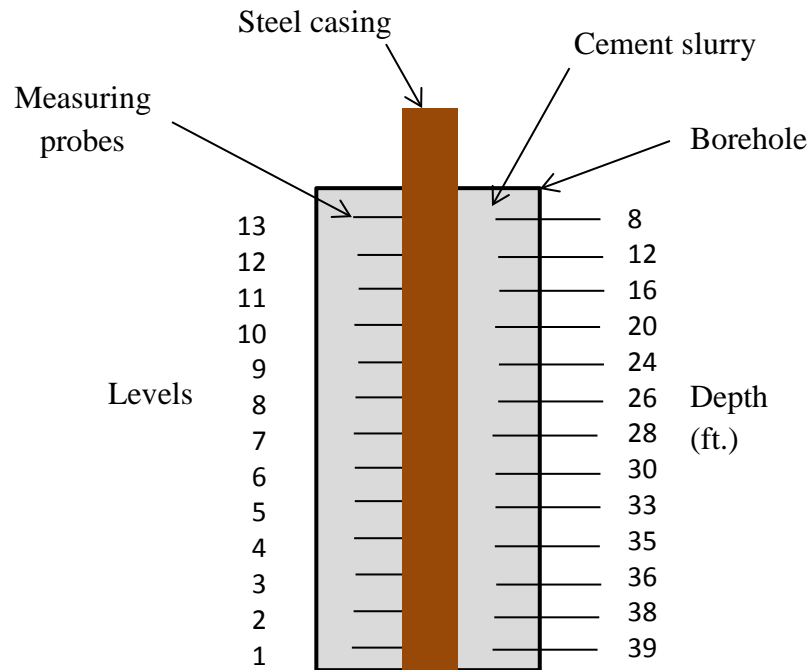


a. Steel casing pipe instruments silver painted wires

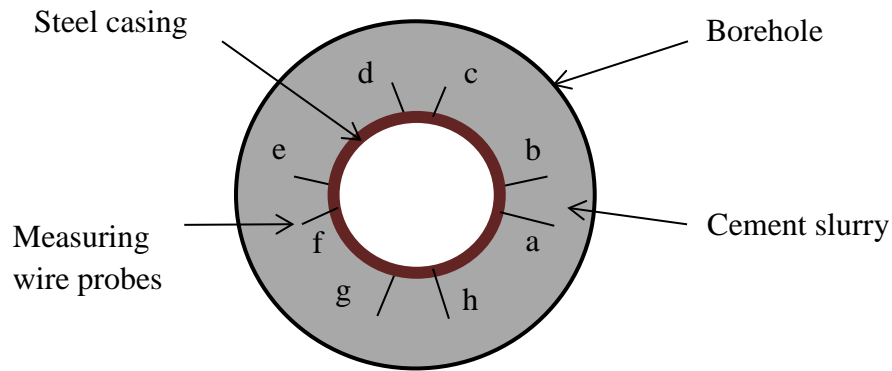


b. Steel casing pipe being buried in a borehole

Figure 6.24 A steel pipe during casing construction



a. Profile view of the casing



b. Plan view of the casing

Figure 6.25 Schematic diagrams for the casing and wires instrumentation

### 6.2.1 Cement Characterization

The impedance of the cement slurry closer to the corroded steel casing was measured with impedance analyzer precision LCR meter. The impedance measurements were performed on a monthly basis for about a year. The frequency range used was from 20 Hz to 300 kHz. The evaluation of impedance measured at the maximum frequency of 300 kHz gave the bulk resistance of the cement slurry.

The bulk resistance of the smart cement slurry ( $R_b$ ) along the depth for the measuring time of 2<sup>nd</sup> week, 6<sup>th</sup> month and 1<sup>st</sup> year were shown in Figure 6.26. From Figure 6.26, it could be observed that the bulk resistance ( $R_b$ ) was generally decreased along the depth up to about 20 ft. after which the bulk resistance ( $R_b$ ) remained in constant range. This could be attributed to the presence of the ground water level at about 20 ft. depth. The bulk resistances above the ground level were much higher compared to

that of close to and below the ground water table reaching Rb at level-13 up to 14 times of Rb at level-1.

The bulk resistance (Rb) for typical measuring levels such as level-1, level-7 and level-13 with respect to time was given in Figure 6.27 and Figure 6.28. From Figure 6.27 and Figure 6.28, it could be observed that the bulk resistance (Rb) at each measuring level remained in stable range during the course of the test time period.

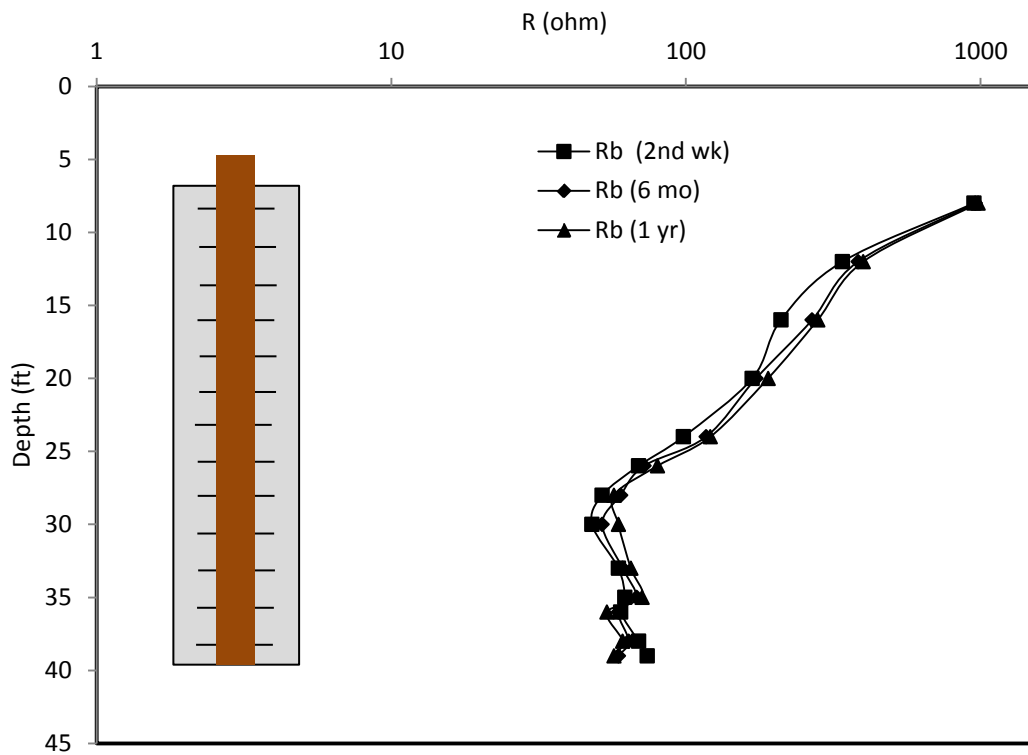


Figure 6.26 Bulk resistance vs. depth of the casing at each measuring level

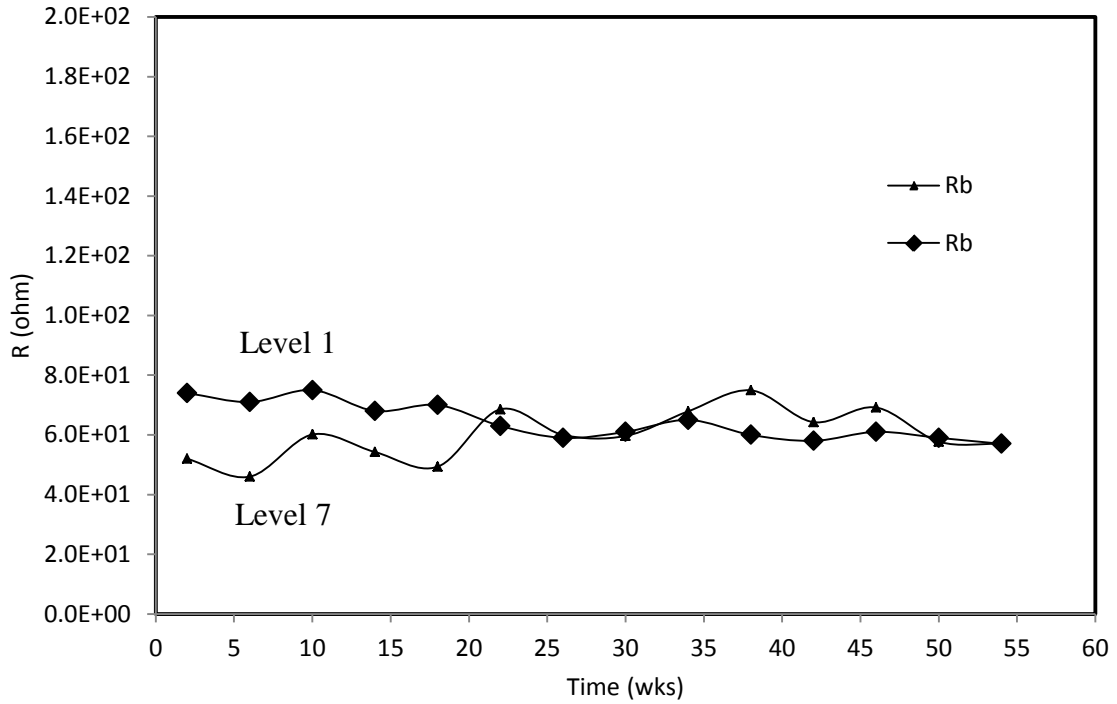


Figure 6.27 Bulk resistance of the casing at level-1 and level-7 for one year period

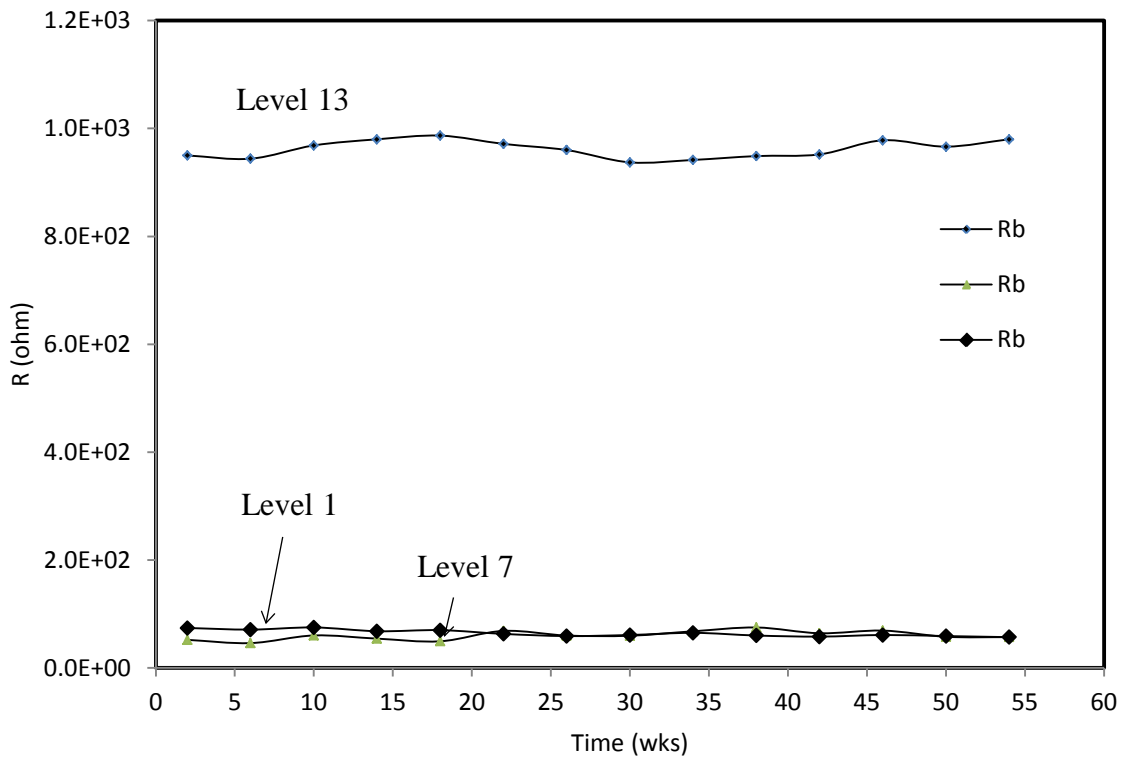


Figure 6.28 Bulk resistance (Rb) of the casing at level-1, level-7 and level-13 for one year period

## 6.2.2 Steel-Cement Characterization

The electrical resistance and capacitance of the cement paste, steel casing, and transitional contact between the cement slurry and the casing were measured with impedance analyzer precision LCR meter. The impedance measurements were performed on a monthly basis for about a year. The frequency range used was from 20 Hz to 300 kHz. For 2<sup>nd</sup> week test, 6<sup>th</sup> month test and 12<sup>th</sup> month test, typical plots of impedance vs frequency for the steel casing buried in smart cement slurry is shown in Figure 6.29, Figure 6.31, and Figure 6.33 for level-1, level-7, and level-13 respectively.

The Bode plot of the adopted equivalent circuit for the steel casing buried in smart cement slurry is shown in Figure 6.30, Figure 6.32, and Figure 6.34 for level-1, level-7, and level-13 respectively. From Figure 6.29 through Figure 6.34, the impedance of steel casing buried in the smart cement slurry had generally increased with time at a given depth of measuring level. From Figure 6.29 through Figure 6.34, the impedance of steel casing buried in the smart cement slurry had generally decreased with depth at a given time of measuring.

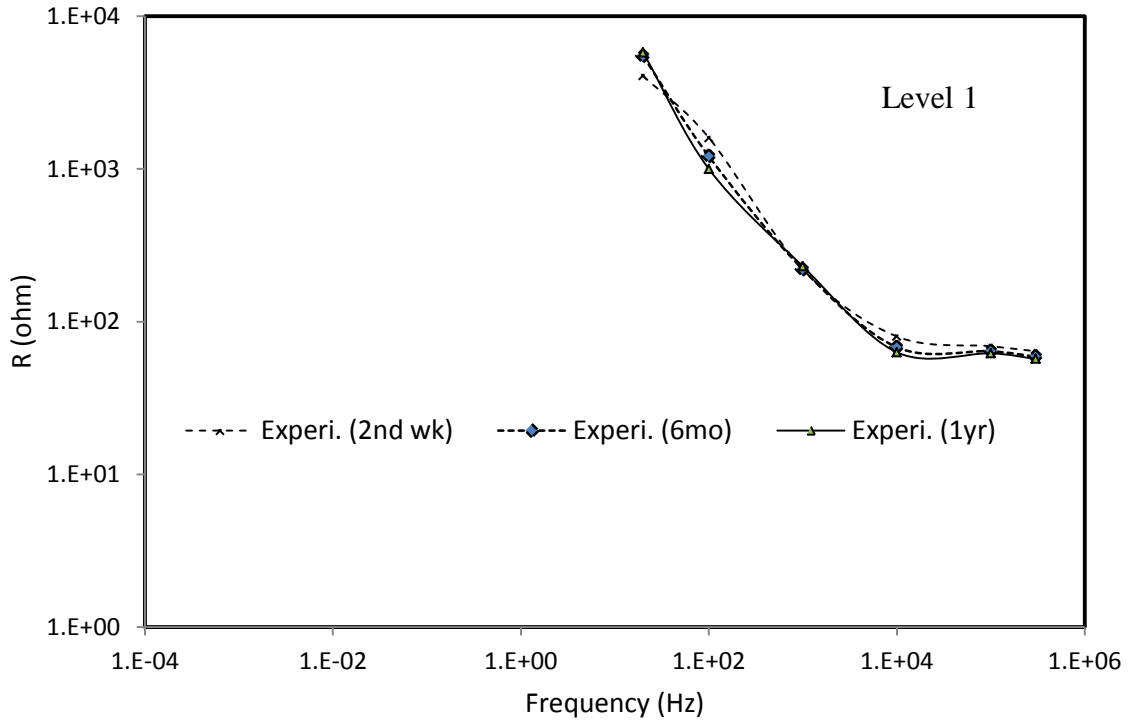


Figure 6.29 Bode plot of casing for level-1

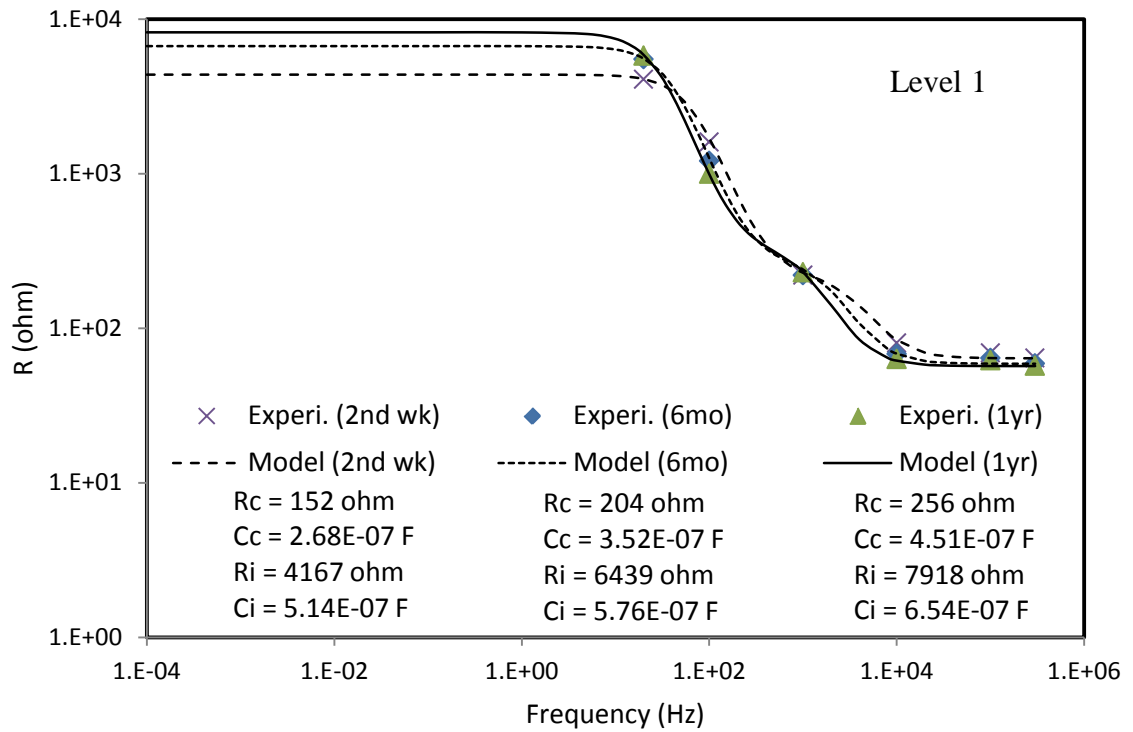


Figure 6.30 Bode plot of casing along respective impedance models for level-1

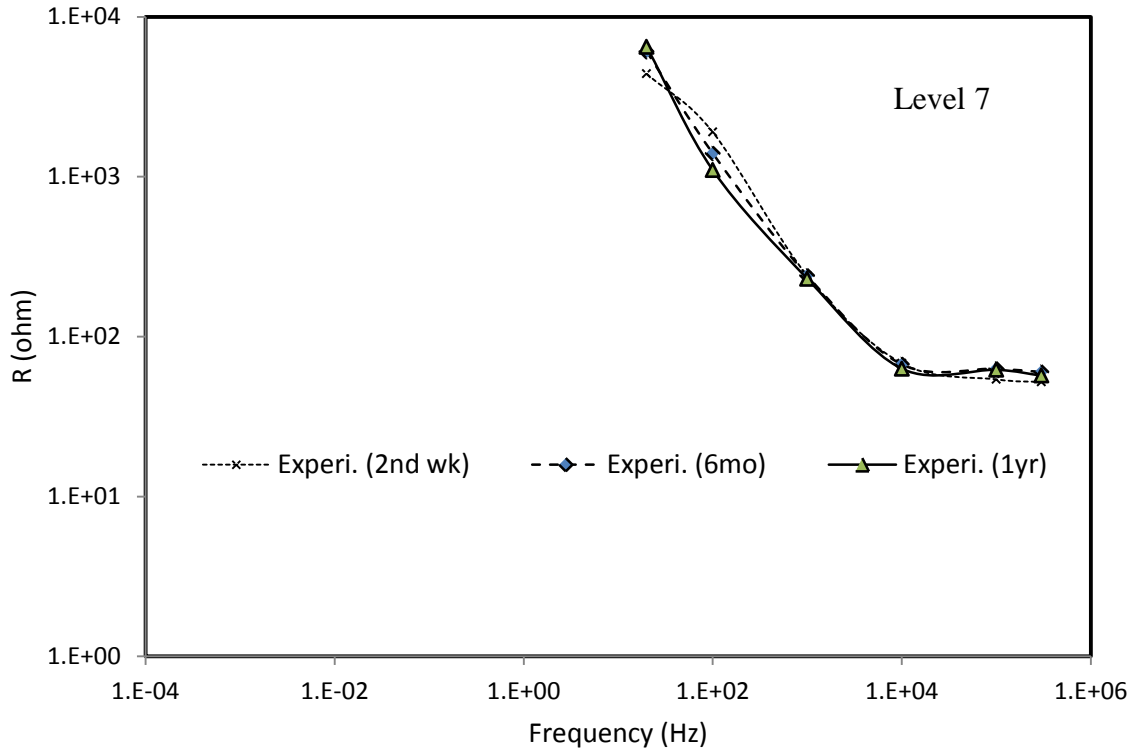


Figure 6.31 Bode plot of casing for level-7

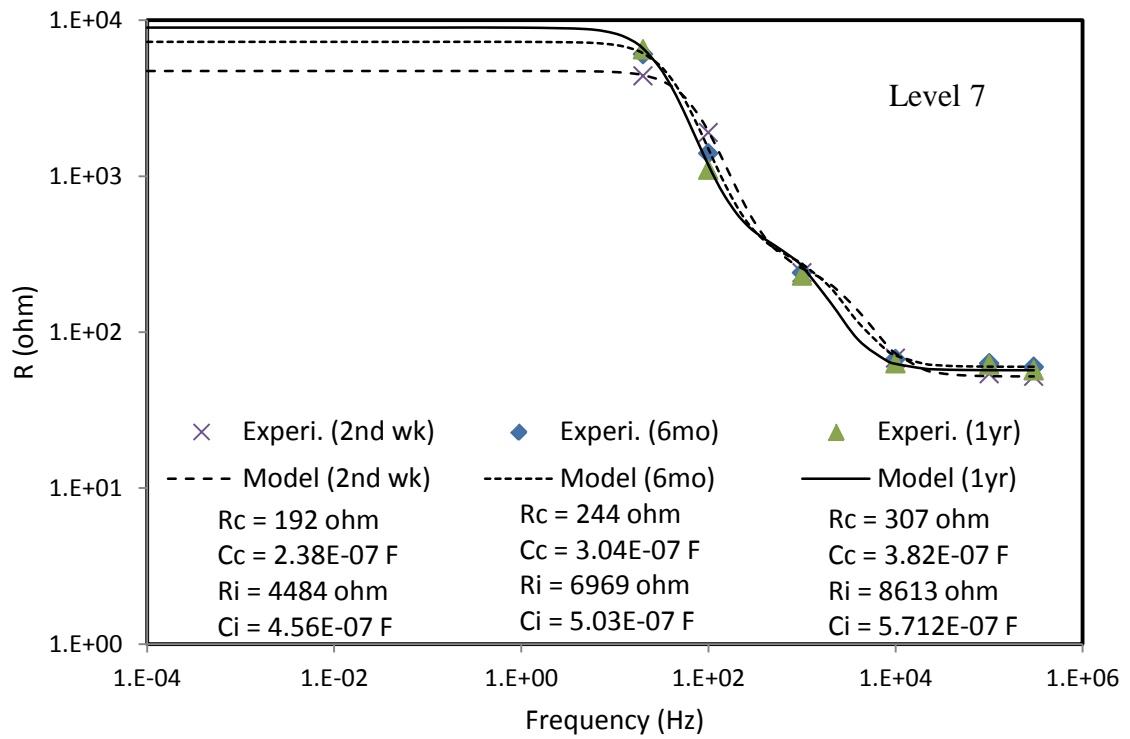


Figure 6.32 Bode plot of casing along respective impedance models for level-7

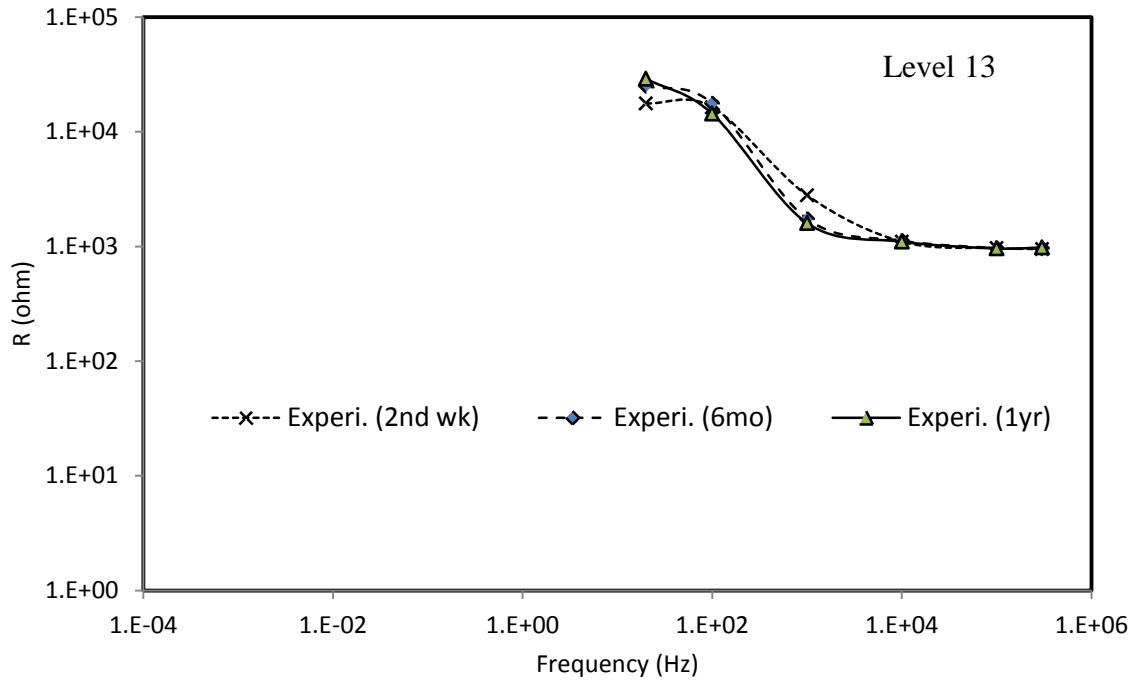


Figure 6.33 Bode plot of casing for level-13

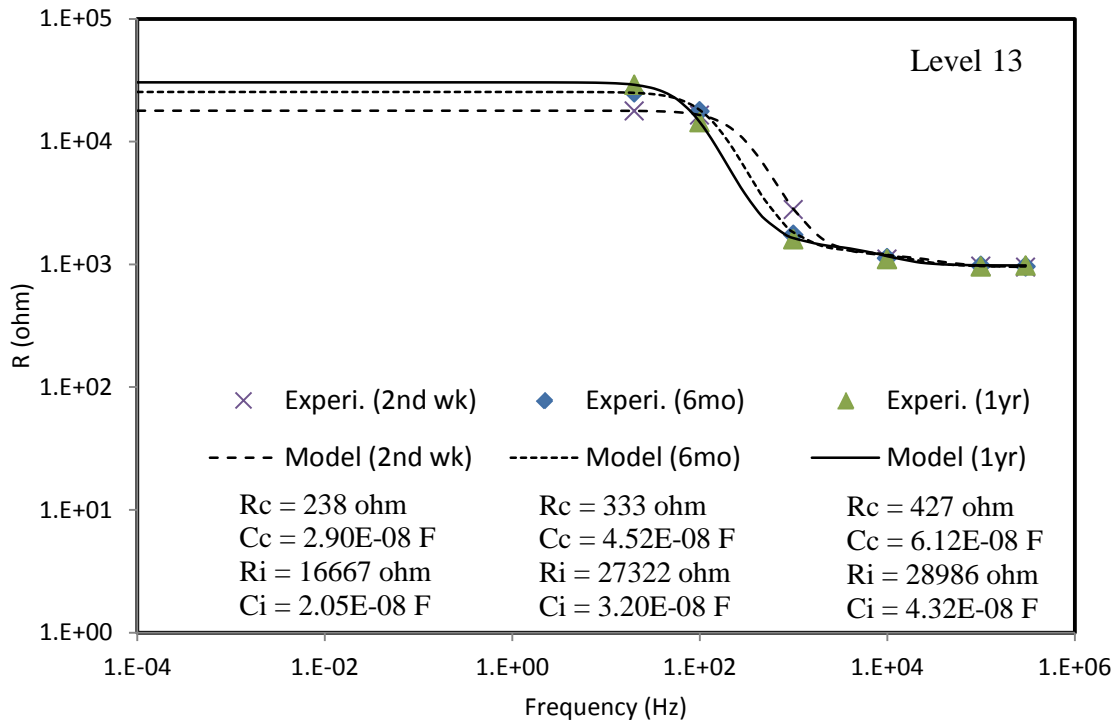


Figure 6.34 Bode plot of casing along respective impedance models for level-13

The resistance at the interface between of steel casing and the smart cement slurry ( $R_i$ ) and the resistance at the contact ( $R_c$ ) along the depth for the measuring time period of a year were shown in Figure 6.35. From Figure 6.35, it could be observed that the interface resistance ( $R_i$ ) was higher than the contact resistance ( $R_c$ ) along the depth during the course of the measuring time period. Both the interface resistance ( $R_i$ ) and the contact resistance ( $R_c$ ) were increased with respect to time and typical plots for levels 1, 7 and 13 were shown in Figure 6.36 through Figure 6.38.

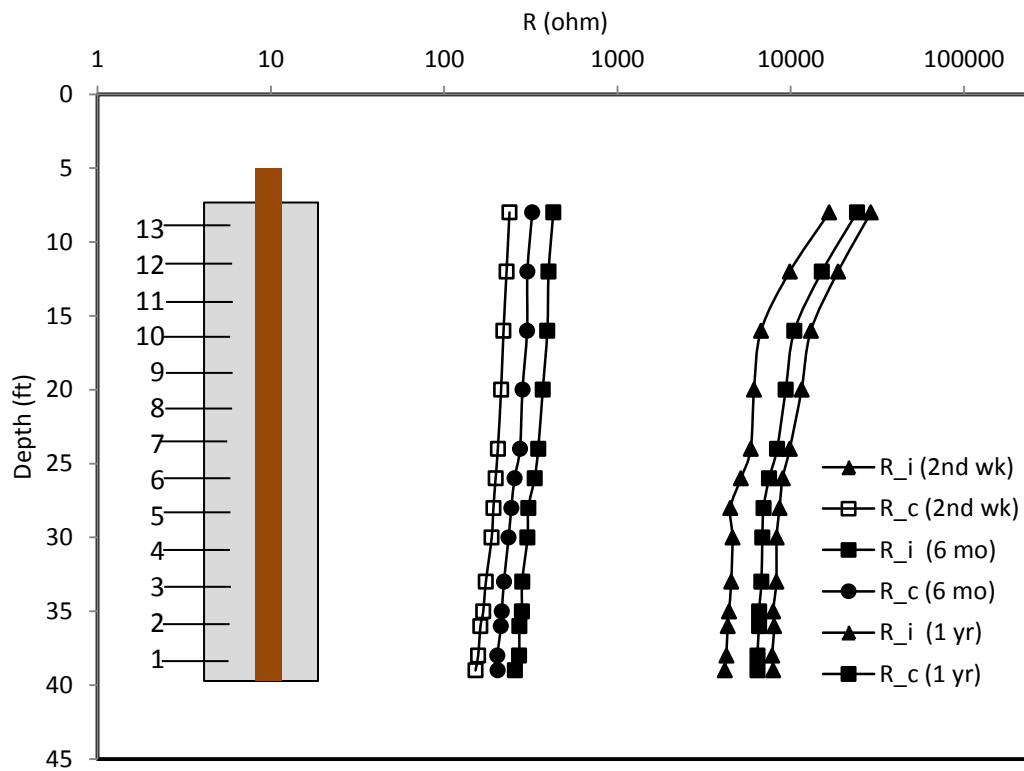


Figure 6.35 Resistance vs. depth of the casing at each measuring level

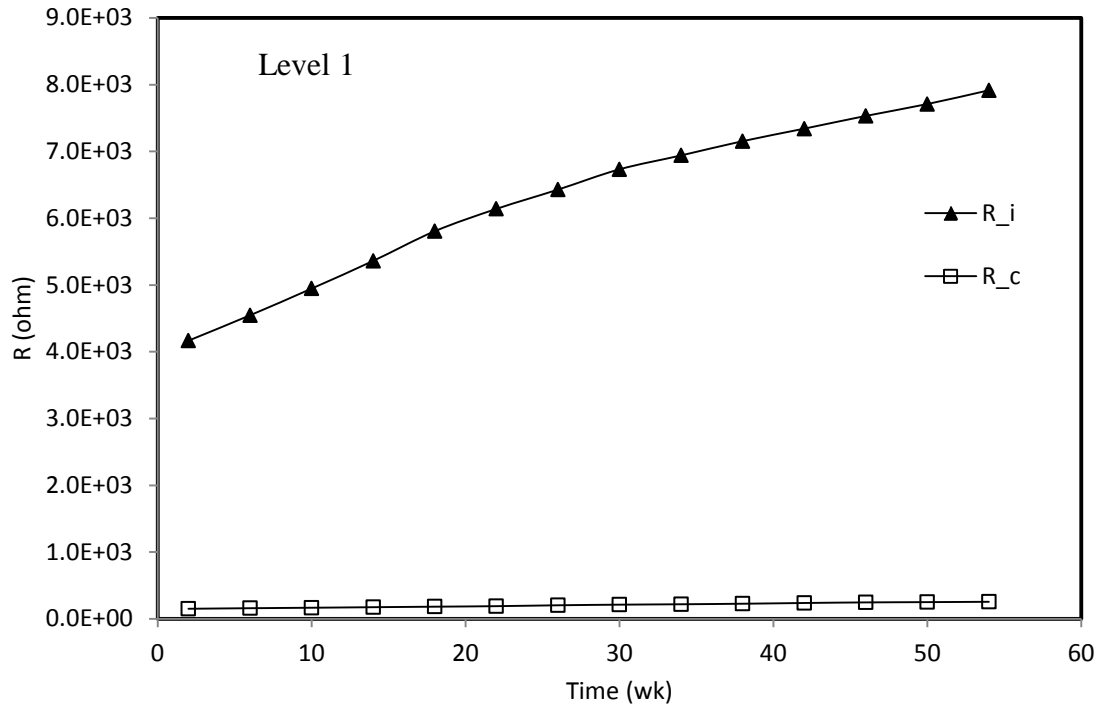


Figure 6.36 Resistances (Ri & Rc) of the casing at level-1 for one year period

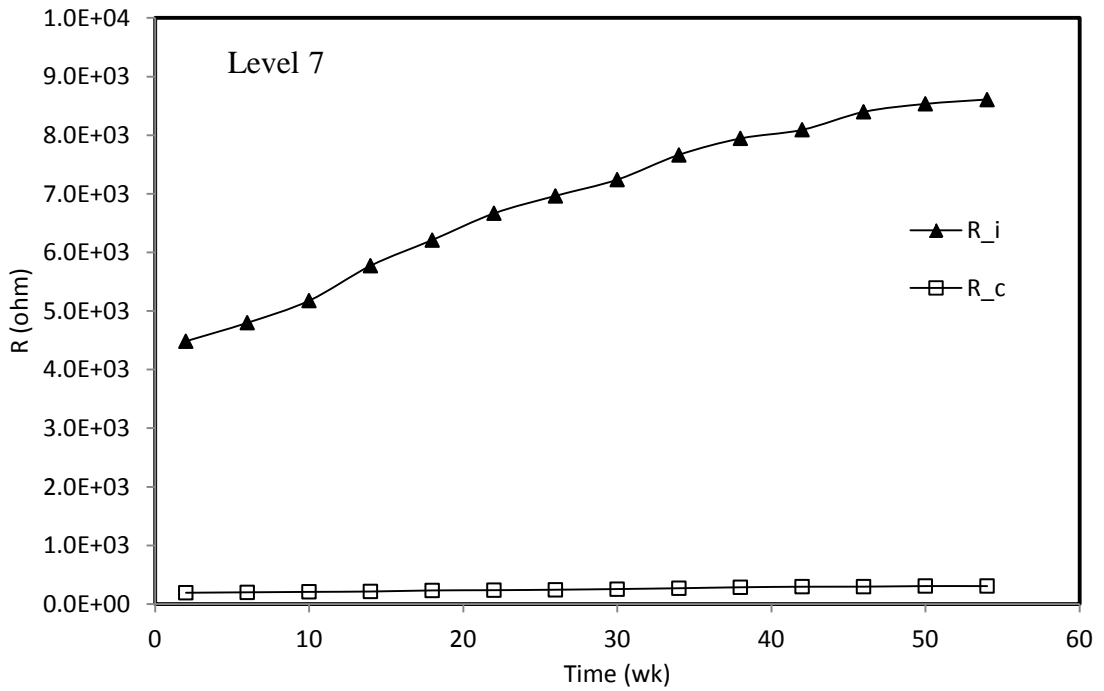


Figure 6.37 Resistances (Ri & Rc) of the casing at level-7 for one year period

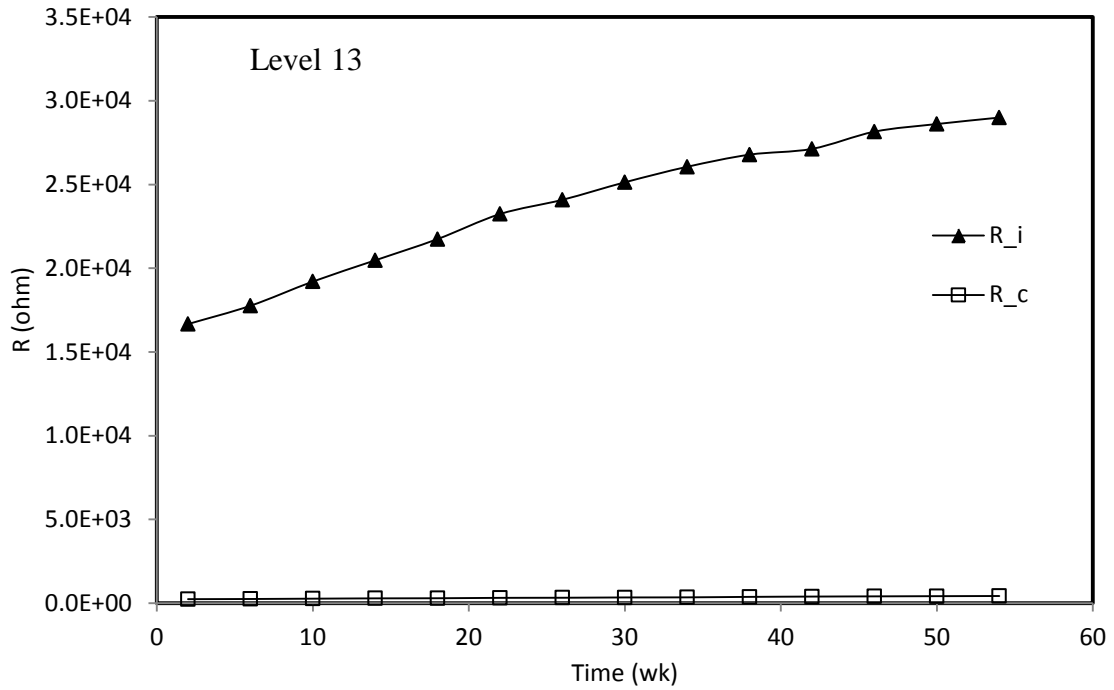


Figure 6.38 Resistances (R<sub>i</sub> & R<sub>c</sub>) of the casing at level-13 for one year period

The capacitance at the interface between of steel casing and the smart cement slurry (C<sub>i</sub>) and the capacitance at the contact (C<sub>c</sub>) along the depth for the measuring time period of a year were shown in Figure 6.39. From Figure 6.39, it could be observed that the interface capacitance (C<sub>i</sub>) was higher than the contact capacitance (C<sub>c</sub>) along the depth during the course of the measuring time period. Both the interface capacitance (C<sub>i</sub>) and the contact capacitance (C<sub>c</sub>) were increased with respect to time and typical plots for levels 1, 7 and 13 were shown in Figure 6.40 through Figure 6.42.

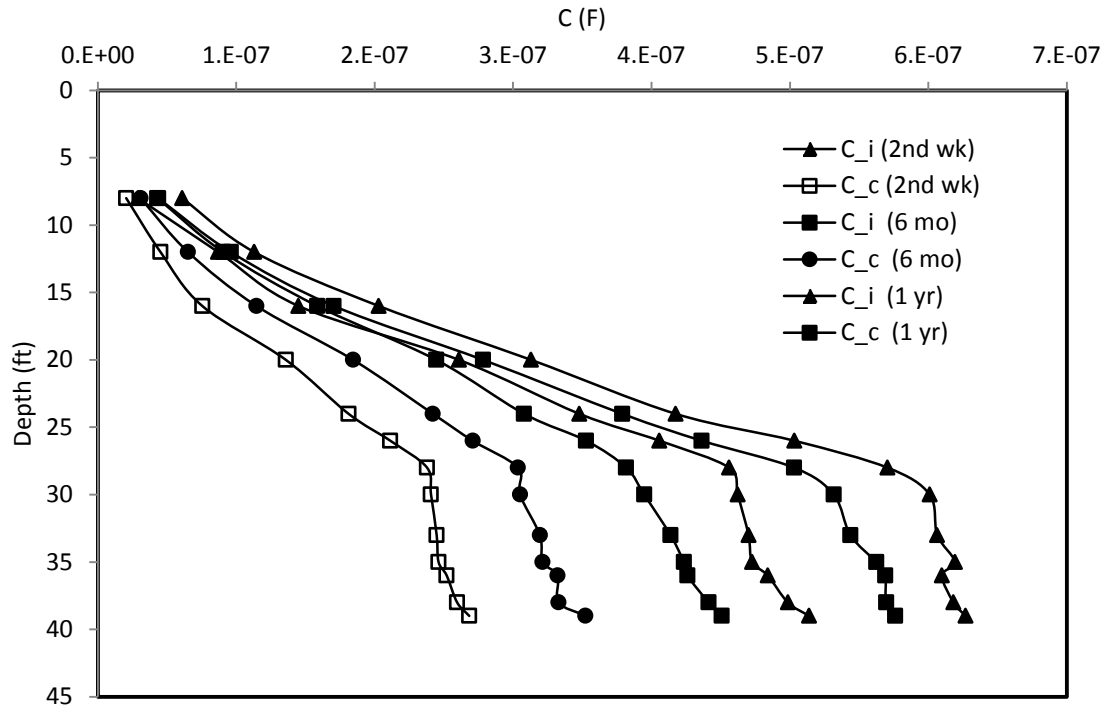


Figure 6.39 Capacitance vs. depth of the casing at each measuring level

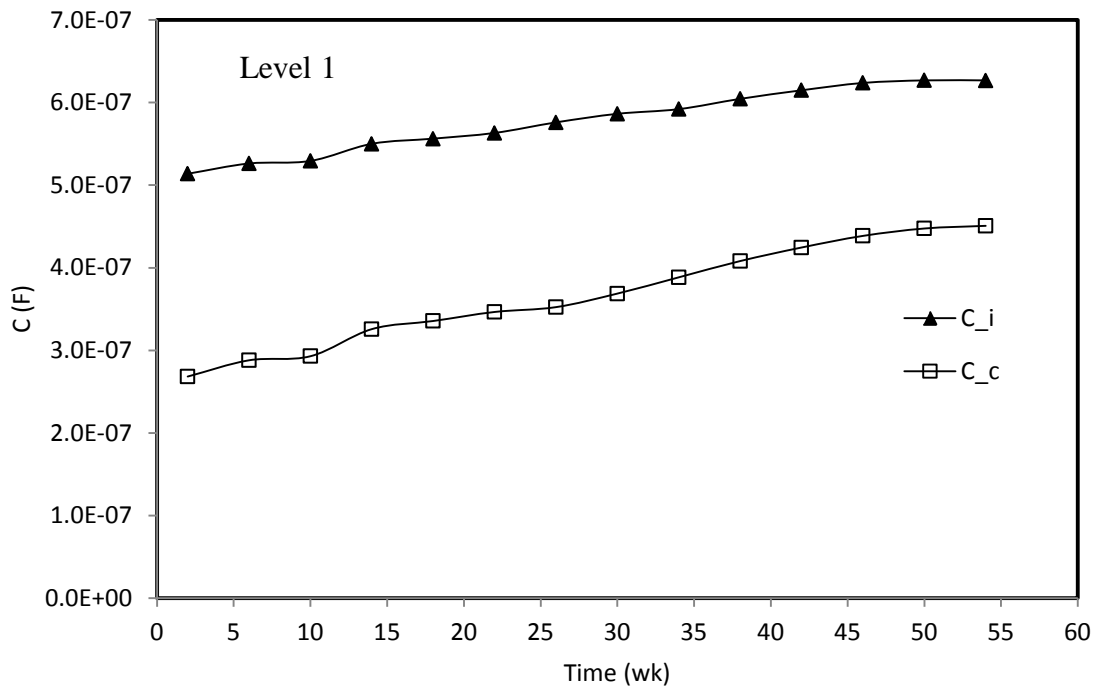


Figure 6.40 Capacities (Ci & Cc) of the casing at level-1 for one year period

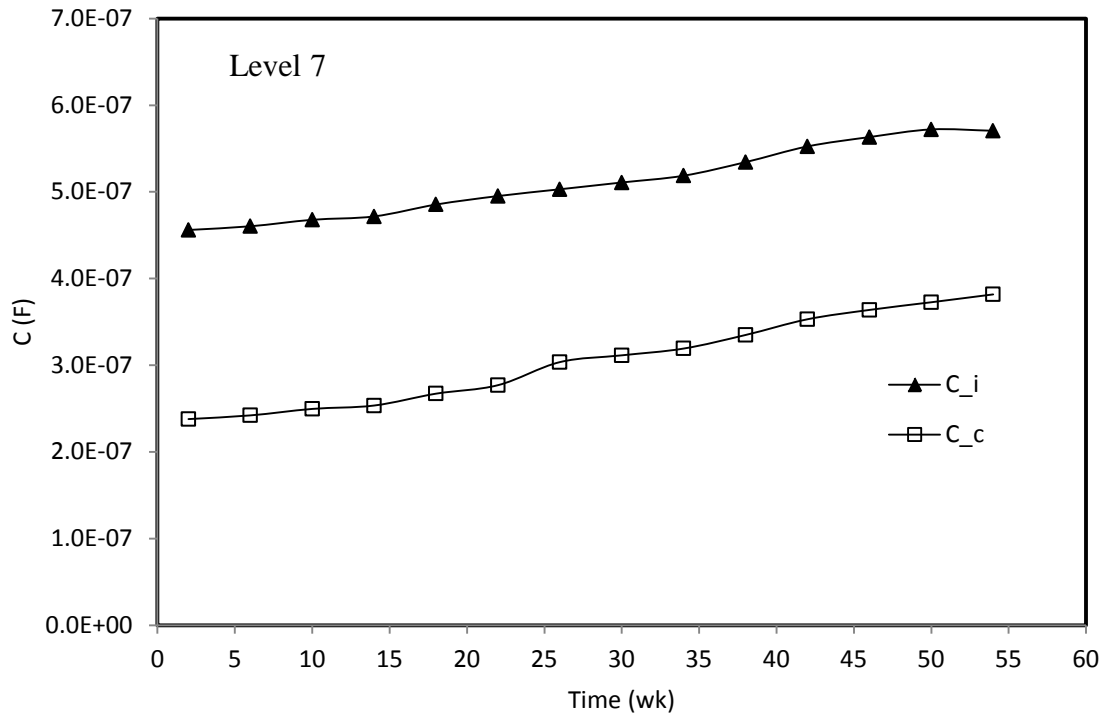


Figure 6.41 Capacities (Ci & Cc) of the casing at level-7 for one year period

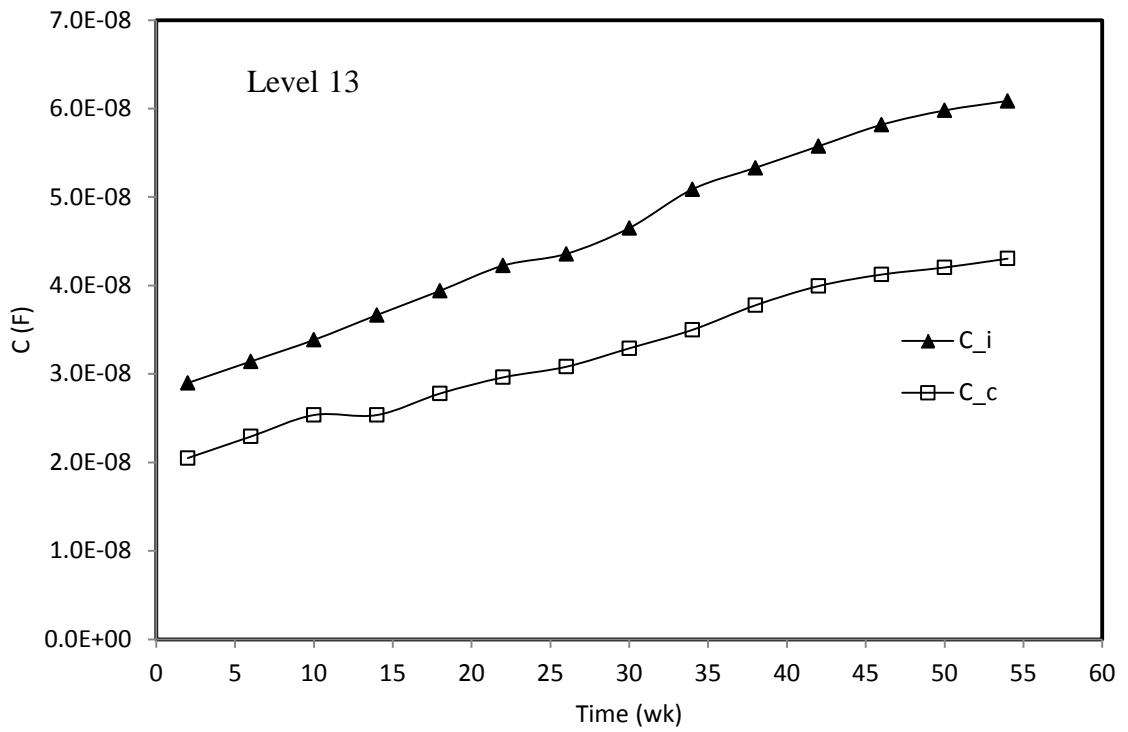


Figure 6.42 Capacities (Ci & Cc) of the casing at level-13 for one year period

The material property parameter defined as product of resistance and capacitance,  $R^*C$ , for the steel casing buried in the smart cement is shown Figure 6.43. From the Figure 6.43, the interface  $R_i^*C_i$  between of the steel casing and the smart cement slurry was greater than the  $R_c^*C_c$  at the cement contact along the depth for the measuring time period of a year. Both the interface  $R_i^*C_i$  and the contact  $R_c^*C_c$  were increased with respect to time and typical plots for levels 1, 7 and 13 were shown in Figure 6.44 through Figure 6.46.

The general trend of rates of increase in both  $R_i^*C_i$  and  $R_c^*C_c$  were changed below the depth of about 20 ft. from the ground. This could be attributed to the presence of ground water in the vicinity at about 20 ft. below the ground. Therefore, from Figure 6.35.through Figure 6.43, it could be observed that it was possible to detect and quantify the presence of the corrosion in the steel casing buried in the cement slurry.

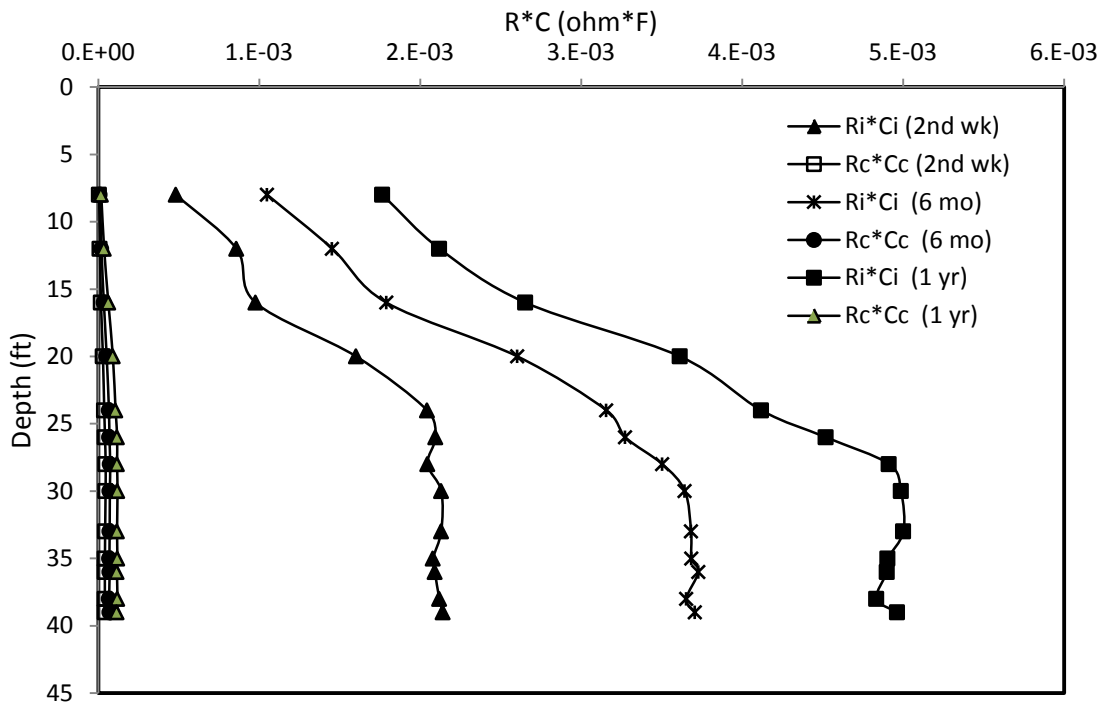


Figure 6.43  $R^*C$  vs. depth of the casing at each measuring level

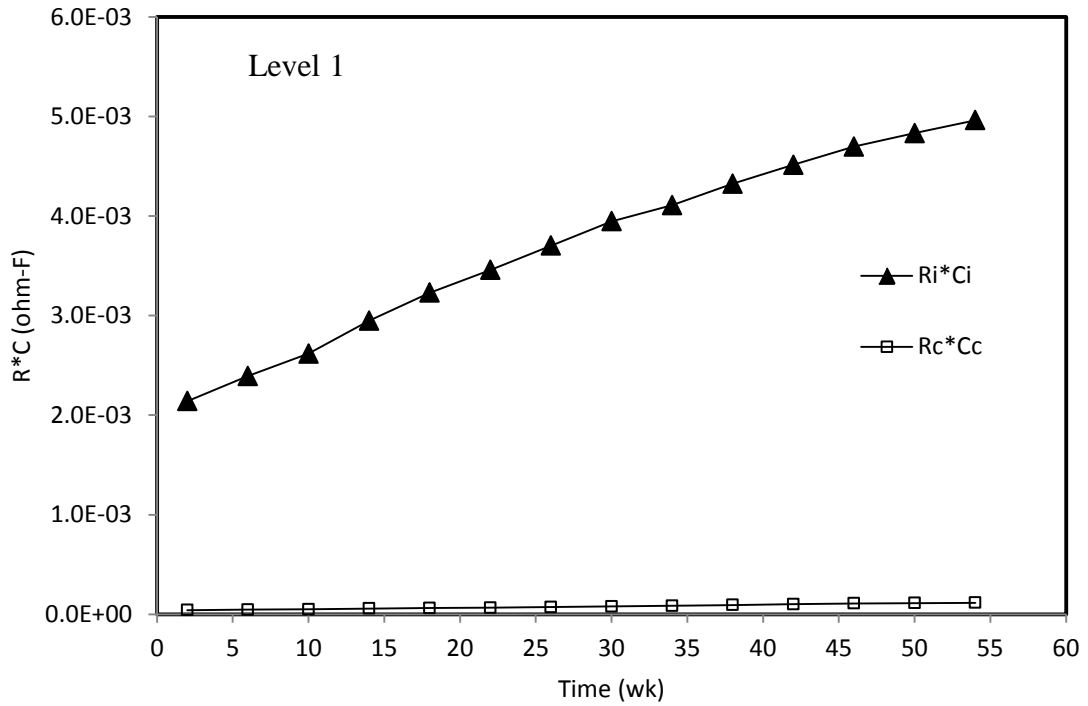


Figure 6.44 R\*C vs. depth of the casing at level-1 for one year period

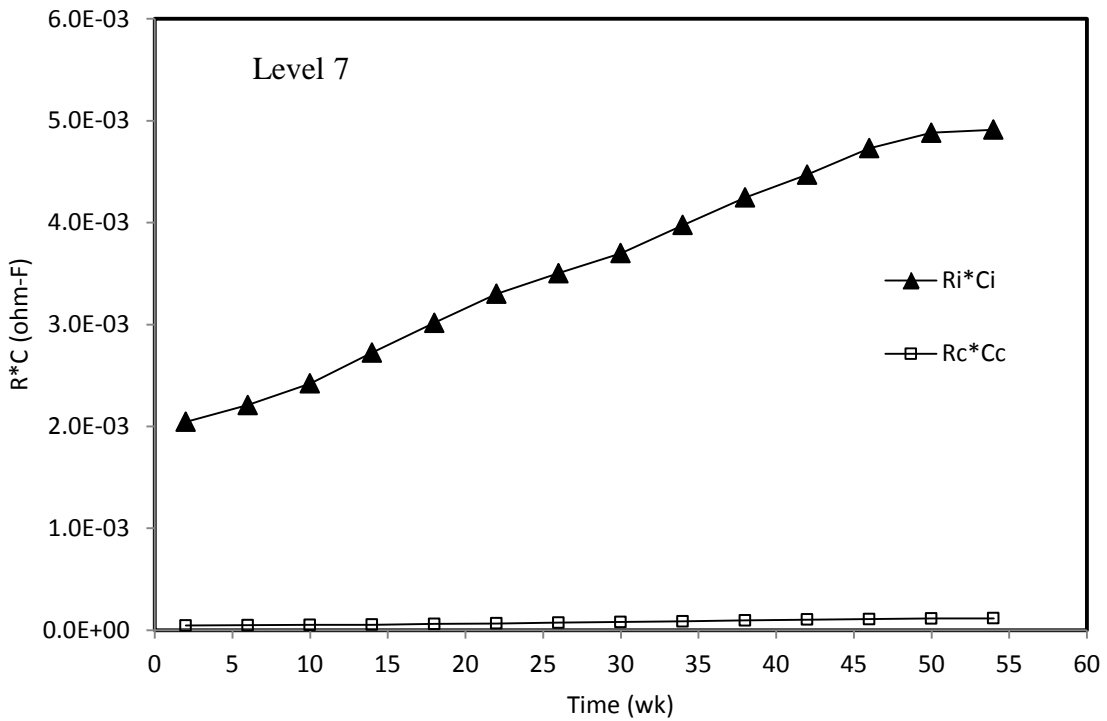


Figure 6.45 R\*C vs. depth of the casing at level-7 for one year period

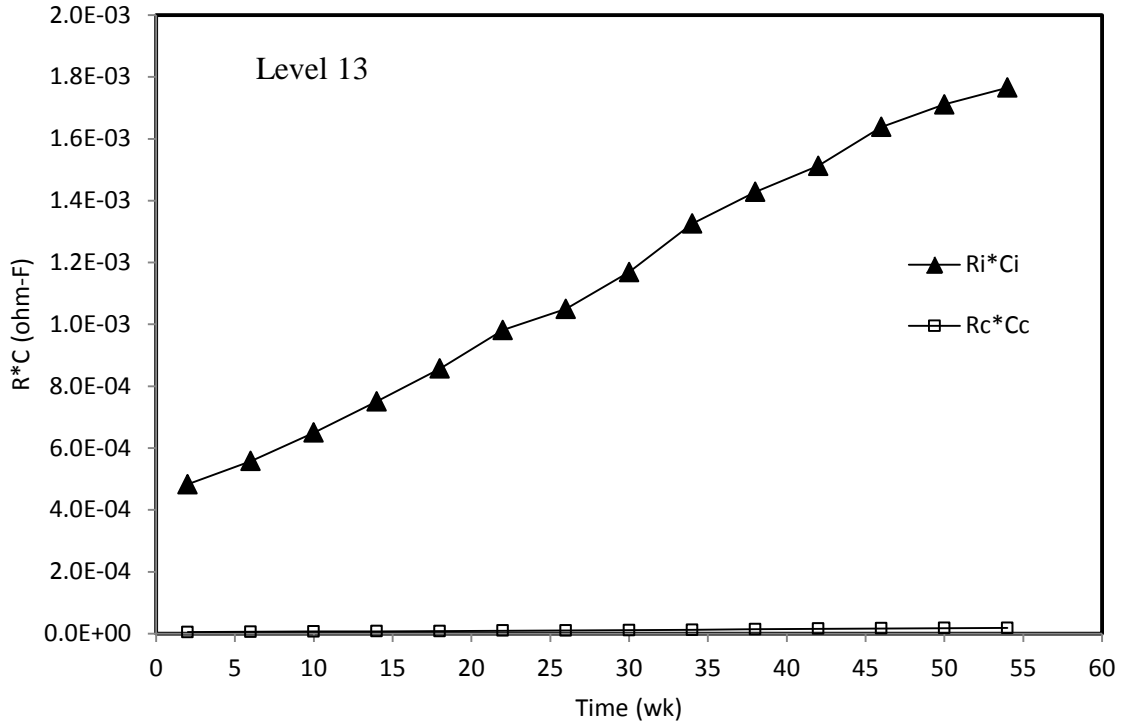


Figure 6.46  $R \cdot C$  vs. depth of the casing at level-13 for one year period

The progression of the interface corrosion with respect to time is modeled using equation (5-10) of p-q model and typical plots for level-1, level-7, and level-13 are shown in Figure 6.47, Figure 6.48, and Figure 6.49 respectively. For level-1, the model parameters p is estimated to be 0.18 and q is estimated to be in range of 0.28 and 0.31. As  $t \rightarrow \infty$ , the corresponding interface corrosion parameter  $R_i C_i$  is estimated to be between 1.13E-02 ohm-F and 1.19E-02 ohm-F using equation (5-11). The initial interface corrosion parameter was  $(R_i C_i)_0$  was 2.14E-03 ohm-F. For level-7, the model parameters p is estimated to be 0.18 and q is estimated to be in range of 0.27 and 0.30. As  $t \rightarrow \infty$ , the corresponding interface corrosion parameter  $R_i C_i$  is estimated to be 1.10E-02 ohm-F and 1.15E-02 ohm-F using equation (5-11). The initial interface corrosion parameter was

$(R_i C_i)_o$  was  $2.05E-03$  ohm-F. For level-13, the model parameters  $p$  is estimated to be 0.18 and  $q$  is estimated to be in range of 0.25 and 0.28. As  $t \rightarrow \infty$ , the corresponding interface corrosion parameter  $R_i C_i$  is estimated to be  $3.48E-03$  ohm-F and  $3.75E-03$  ohm-F using equation (5-11). The initial interface corrosion parameter was  $(R_i C_i)_o$  was  $4.83E-04$  ohm-F.

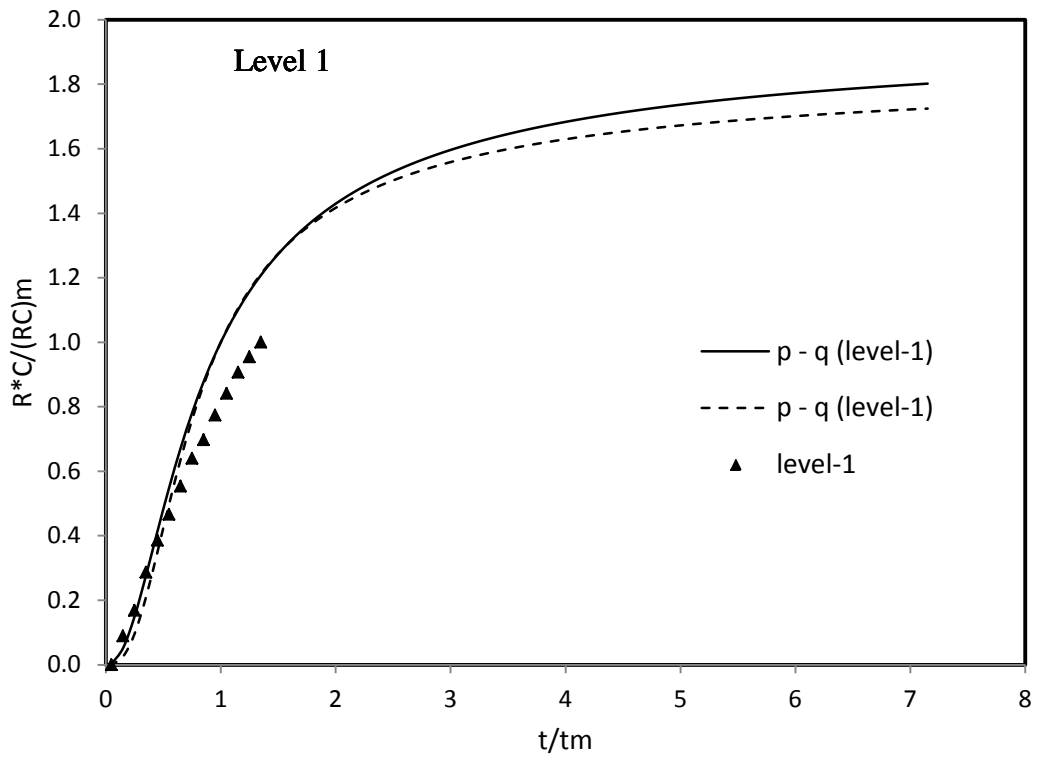


Figure 6.47 Corrosion-time model for the casing at level-1

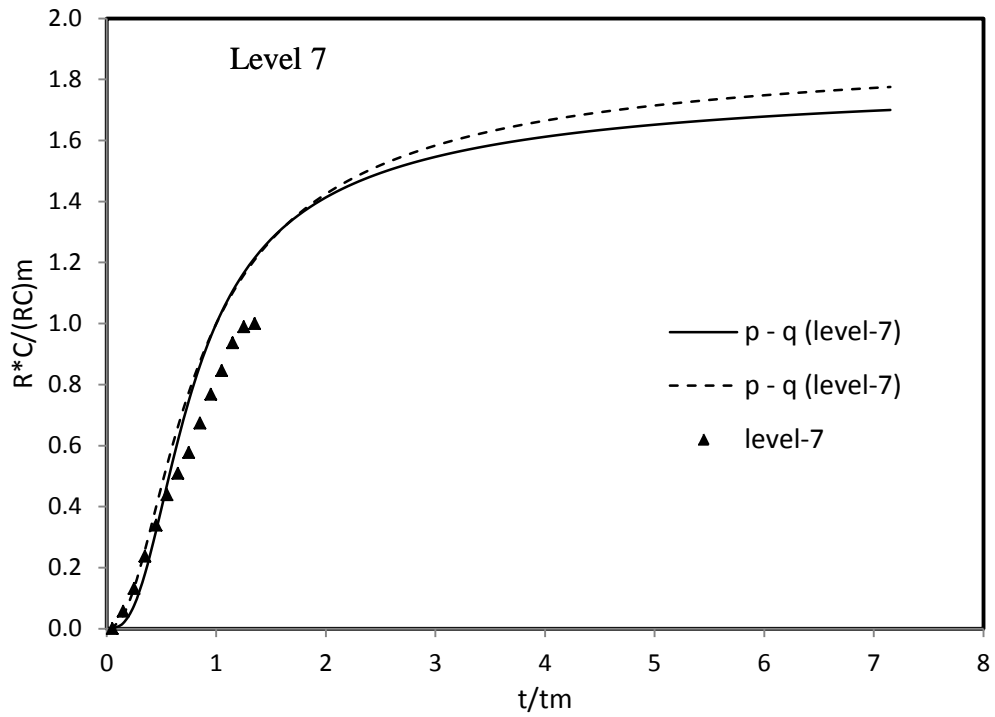


Figure 6.48 Corrosion-time model for the casing at level-7

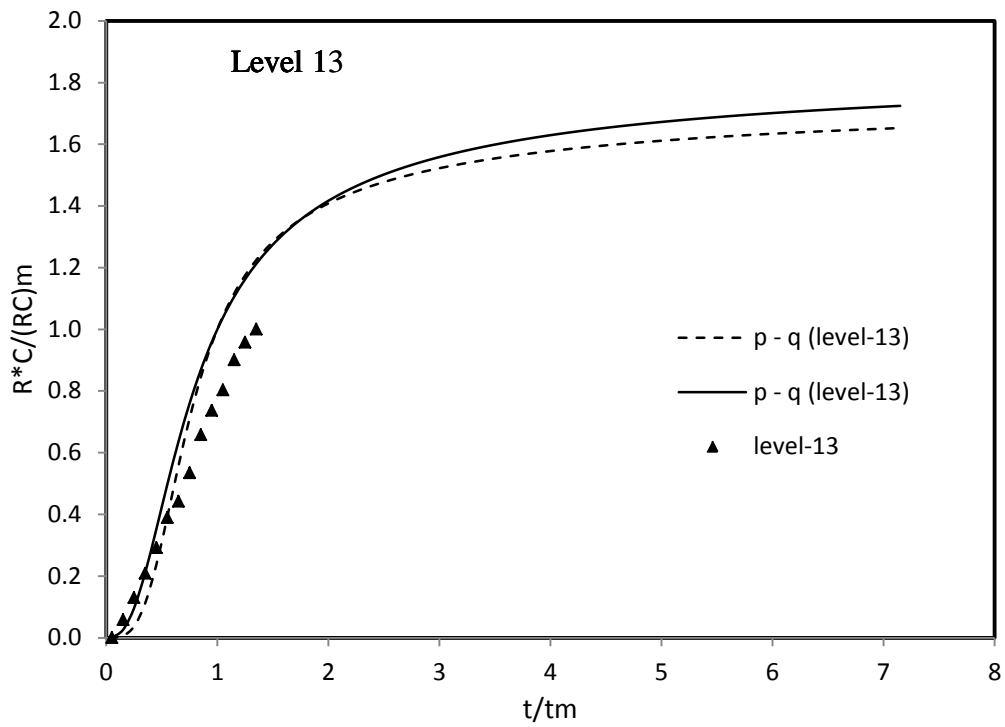


Figure 6.49 Corrosion-time model for the casing at level-13

For comparison purpose, the progression of the interface corrosion with respect to time for the laboratory corroded cement composite tests and the field tests are shown in Figure 6.50. From Figure 6.50, it can be observed that the laboratory tests would result in more severe corrosion level than the field model tests. The non-uniformity of the corrosion presence along the depth of the casing can also be observed from the different p-q model for level-1, level-7, and level-13 from Figure 6.50.

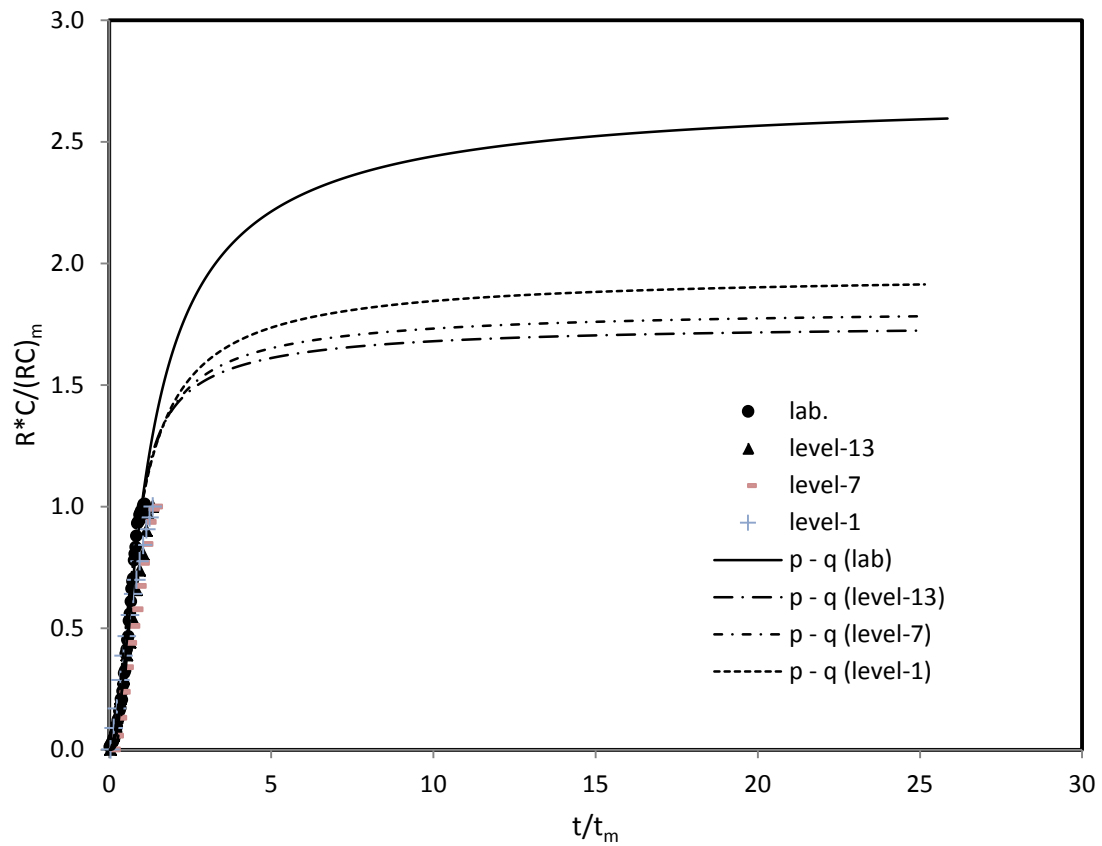


Figure 6.50 Corrosion-time model for corroded cement composite and field casing

### 6.3 Summary

In this study, the interface corrosion between steel and smart cement for large model test and field model test were investigated for their impedances spectroscopy properties. A material property which characterizes the interface corrosion was determined to be as product of interface resistance and interface capacitance,  $R_i \cdot C_i$ . And the following summaries and conclusions could be made:

1. Towards the bottom of the 8 ft. long large model test, the  $R_i \cdot C_i$  of interface corrosion was increased from  $6.67E-5$  ohm-F to  $1.94E-4$  ohm-F during the testing period of about a year.
2. Towards the mid height of the 8 ft. long large model test, the  $R_i \cdot C_i$  of interface corrosion was increased from  $5.30E-5$  ohm-F to  $1.89E-4$  ohm-F during the testing period of about a year.
3. Towards the top of the 8 ft. long large model test, the  $R_i \cdot C_i$  of interface corrosion was increased from  $3.64E-5$  ohm-F to  $1.64E-4$  ohm-F during the testing period of about a year.
4. Towards the bottom of the 40 ft. field model test, the  $R_i \cdot C_i$  of interface corrosion was increased from  $2.14E-3$  ohm-F to  $4.96E-3$  ohm-F during the testing period of about a year.
5. Towards the mid height of the 40 ft. field model test, the  $R_i \cdot C_i$  of interface corrosion was increased from  $4.83E-4$  ohm-F to  $1.74E-3$  ohm-F during the testing period of about a year.

6. Towards the top of the 40 ft. field model test, the  $R_i \cdot C_i$  of interface corrosion increased from  $2.05E-3$  ohm-F to  $4.91E-3$  ohm-F during the testing period of about a year.

## CHAPTER 7

### CONCLUSION AND RECOMMENDATION

This study was focused on the investigation of interface corrosion of steel embedded in smart coating such as smart cement, smart polyester and smart polymer concrete. For laboratory tests, non-corroded and corroded steel bars that were embedded in the smart coatings were investigated under dry-air condition and under salt-water solution for a period of about a year. An 8 ft. long steel casing embedded in smart cement slurry for a laboratory test and 40 ft. long steel casing buried in a borehole with smart cement slurry for field test were also investigated for the interface corrosion for testing time period of about a year.

#### 7.1 Conclusion

Based on the findings of this study, the following conclusions are drawn:

1. The presence of corrosion at interface between steel bar or casing and its coating could be detected and quantified using the presented non-destructive test method.
2. The surface corrosion in steel specimens exposed to acid solutions has been quantified and the changes were in the range of 10% to 1,800% while that of bulk corrosion were in the range of 130% to 370,000%.
3. The interface corrosion in the smart cement composite was generally more corroded than that of smart polyester composite and smart polymer concrete composite.
4. The interface corrosion of smart cement composite embedding corroded steel bars was increased from  $2.56E-4$  ohm-F to  $5.41E-2$  ohm-F while smart cement composite embedding non-corroded was increased  $3.72E-5$  ohm-F to  $7.34E-3$  ohm-F during the

- yearlong testing period. These values are in agreement with the steel bars surface corrosion of  $1.35\text{E-}3$  ohm-F to  $3.82\text{E-}3$  ohm-F.
5. The change in the interface corrosion for the non-corroded steel-cement composite exposed in various environmental conditions varied from 0% to 19,600%.
  6. The change in the interface corrosion for corroded steel-cement composite exposed in various environmental conditions varied from 580% to 145,000%.
  7. The bulk property changes in the smart cement used to protect the corroded steel was in the range of 2,900% to 11,400%.
  8. The interface corrosion of smart polyester composite embedding corroded steel bars was increased from  $3.14\text{E-}4$  ohm-F to  $3.80\text{E-}4$  ohm-F while smart polyester composite embedding non-corroded was between  $2.47\text{E-}4$  ohm-F to  $2.67\text{E-}4$  ohm-F during the yearlong testing period. Since these values are in close the non-corroded steel bar of  $1.87\text{E-}4$  ohm-F, it could be suggested that the steel bars were well protected by the polyester coating and indicated minimal presence of corrosion.
  9. The change in the interface corrosion for the non-corroded steel-polyester composite exposed in various environmental conditions varied from 0% to 8%.
  10. The change in the interface corrosion for corroded steel-polyester composite exposed in various environmental conditions varied from 27% to 54%.
  11. The bulk property changes in the smart polyester used to protect the corroded steel was in the range of 57% to 310%.
  12. The interface corrosion of smart polymer concrete composite embedding corroded steel bars was increased from  $4.95\text{E-}4$  ohm-F to  $5.81\text{E-}4$  ohm-F while smart polymer concrete composite embedding non-corroded was between  $6.16\text{E-}5$  ohm-F to  $7.31\text{E-}5$

- ohm-F during the yearlong testing period. By comparing these values with that of the non-corroded steel bar which is  $1.87E-4$  ohm-F, it could be suggested that the corroded polymer concrete composite exhibited continual corrosion while non-corroded polymer concrete exhibited relatively lesser corrosion.
13. The change in the interface corrosion for the non-corroded steel-polymer concrete composite exposed in various environmental conditions varied from 0% to 19%.
  14. The change in the interface corrosion for corroded steel-polymer concrete composite exposed in various environmental conditions varied from 27% to 54%.
  15. The bulk property changes in the smart polymer concrete used to protect the corroded steel was in the range of 24% to 62%.
  16. For the large model laboratory test, the interface corrosion was increased from  $3.64E-5$  ohm-F to  $1.94E-4$  ohm-F during the yearlong testing period. By comparing these values with that of the non-corroded steel bar which is  $1.87E-4$  ohm-F, it could be suggested that the steel casing underwent minimal corrosion.
  17. The change in the interface corrosion for the large model test varied from 97% to 422%.
  18. For the field model test, the interface corrosion was increased from  $4.83E-4$  ohm-F to  $4.96E-3$  ohm-F during the yearlong testing period. By comparing these values with that of the non-corroded steel bar which is  $1.87E-4$  ohm-F, it could be suggested that the steel casing were initially corroded and got more corroded.
  19. The change in the interface corrosion for the large model test varied from 1,200% to 13,200%.

## **7.2 Recommendation**

Based on the findings in this study, the following recommendations are suggested with reference to future research:

1. The interface corrosion of other types of metals such as aluminum and copper can be studied in similar procedures.
2. The interface corrosion of steel bars in chloride contaminated concrete mix could be studied.
3. The effect of temperature and other severe corrosive environments could be considered into the investigation of their effect on the interface corrosion

## REFERENCES

ASTM G62-07 “Standard Test Methods for Holiday Detection in Pipeline Coatings,”

ASTM International, 2013

ASTM G78-01 “Standard Guide for Crevice Corrosion Testing of Iron-Base and Nickel-

Base Stainless Alloys in Seawater and Other Chloride-Containing Aqueous

Environments,” ASTM International, 2012

ASTM D1654-08 “Standard Test Method for Evaluation of Painted or Coated Specimens

Subjected to Corrosive Environments,” ASTM International, 2008

Wheat, H. G., “Smart Coatings for Corrosion Detection-A Review of Recent Advances,”

International Society of Offshore and Polar Engineers (ISOPE), 2012

Bartels, K.A., Kwun, H., and Hanley, J.J. “Magnetostrictive Sensors for the

Characterization of Corrosion in Bars and Prestressing Strands,” 1996, pp. 40-50

Brondel, D., Edwards, R., Hayman, A., Hill, D., Mehta, S. and Semerad, T., “Corrosion

in Oil and Gas Industry,” Oilfield Review April 1994, Schlumberger, Volume 6, No.2

Champion Technologies, “Corrosion Mitigation for Complex Environments”. Champion

Technologies, Houston, 2012

Chaoyang, F. and Z. Jiashen, (1998) “Corrosion fatigue behavior of carbon steel in

drilling fluids,” Corrosion, Vol.54, No.8, 1998, 651-656

Cheung, C.W.S. and Walsh, F.C., “Microbial Contributions to the Marine Corrosion of

Steel Piling.” International Biodeterioration & Biodegradation, 1994, 259-274

Decker, J. B., Rollins, K. M. and Ellsworth, J. C., "Corrosion Rate Evaluation and Prediction for Pile Based on Long-Term Field Performance." Geotechnical and Geoenvironmental Engineering, 2008, 341-351

Fontana, Mars G., "Corrosion Engineering" 3rd ed, McGraw-Hill, 1987

Javaherdashti, R. "Microbiological Contribution to Accelerated Low Water Corrosion of Support Piles," Australasian Corrosion Conference, 2005

Jeffrey, R. and Melchers, R. E. "Corrosion of Vertical Mild Steel Strips in Sea Water," Corrosion Science 51, 2009, 2291-2297

Kermani M.B. and Smith L.M. (1997) "CO<sub>2</sub> Corrosion Control in Oil and Gas Production: Design Considerations" The Institute of Materials, European

Koch, G.H., Michiel P.H. Brongers, Neil G. Thompson, Y. Paul Virmani, and J.H. Payer, "Historic Congressional Study: Corrosion Costs and Preventative Strategies in the United States, a Supplement to Materials Performance," NACE International, Houston TX, July 2002

Kumar, A. and Stephnson, L. D. (2002). "Accelerated Low Water Corrosion of Steel Piling in Seawater." 30th International Navigation Congress

Li, Y. and Hou, B.R. (1999) "Study on Steel Corrosion in Different Seabed Sediments" Bull. Material Sci., Vol. 22, No. 7, pp 1037-1040

McDonald, M., Barr, k., Dubberley, S.R. and Wadsworth, G. (2007) "Use of Silicate-Based Drilling Fluids to Mitigate Metal Corrosion," Prepared for presentation at the 2007

SPE International Symposium on Oilfield Chemistry held in Houston, Texas, U.S.A., 28 February - 2 March, 2007

Norhazilan, M.N., Nordin, Y., Lim, K.S., Siti, R.O., Safuan, A.R.A., Norhamimi, M.H. (2012) "Relationship between Soil Properties and Corrosion of Carbon Steel" Journal of Applied Sciences Research, 8(3): 1739-1747, 2012 ISSN 1819-544X

Picozzi, O. E., Lamb, S. E., and Frank, A. C. (1993) "Evaluation of Prediction Methods for Pile Corrosion at the Buffalo Skyway," New York State Dept. of Transportation, Technical Services Division, Albany, N.Y.

Popoola, L.T., Grema, A.S., Latinwo, G.K., Gutti, B. and Balogun, A.S. (2013) "Corrosion Problems during Oil and Gas Production and Its Mitigation," International Journal of Industry Chemistry, 2013, 4:35

Roberge P.R. (2000) "Handbook of Corrosion Engineering," McGraw-Hill, New York

Romanoff, M. (1962). "Corrosion of Steel Pilings in Soils," United States Department of Commerce, National Bureau of Standards Monograph, 58

Rozene, D.J. and Draege, E.V., (2009) "Underwater Steel Structures: Inspection, Repair and Maintenance," DOD Corrosion Conference.

Saha, J.K., P.K. Mitra, S. Paul, and D.D.N. Singh, "Corrosion evaluation of painted steel panels by electrochemical measurement," NACE International, April 2010

Tomoe, Y., Shimizu, M. and Nagae, Y. (1999) "Unusual Corrosion of A Drill Pipe in Newly Development Drilling Mud during Deep Drilling," Corrosion, 1999 Federation of Corrosion Publications, London

Vipulanandan, C. and Paul, E. (1990) "Performance of Epoxy and Polyester Polymer Concrete," ACI Materials Journal, Vol. 87, No. 3, pp. 241-251

Vipulanandan, C. and Prashanth, P., "Impedance Spectroscopy Characterization of a Piezoresistive Structural Polymer Composite Bulk Sensor," Journal of Testing and Evaluation, Vol. 41, No. 6, 2013

Xu, Y., Yang, Q, Li, Q. and Chen, B. (2006) "The Oil Well Casing Anticorrosion And Control Technology of Changqing Oil Field," SPE International Oil & Gas Conference and Exhibition in China held in Beijing, China, 5-7 December 2006

Zhao, X. and Duan, J. (2007). "Effect of Sulfate-Reducing Bacteria on Corrosion Behavior of Mild Steel in Sea Mud," J. Mater. Sci. Technology., Vol. 23, pp323-327

